Measurement of the CP violation parameter A_Γ in $D^0 \to K^+K^-$ and $D^0 \to \pi^+\pi^-$ decays

Classe di Scienze Matematiche e Naturali
Corso di Perfezionamento in Fisica

PhD Thesis

SCUOLA NORMALE SUPERIORE

Pietro Marino

Advisor: Dr. Michael J. Morello

February 2017

Abstract

Time-dependent *CP* asymmetries in the decay rates of the singly Cabibbo-suppressed decays $D^0 \to K^+K^-$ and $D^0 \to \pi^+\pi^-$ are measured in pp collision data at centre-of-mass energies of 7 and 8 TeV collected by the LHCb detector during LHC Run I, corresponding to an integrated luminosity of $3\,\text{fb}^{-1}$. The strong-interaction decay $D^{*+} \to D^0\pi^+$ is used to infer the flavour of the D^0 mesons at production. The asymmetries in effective decay widths between D^0 and $\overline{D}^0$ decays, sensitive to indirect *CP* violation, are measured to be

$$A_\Gamma(D^0 \to K^+K^-) = (-0.30 \pm 0.32 \pm 0.10) \times 10^{-3},$$
$$A_\Gamma(D^0 \to \pi^+\pi^-) = (\ \ 0.46 \pm 0.58 \pm 0.12) \times 10^{-3},$$

where the first quoted uncertainty is statistical, and the second systematic. These measurements show no evidence of *CP* violation and improve on the precision of the previous best measurements by nearly a factor of two.

Contents

Abstract i

Contents iii

Introduction 1

1 Theory and motivations 5
- 1.1 The Standard Model of Particle Physics . . . 5
- 1.2 The CKM matrix . . . 9
- 1.3 Unitary triangles . . . 11
  - 1.3.1 Charm triangle parameters . . . 12
- 1.4 Neutral meson mixing . . . 13
  - 1.4.1 Time evolution of flavour eigenstates . . . 14
  - 1.4.2 Mixing phenomenology . . . 17
- 1.5 CP violation formalism . . . 19
  - 1.5.1 CP violation in the decay . . . 20
  - 1.5.2 CP violation in the mixing . . . 21
  - 1.5.3 CP violation in the interference . . . 21
- 1.6 D^0 time-dependent decay rates to CP-eigenstates . . . 21
  - 1.6.1 Effective decay widths . . . 22
- 1.7 Time dependent CP asymmetry . . . 23
- 1.8 A_Γ and y_{CP} observables . . . 24
  - 1.8.1 Experimental approximations . . . 25

2 Measurement overview and current experimental status 29
- 2.1 $D^0 \to h^+h^-$ decays and flavour tag . . . 29
- 2.2 From the theory to the A_Γ measurement . . . 30
  - 2.2.1 Raw CP asymmetry . . . 32
- 2.3 Control channel: $D^0 \to K^-\pi^+$ decays . . . 33
- 2.4 Physical background to A_Γ: secondary decays . . . 33
- 2.5 Current experimental status . . . 34
  - 2.5.1 Experiments at e^+e^- colliders . . . 35
  - 2.5.2 Experiments at hadron colliders . . . 35

3 Experimental apparatus **39**
3.1 LHC . . . 39
3.1.1 Luminosity at LHCb . . . 40
3.2 LHCb Experiment . . . 41
3.2.1 Coordinate system . . . 44
3.2.2 Magnet . . . 44
3.2.3 Vertex Locator . . . 45
3.2.4 Tracker Turicensis . . . 47
3.2.5 T-stations . . . 47
3.2.6 Cherenkov detectors . . . 49
3.2.7 Calorimeter system . . . 50
3.2.8 Muon detectors . . . 51
3.2.9 Trigger . . . 52
3.2.10 Data processing . . . 54
3.2.11 Event reconstruction . . . 54

4 Reconstruction and selection of D^0 mesons **59**
4.1 $D^{*+} \to D^0(\to h^+h^-)\pi^+$ decays at LHCb . . . 59
4.2 Trigger system . . . 61
4.3 Preselection . . . 63
4.4 Offline Selection . . . 64
4.5 Multiple candidates . . . 69
4.6 Sideband subtraction and Δm fit . . . 69
4.7 Charge-randomised sample . . . 74

5 Detector-induced time-dependent charge asymmetries **75**
5.1 Introduction . . . 75
5.2 Control channel pseudo-A_Γ . . . 76
5.3 Time-dependent instrumental effects . . . 78
5.4 Symmetrisation procedure . . . 79
5.4.1 Effects of the correction . . . 84
5.4.2 Could the symmetrisation procedure bias the value of A_Γ? . . . 85
5.4.3 Indirect generation of time-dependent asymmetries . . . 87
5.5 Robustness cross-checks . . . 89

6 The extraction of A_Γ parameter **93**
6.1 Analysis strategy . . . 93
6.2 Results . . . 94
6.3 Robustness cross-checks . . . 98
6.4 Analysis validation . . . 103

7 Systematic uncertainty on secondary decays **105**
7.1 Introduction . . . 105

7.2 Model of secondary decays . . . 106
7.3 Evaluation of secondary fraction f_{sec} . . . 108
7.4 Evaluation of A_{sec} . . . 109
7.5 Systematic uncertainty and robustness checks . . . 111

8 Robusteness checks and systematic uncertanties 115
8.1 Discretisation of the correction procedure . . . 115
8.2 Subtraction of random pion background . . . 116
8.3 Peaking backgrounds . . . 118
8.4 L0 trigger effects . . . 120
8.5 Multiple candidates . . . 121
8.6 Decay time resolution . . . 121
8.7 Summary . . . 122

9 Results and conclusion 123
9.1 Final results . . . 123
9.1.1 Combination . . . 123
9.2 A_Γ implications on charm *CP* violating parameters . . . 125
9.3 Future perspectives . . . 126
9.4 Conclusions . . . 128

A $D^0 \to K^\mp \pi^\pm$ decay rates 129
A.1 Pseudo-A_Γ . . . 130

B Mathematical formalism 133
B.1 Tagged $D^0 \to h^+ h^-$ events . . . 133
B.2 Tagged $D^0 \to K^- \pi^+$ events . . . 135

C A_Γ plots Legend 137

D Proper decay time bins 139

E Reweighing details 143
E.1 Symmetric reweigh . . . 143
E.2 Reweigh procedure of the asymmetry . . . 144
E.3 Reweighing weights . . . 147
E.4 Statistical degradation . . . 150

F Studies of assumptions about secondary decays model 153

Bibliography 157

Introduction

Over the course of the last 30 years, the Standard Model (SM) of elementary particles and their interactions has been extensively tested by experiments, establishing it as an extremely predictive and accurate description of Nature. Nevertheless, open questions and weaknesses remain, which suggest the need for a more fundamental theory. SM is not able to account for the cosmological observed baryonic-asymmetry and for the presence of Dark Matter in our Universe; the very low value of the Higgs mass is explained only through an "unnatural" fine-tuning cancellation between the radiative corrections and the bare mass; many parameters are necessary to account, in one-to-one correspondence, for the observed masses and mixings of quarks and leptons; lastly the gravity is not yet satisfactorily included in the model.

The search for experimental deviations from SM predictions, pointing the way to a different, more fundamental theory, is therefore the primary goal of the High Energy Physics community. From the experimental point of view this quest is conducted at two frontiers: (i) the "high energy frontier", which directly searches for hints of physics beyond the Standard Model (BSM) increasing the energy scale, and (ii) the "high intensity frontier" looking for inconsistencies between experimental measurements and theory predictions. At the first frontier, where ATLAS and CMS experiments are today the major players, New Physics (NP) is directly probed producing particles at more and more high energy and the main limitation comes only from the maximum achievable energy. The second frontier, instead, is based on performing more and more precise measurements, of known processes, by looking for discrepancies from SM predictions, and allows the indirect exploration of energies even higher than those accessible through direct searches. Of particular importance are processes having a low level of "SM noise", or in other words, processes suppressed within the SM or where the SM contribution is known with high precision. This is the domain of Heavy Flavour Physics, currently probed mainly by the LHCb, Belle II and BES III experiments, where the non-invariance of fundamental interactions under the combined symmetry transformations of charge conjugation and parity inversion (*CP* violation) plays a key role.

CP violation is described within the Standard Model through the Cabibbo-Kobayashi-Maskawa (CKM) mechanism [1, 2] by the presence of a single complex phase in the unitary three-generation quark-mixing matrix. All direct measurements of elementary particle phenomena to date support the CKM phase, within the current theoretical and experimental uncertainties, being the dominant source of *CP* violation observed in quark transitions. However, widely

accepted theoretical arguments and cosmological observations, as mentioned above, suggest that the SM might be a lower-energy approximation of more generally valid theories which are likely to possess a different *CP* structure and therefore should manifest themselves as deviations from the CKM scheme.

The charm sector is today a particularly good candidate to probe possible deviations from the theory, since the expected *CP* violation in the SM does not exceed $\mathcal{O}(10^{-2})$ [3–6], and a sizeable *CP* asymmetry would stand up as a possible manifestation of NP. The system of D neutral mesons is the only one in which the oscillation of an up-type quark can occur, and it is the only one sensitive to possible contributions to *CP* violation of up-type quark through mixing loops. In fact, top quarks decay before hadronizing [7], and particles composed by u and $\overline{u}$, like π^0 and η, are their own antiparticle, thus they are not able to oscillate as a matter of principle. Only very recently experiments have been able to collect and analyse huge samples of charm decays $\mathcal{O}(10^7)$ approaching for the first time the upper boundaries of the range of SM predictions, and possible NP contributions may completely have been missed by experimental searches so far. Therefore, the charm sector is a unique portal for obtaining an access to a new flavour dynamics. In addition, the complementarity to B and K meson systems, that have been much more deeply experimentally studied in the past decades, makes the exploration of the charm sector important by itself, for improving the current knowledge of heavy flavour dynamics within the SM. *CP* violation has not yet been observed in the charm sector, and only recently the slow mixing rate of the D^0–$\overline{D}^0$ flavour oscillations has been established [8], providing definitely a full range of probes for mixing and *CP* violation.

Except for a limited series of relevant experimental observables, hadronic uncertainties may greatly impact/limit the sensitivity of charm decays in probing new effects [9]. However, the increasing in precision of experimental measurements, together with the foreseen reduction on the uncertainties of several QCD parameters, should lead to a significant shrinkage of the theoretical uncertainties in the charm sector, and in many other flavour areas, allowing a powerful test of SM predictions in the next and far future. Anyway, it is worth to point out that an extensive study of the charm decays, and in general of the heavy flavour physics, at much higher precision than today is fundamental to over-constrain the theory parameters, and in particular the CKM scheme, that is a crucial ingredient for the SM and for any new exotic theory, which must include the flavour structure.

Examples of experimentally clean channels allowing the study of the *CP* violation in the charm system are the neutral singly-Cabibbo-suppressed decays into *CP*-eigenstates, such as $D^0 \to f$, where $f = K^+K^-$ and $f = \pi^+\pi^-$, which are now available in large numbers from hadron collisions. A golden observable sensitive to possible effects of *CP* violation is the A_Γ parameter, defined as the asymmetry of the effective decay widths $\hat{\Gamma}$, *i.e.* the inverse of the effective lifetimes, of the D^0 and $\overline{D}^0$ decays

$$A_\Gamma \equiv \frac{\hat{\Gamma}(D^0 \to f) - \hat{\Gamma}(\overline{D}^0 \to f)}{\hat{\Gamma}(D^0 \to f) + \hat{\Gamma}(\overline{D}^0 \to f)}. \tag{1}$$

Due to the slow mixing rate ($x = \Delta M/\Gamma < 1\%$, $y = \Delta\Gamma/2\Gamma < 1\%$) [10], and in the limit of negligible *CP* violation in the mixing, it can be found that $A_\Gamma \approx -x \sin\phi_D$ and its measurement translates into a constraint of the mixing phase ϕ_D, if the value of the x parameter is determined elsewhere. This also implies that $A_\Gamma \leq |x| < 5 \times 10^{-3}$, and therefore, from an experimental point of view, it is particularly relevant to increase as much as possible the precision on the measurement of such an observable, well beyond the level of 10^{-3}.

This thesis presents the world best measurement of the *CP* violation A_Γ parameter with pp collision data collected by LHCb in Run I, corresponding to an integrated luminosity of $3\,\text{fb}^{-1}$, with $1\,\text{fb}^{-1}$ collected during 2011 at a centre-of-mass energy of 7 TeV and the remaining $2\,\text{fb}^{-1}$ collected during 2012 at a centre-of-mass energy of 8 TeV. The achieved uncertainty on A_Γ is for the first time approaching a level of about 10^{-4} and the final result fully dominates the world average being the most precise measurement of *CP* violation ever of the LHCb experiment. Beyond the intrinsic importance of searching for first hints of *CP* violation in the charm sector at an unprecedented level of precision, the experimental methodologies developed in the thesis demonstrate that LHCb will be able to perform this measurement even at higher precision by fully exploiting the larger data samples that will be available in the future LHC Runs (LHCb-Upgrade and Future Upgrades).

I personally presented the results described in this thesis, for the first time, on behalf the LHCb Collaboration, at the VIII International Workshop on Charm Physics (CHARM 2016), 5-9 September 2016 - Bologna (Italy) [11] and a public LHCb document [12] was released at that time to accompany them. They have been submitted by the LHCb Collaboration to Physical Review Letters journal [13] on February 2017, and recently they have been accepted for publication.

The thesis is structured as follows. Chapter 1 introduces the theoretical framework of the *CP* violation within the Standard Model and the formal definition of the A_Γ observable. Chapter 2 describes the main experimental techniques to measure A_Γ along with the current experimental status. Chapter 3 briefly outlines the experimental apparatus, with particular attention on the LHCb sub-detectors relevant for the measurement described in the thesis. The candidates reconstruction and selection are reported in chapter 4, together with the signal extraction. Chapter 5 is devoted to the description of the subtle, and therefore very dangerous, time-dependent detection charge asymmetries present in the reconstructed data sample, and to the innovative correction, specifically developed in this thesis, to keep such effects under control at a level of 10^{-4}. Afterwards, chapter 6 reports the measurement of the A_Γ observable in $D^0 \to K^+K^-$ and $D^0 \to \pi^+\pi^-$ decay modes. The following two chapters 7 and 8 are dedicated to the estimation of systematic uncertainties. The dominant systematic uncertainty is separately discussed in chapter 7, where a new approach, which uses both analytical and data-driven information, has been successfully devised. Finally, chapter 9 presents the final results and a discussion of their impact on the current experimental panorama.

1 Theory and motivations

A brief review[1] of the Standard Model of particle physics is given in this chapter, with a particular attention to the Cabibbo-Kobayashi-Maskawa scheme and the charge-parity symmetry (*CP*) violation in the charm sector. The theoretical framework and the formalism, specialised in the two body $D^0 \to h^+ h^-$ decays where h is a charged pion or kaon, are extensively covered. These decays are a privileged laboratory to explore for the first time the *CP* violation mechanism in the charm sector with a precision approaching SM expectations, and are the main subjects of this thesis.

1.1 The Standard Model of Particle Physics

The Standard Model of particle physics describes the three out of the four fundamental known forces of the Nature, which are the strong and weak nuclear forces and the electromagnetic force.[2] The SM consists of twelve half-odd-integer spin particles (fermions), which are the fundamental building blocks of matter, and several bosons, particles having integer spin, that mediate the forces in the SM (see tab. 1.1). The Standard Model is a non-abelian, local gauge-invariant theory, and as such it is defined by its symmetry properties. The group of symmetry of the SM is the direct product of the following Lie groups

$$G_{\mathrm{SM}} = SU(3)_{\mathrm{C}} \otimes SU(2)_{\mathrm{L}} \otimes U(1)_{\mathrm{Y}}. \tag{1.1}$$

The $SU(3)_{\mathrm{C}}$ term describes the symmetry of the strong force theory (Quantum Chromodynamics or QCD), where C refers to the *color* charge of the fields under transformations of this group; the $SU(2)_{\mathrm{L}} \otimes U(1)_{\mathrm{Y}}$ term describes the symmetry of electroweak interactions as introduced by the theory of Glashow-Weinberg-Salam [16–18], where L indicates the *chirality* of the weak interactions and Y refers to the *hypercharge*.

[1] Many sources were used to compile this chapter, but the formalism adopted closely follows ref. [14]. The basic principles of the Standard Model are briefly introduced, while those relevant for the understanding of the *CP* violation are discussed with more details. A comprehensive and detailed description of the Standard Model can be found in many textbooks, as for example in ref. [15]

[2] The fourth force is the gravitational force that is not accounted for in the SM.

Table 1.1 – Particles of the Standard Model.

	fermions			bosons
quarks	u	c	t	g
	d	s	b	γ
leptons	e^-	μ^-	τ^-	Z
	ν_e	ν_μ	ν_τ	$W^\pm$
				H^0

Table 1.2 – The $SU(3)_{\rm C} \otimes SU(2)_{\rm L} \otimes U(1)_{\rm Y}$ representations of the fermions fields of the Standard Model and their transformation properties. Doublets of $SU(2)_{\rm L}$ group are explicitly written. In addition, the transformation properties of the fields with respect to the electromagnetic group $U(1)_{\rm em}$ are also reported.

	Field	$SU(3)_{\rm C}$	$SU(2)_{\rm L}$	$U(1)_{\rm Y}$	$U(1)_{\rm em}$
quarks	$Q^I_{Li} = \begin{bmatrix} u^I_{Li} \\ d^I_{Li} \end{bmatrix}$	**3**	**2**	1/6	$\begin{bmatrix} 2/3 \\ -1/3 \end{bmatrix}$
	u^I_{Ri}	**3**	**1**	2/3	2/3
	d^I_{Ri}	**3**	**1**	$-1/3$	$-1/3$
leptons	$L^I_{Li} = \begin{bmatrix} \nu^I_{Li} \\ l^I_{Li} \end{bmatrix}$	**1**	**2**	$-1/2$	$\begin{bmatrix} 0 \\ -1 \end{bmatrix}$
	l^I_{Ri}	**1**	**1**	-1	-1

The fundamental building blocks of matter are the half-odd-integer spin particles that are representations of the $G_{\rm SM}$ group. They are replicated in three generations, each of them consisting of five representations

$$Q^I_{Li},\ u^I_{Ri},\ d^I_{Ri},\ L^I_{Li},\ \ell^I_{Ri}. \tag{1.2}$$

where $i = 1,2,3$ is the flavour (or generation) index, the index $L(R)$ indicates the left (right) chirality and the index I denotes the interaction eigenstates. The transformation properties of the fields under the $G_{\rm SM}$ group can be compactly indicated by the dimensions of their representations. Thus, any field can be represented by a triplet $(\boldsymbol{\alpha}, \boldsymbol{\beta}, y)$ where $\boldsymbol{\alpha}$ and $\boldsymbol{\beta}$ are the dimensions of the representation of the $SU(3)_{\rm C}$ and $SU(2)_{\rm L}$ groups, respectively, and y is the hypercharge, namely the dimension of the representation of the $U(1)_{\rm Y}$ group. Fields representations are reported in tab. 1.2.

In addition to fermions representation, there is a single scalar representation $(\mathbf{1},\mathbf{2},1/2)$

$$\phi = \begin{bmatrix} \phi^+ \\ \phi^0 \end{bmatrix}, \tag{1.3}$$

which assumes a vacuum expectation value of

$$\langle\phi\rangle = \frac{1}{\sqrt{2}} \begin{bmatrix} 0 \\ v \end{bmatrix}.$$

Thus, it is often parametrised as

$$\phi = \exp\left[i\frac{\sigma_i}{2}\theta_i \right] \frac{1}{\sqrt{2}} \begin{bmatrix} 0 \\ v+H \end{bmatrix},$$

where σ_i are the Pauli's matrices, θ_i are three real fields and H is the Higgs boson field. The non-zero vacuum expectation generates a spontaneous breaking of the gauge group

$$G_{\text{SM}} = SU(3)_{\text{C}} \otimes SU(2)_{\text{L}} \otimes U(1)_{\text{Y}} \rightarrow SU(3)_{\text{C}} \otimes U(1)_{\text{em}},$$

where the $SU(2)_{\text{L}} \otimes U(1)_{\text{Y}}$ "collapses" to the group of symmetry of the electromagnetism $U(1)_{\text{em}}$.

The Standard Model Lagrangian, $\mathscr{L}_{\text{SM}}$, is the most general renormalisable Lagrangian consistent with the gauge symmetry of equation (1.1) and the particles content of eqs. (1.2) and (1.3), and it can be written as the sum of four terms

$$\mathscr{L}_{\text{SM}} = \mathscr{L}_{\text{kinetic}} + \mathscr{L}_{\text{gauge}} + \mathscr{L}_{\text{Higgs}} + \mathscr{L}_{\text{Yukawa}}.$$

The $\mathscr{L}_{\text{kinetic}}$ term contains the kinetic terms for Dirac fermions as $i\overline{\psi}\gamma_\mu\partial^\mu\psi$, where, in order to preserve the gauge invariance, the derivative ∂^μ is replaced with the covariant derivative D^μ defined as

$$D^\mu = \partial^\mu + i g_s G_a^\mu L_a + i g W_b^\mu T_b + i g' B^\mu Y. \tag{1.4}$$

The L_a's, with $a = 1,\ldots,8$, are the $SU(3)_{\text{C}}$ generators (the 3×3 Gell-Mann matrices $\lambda_a/2$ for triplets, 0 for singlets), the T_b's, with $b = 1,2,3$, are the $SU(2)_{\text{L}}$ generators (the 2×2 Pauli matrices $\sigma_b/2$ for doublets, 0 for singlets), and the Y is the $U(1)_{\text{Y}}$ charge. A gauge boson is associated to each generator. Thus, G_a^μ are the eight gluon fields, mediators of the strong force, W_b^μ are the three weak interaction bosons and B^μ is the single hypercharge boson. The W_b^μ and B^μ bosons, after the spontaneous symmetry breaking, translate to the $W^\pm$ and Z massive bosons and to the massless photon, since $U(1)_{\text{em}}$ remains a symmetry of the Lagrangian. The coefficients g_s, g and g' are the coupling constants. Thus, the kinetic term in the case of

left-handed quarks Q_L^I becomes

$$\mathscr{L}_{\text{kinetic}}(Q_L^I) = i\overline{Q}_{Li}^I \gamma_\mu \left(\partial^\mu + \frac{i}{2} g_s G_a^\mu \lambda_a + \frac{i}{2} g W_b^\mu \sigma_b + \frac{i}{6} g' B^\mu\right) Q_{Li}^I. \tag{1.5}$$

Similarly, the other kinetic terms can be written for all the fermions fields of tab. 1.2 and for the scalar field of eq. (1.3). The $\mathscr{L}_{\text{kinetic}}$ part of the SM Lagrangian is *CP* invariant.

The interaction of the fermions with the gauge bosons is introduced through the covariant derivative. These bosons have gauge kinetic terms as well, and these are grouped in the $\mathscr{L}_{\text{gauge}}$ term of the Lagrangian

$$\mathscr{L}_{\text{gauge}} = -\frac{1}{4}(G_{\mu\nu}^a G_a^{\mu\nu} + W_{\mu\nu}^b W_b^{\mu\nu} + B_{\mu\nu} B^{\mu\nu}),$$

where $B_{\mu\nu} = \partial_\mu B_\nu - \partial_\nu B_\mu$, $W_{\mu\nu}^b = \partial_\mu W_\nu^b - \partial_\nu W_\mu^b - g\epsilon^{bjk} W_\mu^j W_\nu^k$ and $G_{\mu\nu}^a = \partial_\mu G_\nu^a - \partial_\nu G_\mu^a - g_s f^{ajk} G_\mu^j G_\nu^k$ are the field strengths tensors. This term of the Lagrangian is also *CP* invariant[3].

The Higgs term, instead, describes the scalar self interaction and it can be written as

$$-\mathscr{L}_{\text{Higgs}} = \mu^2 \phi^\dagger \phi - \lambda(\phi^\dagger \phi)^2,$$

where λ is the Higgs self-coupling strength and $\mu = v\sqrt{\lambda}$. This term of the Lagrangian is also *CP* invariant.

Lastly, the Yukawa quark interaction term is given by the following equation

$$-\mathscr{L}_{\text{Yukawa}} = Y_{ij}^d \overline{Q}_{Li}^I \phi d_{Rj}^I + Y_{ij}^u \overline{Q}_{Li}^I \tilde{\phi} u_{Rj}^I + Y_{ij}^l \overline{L}_{Li}^I \phi \ell_{Rj}^I + \text{h.c.}, \tag{1.6}$$

where $\tilde{\phi} = i\sigma_2 \phi^\dagger$ and h.c. stands for the hermitian conjugate terms. The $\mathscr{L}_{\text{Yukawa}}$ term is generally *CP* violating. Due to the spontaneously symmetry breaking (recalling that $\Re(\phi^0) \rightarrow (v + H)/\sqrt{2}$) the ground state of ϕ generates in the Yukawa interactions of eq. (1.6) the Lagrangian mass terms

$$-\mathscr{L}_M = M_d^{ij} \overline{d}_{Li}^I d_{Rj}^I + M_u^{ij} \overline{u}_{Li}^I u_{Rj}^I + M_\ell^{ij} \overline{\ell}_{Li}^I \ell_{Rj}^I + \text{h.c.}, \tag{1.7}$$

with masses $M_{q,\ell} = v Y^{q,\ell}/\sqrt{2}$ $(q = u, d)$. Since neutrinos do not have Yukawa interactions in the Standard Model, they are predicted to be massless. Equation (1.7) contains terms involving different quark flavours, $i \neq j$. It is known that quarks are produced by strong interactions and these mass (or strong) eigenstates do not necessarily need to be identical to the interaction (or weak) eigenstates of eq. (1.7). The mass eigenstates correspond, by definition, to the states where the mass matrices are diagonal, thus, it is possible to find two unitary matrices, $\boldsymbol{V}_{qL}$ and

[3] There is an additional gauge–invariant and renormalisable operator in the QCD Lagrangian that could violate the *CP* symmetry. However, experimentally this is very suppressed. More details about this "strong *CP* problem" can be found in ref. [19].

$\boldsymbol{V}_{qR}$, such that

$$\boldsymbol{V}_{qL}\,\boldsymbol{M}_q\,\boldsymbol{V}_{qR}^{\dagger} = \boldsymbol{m}_q \quad (q = u, d),$$

with $\boldsymbol{m}_q$ diagonal and real. The quark mass eigenstates are then identified as

$$q_L^i = V_{qL}^{ij}\, q_{Lj}^I, \qquad q_R^i = V_{qR}^{ij}\, q_{Rj}^I, \quad (q = u, d), \tag{1.8}$$

and in terms of mass eigenstates eq. (1.7) can be written as

$$-\mathscr{L}_M = m_d^{ij}\overline{d}_{Li}\, d_{Rj} + m_u^{ij}\overline{u}_{Li}\, u_{Rj} + \text{h.c.},$$

where

$$m_q^{i,j} = \frac{v}{\sqrt{2}}(V_{L,q}^{i\alpha})^*\, Y_{\alpha\beta}^q\, V_{R,q}^{\beta j}.$$

The charged current interactions for quarks (that are the interactions of the charged $SU(2)_{\text{L}}$ gauge bosons $W_\mu^\pm = (W_\mu^1 \mp i W_\mu^2)/\sqrt{2}$), described in eq. (1.5) in the interaction basis, have the following form in the mass basis

$$-\mathscr{L}_{W^\pm}^q = \frac{g}{\sqrt{2}}\overline{u}_L^i \gamma^\mu\, (\boldsymbol{V}_{uL}\boldsymbol{V}_{dL}^{\dagger})_{ij}\, d_L^j W_\mu^+ + \text{h.c.}.$$

where the unitary matrices $\boldsymbol{V}_{uL}$ and $\boldsymbol{V}_{dL}$ account for the rotation between the interaction eigenstates and the mass eigenstates.

1.2 The CKM matrix

The unitary 3×3 matrix,

$$\boldsymbol{V}_{\text{CKM}} \equiv \boldsymbol{V}_{uL}\boldsymbol{V}_{dL}^{\dagger} = \begin{bmatrix} V_{ud} & V_{us} & V_{ub} \\ V_{cd} & V_{cs} & V_{cb} \\ V_{td} & V_{ts} & V_{tb} \end{bmatrix}, \tag{1.9}$$

is the Cabibbo-Kobayashi-Maskawa (CKM) mixing matrix of quarks [1, 2]. Generally, a $n \times n$ complex matrix $\boldsymbol{U}$ has $2n^2$ degrees of freedom, however unitarity ($\boldsymbol{U}^\dagger = \boldsymbol{U}^{-1} \Leftrightarrow \boldsymbol{U}\boldsymbol{U}^\dagger = \boldsymbol{I}$) provides n^2 constraints, reducing the number of degrees of freedom to n^2. In addition, in the particular case of the CKM matrix, the Lagrangian allows the redefinition of the phases of each quark field, obtaining (see eq. (1.8))

$$\begin{cases} u_{Li} \to (\boldsymbol{V}_{uL})_{il}\, \mathrm{e}^{-i\phi_l}\, u_{Ll}^I \\ d_{Lj} \to (\boldsymbol{V}_{dL})_{jk}\, \mathrm{e}^{-i\omega_k}\, d_{Lk}^I \end{cases} \Rightarrow (\boldsymbol{V}_{uL}\boldsymbol{V}_{dL}^{\dagger})_{ij} \to \mathrm{e}^{i\phi_l}\,(\boldsymbol{V}_{uL}\boldsymbol{V}_{dL}^{\dagger})_{ij}\,\mathrm{e}^{-i\omega_k} = \mathrm{e}^{i(\phi_l-\omega_k)}(\boldsymbol{V}_{uL}\boldsymbol{V}_{dL}^{\dagger})_{ij},$$

where, for n generations, there are $2n-1$ phase differences that can be removed from CKM matrix opportunely choosing ϕ_l and ω_k (with $l = 1, \ldots, n$ and $k = 1, \ldots, n$). Consequently, any

$n \times n$ complex matrix, describing the mixing between n generations of quarks has a number of free parameters equal to

$$2n^2 - n^2 - (2n-1) = (n-1)^2,$$

and since an orthogonal $n \times n$ matrix ($\boldsymbol{U}^T = \boldsymbol{U}^{-1} \Leftrightarrow \boldsymbol{U}\boldsymbol{U}^T = 1$) has $n(n-1)/2$ real parameters (angles), the number of complex phases is equal to

$$(n-1)^2 - \frac{n}{2}(n-1) = \frac{(n-1)(n-2)}{2}.$$

For $n = 2$, corresponding only two generations, the mixing matrix has only one free real parameter, the so-called Cabibbo angle θ_C

$$\boldsymbol{V}_C = \begin{bmatrix} \cos\theta_C & \sin\theta_C \\ -\sin\theta_C & \cos\theta_C \end{bmatrix},$$

and the *CP* symmetry cannot be violated. For $n = 3$, instead, the physical free parameters are four: three rotation angles (corresponding to the Euler angles) and one complex phase, and therefore the *CP* symmetry can be violated. This can be made manifest by choosing an explicit parametrization of the CKM matrix [20]

$$\boldsymbol{V}_{\text{CKM}} = \begin{bmatrix} c_{12}c_{13} & s_{12}c_{13} & s_{13}e^{-i\delta} \\ -s_{12}c_{23} - c_{12}s_{23}s_{13}e^{i\delta} & c_{12}c_{23} - s_{12}s_{23}s_{13}e^{i\delta} & s_{23}c_{13} \\ s_{12}s_{23} - c_{12}c_{23}s_{13}e^{i\delta} & -c_{12}s_{23} - s_{12}c_{23}s_{13}e^{i\delta} & c_{23}c_{13} \end{bmatrix}, \tag{1.10}$$

where $c_{ij} \equiv \cos\theta_{ij}$ and $s_{ij} \equiv \sin\theta_{ij}$, the three θ_{ij} are the real angles corresponding to a xyz-Euler rotation and δ is the CKM phase and corresponds to the single source of *CP* violation in the quark sector in the Standard Model. The mass and interaction eigenstates are schematically represented in fig. 1.1a.

Although the representation of eq. (1.10) is exact and makes explicit the rotation between the two quark bases (interactions and masses), the phenomenological behaviour is not easily evident. With this aim, a useful parametrization is that one from Wolfenstein [21], where the hierarchy of the various elements is made manifest. A set of four real parameters (λ, A, ρ, η) are defined as follows

$$\lambda = s_{12}, \quad A\lambda^2 = s_{23}, \quad A\lambda^3(\rho - i\eta) = s_{13}\mathrm{e}^{-i\delta},$$

where the parameter $\lambda = |V_{us}| \approx 0.22$ (the Cabibbo angle) plays the role of an expansion parameter. By expanding to $\mathcal{O}(\lambda^5)$ the CKM matrix can be written as [21]

$$\boldsymbol{V}_{\text{CKM}} = \begin{bmatrix} 1 - \frac{1}{2}\lambda^2 - \frac{1}{8}\lambda^4 & \lambda & A\lambda^3(\rho - i\eta) \\ -\lambda + \frac{1}{2}\lambda^5 A^2(1 - 2(\rho + i\eta)) & 1 - \frac{1}{2}\lambda^2 - \frac{1}{8}\lambda^4(1 + 4A^2) & A\lambda^2 \\ A\lambda^3[1 - (\rho + i\eta)] + \frac{1}{2}\lambda^5 A(\rho + i\eta) & -A\lambda^2 + \frac{1}{2}\lambda^4 A(1 - 2(\rho + i\eta)) & 1 - \frac{1}{2}\lambda^4 A^2 \end{bmatrix} + \mathcal{O}(\lambda^6),$$

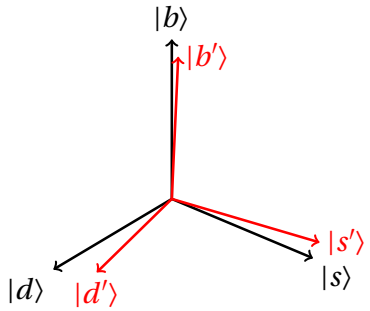

(a) Quark mass eigenstates interactions representation.

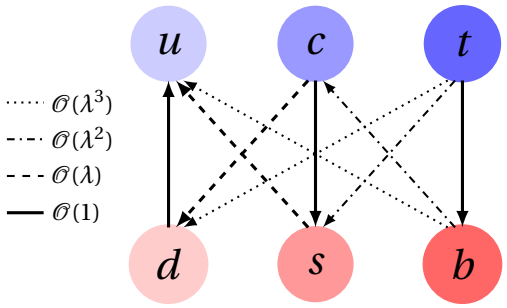

(b) Mass and interaction eigenstates decay scheme.

Figure 1.1 – Graphical representation of CKM mechanism.

where it clearly appears that, with a good approximation, the $\boldsymbol{V}_{\text{CKM}}$ matrix is close to the unit matrix with small off-diagonal terms. The order of magnitude of each element can be also easily read from the power of λ (see fig. 1.1b).

The current knowledge of the modulus of the CKM matrix elements, extracted from a global fit to all the experimental observables, as obtained from ref. [22], is reported below

$$|\boldsymbol{V}_{\text{CKM}}| = \begin{bmatrix} 0.97425^{+0.000071}_{-0.000097} & 0.22542^{+0.00042}_{-0.00031} & 0.003714^{+0.000072}_{-0.000060} \\ 0.22529^{+0.00041}_{-0.00032} & 0.973394^{+0.000074}_{-0.000096} & 0.04180^{+0.00033}_{-0.00068} \\ 0.008676^{+0.000087}_{-0.000150} & 0.04107^{+0.00031}_{-0.00067} & 0.999118^{+0.000024}_{-0.000014} \end{bmatrix}.$$

1.3 Unitary triangles

As stated above, the CKM matrix is a unitary matrix and the unitarity condition $\boldsymbol{V}^{\dagger}_{CKM}\boldsymbol{V}_{CKM} = \boldsymbol{I}$ leads to nine relationships among the matrix elements that can be summarised as

$$\sum_{k\in\{u,c,t\}} V^*_{ki}V_{kj} = \delta_{ij}, \qquad i,j \in \{d,s,b\}, \tag{1.11}$$

where δ_{ij} is the Kronecker delta. Six of these nine relationships, with $i \neq j$, imply that a sum of three complex numbers is zero and it can be visualised as a triangle in the complex plane (this explains the name "unitary triangles"). Among these six unitary triangles, one is chosen to be "The Unitary Triangle" ($i = d, j = b$)

$$V^*_{ud}V_{ub} + V^*_{cd}V_{cb} + V^*_{td}V_{tb} = 0, \tag{1.12}$$

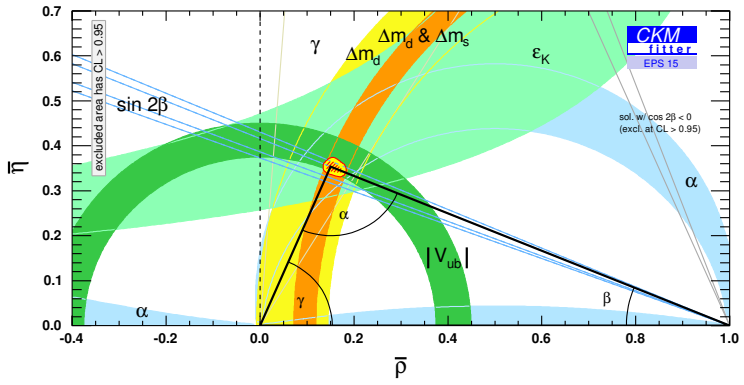

Figure 1.2 – Current experimental status of the global fit to all available experimental measurements related to the unitarity triangle phenomenology [22]. The parameters $\overline{\rho}$ and $\overline{\eta}$ are related to the CKM matrix elements by the equation $\overline{\rho}+i\overline{\eta}=-\frac{V_{ud}^*V_{ub}}{V_{cd}^*V_{cb}}$ (see text for details).

where the phase convention is chosen in order to make the $V_{cd}^*V_{cb}$ term real (aligning one side of the triangle to the real axis). In addition, eq. (1.12) is rescaled by $V_{cd}^*V_{cb}$ to make the length of this side equal to the unit, obtaining the following relationship

$$\frac{V_{ud}^*V_{ub}}{V_{cd}^*V_{cb}}+1+\frac{V_{td}^*V_{tb}}{V_{cd}^*V_{cb}}=0. \tag{1.13}$$

The parameters describing the amount of *CP* violation are therefore the angles of the triangle which are defined as

$$\alpha=\arg\left[\frac{V_{ud}^*V_{ub}}{V_{td}^*V_{tb}}\right],\quad \beta=\arg\left[\frac{V_{td}^*V_{tb}}{V_{cd}^*V_{cb}}\right],\quad \gamma=\arg\left[\frac{V_{cd}^*V_{cb}}{V_{ud}^*V_{ub}}\right].$$

The current experimental knowledge of the unitary triangle is reported in fig. 1.2.

1.3.1 Charm triangle parameters

Charmed meson decays involve quark transitions from the c quark to lighter quarks, and therefore the elements of the CKM matrix involved are those of the first two rows. The relevant unitary relationship for charm mesons is then

$$V_{cd}^*V_{ud}+V_{cs}^*V_{us}+V_{cb}^*V_{ub}=0,$$

that can be rewritten into a more compact form, introducing the coefficient $\Lambda_q=V_{cq}^*V_{uq}$ ($q\in\{d,s,b\}$), obtaining

$$\Lambda_d+\Lambda_s+\Lambda_b=0.$$

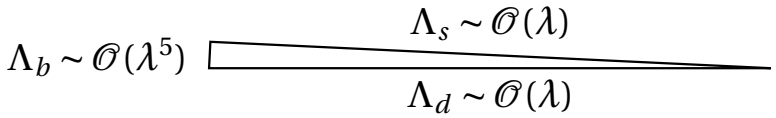

Figure 1.3 – Schematic representation of unitary triangle for charm meson decays. The vertical direction is enlarged by a factor of twenty with respect to the horizontal one.

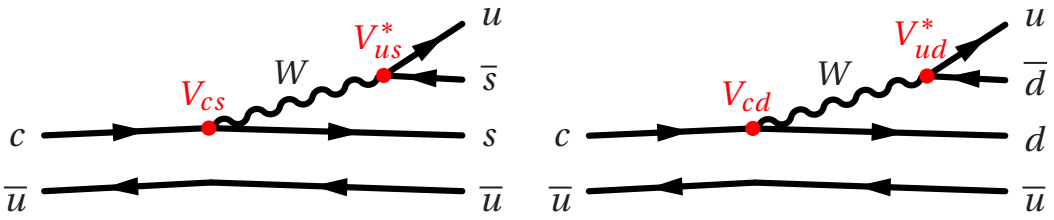

Figure 1.4 – Leading tree-level Feynman diagrams for the singly Cabibbo-suppressed $D^0(c\bar{u}) \to K^-(s\bar{u})\,K^-(\bar{s}u)$ and $D^0(c\bar{u}) \to \pi^+(u\bar{d})\,\pi^-(\bar{u}d)$ decays.

In the Wolfenstein parametrisation the values of Λ_q are the following

$$\Lambda_d = -\lambda + \frac{\lambda^3}{2} + \frac{\lambda^5}{8}(1+4A^2) - \lambda^5 A^2(\rho + i\eta) + \mathcal{O}(\lambda^7),$$
$$\Lambda_s = \lambda - \frac{\lambda^3}{2} - \frac{\lambda^5}{8}(1+4A^2) + \mathcal{O}(\lambda^7),$$
$$\Lambda_b = \lambda^5 A^2(\rho - i\eta) + \mathcal{O}(\lambda^{11}),$$

resulting into a squashed triangle for the charm physics, since it has two sides having almost the same size ($|\Lambda_d| = |\Lambda_s| + \mathcal{O}(\lambda^4)$), as schematically reported in fig. 1.3.

Charmed meson decays involving amplitudes proportional to $\Lambda_d \approx \Lambda_s \approx \lambda$, are called singly Cabibbo-suppressed (SCS) amplitudes, as $D^0 \to K^+K^-$ and $D^0 \to \pi^+\pi^-$ decays, see fig. 1.4, and they are the main subjects of this thesis. Instead, $D^0 \to K^-\pi^+$ decays, involving amplitudes proportional to $V_{cs}^* V_{ud} \approx 1 - \lambda^2/2$ are therefore called Cabibbo-favoured (CF), see fig. 1.5. In addition, $D^0 \to K^+\pi^-$ decays are called doubly Cabibbo-suppressed (DCS) since they involve amplitudes proportional to $V_{cd}^* V_{us} \approx \lambda^2$.

1.4 Neutral meson mixing

As described in the previous sections, the quark flavour eigenstates are not eigenstates of the weak Hamiltonian, leading to processes that link quarks of different flavours, as shown in fig. 1.1b. These processes allow connecting a neutral ($q\bar{q}'$) meson to its antimeson through a rotation between flavour eigenstates and mass eigenstates. Therefore, neutral mesons are not eigenstates of the free Hamiltonian, hence they do not evolve as free particles but through the so-called "mixing"phenomenon. The formalism of the time evolution of the $D^0(c\bar{u})$–$\overline{D}^0(\bar{c}u)$

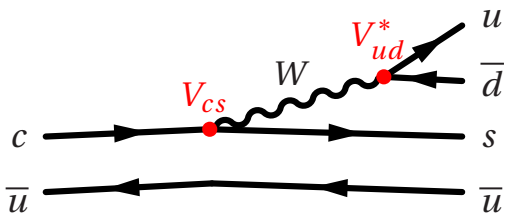

Figure 1.5 – Leading tree-level Feynman diagram for the Cabibbo-favoured $D^0(c\overline{u}) \to K^-(s\overline{u})\,\pi^+(u\overline{d})$ decay.

system is described in the following and the resulting equations can be also applied to the other three meson systems where the mixing occurs in the SM: K^0–$\overline{K}^0$, B^0–$\overline{B}^0$, B^0_s–$\overline{B}^0_s$. While the equations are general, the mixing phenomenology is completely different among these four systems, and it will discussed in sub-sec. 1.4.2.

1.4.1 Time evolution of flavour eigenstates

Neutral charm mesons are produced by strong interactions and they are flavour eigenstates. An initial state, $|\psi(0)\rangle$, is therefore a superposition of $|D^0\rangle$ and $|\overline{D}^0\rangle$ states

$$|\psi(0)\rangle = a(0)|D^0\rangle + b(0)|\overline{D}^0\rangle,$$

and it will evolve into a superposition of all states allowed by energy-momentum conservation

$$|\psi(t)\rangle = a(t)|D^0\rangle + b(t)|\overline{D}^0\rangle + \sum_n c_n(t)|n\rangle,$$

where $|n\rangle$ represents all the possible states that can decay into, with coefficients $c_n(t) = \langle n|\mathscr{H}|\psi\rangle$ and $\mathscr{H}$ is the effective Hamiltonian. Since we are interested in $a(t)$ and $b(t)$, for t values much larger than typical scale of strong interactions, the time evolution of a single state $|\xi\rangle$ can be schematised, using the *Wigner-Weisskopf approximation* [20, 23], as

$$|\xi(t)\rangle = \mathrm{e}^{-iMt}\mathrm{e}^{-\Gamma t/2}|\xi(0)\rangle, \tag{1.14}$$

where e^{-iMt} describes the time evolution of a stable state with energy $E = M$, while $\mathrm{e}^{-\Gamma t/2}$ takes into account the unstable nature of the state. The probability to find the state at time t is therefore equal to

$$|\langle\xi(0)|\xi(t)\rangle|^2 = \mathrm{e}^{-\Gamma t}.$$

The time evolution reported in eq. (1.14) is the solution of the following Schödinger equation

$$i\frac{\mathrm{d}}{\mathrm{d}t}|\xi(t)\rangle = \left(M - i\frac{\Gamma}{2}\right)|\xi(t)\rangle, \tag{1.15}$$

where $M - i\Gamma/2$ is a non-Hermitian Hamiltonian (otherwise the state cannot decay). The equation (1.15) can be generalised as a two-state system describing the neutral mesons as follows

$$i\frac{\mathrm{d}}{\mathrm{d}t}\begin{bmatrix}|D^0(t)\rangle\\ |\overline{D}^0(t)\rangle\end{bmatrix} = \left(\boldsymbol{M} - i\frac{\boldsymbol{\Gamma}}{2}\right)\begin{bmatrix}|D^0(t)\rangle\\ |\overline{D}^0(t)\rangle\end{bmatrix} = \left(\begin{bmatrix}M_{11} & M_{12}\\ M_{21} & M_{22}\end{bmatrix} - \frac{i}{2}\begin{bmatrix}\Gamma_{11} & \Gamma_{12}\\ \Gamma_{21} & \Gamma_{22}\end{bmatrix}\right)\begin{bmatrix}|D^0(t)\rangle\\ |\overline{D}^0(t)\rangle\end{bmatrix}. \quad (1.16)$$

The CPT invariance implies that $M_{11} = M_{22} = M$ and $\Gamma_{11} = \Gamma_{22} = \Gamma$. In addition, $M_{12} = M_{21}^*$ and $\Gamma_{12} = \Gamma_{21}^*$ since the matrices $\boldsymbol{M}$ and $\boldsymbol{\Gamma}$ are Hermitian. The $\boldsymbol{M}$ matrix represents the transitions with dispersive intermediate states ("off-shell" transitions), while $\boldsymbol{\Gamma}$ represents the transitions with absorptive intermediate states ("on-shell" transitions). The eigenvalues can easily calculated and are

$$\lambda_\pm = M + i\frac{\Gamma}{2} \pm pq;$$

where p and q are two complex numbers given by

$$p = \sqrt{M_{12} - i\frac{\Gamma_{12}}{2}} \quad \text{and} \quad q = \sqrt{M_{21} - i\frac{\Gamma_{21}}{2}} = \sqrt{M_{12}^* - i\frac{\Gamma_{12}^*}{2}}. \quad (1.17)$$

The eigenvectors are $(p, \pm q)^T$, corresponding to the $\lambda_\pm$ eigenvalues, thus the neutral meson mass eigenstates $|D_{1,2}\rangle$ are linear combinations of the strong interactions eigenstates $|D^0\rangle$ and $|\overline{D}^0\rangle$,

$$\begin{bmatrix}|D_1\rangle\\ |D_2\rangle\end{bmatrix} = \begin{bmatrix}p & q\\ p & -q\end{bmatrix}\begin{bmatrix}|D^0\rangle\\ |\overline{D}^0\rangle\end{bmatrix} = \boldsymbol{Q}\begin{bmatrix}|D^0\rangle\\ |\overline{D}^0\rangle\end{bmatrix}. \quad (1.18)$$

Thus, the time evolution for $|D_1\rangle$ and $|D_2\rangle$ is the following

$$|D_{1,2}(t)\rangle = \mathrm{e}^{-i\lambda_\pm t}|D_{1,2}\rangle,$$

that can be rewritten in the flavour states basis (using eq. (1.18)) as

$$\begin{bmatrix}|D^0(t)\rangle\\ |\overline{D}^0(t)\rangle\end{bmatrix} = \boldsymbol{Q}^{-1}\begin{bmatrix}\mathrm{e}^{-i\lambda_+ t} & 0\\ 0 & \mathrm{e}^{-i\lambda_- t}\end{bmatrix}\boldsymbol{Q}\begin{bmatrix}|D^0\rangle\\ |\overline{D}^0\rangle\end{bmatrix} = \begin{bmatrix}g_+(t) & \frac{q}{p}g_-(t)\\ \frac{p}{q}g_-(t) & g_+(t)\end{bmatrix}\begin{bmatrix}|D^0\rangle\\ |\overline{D}^0\rangle\end{bmatrix}, \quad (1.19)$$

where

$$\begin{aligned} g_+(t) &= \mathrm{e}^{-iMt}\mathrm{e}^{-\Gamma t/2}\cos(pqt),\\ g_-(t) &= -\mathrm{e}^{-iMt}\mathrm{e}^{-\Gamma t/2}i\sin(pqt). \end{aligned} \quad (1.20)$$

The mass eigenstates $|D_{1,2}\rangle$ are eigenstates of the Hamiltonian of eq. (1.16) with masses, $M_{1,2}$, and widths, $\Gamma_{1,2}$, therefore the $\lambda_\pm$ eigenvalues correspond to the eigenvalues $\lambda_{1,2}$

$$\lambda_\pm = M + i\frac{\Gamma}{2} \pm pq = M_{1,2} - i\frac{\Gamma_{1,2}}{2} = \lambda_{1,2}.$$

Thus, the following relationships hold:

$$\begin{aligned} pq &= \frac{1}{2}\left(\Delta M - \frac{i}{2}\Delta\Gamma\right), \\ M &= \frac{M_1 + M_2}{2}, \\ \Gamma &= \frac{\Gamma_1 + \Gamma_2}{2}, \end{aligned}$$

where

$$\Delta M \equiv M_2 - M_1 = -2\Re(pq), \qquad \Delta\Gamma \equiv \Gamma_2 - \Gamma_1 = 4\Im(pq). \tag{1.21}$$

The time evolution functions of eq. (1.20) can be written in terms of the mass eigenstate parameters as

$$\begin{aligned} g_+(t) =& e^{-iMt}e^{-\Gamma t/2}\left[\ \cos\frac{\Delta M t}{2}\cosh\frac{\Delta\Gamma t}{4} - i\sin\frac{\Delta M t}{2}\sinh\frac{\Delta\Gamma t}{4}\right], \\ g_-(t) =& e^{-iMt}e^{-\Gamma t/2}\left[-\cos\frac{\Delta M t}{2}\sinh\frac{\Delta\Gamma t}{4} + i\sin\frac{\Delta M t}{2}\cosh\frac{\Delta\Gamma t}{4}\right], \end{aligned} \tag{1.22}$$

Thus, a pure $|D^0\rangle$ or $|\overline{D}^0\rangle$ state at time $t = 0$ will therefore evolve as

$$\begin{aligned} |D^0(t)\rangle &= g_+(t)|D^0\rangle + \frac{q}{p}g_-(t)|\overline{D}^0\rangle, \\ |\overline{D}^0(t)\rangle &= g_+(t)|\overline{D}^0\rangle + \frac{p}{q}g_-(t)|D^0\rangle, \end{aligned}$$

respectively. The probability for a state, produced at $t = 0$ with a well-defined flavour content, of having the same initial flavour content at $t > 0$, is then

$$\begin{aligned} \text{Prob}(D^0 \to D^0; t) &= |\langle D^0(t)|D^0\rangle|^2 = |g_+(t)|^2, \\ \text{Prob}(\overline{D}^0 \to \overline{D}^0; t) &= |\langle \overline{D}^0(t)|\overline{D}^0\rangle|^2 = |g_+(t)|^2. \end{aligned}$$

Instead the probability of changing the flavour content is given by

$$\begin{aligned} \text{Prob}(D^0 \to \overline{D}^0; t) &= |\langle D^0(t)|\overline{D}^0\rangle|^2 = \left|\frac{q}{p}\right|^2 \cdot |g_-(t)|^2, \\ \text{Prob}(\overline{D}^0 \to D^0; t) &= |\langle \overline{D}^0(t)|D^0\rangle|^2 = \left|\frac{p}{q}\right|^2 \cdot |g_-(t)|^2, \end{aligned}$$

where, as results from eq. (1.22),

$$|g_\pm(t)|^2 = \frac{1}{2}e^{-\Gamma t}\left[\cosh\frac{\Delta\Gamma t}{2} \pm \cos\Delta M t\right].$$

It is worth noting that the probability for a $D^0 \to \overline{D}^0$ transition is different from the probability of $\overline{D}^0 \to D^0$ if $|q/p| \neq 1$.

Table 1.3 – Approximate values for ΔM and $\Delta\Gamma$ in the four neutral meson systems.

meson system	$\Delta M/\Gamma$	$\Delta\Gamma/(2\Gamma)$
K^0–$\overline{K}^0$	−0.95	0.99
D^0–$\overline{D}^0$	0.005	0.006
B^0–$\overline{B}^0$	0.77	−0.001
B_s^0–$\overline{B}_s^0$	26.7	0.06

1.4.2 Mixing phenomenology

In the previous sub-section the time-evolution of the flavour eigenstates has been determined in terms of ΔM and $\Delta\Gamma$ parameters, and approximate measured values of ΔM and $\Delta\Gamma$ are reported in tab. 1.3. The probability as a function of the decay time for flavour-changing and flavour-unchanging for all the four meson systems are also drawn in fig. 1.6, showing that the D^0–$\overline{D}^0$ mixing proceeds very slowly, being almost indistinguishable from the single exponential behaviour.

The dynamics behind the ΔM and $\Delta\Gamma$ values is enclosed in the effective Hamiltonian of eq. (1.16), precisely through the M_{12} and Γ_{12} elements, as it can be seen in eq. (1.17) and eq. (1.21). The knowledge of such parameters is therefore crucial for the understanding of the SM dynamics in the charm sector. There are two types of contributions to the mixing amplitudes: the short distance and the long distance contributions.

Short distance contributions are fourth order interactions in the weak coupling as represented by the Feynman diagram drawn in fig. 1.7a. These processes are called short distance contributions since their typical scale length is much lower than the QCD scale ($1/\Lambda_{\mathrm{QCD}}$). However, these contributions are strongly suppressed in the charm system, contrary to the B system where the analogous box diagrams are dominant. The contribution of the b quark in the charm box diagram (see fig. 1.7a) is CKM-suppressed by a factor $|V_{ub}V_{cb}^*|^2/|V_{us}V_{cs}^*|^2 \approx \mathcal{O}(10^{-6})$. The contribution from down and strange quarks is also strongly suppressed in the limit of $SU(3)$ flavour symmetry [9, 24] (GIM suppression mechanism is remarkable effective in the charm system, $\Lambda_b^2 = |V_{cb}V_{ub}^*|^2 \approx \lambda^{10} \Rightarrow \Lambda_d = -\Lambda_s$). Even taking into account also the next-to-leading order, the short distance contributions to $x \equiv \Delta M/\Gamma$ and $y \equiv \Delta\Gamma/(2\Gamma)$ mixing parameters are predicted to be about $\mathcal{O}(10^{-6})$ [25]. These values are far below the current experimental measured values of x, y of the order $\mathcal{O}(10^{-2})$, thus the long distance contributions are dominant in the D^0–$\overline{D}^0$ mixing.

On the other hand, mixing can proceed through intermediate on-shell states common to the D^0 and the $\overline{D}^0$ meson, as schematically represented in fig. 1.7b, the so-called long distance contributions. Unfortunately, precise calculations of long distance effects are difficult, and have large uncertainties, being the value of charm quark mass placed somewhere on the border of heavy and light quark systems. Prediction of D^0–$\overline{D}^0$ mixing parameters from the

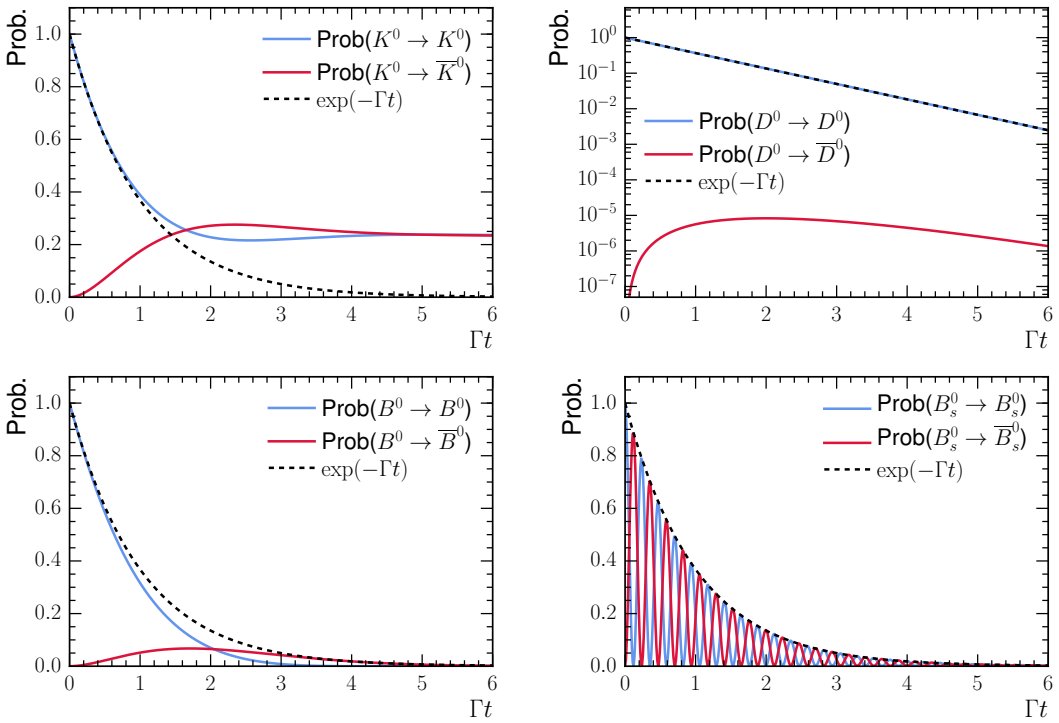

Figure 1.6 – Flavour-changing and flavour-unchanging PDFs for the four neutral meson systems (from left to right and from top to bottom): K^0–$\overline{K}^0$, D^0–$\overline{D}^0$ (note the logarithmic scale), B^0–$\overline{B}^0$, B_s^0–$\overline{B}_s^0$. The single exponential function, black-dashed line, it is also drawn.

theory is a challenging task, and several orders of magnitude are spanned in the literature [26]. The size of the long distance contributions is determined by the amount of phase space of the final states in common to the meson and the anti-meson. In the K^0–$\overline{K}^0$ system this contribution is almost maximal since there is a small number of possible final states for K^0 and almost all of them are accessible also to the $\overline{K}^0$. In the B^0 system the situation is the opposite, there is a large number of possible final states for the B^0 but just a small fraction of them are also accessible to the $\overline{B}^0$. Several techniques are used to calculate the mixing parameters in the SM. Inclusive approaches such as heavy quark effective field theory rely on expansions in powers of the inverse of the quark mass, which are of limited validity because the intermediate value of the charm quark mass [27, 28]. Alternatively, exclusive approaches are used [29, 30]. They rely on explicitly accounting for all possible intermediate states, which may be modelled or fitted directly to experimental data. However, the D meson is not light enough to have few final states, and in absence of sufficiently precise measurements of amplitudes and strong phases of many decays, several assumptions are made limiting the predictions of such an approach.

As a consequence, the SM predictions for mixing and for *CP* violation are affected by large theory uncertainties. Thus, it is crucial to provide very precise measurements in the charm

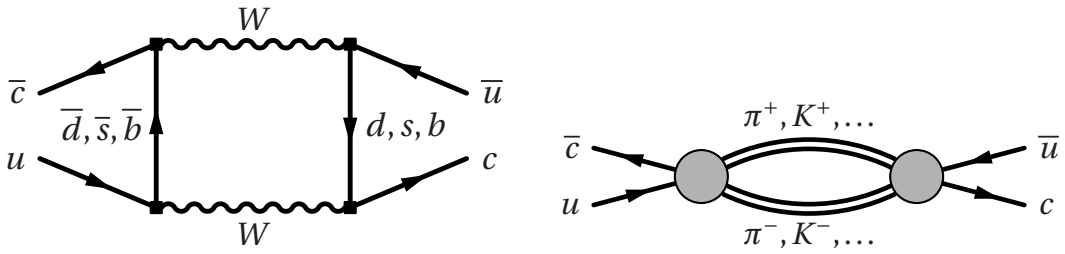

(a) Short distance contribution. **(b)** Illustrative long distance contribution.

Figure 1.7 – Two diagrams contributing to the $D^0(c\overline{u})$–$\overline{D}^0(\overline{c}u)$ mixing: (a) Feynman diagram of short distance contribution, (b) long distance contribution.

sector.

1.5 *CP* violation formalism

The *CP* transformation law for a final state f is $CP|f\rangle = \omega_f|\overline{f}\rangle$ and $CP|\overline{f}\rangle = \omega_f^*|f\rangle$, where ω_f is a complex phase ($|\omega_f| = 1$). For the particular case of a final *CP* eigenstate, as K^+K^- and $\pi^+\pi^-$, where $f = \overline{f}$, one obtains

$$CP|f\rangle = \eta_{CP}|f\rangle,$$

with $\eta_{CP} = \pm 1$ for even (+1) and odd (−1) final states. In addition, for a D^0 meson decaying to a *CP* eigenstate f the decay amplitudes can be defined as

$$A_f = \langle f|\mathscr{H}|D^0\rangle, \qquad \overline{A}_f = \langle f|\mathscr{H}|\overline{D}^0\rangle,$$

where $\mathscr{H}$ is the decay Hamiltonian. It is important to discuss the phases that can arise in those amplitudes since they are responsible for the phenomenon of *CP* violation. Usually, two types of phases are present and are called: weak and strong phases.

Weak phases come from any complex term in the Lagrangian appearing as complex conjugated in the *CP*-conjugate amplitude. Thus, they have different signs between A_f and $\overline{A}_f$. Since in the Standard Model Lagrangian these phases occur only in the CKM matrix, which is part of the electroweak sector, they are called "weak phases".

Strong phases come from final state interactions and they contribute to the amplitudes through the intermediate on-shell states in the decay process. These phases arise even if the Lagrangian is real and are called "rescatting phases". If there are hadrons in the final state, they are generated by strong interactions and therefore are also called "strong phases". Strong phases do not change sign under *CP* transformation.

Since all the observables are related to the squared amplitudes, phases are not experimentally measurable, but only phases differences are accessible. Thus, *CP* violation in the decay appears as a result of the interference among various terms in the decay amplitude, and it does not occur unless at least two terms have different weak phases and different strong phases. As an example, let us consider a decay process which can proceed through several amplitudes

$$A_f = \sum_k |A_k| e^{i(\phi_k+\delta_k)}, \qquad \overline{A}_f = \sum_k |A_k| e^{i(-\phi_k+\delta_k)}$$

where δ_k are the strong phases, which do not change sign under *CP*, and ϕ_k are the weak phases. The difference between the two amplitudes is

$$|A_f|^2 - |\overline{A}_f|^2 = -2\sum_{l,k} |A_l||A_k| \sin(\phi_l - \phi_k)\sin(\delta_l - \delta_k).$$

To observe *CP* violation one needs $|A_f| \neq |\overline{A}_f|$, therefore there must be a contribution from at least two processes with different weak and strong phases in order to have a non vanishing interference term.

Experimentally, there are three manifestations of *CP*-violation and they are enclosed in the following variable

$$\lambda_f = \frac{q\overline{A}_f}{pA_f} = -\eta_{CP} R_m R_f e^{i\phi_f}, \tag{1.23}$$

where

$$R_m = \left|\frac{q}{p}\right|, \qquad R_f = \left|\frac{\overline{A}_f}{A_f}\right|, \qquad \phi_f = \arg\left(\frac{q\overline{A}_f}{pA_f}\right).$$

1.5.1 *CP* violation in the decay

CP violation in the decay (also called direct *CP* violation) occurs when the decay amplitudes for *CP*-conjugated processes are not equal. A golden observable sensitive to the *CP* violation in the decay is the *CP* asymmetry defined as

$$A_{CP}(f) = \frac{\Gamma(D\to f) - \Gamma(\overline{D}\to f)}{\Gamma(D\to f) + \Gamma(\overline{D}\to f)},$$

where Γ is the time-integrated decay width of the $D\to f$ decay process and it is proportional to the squared amplitude ($\Gamma(P\to f) \propto |A_f|^2$ and $\Gamma(\overline{P}\to f) \propto |\overline{A}_f|^2$), thus

$$A_{CP}(f) = A_{CP}^{\text{dir}} = \frac{|A_f|^2 - |\overline{A}_f|^2}{|A_f|^2 + |\overline{A}_f|^2} = \frac{1-R_f^2}{1+R_f^2}.$$

Therefore, CP violation in the decay occurs if

$$R_f = \left| \frac{\overline{A}_f}{A_f} \right| \neq 1.$$

1.5.2 CP violation in the mixing

CP violation in the mixing occurs when the probability for the oscillation process depends on the initial state, *i.e.* the probability for the $D^0 \to \overline{D}^0$ process is different from the CP-conjugated one, $\overline{D}^0 \to D^0$. This is defined as

$$R_m = \left| \frac{q}{p} \right| \neq 1,$$

From the definition of q and p (see eq. (1.17)) follows

$$\left| \frac{q}{p} \right|^2 = \frac{|M_{12}^* - i\Gamma_{12}^*/2|}{|M_{12} - i\Gamma_{12}/2|},$$

where only off-diagonal elements of the Hamiltonian of eq. (1.16) contribute. The off-diagonal terms are proportional to the probability for the transition of $|D^0\rangle$ to $|\overline{D}^0\rangle$ and vice versa; if these terms are different CP violation in mixing follows.

1.5.3 CP violation in the interference

In the case of a common final state f shared simultaneously by the D^0 and the $\overline{D}^0$ meson, the CP symmetry can be violated in the interference between the decay without mixing, $D^0 \to f$, and the decay with mixing, $D^0 \to \overline{D}^0 \to f$. It occurs when

$$\arg(\lambda_f) + \arg(\lambda_{\overline{f}}) \neq 0.$$

For final CP eigenstates, as K^+K^- and $\pi^+\pi^-$, the above condition simplifies to

$$\Im(\lambda_f) \neq 0,$$

which is equivalent to $\phi_f \neq \{0, \pi\}$.

1.6 D^0 time-dependent decay rates to CP-eigenstates

The singly Cabibbo-suppressed $D^0 \to K^+K^-$ and $D^0 \to \pi^+\pi^-$ decays are the main subject of this thesis. Their time evolution is then described in detail in the following, along with the standard formalism currently used in the literature [10, 20]. The decay rates of these decays

are defined as

$$\Gamma(D^0(t)\to f) = N_f|\langle f|\mathscr{H}|D^0(t)\rangle|^2, \qquad \Gamma(\overline{D}^0(t)\to f) = N_f|\langle f|\mathscr{H}|\overline{D}^0(t)\rangle|^2,$$

where N_f is the time-independent normalisation factor, including the results of the phase-space integration[4], and the effective weak interaction Hamiltonian is represented with $\mathscr{H}$. The decay rates can be calculated from eq. (1.19), obtaining

$$\Gamma(D^0(t)\to f) = \left|g_+(t)A_f + \frac{q}{p}g_-(t)\overline{A}_f\right|^2, \qquad \Gamma(\overline{D}^0(t)\to f) = \left|\frac{p}{q}g_-(t)A_f + g_+(t)\overline{A}_f\right|^2,$$

and making use of eq. (1.22), they can be written as [31]

$$\begin{aligned}
\Gamma(D^0(t)\to f) &= \frac{1}{2}e^{-\Gamma t}|A_f|^2\{(1+|\lambda_f|^2)\cosh(y\Gamma t) + (1-|\lambda_f|^2)\cos(x\Gamma t) \\
&\qquad +2\Re(\lambda_f)\sinh(y\Gamma t) - 2\Im(\lambda_f)\sin(x\Gamma t)\} \\
\Gamma(\overline{D}^0(t)\to f) &= \frac{1}{2}e^{-\Gamma t}|\overline{A}_f|^2\{(1+|\lambda_f^{-1}|^2)\cosh(y\Gamma t) + (1-|\lambda_f^{-1}|^2)\cos(x\Gamma t) \\
&\qquad +2\Re(\lambda_f^{-1})\sinh(y\Gamma t) - 2\Im(\lambda_f^{-1})\sin(x\Gamma t)\}, \\
&= \frac{1}{2}e^{-\Gamma t}|A_f|^2\left|\frac{p}{q}\right|^2\{(1+|\lambda_f|^2)\cosh(y\Gamma t) - (1-|\lambda_f|^2)\cos(x\Gamma t) \\
&\qquad +2\Re(\lambda_f)\sinh(y\Gamma t) + 2\Im(\lambda_f)\sin(x\Gamma t)\},
\end{aligned} \tag{1.24}$$

where two dimensionless parameters $x \equiv \Delta M/\Gamma$ and $y \equiv \Delta\Gamma/(2\Gamma)$ are introduced.

1.6.1 Effective decay widths

Taking into account the current experimental sensitivity on x and y of the order of $\mathscr{O}(10^{-2})$ [10], and also considering a time window $\Gamma t \sim \mathscr{O}(1)$, the time-dependent decay rates of equation (1.24) are well approximated by the following expressions

$$\begin{aligned}
\Gamma(D^0(t)\to f) &= e^{-\Gamma t}|A_f|^2\{1+\Re(\lambda_f)y\Gamma t - \Im(\lambda_f)x\Gamma t\} + \mathscr{O}((y\Gamma t)^2) + \mathscr{O}((x\Gamma t)^2) \\
\Gamma(\overline{D}^0(t)\to f) &= e^{-\Gamma t}|\overline{A}_f|^2\{1+\Re(\lambda_f^{-1})y\Gamma t - \Im(\lambda_f^{-1})x\Gamma t\} + \mathscr{O}((x\Gamma t)^2) + \mathscr{O}((y\Gamma t)^2).
\end{aligned}$$

Expanding λ_f as in eq. (1.23), one obtains

$$\begin{aligned}
\Gamma(D^0(t)\to f) &= e^{-\Gamma t}|A_f|^2\{1-\eta_{CP}R_mR_f(y\cos\phi_f - x\sin\phi_f)\Gamma t\} \\
\Gamma(\overline{D}^0(t)\to f) &= e^{-\Gamma t}|\overline{A}_f|^2\{1-\eta_{CP}R_m^{-1}R_f^{-1}(y\cos\phi_f + x\sin\phi_f)\Gamma t\},
\end{aligned}$$

where the above expressions can be further approximated as a purely exponential forms (by using $\Gamma(D^0(t)\to f) \propto e^{-\Gamma t}(1-z\Gamma t+\ldots) \approx e^{-\hat{\Gamma}t}$, if $|z| \ll 1$, with $\hat{\Gamma} = \Gamma(1+z)$) with the following

[4] Since the main topic of this thesis is a measurement of an asymmetry, the normalisation factor N_f can be neglected without any loss of generality.

effective decay widths

$$\begin{aligned}\hat{\Gamma} &= \Gamma\{1+\eta_{CP}R_m R_f(y\cos\phi_f - x\sin\phi_f)\}\\ \hat{\overline{\Gamma}} &= \Gamma\{1+\eta_{CP}R_m^{-1}R_f^{-1}(y\cos\phi_f + x\sin\phi_f)\}.\end{aligned} \tag{1.25}$$

$\hat{\Gamma}$ and $\hat{\overline{\Gamma}}$ are defined as the effective decay widths of the D^0 and $\overline{D}^0$ decaying to f, respectively.

1.7 Time dependent *CP* asymmetry

The time-dependent *CP* asymmetry is defined as the normalised rate difference of a D^0 decaying to a final state f and a $\overline{D}^0$ decaying to the same final state

$$A_{CP}(t) \equiv \frac{\Gamma(D^0(t)\to f) - \Gamma(\overline{D}^0(t)\to f)}{\Gamma(D^0(t)\to f) + \Gamma(\overline{D}^0(t)\to f)}.$$

Substituting the time-dependent rates from eq. (1.24) it follows that

$$A_{CP}(t) = \frac{\begin{array}{c}[(R_m^2-1)(1+|\lambda_f|^2)\cosh(y\Gamma t) + (R_m^2+1)(1-|\lambda_f|^2)\cos(x\Gamma t) +\\ 2(R_m^2-1)\Re(\lambda_f)\sinh(y\Gamma t) - 2(R_m^2+1)\Im(\lambda_f)\sin(x\Gamma t)]\end{array}}{\begin{array}{c}[(R_m^2+1)(1+|\lambda_f|^2)\cosh(y\Gamma t) + (R_m^2-1)(1-|\lambda_f|^2)\cos(x\Gamma t) +\\ 2(R_m^2+1)\Re(\lambda_f)\sinh(y\Gamma t) - 2(R_m^2-1)\Im(\lambda_f)\sin(x\Gamma t)]\end{array}}.$$

As in the previous section, the fact that x and y are small ($\lesssim \mathcal{O}(10^{-2})$) allows expanding at the first order (linear approximation[5]) in $x\Gamma t$ and $y\Gamma t$ the expression of $A_{CP}(t)$, obtaining

$$A_{CP}(t) = A_{CP}^{\text{dir}} + A_{CP}^{\text{ind}}\Gamma t + \mathcal{O}((x\Gamma t)^2) + \mathcal{O}((y\Gamma t)^2). \tag{1.26}$$

The intercept term of $A_{CP}(t)$ is

$$A_{CP}^{\text{dir}} = \frac{R_m^2 - |\lambda_f|^2}{R_m^2 - |\lambda_f|^2} = \frac{1-R_f^2}{1+R_f^2} = \frac{|A_f|^2 - |\overline{A}_f|^2}{|A_f|^2 + |\overline{A}_f|^2},$$

which vanishes if no-*CP* violation is present in the decay, $R_f = 1$. The slope of $A_{CP}(t)$ is

$$A_{CP}^{\text{ind}} = \frac{2\eta_{CP}R_f^2}{(1+R_f^2)^2}\left[(R_f R_m + R_f^{-1}R_m^{-1})x\sin\phi_f - (R_f R_m - R_f^{-1}R_m^{-1})y\cos\phi_f\right], \tag{1.27}$$

and it contains all the three types of *CP* violation: in the decay ($R_f \neq 1$), in the mixing ($R_m \neq 1$) and in the interference between mixing and decay ($\phi_f \neq 0,\pi$). The comparison between the time-dependent asymmetry and the linear approximation is reported in fig. 1.8 for the values of parameters reported in tab. 1.4. The linear approximation of $A_{CP}(t)$ works well with

[5] Note that this is the definition of A_{CP}^{ind}.

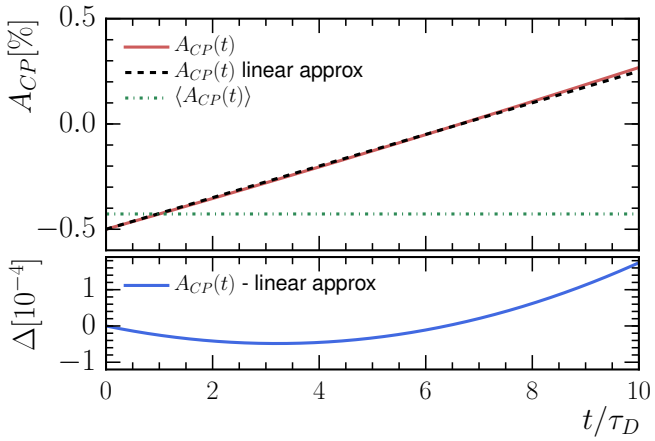

Figure 1.8 – Comparison between the exact model of $A_{CP}(t)$ and its linear approximation, as reported in eq. (1.26). In addition, the time-integrated *CP* violation, $\langle A_{CP}(t)\rangle$, is also reported. The values used for the parameters are reported in tab. 1.4.

Table 1.4 – Approximated values of D^0-system parameters.

x[%]	y[%]	ϕ[deg]	$\mathcal{A}_{\rm d}[\%] = \frac{1-R_f^2}{1+R_f^2}$	$\mathcal{A}_{\rm m}[\%] = \frac{R_m^2-R_m^{-2}}{R_m^2+R_m^{-2}}$
0.06	0.46	9	−0.5	1

discrepancies of about $\mathcal{O}(10^{-4})$.

1.8 A_Γ and y_{CP} observables

Among all the various *CP*-violating observables in the charm sector, the following two observables are the more promising, and are defined as

$$A_\Gamma \equiv \frac{\hat{\Gamma}(D^0\to f)-\hat{\Gamma}(\overline{D}^0\to f)}{\hat{\Gamma}(D^0\to f)+\hat{\Gamma}(\overline{D}^0\to f)}, \qquad y_{CP} \equiv \frac{\hat{\Gamma}(D^0\to f)+\hat{\Gamma}(\overline{D}^0\to f)}{2\Gamma}-1. \tag{1.28}$$

where $\hat{\Gamma}$, the effective decay width, is defined as

$$1/\hat{\Gamma} = \hat{\tau} = \frac{\int t\,\Gamma(t)\,dt}{\int \Gamma(t)\,dt}, \tag{1.29}$$

and it refers to the value of lifetime, $\hat{\tau}$, measured using a single exponential model as it has been done in eq. (1.25). Therefore, A_Γ can be written as

$$A_\Gamma = \frac{\hat{\Gamma}-\hat{\overline{\Gamma}}}{2\Gamma(1+y_{CP})} \simeq \frac{\hat{\Gamma}-\hat{\overline{\Gamma}}}{2\Gamma},$$

where the contribution of $y_{CP} \lesssim \mathcal{O}(10^{-2})$ is neglected. Substituting the effective decay widths reported in eq. (1.25)

$$A_\Gamma = \frac{\eta_{CP}}{2}\left[(R_m R_f - R_m^{-1} R_f^{-1}) y \cos\phi_f - (R_m R_f + R_m^{-1} R_f^{-1}) x \sin\phi_f\right], \tag{1.30}$$

$$y_{CP} = \frac{\eta_{CP}}{2}\left[(R_m R_f + R_m^{-1} R_f^{-1}) y \cos\phi_f - (R_m R_f - R_m^{-1} R_f^{-1}) x \sin\phi_f\right]. \tag{1.31}$$

The value of A_Γ is related to the indirect *CP* violation (see eq. (1.27)) as follows

$$A_\Gamma = -\frac{1}{4}\frac{(1+R_f^2)^2}{R_f^2} A_{CP}^{\text{ind}}. \tag{1.32}$$

1.8.1 Experimental approximations

The current experimental values for the direct *CP* violation $A_{CP}(D^0 \to K^+K^-) = (0.01 \pm 0.14) \times 10^{-2}$ and $A_{CP}(D^0 \to \pi^+\pi^-) = (-0.11 \pm 0.13) \times 10^{-2}$ for $D^0 \to K^+K^-$ and $D^0 \to \pi^+\pi^-$ decays [10], respectively, allows neglecting the *CP* violation in the decay and this implies of assuming $R_f = |\overline{A}_f / A_f| = 1$. Thus, the more common expression of A_Γ and y_{CP} are

$$A_\Gamma = \frac{1}{2}\left[\left(\left|\frac{q}{p}\right| - \left|\frac{p}{q}\right|\right) y \cos\phi_f - \left(\left|\frac{q}{p}\right| + \left|\frac{p}{q}\right|\right) x \sin\phi_f\right], \tag{1.33}$$

$$y_{CP} = \frac{1}{2}\left[\left(\left|\frac{q}{p}\right| + \left|\frac{p}{q}\right|\right) y \cos\phi_f - \left(\left|\frac{q}{p}\right| - \left|\frac{p}{q}\right|\right) x \sin\phi_f\right], \tag{1.34}$$

where $R_m = |q/p|$ and $\eta_{CP} = +1$, both for K^+K^- and $\pi^+\pi^-$ final states. The contribution of the *CP* violation in the mixing and in the interference are clearer visible in A_Γ, than y_{CP}. The first term in A_Γ (proportional to $y\cos\phi_f$) vanishes if no *CP* violation in the mixing is present, $|q/p| = 1$. The second term of eq. (1.33) (proportional to $x\sin\phi_f$) is related to the *CP* violation in the interference, and it is zero if and only if there is no *CP* violation in the interference $\phi_f = \{0, \pi\}$.

In the approximation of no *CP* violation in the decay ($R_f = 1$), the absolute value of A_Γ is equal to the indirect *CP* violation, as found in eq. (1.32)

$$A_\Gamma = -\frac{1}{4}\frac{(1+R_f^2)^2}{R_f^2} A_{CP}^{\text{ind}} \approx -A_{CP}^{\text{ind}}. \tag{1.35}$$

Therefore, the time-dependent *CP* asymmetry of eq. (1.26) can be rewritten as

$$A_{CP}(t) = A_{CP}^{\text{dir}} - A_\Gamma \frac{t}{\tau_D},$$

where $\tau_D = 1/\Gamma$ is the lifetime of the flavour-specific mode $D^0 \to K^-\pi^+$ decay[6].

[6] Note that a possible contribution of the doubly Cabibbo-suppressed (DCS) $D^0 \to K^+\pi^-$ decay mode can be

Universality

The values of A_Γ and y_{CP} are final state dependent, and such a dependency is enclosed in the angle ϕ_f, see eq. (1.33) and eq. (1.34), which is defined as

$$\phi_f = \arg\left(\frac{q\overline{A}_f}{pA_f}\right),$$

where the phase $\arg(\overline{A}_f/A_f)$ can be different for $f = K^+K^-$ or $f = \pi^+\pi^-$ final states. Generally, amplitudes for *CP* eigenstate final states can be written as

$$\begin{aligned} A_f &= \quad A_f^T e^{+i\phi_f^T}\left[1 + r_f e^{i(\delta_f+\varphi_f)}\right], \\ \overline{A}_f &= \eta_{CP} A_f^T e^{-i\phi_f^T}\left[1 + r_f e^{i(\delta_f-\varphi_f)}\right], \end{aligned}$$

where $A_f^T e^{\pm i\phi_f^T}$ is the Standard Model tree level amplitude with its relative weak (*CP* violating) phase. The ratio r_f is the relative magnitude of contributions coming from all non-tree level diagrams, that can introduce a different weak phase φ_f, and δ_f is a strong phase (*CP* conserving). Since penguin diagrams contribution is expected to be small ($\mathcal{O}(10^{-6})$)[32], the terms proportional to r_f can be neglected obtaining

$$\frac{\overline{A}_f}{A_f} = \eta_{CP}\frac{A_f^T e^{-i\phi_f^T}\left[1 + r_f e^{i(\delta_f-\varphi_f)}\right]}{A_f^T e^{+i\phi_f^T}\left[1 + r_f e^{i(\delta_f+\varphi_f)}\right]} \approx \eta_{CP} e^{-2i\phi_f^T}.$$

In addition, as reported in sec. 1.3.1, neglecting terms of the order $\Lambda_b/\Lambda_s = |V_{cb}^* V_{ub}|/|V_{cs}^* V_{us}| \approx \mathcal{O}(10^{-3})$, the angle ϕ_f^T is zero or π, since only real CKM elements are involved. In this assumptions, ϕ_f is therefore independent from the final state (universal) and it is equal to ϕ_D, defined as

$$\phi_D = \arg\left(\frac{q}{p}\right).$$

Therefore, with the approximations described above, the universal expressions of A_Γ and y_{CP} are

$$A_\Gamma = \frac{1}{2}\left[\left(\left|\frac{q}{p}\right| - \left|\frac{p}{q}\right|\right) y\cos\phi_D - \left(\left|\frac{q}{p}\right| + \left|\frac{p}{q}\right|\right) x\sin\phi_D\right], \tag{1.36}$$

$$y_{CP} = \frac{1}{2}\left[\left(\left|\frac{q}{p}\right| + \left|\frac{p}{q}\right|\right) y\cos\phi_D - \left(\left|\frac{q}{p}\right| - \left|\frac{p}{q}\right|\right) x\sin\phi_D\right], \tag{1.37}$$

where the universality holds only in the SM.

safely neglected. Corrections to the flavour-specific $D^0 \to K^-\pi^+$ decay lifetime are of the order DCS/CF$\cdot(x, y)$, where DCS/CF $= |V_{cd}V_{us}^*|/|V_{cs}V_{ud}^*| \approx \mathcal{O}(10^{-2})$. Thus, corrections to the lifetime are about $\mathcal{O}(10^{-4})$ and in $A_{CP}(t)$ of about $\mathcal{O}(10^{-6})$, hence completely negligible with the current experimental sensitivity.

Given the current experimental measurements of x, y [10], in the limit of small *CP* violation in the mixing, $|q/p| \simeq 1$, A_Γ can be approximated as $-x \sin\phi_D$ and its measurement translates into a constraint of the mixing phase ϕ_D, if the value of x is determined elsewhere. This implies $A_\Gamma \leq |x| \lesssim 5 \times 10^{-3}$. For y_{CP} instead, $y_{CP} \approx y \cos\phi_D$ and again $y_{CP} \leq |y| \lesssim 7 \times 10^{-3}$. Therefore, it is crucial, from an experimental point of view, to increase as much as possible the precision on the measurement of these two observables, well below the level of 10^{-3}, in order to search for hints of *CP* violation in the charm sector, which are still unobserved.

The work described in this thesis is focussed on the measurement of only one of the two, A_Γ, and aims at performing the world best measurement using the full Run I data sample of $D^0 \to K^+K^-$ and $D^0 \to \pi^+\pi^-$ decays, collected with the LHCb experiment at the Large Hadron Collider. Beyond the intrinsic importance of searching for first hints of *CP* violation in the charm sector at an unprecedented level of precision, the experimental methodologies developed in the thesis aim also at demonstrating that LHCb will be able to perform the measurement of the A_Γ parameter at even higher precision by fully exploiting the larger data samples that will be available in the future LHC Runs (LHCb-Upgrade (Run III) and Future Upgrades of LHCb). A_Γ is a golden observable and it is very likely that it will be the first place where *CP* violation in the charm sector will be experimentally observed.

2 Measurement overview and current experimental status

A brief description of the main experimental techniques to measure A_Γ observable is given. These are common to all the experiments, either for those installed at hadron colliders or at e^+e^- colliders, and deserve a brief introduction for a better understanding of the next chapters.

2.1 $D^0 \to h^+h^-$ decays and flavour tag

A measurement of *CP* asymmetry requires to identify the flavour of the decaying particle. While the flavour of a charged particle can be easily determined by the total charge of its decay products, for a neutral particle, where the total charge of the final state is null, the situation is more difficult. To overcome this challenge, usually, the production mechanisms are exploited. The idea is to collect the neutral mesons produced into a charged final state where the particles produced together with the neutral meson are used to infer its flavour. This is also particular relevant because the flavour can change during the time evolution of the meson, and the A_Γ observable requires to know the flavour at the production (see eq. (1.28)).

The flavour of the $D^0(\overline{D}^0)$ mesons decaying to h^+h^- (where h stands for a kaon or a pion) is determined at the production ($t = 0$) in general through two decay chains

- $D^{*+} \to D^0\pi^+$ and $D^{*-} \to \overline{D}^0\pi^-$,
- $\overline{B} \to D^0\ell^-\overline{\nu}_\ell X$ and $B \to \overline{D}^0\ell^+\nu_\ell X$.

In the latter, D^0 mesons are produced in a semileptonic B decay, and the charge of the lepton ℓ can be used to infer their flavour. The relationship between the lepton charge and the D^0 flavour is assured by the transitions $b \to cW^-$ and $\overline{b} \to \overline{c}W^+$, as shown in fig. 2.1. These D^0 decays are called "secondary decays", since they come from a subsequent B meson decay. The measured relative branching fraction for a mixture of $B^\pm/B^0/B_s^0$ decaying to $D^0\ell^-\overline{\nu}_\ell X$ is $\Gamma(b \to D^0\ell^-\overline{\nu}_\ell X)/\Gamma_{\text{tot}} = (6.81 \pm 0.34)\%$, where X indicates anything needed to complete the decay [20].

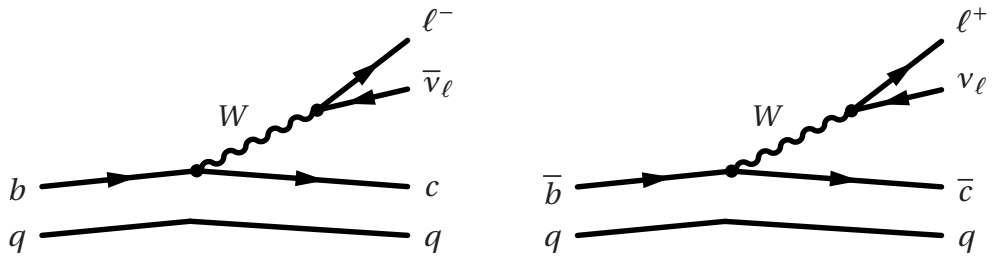

Figure 2.1 – Tree-level Feynman diagrams for (left) $\overline{B} \to D^0 \ell^- \overline{\nu}_\ell X$ and (right) $B \to \overline{D}^0 \ell^+ \nu_\ell X$ decays.

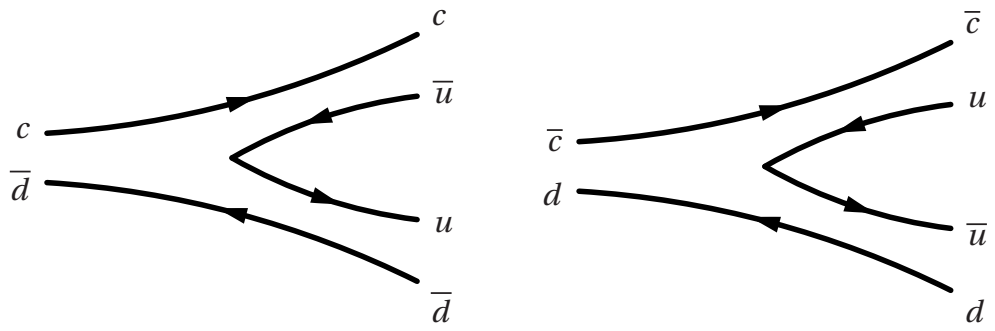

Figure 2.2 – Tree-level Feynman diagrams for (left) $D^{*+} \to D^0 \pi^+$ and (right) $D^{*-} \to \overline{D}^0 \pi^-$.

On the other hand, $D^{*+} \to D^0 \pi^+$ and $D^{*-} \to \overline{D}^0 \pi^-$ decays are called "prompt decays", since $D^{*\pm}$ mesons decay immediately after being produced. They occur because of the strong interaction, implying that the quarks flavour remains unchanged, leading to the correspondence between the charge of the pion and the D^0 flavour, as reported in fig. 2.2. The relative branching fraction for these decays is $\Gamma(D^{*+} \to D^0 \pi^+)/\Gamma_{\text{tot}} = (67.7 \pm 0.5)\%$ [20].

Since the measurement of A_Γ described in this thesis uses the strong $D^{*+} \to D^0 \pi^+$ decay chain, the following sections are devoted to the experimental challenges of this method, unless otherwise stated.

2.2 From the theory to the A_Γ measurement

Historically, the measurement of A_Γ has been performed starting from its definition, as reported in eq. (1.33). This can be easily rewritten in terms of the effective lifetimes

$$A_\Gamma \equiv \frac{\hat{\Gamma}(D^0 \to f) - \hat{\Gamma}(\overline{D}^0 \to f)}{\hat{\Gamma}(D^0 \to f) + \hat{\Gamma}(\overline{D}^0 \to f)} = \frac{\hat{\tau}(\overline{D}^0 \to f) - \hat{\tau}(D^0 \to f)}{\hat{\tau}(\overline{D}^0 \to f) + \hat{\tau}(D^0 \to f)}, \tag{2.1}$$

since $\hat{\Gamma} = 1/\hat{\tau}$, where $\hat{\tau}$ is the effective lifetime defined in eq. (1.29). Thus, A_Γ can be extracted measuring the lifetime separately for the D^0 and the $\overline{D}^0$ meson using a single exponential model. However, the measurement of an absolute lifetime in an hadron collider environment

is challenging due to the bias introduced by trigger requirements (see sub-sec. 3.2.9 and sec. 4.2), that are based on lifetime related quantities, in order to efficiently select D^0 meson decays. As a result, the D^0 decay time distribution is not anymore a pure exponential, being sculpted in a non trivial manner. For this reason, the measurement of A_Γ has been in the past a prerogative of e^+e^- machines, where events are inclusively triggered without any bias to the decay time [33, 34].

The challenge of measuring absolute lifetimes is to know (with the desired level of accuracy) the acceptance function. In general, the acceptance function, A, maps the true distribution, F, to the reconstructed one, f,

$$f(\boldsymbol{\theta}) = A(\boldsymbol{\theta}) \cdot F(\boldsymbol{\theta}),$$

where $\boldsymbol{\theta}$ represent one or more observables, as the proper decay time, the momentum of the particle, the pseudo-rapidity and so forth. A standard approach to extract the acceptance function uses the realistic Monte Carlo simulation. However, that is not sufficiently reliable for the A_Γ measurement, approaching an unprecedented level of precision ($\mathcal{O}(10^{-4})$). A fully data-driven method to extract the acceptance function has been used in LHCb for the A_Γ measurement, performed in 2010 and 2011 with an integrated luminosity of 209 pb^{-1} and 1 fb^{-1}, respectively (see sec. 2.5). This method, called "swimming", consists in moving the D^0 along its momentum-direction and re-run all the trigger and offline reconstruction algorithms to know if the event would pass or not the selection [35]. In this way, a per-candidate acceptance function versus the D^0 proper decay time can be extracted, from which is possible to obtain the total acceptance function, re-running the swimming procedure for *each* event in the data sample. The systematic uncertainties achieved using this procedure have been assessed to be much lower than the statistical uncertainty allowing a competitive measurement of A_Γ [36]. Although its success, it is not clear if the implementation of such technique is affordable also in the future, with data samples much larger in size than the current available statistics. The swimming method demands a huge computing power, since it requires to re-run the full trigger chain and the reconstruction algorithms around a hundred of times on each event [37].

To overcome the challenge of measuring the acceptance function, an alternative approach is used to measure A_Γ. The value of indirect *CP* violation is approximatively equal to A_Γ, expect for the sign, as reported in eq. (1.35), and therefore the time-dependent *CP* asymmetry is well approximated as

$$A_{CP}(t) \approx A_{CP}^{\text{dir}} + A_{CP}^{\text{ind}} \frac{t}{\tau_{D^0}} = A_{CP}^{\text{dir}} - A_\Gamma \frac{t}{\tau_D}, \tag{2.2}$$

and A_Γ can be extracted from a fit to a straight line of the measured $A_{CP}(t)$. This approach does not require the knowledge of the acceptance function since any acceptance effect cancels out in the asymmetry. The measurement of A_Γ with this approach has been already performed by CDF [38] and LHCb [36, 39].

2.2.1 Raw *CP* asymmetry

From an experimental point of view, the observed decay widths asymmetry, $A_{\text{raw}}(t)$, is defined as

$$A_{\text{raw}}(t) = \frac{\Gamma_{\text{obs}}(t) - \overline{\Gamma}_{\text{obs}}(t)}{\Gamma_{\text{obs}}(t) + \overline{\Gamma}_{\text{obs}}(t)},$$

where the observed decay width is

$$\Gamma_{\text{obs}}(t) = \frac{1}{N}\frac{\mathrm{d}N(t)}{\mathrm{d}t},$$

and $\mathrm{d}N(t)$ is the number of the reconstructed D^* mesons associated to a D^0 meson having a decay time in the interval $[t, t+\mathrm{d}t]$. This is related to the number of generated D^* meson decays, $n(t)$, through

$$N(t) \propto \epsilon A n(t),$$

where A is the acceptance function and ϵ is total efficiency for reconstructing a D^* meson. Thus, the observed asymmetry does not directly correspond to the *CP* asymmetry needed to extract A_Γ, reported in eq. (2.2). Indeed, the raw asymmetry is

$$A_{\text{raw}}(t) = \frac{\epsilon^+ n^+(t) - \epsilon^- n^-(t)}{\epsilon^+ n^+(t) + \epsilon^- n^-(t)},$$

where the acceptance function A cancels in the ratio, while in general reconstruction efficiencies are different. For small asymmetries $\mathcal{O}(1\%)$, $A_{\text{raw}}(t)$ can be rewritten as

$$A_{\text{raw}}(t) = A_{CP}(t) + A_{\text{D}} + A_{\text{P}} + \mathcal{O}(A^3). \tag{2.3}$$

where A_{P} is the initial production asymmetry and A_{D} is the detection asymmetry in reconstructing D^{*+} decay, and $\mathcal{O}(A^3)$ indicates terms as $A_{\text{D}} A_{\text{P}} A_{CP}$ (see app. B for the mathematical formalism). When the $D^{*+} \to D^0\pi^+ \to [h^+h^-]_D\pi^+$ meson decays to K^+K^- or $\pi^+\pi^-$ *CP* eigenstates, the non-vanishing part of the detection asymmetry can be ascribed only to the detection (trigger, reconstruction and selection) of the soft pion

$$A_{\text{D}} = A_{\text{D}}^{\pi_s},$$

assuming that the total efficiency can be factorised into $\epsilon(D^{*+}) = \epsilon(D^0)\cdot\epsilon(\pi^+)$. In general soft pion and production asymmetries are independent of D^0 decay time, however, due to second-order effects and artificial detector-induced correlation between momentum and decay time, a small D^0 decay time dependence can appear, as described in chap. 5, and must be correctly accounted for. Thus, after correcting for any detector induced time-dependent instrumental effects, any observed significant slope in $A_{\text{raw}}(t)$ would indicate a significant time-dependence of $A_{CP}(t)$, namely a non-zero A_Γ.

2.3 Control channel: $D^0 \to K^-\pi^+$ decays

The measurement of the A_Γ parameter is very precise, therefore the entire analysis procedure must be validated to ensure the robustness and reliability of the experimental methods and a complete control of the systematic uncertainties. The high statistics Cabibbo-favoured $D^0 \to K^-\pi^+$ decays fulfil this need, since the genuine physical time-dependent *CP* asymmetry is expected to be undetectable [40] (see also app. A). In analogy to the time-dependent asymmetry of $D^0 \to K^+K^-$ and $D^0 \to \pi^+\pi^-$ decays, the time-dependent asymmetry of the $D^0 \to K^-\pi^+$ decays can be written as

$$A_{CP}^{K\pi}(t) = A_{CP}^{\text{dir}} - A_\Gamma^{K\pi}\frac{t}{\tau_D}, \tag{2.4}$$

where $A_\Gamma^{K\pi} \lesssim \mathcal{O}(10^{-5})$ is called "pseudo-A_Γ". Instrumental asymmetries are expected to be larger in the $D^0 \to K^-\pi^+$ sample because of the additional effects coming from the different interaction probability with matter of opposite-charged kaons. Also in this case for small asymmetries, the raw asymmetry can be rewritten as

$$A_{\text{raw}}^{K\pi} = A_{\text{D}} + A_{\text{P}} + \mathcal{O}(A^3). \tag{2.5}$$

where A_{P} is the initial production asymmetry and A_{D} is the detection asymmetry in reconstructing D^{*+} final decay products, which contains also non-vanishing term from the D^0 decay products, being no *CP* symmetric

$$A_{\text{D}} = A_{\text{D}}^{K\pi} + A_{\text{D}}^{\pi_s}.$$

The time-dependent term $A_{CP}(t)$ is omitted in eq. (2.5) because it is expected to be much smaller than our current experimental uncertainty (see ref. [40] and app. A). As explained above, generally, detection and production asymmetries are independent of D^0 decay time. However, a small D^0 decay time dependence is found for $A_{\text{raw}}^{K\pi}$, as will be described in chap. 5, and it can be only ascribed to detector induced effects. These effects are very dangerous and must be corrected in order to measure A_Γ on $D^0 \to K^+K^-$ and $D^0 \to \pi^+\pi^-$ decays.

2.4 Physical background to A_Γ: secondary decays

When the flavour of the D^0 meson is tagged through the D^{*+} decays, it is necessary account for the fact that the D^{*+} meson can be produced either directly from the primary interaction or from a decay of a B meson, the so-called secondary decays[1]. Proper decay time of D^0 mesons is reconstructed from the distance of the decay vertex of the D^0 to the primary vertex of collision, therefore the reconstructed decay time of secondary decays is biased towards larger values, because of the large lifetime of B meson (more details on secondary decays are

[1] These processes are very similar to those described in sec. 2.1 used to tag the flavour of the D^0 meson, and therefore are indicated as secondary decays.

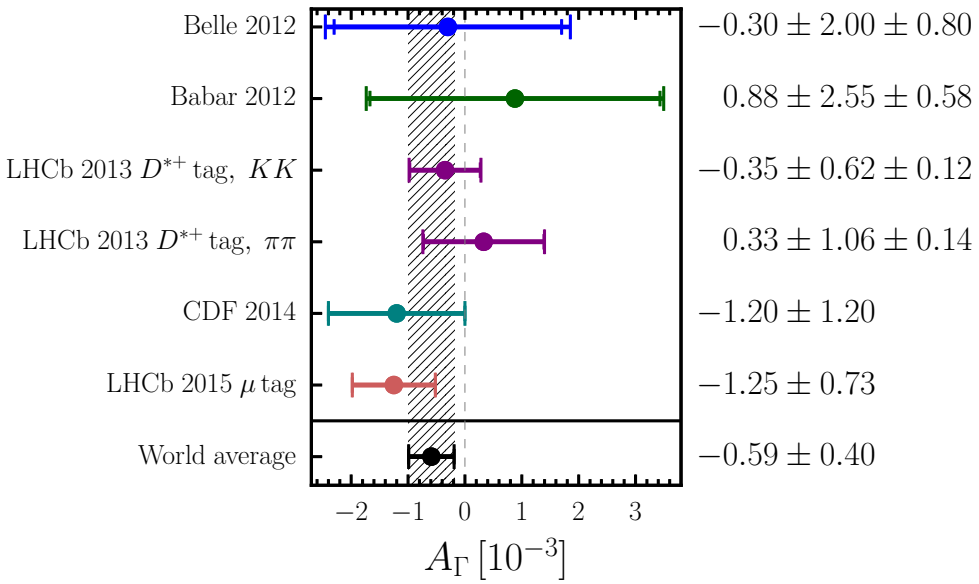

Figure 2.3 – Current experimental status on A_Γ. From top to bottom Belle 2012 [33], BaBar 2012 [34], LHCb 2013 D^{*+} tag KK [36], LHCb 2013 D^{*+} tag $\pi\pi$ [36], CDF 2014 [38], LHCb 2015 μ tag [39].

given in chap. 7). Thus, secondary decays represent a physical background that has to be subtracted to avoid biases in the A_Γ measurements.

At e^+e^- machines, secondary decays background is reduced to a negligible level requiring a threshold on D^0 momentum measured in the centre-of-mass frame. At hadron colliders, instead, secondary decays are subtracted using variables related to the impact parameter of the D^0 mesons.[2]

The situation is different if the D^0 meson flavour is tagged through secondary decays (sec. 2.1), *i.e.* D^0 coming from B meson decays. In this case, the D^0 decay time is measured from the decay vertex of the B meson, therefore it is independent from the B decay time, and no bias is introduced.

2.5 Current experimental status

The value of A_Γ was measured in the past at the B-factories and recently also at CDF. In the last years LHCb entered the game as the leading player. All the available measurements are reported in fig. 2.3.

[2] The definition of the impact parameter is reported in chap. 4.

2.5.1 Experiments at e^+e^- colliders

Two measurements are available from the experiments at e^+e^- colliders: one from Belle collaboration [33] and the other one from BaBar collaboration [34]. Both exploit the D^{*+} decays to tag the flavour of the D^0 mesons, as explained in sec. 2.1. The value of A_Γ is measured simultaneously for the $D^0 \to K^+K^-$ and the $D^0 \to \pi^+\pi^-$ decays. The effective lifetimes (see eq. (2.1)) of D^0 and $\overline{D}^0$ mesons, decaying to K^+K^- and $\pi^+\pi^-$, are extracted through a likelihood fit to the decay time distributions. The analyses strategies are validated on the $D^0 \to K^-\pi^+$ decay mode, as explained in sec. 2.3. Secondary decays background (see sec. 2.4), as already mentioned, is reduced to a negligible level with a requirement on the D^0 momentum in the centre-of-mass frame of the e^+e^- collision for both measurements. The measured values of A_Γ are

$$A_\Gamma(KK+\pi\pi;\text{Belle}) = (-0.30 \pm 2.00 \pm 0.80) \times 10^{-3},$$
$$A_\Gamma(KK+\pi\pi;\text{BaBar}) = (\ \ 0.88 \pm 2.55 \pm 0.58) \times 10^{-3},$$

where the first error is statistical and the second one is systematic. The dominant sources of systematic uncertainties come from the uncertainty on acceptance function and from the background parametrisation for the Belle measurement [33]. Instead, for the BaBar measurement [34], the total systematic uncertainty is driven by the uncertainty on the selection made on D^0 candidates decay time error.

2.5.2 Experiments at hadron colliders

The A_Γ value was also measured at CDF experiment based on a $p\overline{p}$ collider, and at LHCb experiment based on a pp collider.

A_Γ at CDF

The A_Γ measurement at CDF [38] exploits the indirect *CP* method, as reported in eq. (2.2), therefore the sample is divided in bins of the D^0 decay time and a linear fit to the time-dependent *CP* asymmetry is performed to extract the value of A_Γ. The flavour of the D^0 is tagged using the D^{*+} decays, as explained in sec. 2.1. In each decay time bin, secondary decays background is subtracted through a fit to the distribution of the D^0 impact parameter. The value of A_Γ is measured independently in the $D^0 \to K^+K^-$ and $D^0 \to \pi^+\pi^-$ decays and they are found to be [38]

$$A_\Gamma(KK;\text{CDF}) = (-1.90 \pm 1.50 \pm 0.40) \times 10^{-3},$$
$$A_\Gamma(\pi\pi;\text{CDF}) = (-0.10 \pm 1.80 \pm 0.30) \times 10^{-3},$$

where the first uncertainty is statistical and the second one is systematic. The dominant systematic uncertainty is due to the subtraction of the secondary decays, in particular due to the parametrisation of the secondary component in the D^0 impact parameter fit. Back-

ground subtraction in the $D^0 \to K^+K^-$ decay sample largely contributes to the final systematic uncertainty of $A_\Gamma(KK)$, due to the larger mis-reconstructed background with respect to the $D^0 \to \pi^+\pi^-$ decay mode. The two measurements of A_Γ in the $D^0 \to K^+K^-$ and $D^0 \to \pi^+\pi^-$ decays are then combined together obtaining

$$A_\Gamma(KK+\pi\pi;\text{CDF}) = (-1.20 \pm 1.20) \times 10^{-3}.$$

A_Γ at LHCb

The A_Γ observable is measured with two statistically independent samples by the LHCb collaboration. One measurement uses the D^{*+} decays to identify the D^0 meson flavour [36], while the other one uses the D^0 meson coming from the semileptonic B decays ($B \to D^0\mu\nu_\mu X$ decays), called semileptonic A_Γ [39]. The two measurements adopt a different approach to extract the value of A_Γ. Thus, they will be separately discussed.

Semileptonic A_Γ The semileptonic A_Γ measurement [39] is performed over the full Run I data sample collected by LHCb, corresponding to an integrated luminosity of 3 fb^{-1}. The method used to extract A_Γ is the one reported in eq. (2.2), and therefore the sample is divided in bins of D^0 decay time. The D^0 signal yield is extracted through a simultaneous (between D^0 and $\overline{D}^0$) maximum likelihood fit to the D^0 invariant mass in each decay time bin. The measurement is validated on the $D^0 \to K^-\pi^+$ sample obtaining a value for pseudo-A_Γ in good agreement with the hypothesis of no CP violation, $A_\Gamma(K\pi) = (0.09 \pm 0.32) \times 10^{-3}$. The measured values of A_Γ in $D^0 \to K^+K^-$ and $D^0 \to \pi^+\pi^-$ decays are

$$A_\Gamma(KK;\text{LHCb}\,\mu\,\text{tag}) = (-1.34 \pm 0.77^{+0.26}_{-0.34}) \times 10^{-3},$$
$$A_\Gamma(\pi\pi;\text{LHCb}\,\mu\,\text{tag}) = (-0.92 \pm 1.45^{+0.25}_{-0.33}) \times 10^{-3},$$

where the first uncertainty is statistical and the second one is systematic. The dominant systematic uncertainty is due to the mis-tag of the D^0 meson flavour. Other systematic uncertainties come from the detection asymmetry and from the D^0 mass model, especially in the $D^0 \to K^+K^-$ decay mode. The combined value of A_Γ is

$$A_\Gamma(KK+\pi\pi;\text{LHCb}\,\mu\,\text{tag}) = (-1.25 \pm 0.073) \times 10^{-3}.$$

D^{*+} tagged A_Γ The A_Γ observable is measured in the D^{*+}-tagged sample, using only about one third of the total integrated luminosity of the full Run I data sample, corresponding to 1 fb^{-1} [36]. The value of A_Γ is extracted with both methods: measuring the effective lifetimes as in eq. (2.1) and extracting A_Γ from the time-dependent asymmetry as described in eq. (2.2).

To extract the value of A_Γ from the individual effective lifetime measurements an accurate knowledge of the acceptance function is needed, since the requirements applied to select the D^0 candidates sculpt the decay time distribution. The *swimming* technique (see sec. 2.2) is

used to overcome this challenge. The secondary decays background is subtracted though a maximum likelihood fit to the $\chi^2_{\rm IP}(D^0)$, a variable related to the impact parameter[3] of the D^0 meson. The results for A_Γ are

$$A_\Gamma(KK;\,\text{LHCb}\,D^{*+}\,\text{tag}) = (-0.35 \pm 0.62 \pm 0.12) \times 10^{-3},$$
$$A_\Gamma(\pi\pi;\,\text{LHCb}\,D^{*+}\,\text{tag}) = (\ \ 0.33 \pm 1.06 \pm 0.14) \times 10^{-3},$$

where the first error is statistical and the second one is systematic. The systematic uncertainties are driven by the knowledge of the acceptance function (0.09×10^{-3} and 0.11×10^{-3} for $D^0 \to K^+K^-$ and $D^0 \to \pi^+\pi^-$ decay modes, respectively). The other dominant contribution comes from the subtraction of secondary decays background (0.07×10^{-3} for both decay modes).

The second measurement uses the same data sample, corresponding to 1 fb^{-1}, and extracts A_Γ through the time-dependent charge asymmetry (see eq. (2.2)). Signal yields and secondary decays background are assessed simultaneously through a maximum likelihood fit to the D^0 mass, the mass difference between the D^* and the D^0, and the $\chi^2_{\rm IP}(D^0)$ in each decay time bin. However, a significant discrepancy between results for the two magnet polarities is observed[4]. A systematic uncertainty is therefore assigned of 0.58×10^{-3} (0.82×10^{-3}) for $A_\Gamma(KK)$ ($A_\Gamma(\pi\pi)$), comparable with the statistical uncertainty of 0.65×10^{-3} (1.22×10^{-3}). In addition, the systematic uncertainty associated to the secondary decays background are of the same magnitude. Thus, this analysis has been used as a cross-check of the first one (the one with the effective lifetimes method).

A_Γ in this thesis

In this thesis the measurement of A_Γ with the full LHCb Run I data sample, corresponding to an integrated luminosity of 3 fb^{-1}, is presented. The identification of the D^0 meson flavour at production is inferred by the the sign of the charge of the pion of the strong $D^{*+} \to D^0\pi^+$ decay. The aim of this work is double, providing the world best measurement of the A_Γ parameter in order to look for the first hints of *CP* violation in the charm sector and simultaneously to demonstrate that this measurement can be performed even at much higher statistics by drastically reducing the current systematic uncertainties.

Since the method of performing the individual measurement of the effective lifetimes is not practicable for future measurements because its excessive demanding of computing power, the approach of measuring A_Γ through the slope of the time-dependent *CP* asymmetry remains the only possible way to be pursued in order to achieve a precision of order 10^{-4} or below. However, the current available LHCb measurement [36] on 1 fb^{-1}, where both approaches have been carried on for extracting A_Γ, seems to point to a unsatisfactory picture where the level of systematic uncertainties (0.89×10^{-3} for the $D^0 \to K^+K^-$ and 1.13×10^{-3} for the $D^0 \to \pi^+\pi^-$) would prevent any attempt to improve the precision of the measurement by using

[3] The definition of the $\chi^2_{\rm IP}$ is reported in chap. 4.
[4] Magnetic field is periodically reversed at LHCb, see sec. 3.2.

the second method.

The work described in this thesis is therefore focussed on the the approach of measuring A_Γ through the slope of the time-dependent *CP* asymmetry. The idea is to completely revisit such a methodology, in order to simplify the analysis as much as possible in preparation of future high precision measurement with larger data samples, and simultaneously in order to drastically reduce the systematic uncertainties at the level or better than the approach of the measurement of effective lifetimes. This analysis is therefore devised to overcome the challenges of the previous LHCb measurement [36], and it is driven by the simplicity. The three-dimensional simultaneous likelihood fit is avoided due to the complexity of such technique in an high statistics regime. Signal yields are simply extracted through a sideband subtraction (see chap. 4). The source of the discrepancy between the two magnet polarities is tracked down and an innovative technique is devised to correct for such an effect (see chap. 5). The secondary decays background is faced with a new method specifically devised to keep under control the associated systematic uncertainty (see chap. 7).

3 Experimental apparatus

This chapter briefly describes the Large Hadron Collider accelerator and the LHCb experiment, focusing on the relevant subsystems for the measurement of the A_Γ observable, such as the tracking and trigger systems. Exhaustive descriptions of the experimental apparatus can be found in the references given through the chapter.

3.1 LHC

The Large Hadron Collider (LHC) is a two-ring-hadron accelerator installed inside a 27 km tunnel, placed 100 m underground across the Swiss and French borders [41]. The LHC is a part of the accelerator complex, see fig. 3.1 at the European Organisation for Nuclear Research laboratory (CERN). The LHC machine is designed to collide protons up to a centre-of-mass energy, $\sqrt{s}$, of 14 TeV, at an instantaneous luminosity of $10^{34}\,\mathrm{cm}^{-2}\,\mathrm{s}^{-1}$.

Before the injection into the LHC ring, the protons (obtained from ionised hydrogen atoms deprived of their electrons) have to pass several accelerator systems. First of all, they are accelerated at the Linear Accelerator (LINAC 2) to an energy of 50 MeV, and then injected into the Proton Synchrotron Booster (BOOSTER), where the beams reach energies of 1.5 GeV. At this point, the beams are further accelerated in the Proton Synchrotron (PS) to 25 GeV and in the Super Proton Synchrotron (SPS) reaching the energy of 450 GeV needed for the injection in the LHC ring. Finally, the beams are accelerated in the main LHC ring, through radiofrequency cavities, reaching the highest energy. The orbit of beams are controlled through a complex system of magnets (called the "optics" of the machine), using several dipole, quadrupole, sextupole and octupole superconducting magnets. Beams are not continuous but divided in *bunches*, packets of protons that collide in four nominal interaction points, where the four main experiments are set up, which are LHCb, ATLAS, CMS and ALICE.

Currently, the LHC is running at its highest energy of 13 TeV. However, the analysis described in this thesis uses data collected in the past run of the LHC machine, called Run I. Run I starts on March 30th 2010 when the first proton-proton collision at 3.5 TeV occurred. The beam

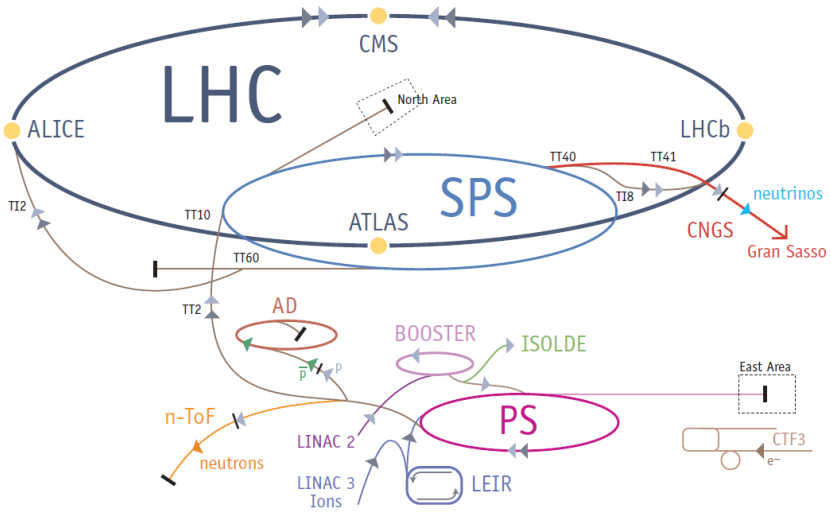

Figure 3.1 – Schematic view of the complex of CERN accelerators.

energy remained constant until the end of 2011. Then, it was increased to 4 TeV for all the 2012, when the Run I ends. After a pause of two years, where several checks and upgrades have been made on magnets, LHC restarts at the beginning of 2015 at an energy of 13 TeV.

3.1.1 Luminosity at LHCb

The events rate (number of events per second) of any process generated in the LHC proton-proton collisions is given by

$$\frac{\mathrm{d}N}{\mathrm{d}t} = \mathscr{L} \cdot \sigma, \tag{3.1}$$

where σ is the cross section of the given process and $\mathscr{L}$ is the instantaneous luminosity of the machine. For Gaussian distributed colliding bunches, the luminosity can be written as [41]

$$\mathscr{L} = n_b f_{\mathrm{rev}} \frac{n^2 \gamma}{4\pi \sigma_x^{\mathrm{eff}} \sigma_y}$$

where n_b is the number of bunches per beam, f_{rev} is the revolution frequency, γ is the relativistic gamma factor and n is the number of protons in each bunch. σ_x^{eff} is the standard deviation of the transverse profile of bunch modified for a geometrical correction factor that takes into account that the collision is not head-on but there is a crossing angle, θ_c, between the two beams

$$\sigma_x^{\mathrm{eff}} = \sigma_x \cdot \sqrt{1 + \left(\frac{\theta_c \sigma_z}{2\sigma^*}\right)^2},$$

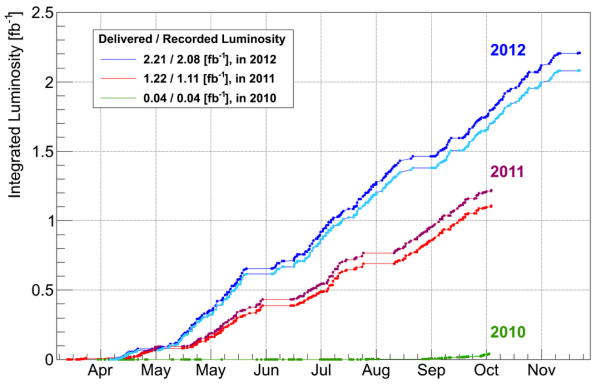

Figure 3.2 – Delivered (dark coloured lines) and recorded (light coloured lines) LHCb integrated luminosities.

where σ_z is the RMS bunch length, and σ^* the transverse RMS of the beam size at the interaction point. At LHCb the cross angle is about 0.4 mrad.

While CMS and ATLAS aim to the maximum peak luminosity of $10^{34}\,\mathrm{cm}^{-2}\,\mathrm{s}^{-1}$, LHCb is designed to operate at an instantaneous luminosity of $2\times10^{32}\,\mathrm{cm}^{-2}\,\mathrm{s}^{-1}$. Thus, LHCb is equipped with a luminosity levelling apparatus, consisting into an adjustment of the transversal beams overlap, in order to keep constant the instantaneous luminosity during the fill. However, in the 2012 data taking, given the good response of the detector, LHCb was able to run at a luminosity of $4\times10^{32}\,\mathrm{cm}^{-2}\,\mathrm{s}^{-1}$, the double of the design luminosity.

The instantaneous luminosity, $\mathscr{L}$, integrated over the data-taking time provides the integrated luminosity $L=\int\mathscr{L}\,\mathrm{d}t$, which is directly related to the number of events delivered, see eq. (3.1). The integrated luminosity recorded by the LHCb experiment is $1.11\,\mathrm{fb}^{-1}$ in 2011 at $\sqrt{s}=7\,\mathrm{TeV}$ and $2.08\,\mathrm{fb}^{-1}$ in 2012 at $\sqrt{s}=8\,\mathrm{TeV}$, as shown in fig. 3.2.

3.2 LHCb Experiment

The LHCb experiment is designed to study the physics of beauty and charm quarks. Charm and beauty hadrons cannot be produced directly from the valence quarks of the proton (uud), but from the interactions of two partons leading to the creation of $b\bar{b}$ and $c\bar{c}$ pairs.[1] These pairs are likely to be produced along the beam axis, as shown in fig. 3.3, and therefore, the LHCb detector is designed as a single arm forward spectrometer with a pseudorapidity ($\eta=-\log(\tan(\theta/2))$) of $2<\eta<5$, with an acceptance between 10 and 250 mrad (300 mrad) in

[1] b and c could be also produced from decays of heavier resonances, *e.g.* $t\to W^+b$, $W^+\to c\bar{s}$, $Z\to b\bar{b}(c\bar{c})$ *etc.*. However, these production mechanisms are suppressed with respect to the strong pairs production. For instance, the production with the top contributes to the total $b\bar{b}$ cross section of about $\sigma(pp\to t\bar{t}\to b\bar{b}X)/\sigma(pp\to b\bar{b}X)\approx 174\,\mathrm{pb}/72\,\mu\mathrm{b}\approx 2\times10^{-6}$ at $\sqrt{7}\,\mathrm{TeV}$ [20].

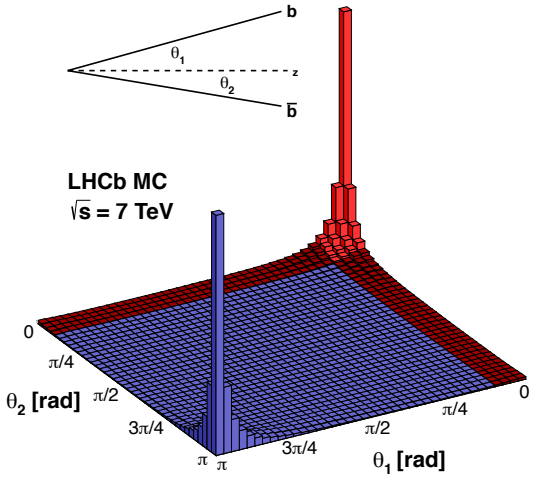

Figure 3.3 – $b\bar{b}$ angular production distribution at $\sqrt{s} = 7$ TeV obtained from PYTHIA [42].

the vertical (horizontal) plane. In addition, the forward geometry favours the reconstruction og b- and c-hadrons with large Lorentz boost. A big boost allows a precise measurement of secondary vertex since the space travelled in the laboratory system is sufficiently large and a very good decay time resolution can be achieved.

The LHCb detector is schematically represents in fig. 3.4, and from left to right the main subdetectors are:

VELO the Vertex Locator, placed around the interaction region, is a silicon strip detector which provides a precise reconstruction of the decay vertices;

RICH1 the Ring Imaging Cherenkov detector providing information for particle identification and it is placed just after the VELO;

TT the Tracker Turicensis is the first tracking station placed just before the magnet;

T1, T2, T3 the tracking stations placed forward with respect to the magnet;

RICH2 the second Ring Imaging Cherenkov detector covering a different momentum range with respect to the RICH1;

ECAL the electromagnetic calorimeter system, which is necessary for triggering besides the identification of electrons and photons;

HCAL the hadronic calorimeter system, used also for trigger on hadrons;

Muon Stations the Muon Stations are placed in the furthest part of the detector from the interaction region. Only muons can reach these stations without being stopped from the detector material placed before.

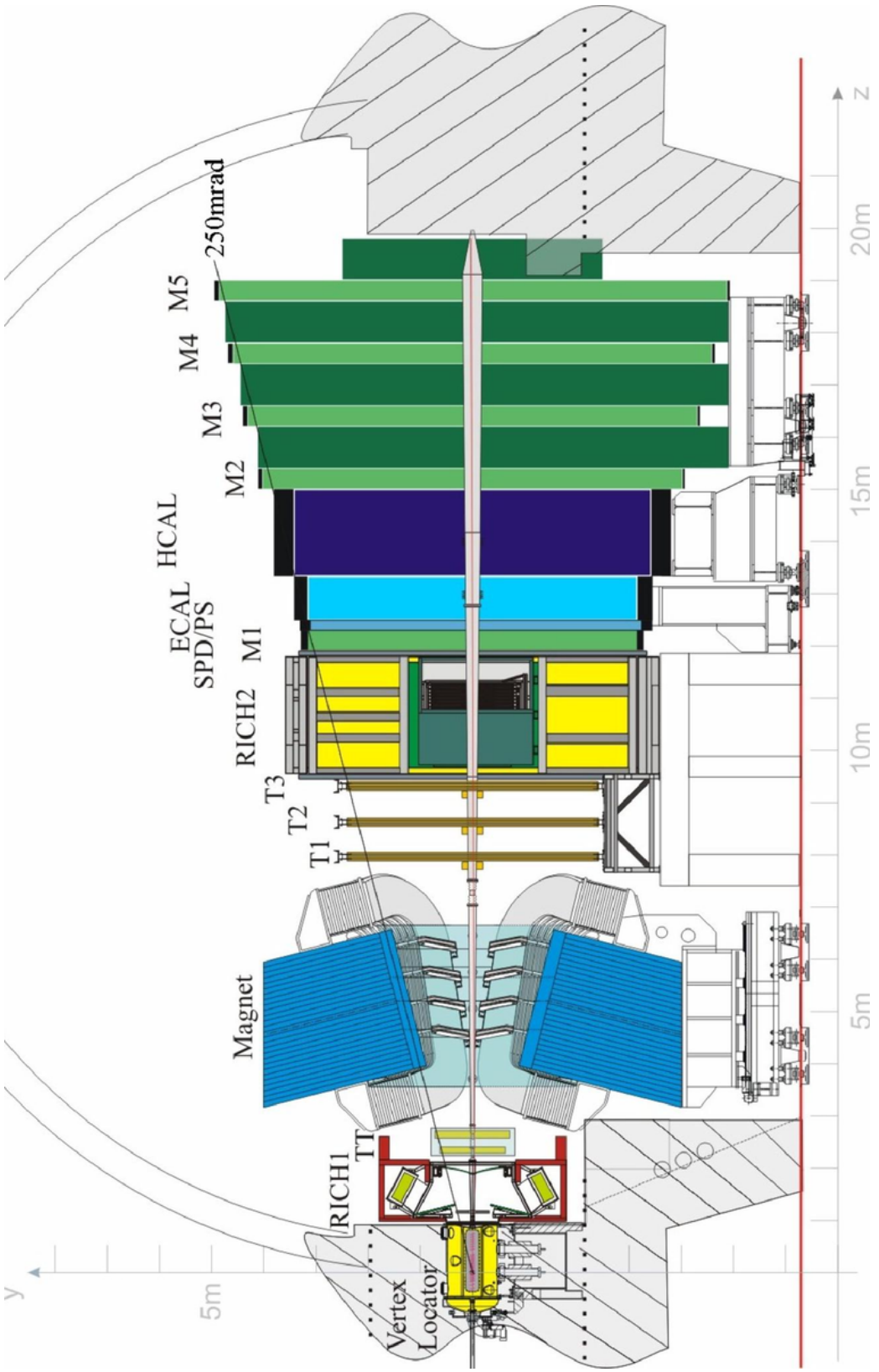

Figure 3.4 – Schematic representation of a section of the LHCb detector.

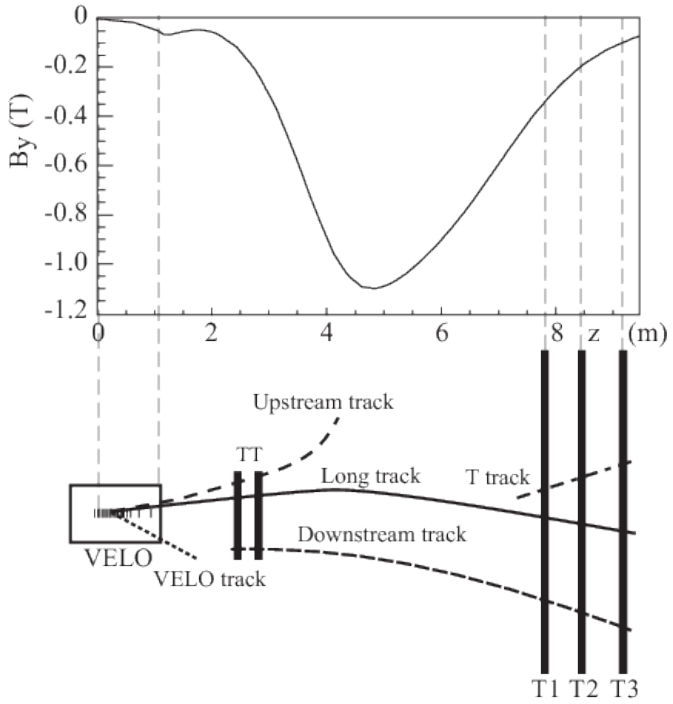

Figure 3.5 – The magnetic field strength along the y-axis as function of z coordinate. Below the corresponding z location of the tracking detectors are shown. The different type of tracks distinguished in LHCb are also reported. Image taken from ref. [43].

3.2.1 Coordinate system

The LHCb coordinate system is a right-handed system, centered in the nominal LHC interaction point. The z-axis points along the clockwise rotating beam direction (looking at the LHC ring from above). The x-axis points in the horizontal direction away from the centre of the LHC. The y-axis completes the right-handed system pointing vertically upwards.

3.2.2 Magnet

A no-superconducting dipole magnet is placed between the TT and the T-stations and it is used to measure the momentum of particles. The magnet is formed by two coils placed with a small angle with respect to the beam axis, to increase the opening window with z in order to follow the acceptance of the LHCb detector (see fig. 3.4). The main component of the magnetic field is along the y-axis (B_y) as shown in fig. 3.5, therefore, the (x,z)-plane can be considered with good approximation the bending plane. The maximum magnetic field strength is above 1 T, while its integral is about $\int \vec{B} \cdot d\vec{l} = 4\,\text{Tm}$. All the tracking detectors are located outside the magnetic dipole, as shown in fig. 3.5. The magnetic field is measured before the data-taking periods with Hall probes to obtain a precise map, which is crucial to have a good momentum resolution and consequently a good mass resolution that helps to

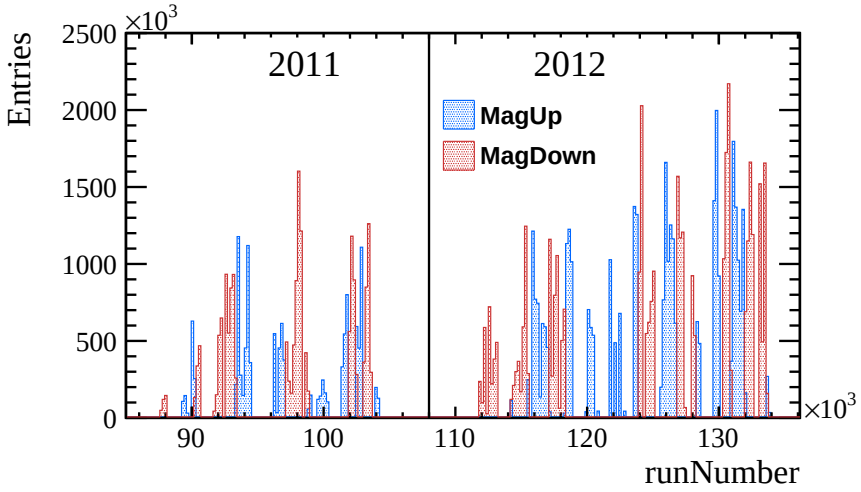

Figure 3.6 – Run number distribution divided by magnet polarity for 2011 and 2012 data sample.

select more efficiently processes of interest.

Among the main LHC experiments, the LHCb detector has a unique feature consisting into the possibility to reverse the polarity of the magnetic field (*MagUp* or *MagDown*). This allows a precise control of the charge asymmetries introduced by the detector. Particles hit preferentially one side of the detector, depending on their charges, generating large detection asymmetries. If data samples collected with the two different polarities have approximately equal size and the operating conditions are stable enough, effects of detection charge asymmetries are expected to cancel. The magnet polarity is therefore reversed approximatively every two weeks to meet these constraints as shown in fig. 3.6. In the measurement reported in this thesis, the polarity reversing is not explicitly exploited since the two samples with different polarities are analysed independently. However, this feature allows testing the robustness and the reliability of the analysis, since the measured value of A_Γ has to come out to be independent from the magnet polarity, see chap. 5.

3.2.3 Vertex Locator

The VErtex LOcator (VELO) is a silicon detector placed close to the collision point [44]. Its main purpose is to precisely measure tracks direction in order to find displaced vertices with respect to the primary vertex of collision. At the energy provided by LHC, B (D) hadrons produced by the proton-proton collisions have a mean distance flight of about 1 cm (0.3 cm). The VELO exploits this feature in order to select signals decays and reject most of the backgrounds. It consists of a series of 21 circular silicon modules arranged perpendicularly along the beam line, as shown in fig. 3.7. Each module is subdivided into two halves placed on the left and on the right of the beam direction. Each of them includes two sensors specialised to measure

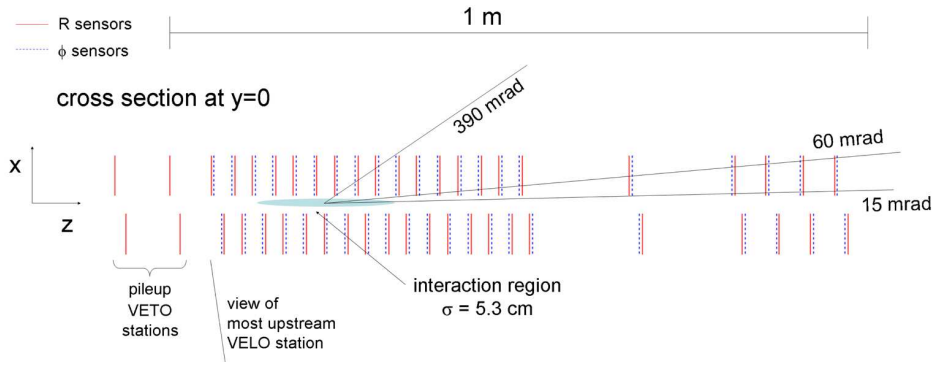

Figure 3.7 – Position of the VELO modules along the beam axis. Figure taken from ref. [45].

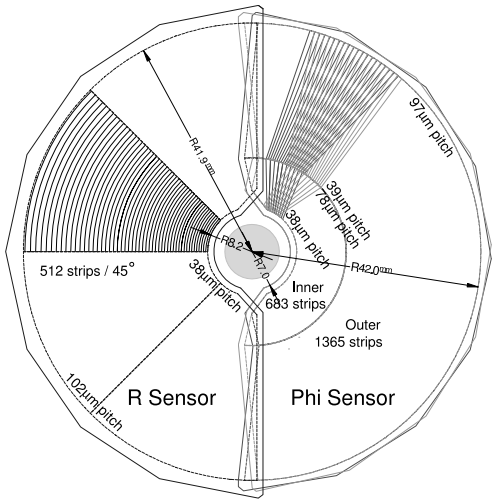

Figure 3.8 – Illustration of R and φ sensors of the VELO modules. Figure taken from from ref. [45].

R and φ coordinates (see fig. 3.7). The R-sensors measure the radial distance with circular-shaped strips with a minimum pitch of 38 µm at the innermost radius of 8.2 mm, increasing linearly to 101.6 µm at the outer radius of about 41.9 mm (see fig. 3.8). The φ-sensors are subdivided in two regions to cope with the high occupancy. The inner region consists of 683 strips extending to a radius of 17.25 mm, where the outer region starts filling all the remaining active area with 1365 strips (see fig. 3.8). The VELO sensors are mounted on retractile modules inside a vessel that maintains vacuum allowing to move them far (VELO open) or close (VELO close) to the beam. Indeed, during the injection procedures the aperture needed by the LHC is larger than the VELO beam-hole (active area starts at 8.2 mm). Therefore, VELO modules are moved away from the beam at a distance of 3 cm to avoid damage sensors. The modules are in addition shielded by a 300 µm-thick radio-frequency foil (RF-foil), made of an alloy of aluminium ($AlMg_3$), from the beam induced currents.

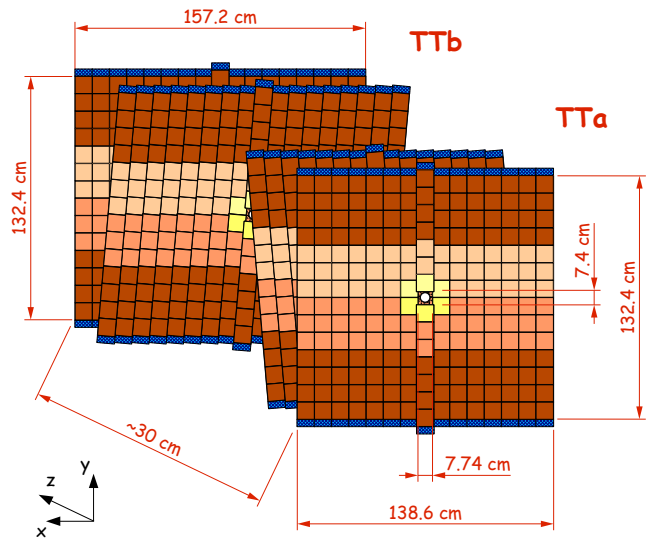

Figure 3.9 – Illustration of the TT detector. Figure taken from ref. [47].

3.2.4 Tracker Turicensis

The Tracker Turicensis (TT) [46] is a silicon microstrip detector placed just before the dipole magnet (see fig. 3.4 and fig. 3.5). It consists of four layers (150 cm × 130 cm) grouped in two stations separated of about 30 cm along the beam line. The four layers are arranged in a "x-u-v-x" pattern. The first and last layer ("x" configuration) consist of vertical strips, see fig. 3.9, while the "u" and "v" layers are rotated by ±5°. The slight rotation with respect to the vertical layers avoid the ambiguities that would arise with an horizontal orientation providing a measurement in y-direction as well, albeit at lower resolution. The sensors of the TT are 11 cm long and 7.8 cm wide counting 384 strips with a strip pitch of 198 µm. The TT has a duplice purpose: firstly it is mainly used to reconstruct trajectory of low-momentum particles that are swept away from the acceptance by the magnet. Moreover, it is also used to reconstruct long-lived particles, as K_S^0 and Λ^0, which decay outside the VELO region.

3.2.5 T-stations

The T-stations, T_1, T_2, T_3, are placed right after the magnet dipole, as shown in fig. 3.4. They cover an area of approximatively $(6 \times 5)\,m^2$ as shown in fig. 3.10. T-stations are made by two parts, an Inner Tracker (IT) and an Outer Tracker (OT). To cope with the high occupancy in the region close to the beam pipe, the IT is based on silicon micro-strip device. Instead, the OT covering the majority of the T-stations are made by a more affordable straw tube detector.

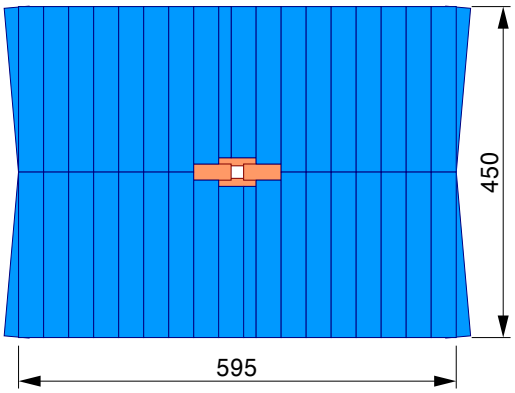

Figure 3.10 – Front view of the T-stations. The orange inner part represents the IT, while the blue part represents the OT. All the dimensions reported are in cm. Figure taken from ref. [46].

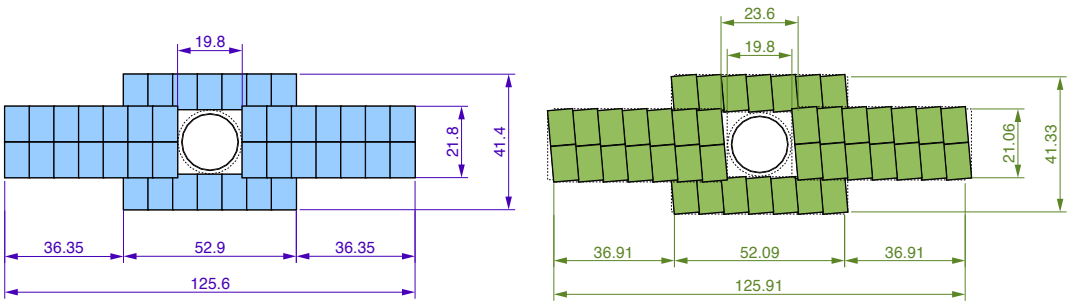

Figure 3.11 – Front view of one station of the IT station. Left, the vertically-oriented layer, right, a tilted one. All the dimensions reported are in cm. Figure taken from ref. [46].

Inner Tracker

The Inner Tracker (IT) [46] is a micro-strip silicon detector mounted in the three tracking stations (T_1, T_2, T_3). Each station consists of four overlapped detection planes. The planes configuration is the same of TT subdetector with two of them oriented vertically and the other two mounted with a stereo angle $\pm 5°$, see fig. 3.11. The characteristics of silicon microstrip sensors are the same as those used for the TT with a pitch of 198 µm but are up to 22 cm long. Overall, the IT contains 129,024 strips, with a hit efficiency of above 99% and the occupancies are in order of few percent [46]. The total size of Inner Tracker subdetector is about 1.2 m on the bending plane (x coordinate) and about 40 cm on the vertical plane (y coordinate).

Outer Tracker

The Outer Tracker (OT) [48] is a gaseous ionisation detector consisting of straw tubes operating as proportional counters. As the IT, the OT is arranged in three stations composed by four

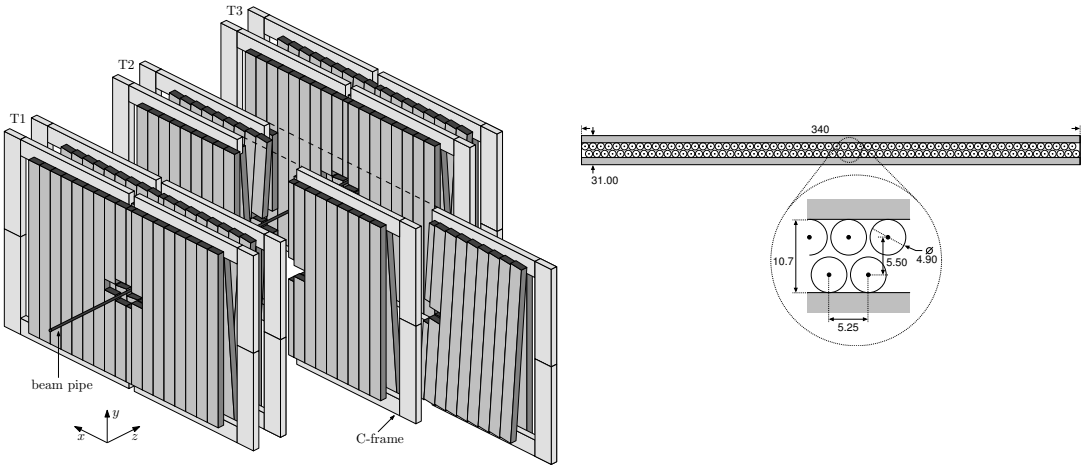

Figure 3.12 – Left, illustration of the OT detector planes. Right, module section. All the dimensions are in cm. Figures taken from ref. [48].

detection planes, as shown in fig. 3.12. The planes configuration is equal to the IT and the TT ones (x-u-v-x) with two planes vertically oriented and the others two tilted of ±5°. The drift tubes are 2.4 m long with an inner diameter of 4.9 mm, see fig. 3.12. The anode is a tungsten wire with a diameter of 25 µm coated with gold. The anode wires operate at a difference of potential of +1150 V with respect to the conducting plated tube. The gas mixture filling the tube is $Ar/CO_2/O_2$ (70%/28.5%/1.5%) to achieve a drift time of 50 ns. Typical occupancies are at the order of 10% and hit efficiency above 99% for tracks passing close to the centre of a tube.

3.2.6 Cherenkov detectors

Two Ring Imaging Cherenkov detectors (RICH) are used in LHCb to discriminate charged pions, kaons and protons. A charged particle crossing with a velocity v a medium with refraction index n, emits Cherenkov light, where photons have an angle Θ_C with respect to the particle momentum given by the following relation

$$\cos\Theta_C = \frac{1}{\beta n},$$

with $\beta = v/c$, and c is the speed of light. If the particle momentum p is known, a relation between the Cherenkov angle Θ_C and the mass of the particle holds

$$\Theta_C = \arccos\left(\frac{1}{n}\sqrt{1+\left(\frac{mc}{p}\right)^2}\right), \tag{3.2}$$

allowing the identification of the particle. For higher momenta the equation above tends to $\cos\Theta_C = 1/n$, thus in order to cover a large range of momenta two RICH detectors are used in

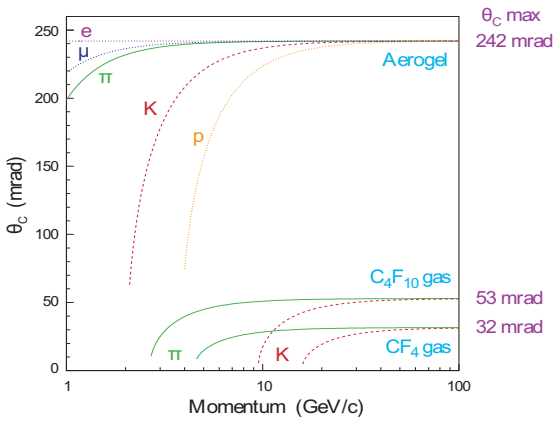

Figure 3.13 – Cherenkov angle versus particle momentum. The curves corresponding to the various radiators used in RICH1 and RICH2 and to the various particle types are reported. Figure taken from ref. [45].

LHCb with radiation media with a different refraction index. The RICH1 placed right after the VELO and before the TT covers the low momentum particles in a range of 1–60 GeV/c using as radiation media the aerogel ($n = 1.03$) and C_4F_{10} ($n = 1.0014$) which produce Cherenkov angles of $\Theta_C^{max} = 242$ mrad and $\Theta_C^{max} = 53$ mrad, respectively. The second RICH detectors RICH2, located instead behind the T-stations, uses CF_4 ($n = 1.0005$) as radiator and covers a momentum range between 15 GeV/c and 100 GeV/c, see fig. 3.13. The emitted Cherenkov photons in both RICH detectors are directed to a lattice of photo-detectors (Hybrid Photon Detector, HPD) by an optical system made of spherical and plane mirrors. Photo-detectors are placed outside the detector acceptance and shielded against residual magnetic fields. The HPDs detect photons in the 200–600 nm spectrum.

3.2.7 Calorimeter system

The LHCb calorimeter system [49] measures the energy depositions and their positions and it performs electron, photon and hadron identification. It also provides information for the first hardware level of the trigger (see sub-sec. 3.2.9). The calorimeter system consists of four main sub-detectors (see fig. 3.14): the Scintillator Pad Detector (SPD), the PreShower detector (PS), the electromagnetic (ECAL) and hadron (HCAL) calorimeters. The SPD allows separating charged and uncharged particles as photons from electrons. The PS placed after 15 mm of lead absorber, is used to separate charged pions from electrons. The ECAL and the HCAL calorimeters measure the deposited energy and the position of the electromagnetic showers, produced by electrons and by photons, and of the hadron showers, respectively. Each sub-detector is divided into regions where differently sized sensors are used. The PS, SPD and ECAL are divided into three regions while the HCAL only into two regions, as shown in fig. 3.15. The size of sensor elements increases going far from the beam-pipe where occupancy decreases. All four subsystems use scintillating light that is produced and transmitted to the

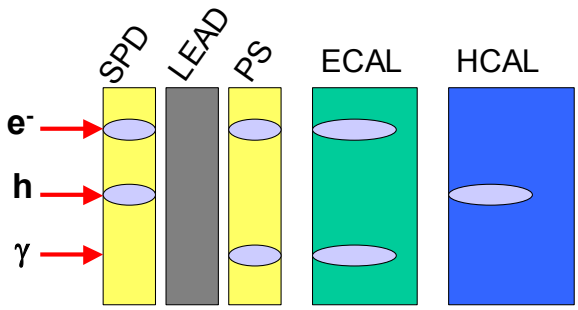

Figure 3.14 – Signal deposit by electrons, photons and hadrons in different sub-detectors of the calorimeter system. Figure taken from ref. [50].

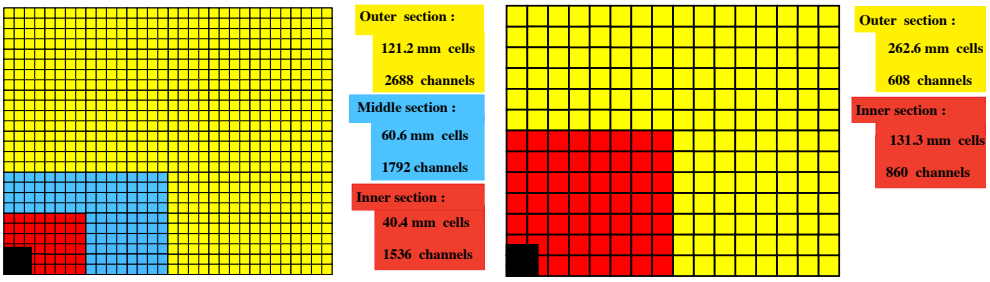

Figure 3.15 – Segmentation of one quadrant of (left) PS, SPD, ECAL and (right) HCAL. Cells dimension are also given. Figure taken from ref. [45].

photomultipliers (PMTs) through wave shifting fibres. The thickness of PS and SPD is 0.1 nuclear interaction length (λ_{int}) and 2 electromagnetic interaction lengths (X_0). The ECAL have a thickness of $25X_0$ ($1.2\lambda_{\text{int}}$) to fully contained the electromagnetic showers from high energy photons. The energy resolution for ECAL is $\sigma(E)/E = 10\%/\sqrt{E/\text{GeV}} \oplus 0.9\%$ [51]. Instead the HCAL has a thickness of only 5.6 nuclear interaction lengths due to the limited space available and its energy resolution is $\sigma(E)/E = 69\%/\sqrt{E/\text{GeV}} \oplus 9\%$ [51].

3.2.8 Muon detectors

The muon system [52] placed at the end of the LHCb detector is designed to detect muons in the LHCb acceptance. It provides trigger information and particle identification in the offline analysis. It consists into five stations (M1–M5). The first one, M1, is placed before the calorimeter system in order to reduce possible effects of multiple scattering of muons trajectory due to the calorimeter material budget. M2–M5 are placed after the hadronic calorimeter and iron absorber planes with a thickness of 80 cm are placed between them, as shown in fig. 3.16. The minimum muon momentum to go through all the stations and absorbers is of about 6 GeV/c. Each of the muon stations is divided in four regions R1–R4 with finer segmentation close to the beam pipe where particle multiplicity is higher. All stations

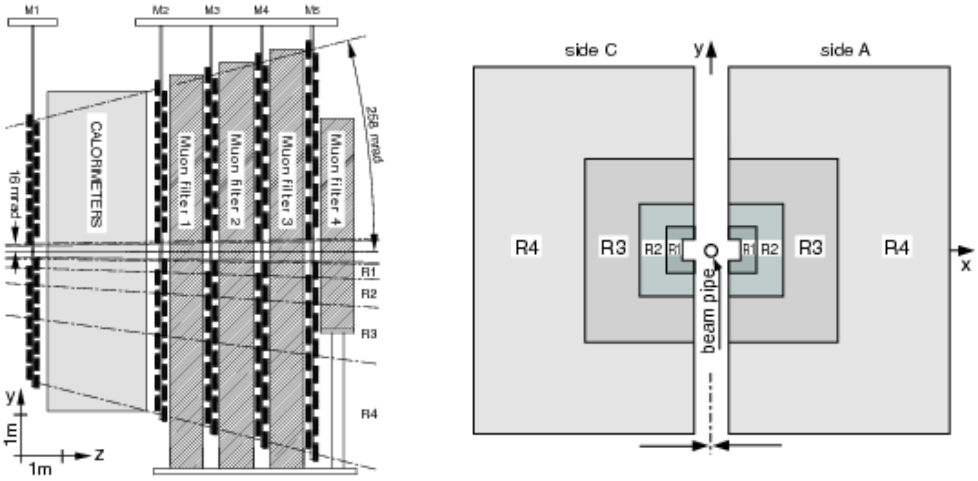

Figure 3.16 – Illustrations of the muon system. Left, a side-view of the muon detectors, right, a front-view of the stations layout. Figure taken from ref. [52].

use multiwire proportional chambers (MWPC) except for the region of M1 stations closest to the beam pipe, which uses triple-GEM detectors (to cope with the higher flux and occupancy). Both detectors are able to collect the signal in less than 20 ns with an efficiency larger than 95%, satisfying the requirements to be used in the hardware stage of the trigger.

3.2.9 Trigger

The LHCb trigger is designed to select bottom and charmed hadrons from pp collisions, reducing the nominal bunch crossing of 40 MHz to a 5 kHz output rate, as shown in fig. 3.17. This is done in three stages. The earliest trigger level (Level-0 or L0) based on custom electronics is designed to perform the first filtering of the events, reducing the event rate to 1 MHz for the next trigger level. Second (High Level Trigger 1 or HLT1) and third (High Level Trigger 2 or HLT2) trigger levels are software based running on a dedicated computing farm, performing a full reconstruction of the events. HLT1 filters heavy hadron events in an inclusive way and reduces the rate of accepted events to about 80 kHz. HLT2 is based on the same software used by HLT1 but it performs an exclusive selection of beauty and charm decays. The HLT2 trigger reduces the events rate to 5 kHz (3 kHz in 2011) in order to be stored.

Level-0 Trigger (L0)

The L0 exploits fast detectors, able to provide valuable information without performing complicated reconstruction algorithms. It aims at finding hadrons, electrons, photons and muons with high transverse momentum, which are a distinctive signature for beauty and charmed hadrons decays. Three independent triggers running in parallel are used.

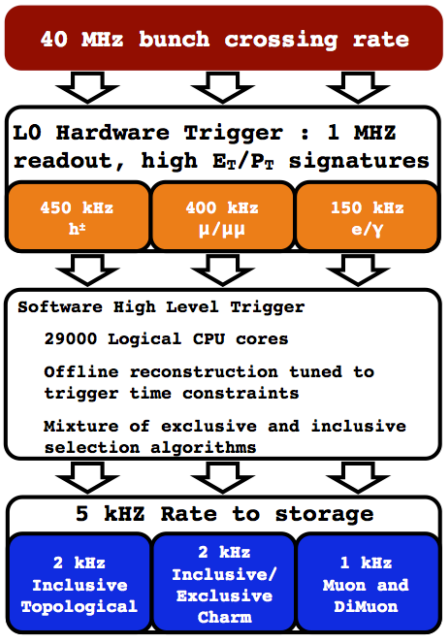

Figure 3.17 – Illustration of the trigger scheme of the LHCb experiment.

L0 Muon It uses information coming from the hits in the five muon chambers to identify high transverse momentum muons. Chambers are divided into fields of interest, hits in the same field of interest from different chambers are connected to form muon segments. The reconstructed segments are then extrapolated to the nominal interaction point and a value for the transverse momentum of the muon is estimated. Two classes of events are accepted: events where at least one muon candidate has a transverse momentum greater than a threshold and events where a muon pair with the product of transverse momenta exceeding a given threshold.

L0 Hadron It uses the information of HCAL. Hadronic showers are identified and their transverse energy is measured. The transverse energy is calculated in a cluster of 2×2 cells as

$$E_{\mathrm{T}} = \sum_{i=1}^{4} E_i \sin\theta_i,$$

where E_i is energy deposited in the cell i and θ_i is the angle between the beam axis and the direction of a neutral particle, assumed to come from the mean position of the interaction point. An event is accepted if at least one cluster with transverse energy greater than a given threshold is present. The threshold for E_{T} during 2011 (2012) data-taking period was 3.5 GeV (3.7 GeV).

L0 Photon/Electron It uses the electromagnetic calorimeter ECAL, the PS and the SPD detectors, working as the L0 Hadron trigger described above.

The High Level Trigger (HLT)

For events passing the L0 trigger, the full set of detector information is transferred to the Event Filter Farm (EFF), where the HLT runs asynchronously to the bunch crossing. The HLT is a software based C++ application performing a fast full reconstruction of events. About 29 000 copies of the HLT application run concurrently in the EFF. The HLT consists of two stages. The first stage (HLT1) processes the full L0 rate (1 MHz) and uses partial event reconstruction to reduce the rate to 80 kHz. Then in the second stage (HLT2) a complete event reconstruction is performed with some simplifications that are needed to satisfy the time constraints.

HLT1 The VELO reconstruction is fast enough to perform a full 3D pattern recognition and primary vertex (PV) finding for all events entering the HLT. Only the VELO tracks having a significant impact parameter (IP) with respect to all PVs and a minimum p_{T} are passed through the forward tracking algorithm that searches for matching hits in the tracking stations. The tracks are required to be separated from the primary vertex, to have a good track quality and a high transverse momentum to fire the trigger.

HLT2 The HLT2 stage performs a full event reconstruction in an almost offline-like reconstruction quality. Only tracks with $p > 5\,\mathrm{GeV}/c$ and $p_{\mathrm{T}} > 300\,\mathrm{MeV}/c$ are used due to time constraints. HLT2 is composed of inclusive and exclusive selections. A number of different event selection strategies can be used according to the topology of the decays of interest.

Trigger decisions are organised in *trigger lines*, which are sequences of reconstruction and selection algorithms to trigger a given category of events. Different trigger lines select decays with different signatures. Specific choices of the trigger selection used for the A_{Γ} measurements described in this thesis are reported in sec. 4.2.

3.2.10 Data processing

Events accepted by the trigger system are recorded on streamed files (so called RAW files) and sent to different TIER[2] computing centres. There, data are replicated, reconstructed and after successful verification, they are permanently stored. The majority of the physics analyses requires very specialised selections, and further reconstruction steps, that is very CPU-time and storage consuming. This further offline step is centralised into the so-called *stripping* phase, the output of which is finally available to the analysts.

3.2.11 Event reconstruction

Events contain information about one or more interesting decays that has to be collected and categorised. Particles trajectories, identification of the vertices, and identification of the type

[2] Telecomunications Infrastructure Standard for Data Centre.

of the particles involved, are the fundamental information to perform the final measurement and are briefly outlined below.

Track reconstruction

Trajectories of charged particles, here referred as tracks, are reconstructed in the LHCb using the hits of the tracking subdetectors (VELO, TT and T-stations). Tracks reconstruction starts with the *pattern recognition* where a sequence of hits produced by the charged particle is identified. Different types of tracks are distinguished in LHCb according to the subdetectors crossed, as shown in fig. 3.5

- *VELO tracks* are tracks with only VELO hits. They are used in the primary vertex reconstruction and as seeds for reconstructing long and upstream tracks.
- *Upstream tracks* are low momentum tracks with hits only in the VELO and TT since they are swept out the LHCb acceptance by the magnetic field.
- *T tracks* are formed only using hits into the T-stations. They are used to form downstream and long tracks.
- *Downstream tracks* are reconstructed only in the TT and in the T-stations. These are mainly long-lived particles as the K^0_S decaying outside the VELO region.
- *Long tracks* require particles traversing the full tracking system. They are reconstructed combining hits from the VELO and the T-stations, and when possible hits from TT are added. These tracks have the most precise momentum resolution and they are the tracks used in the A_Γ measurement.

Long tracks are reconstructed with two different algorithms in LHCb: one proceeds forward (*forward tracking*) in which VELO tracks are extrapolated to the T-stations, the other one uses the T tracks as seeds extrapolating them backward to the VELO looking for a match with the VELO tracks. Then a Kalman filter [53] is applied to extract precisely track parameters taking into account multiple scattering and energy loss due to the ionisation. The χ^2/ndf of the fit is used to determine the quality of the reconstructed track. If tracks share the same hits, the one with the best χ^2/ndf is retained. Mis-reconstructed (fake) tracks, those not corresponding to a trajectory of any real charged particle, are reduced with a neural network classifier which uses as input the result of the track fit, the kinematics of the reconstructed track and the number of measured hits in the tracking stations versus the number of expected hits. The tracking algorithms can also generate *clones* which does not have any hits in common. This happens when hits of different tracking detectors are reconstructed as independent tracks even though they belong to the same charged particle. Since these clones share the same information, they are reduced with a requirement based on the Kullback-Liebler divergence which exploits the Shannon information of the track [54].

The relative momentum resolution for particles traversing the whole tracking system is about $\delta p/p = 0.5\%$ at 20 GeV/c, rising to about 0.8% for particles around 100 GeV/c [43]. This translates into a relative mass resolution, σ_m/m, of about 5 per mille up to Υ masses. The primary

vertex resolution, which is mainly driven by the VELO reconstruction, depends on the number of tracks originating from the primary vertex. For vertices with more than about 25 tracks, a primary vertex resolution of 13 μm in the x–y plane and 71 μm along the beam axis is achieved. The impact parameter resolution with respect to these vertices is less than 35 μm for particle with transverse momenta greater than 1 GeV/c.

Particle identification

Particle identification in LHCb is achieved exploiting different subdetectors: the calorimeter, the two RICH detectors and the muon stations. The measured Cherenkov angle in the RICH detectors is combined with the momentum measured by the tracking system to infer the mass of the particle (see eq. (3.2)). The identification of a track reconstructed in the tracking system as a muon is based on the association of hits around its extrapolated trajectory in the muon system. The calorimeter system is used to identify photons, electrons and π^0 candidates. Neutral particles are distinguished from charged studying the presence or absence of tracks in front of the energy deposits. The shape of the cluster provides the information to distinguish photons from π^0 mesons. The particle identification (PID) information obtained separately from the muon, RICH, and calorimeter systems is combined to provide a more powerful identification. A likelihood information for a particle hypothesis X is produced by each sub-system and added linearly to a combined likelihood, $\mathscr{L}(X)$. The likelihood is usually calculated relatively to the pion hypothesis, $\mathscr{L}(\pi)$, since pions are the most abundant species produced and detected at LHCb. The difference between the logarithms of two likelihoods with the X and the π hypothesis is referred as $DLL_{X\pi} \equiv \log\mathscr{L}(X) - \log\mathscr{L}(\pi)$. The larger the $DLL_{X\pi}$ value is, the more likely is for the particle to belong to the X species, rather than to be a pion. To select pions small or negative values can be required. The performances in the K–π separation are reported in fig. 3.18.

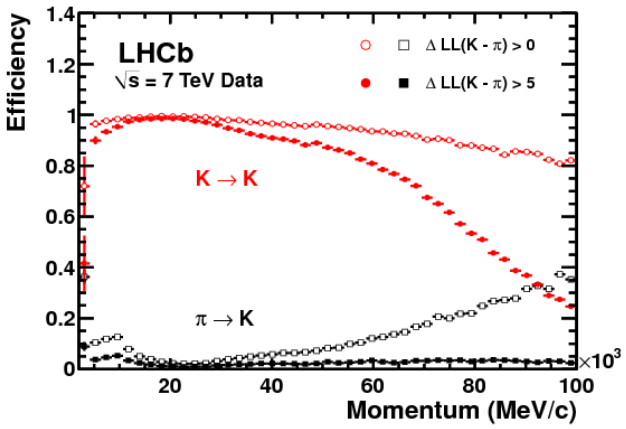

Figure 3.18 – Kaon identification efficiency (red) and pion misidentification rate (black) measured on data as a function of track momentum for two different requirements on *DLL*. Taken from ref. [55].

4 Reconstruction and selection of D^0 mesons

This chapter describes the main stages used to extract the $D^{*+} \to D^0(\to h^+h^-)\pi^+$ decays (referred as "signal") from other events ("background").

4.1 $D^{*+} \to D^0(\to h^+h^-)\pi^+$ decays at LHCb

The measurement reported in this thesis uses pp collision data produced at the LHC and recorded with the LHCb experiment. Two data samples are analysed: one, collected during 2011, with an energy at centre-of-mass of $\sqrt{s} = 7\,\text{TeV}$; the other one with an energy of $\sqrt{s} = 8\,\text{TeV}$, collected during 2012. The 2011 and 2012 data samples correspond to a integrated luminosity of $1.1\,\text{fb}^{-1}$ and $2.1\,\text{fb}^{-1}$, respectively.

The total data sample is divided into four subsamples by the year of data-taking {2011, 2012} (which corresponds also to a different energy) and by the magnet polarity {*MagUp*, *MagDown*}. The value of A_Γ is measured independently on the four subsamples. In this way, the robustness and reliability of the analysis strategy can be tested, since the measured value of the A_Γ observable has to come out to be compatible among the four subsamples, independently from the centre-of-mass energy and the magnet polarity.

The $D^{*+} \to D^0\pi^+$ and $D^{*-} \to \overline{D}^0\pi^-$ decay chains are reconstructed, where the D^0 and the $\overline{D}^0$ mesons decay to the final state h^+h^-, and h stands for a pion or a kaon.[1] The $D^{*\pm}$ mesons are mainly produced by strong interactions in the primary vertex of the pp collision and immediately decay to $D^0\pi^+$ and $\overline{D}^0\pi^-$ products. The Q-value of $D^{*\pm}$ decays is very small, less than $6\,\text{MeV}/c^2$, thus the pion momentum is very low translating into a large track curvature, consequently it is referred as "soft pion". The D^0 lifetime is about 0.41 ps [20] and the average momentum at LHCb is about $60\,\text{GeV}/c$ leading to a typical flight distance of about 4 mm. The decay vertices of D^0 mesons can be therefore distinguished from the primary vertex of the pp interaction, as depicted in fig. 4.1. Due to the *long* D^0 lifetime, the two daughter tracks have generally a large impact parameter, allowing a good signal background separation. Due to the

[1] Except when otherwise explicitly stated, charge-conjugate processes are implied.

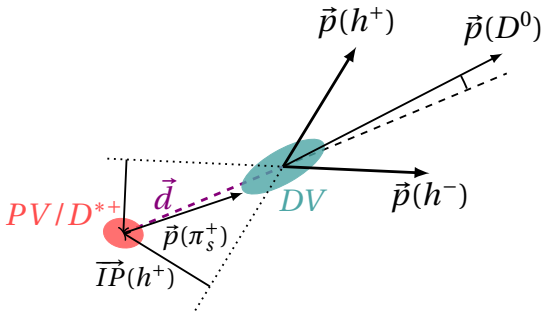

Figure 4.1 – Schematic illustration of a $D^0 \to h^+h^-$ decay, not drawn to scale. The ellipse represents the primary (red) and secondary (green) vertex. Particles momenta are reported as thick black arrows. Impact parameters vector ($\overrightarrow{IP}$) for the two daughter tracks and the displacement vector ($\vec{d}$) for the D^0 are also reported.

large number of soft tracks produced in the event, the major source of background are fake D^{*+} candidates formed by a true D^0 meson and a random pion from the event.

Prior of discussing the details of online and offline selection, it is useful to define some relevant quantities used in the analysis. All these quantities are calculated in the laboratory frame, and some of them are illustrated in fig. 4.1. The quantities reported are general and can be applied to each particle or a set of particles depending on the variable.

Primary vertex (PV) the space-point of the reconstructed primary pp interaction.

Secondary decay vertex (DV) the space-point in which the decay of the long-lived particle occurs. The spatial vector from the primary vertex to the secondary vertex is denominated displacement vector ($\vec{d}$), and for a particle with mass m and momentum $\vec{p}$ the displacement vector is defined as $\vec{d} = \gamma\vec{\beta}ct = (\vec{p}/m)ct$, where c indicates the speed of light and t is the proper decay time of the particle.

Impact Parameter (*IP*) the module of the three-dimensional impact parameter vector of a particle. Generally, given a vertex $\vec{v}_0$ and a particle trajectory that can be parametrised in the VELO (straight line) as $\vec{v}(t) = \vec{v}_p + \vec{p}\,t$, where $\vec{p}$ is the particle momentum and $\vec{v}_p$ is a generic point of the trajectory, the impact parameter vector is defined as the vector formed by the nearest point of the track to $\vec{v}_0$

$$\overrightarrow{IP} = (\vec{v}_p - \vec{v}_0) - \frac{\vec{p}\cdot(\vec{v}_p - \vec{v}_0)}{|\vec{p}|^2}\vec{p}.$$

D^0 daughters have in general large impact parameters with respect to the primary vertex because of the displaced vertex of the D^0 meson. Instead, the IP of D^0 meson with respect to the PV tends to be close to zero within the experimental uncertainty, in the assumption of "prompt" decays (*i.e.* coming from the PV, see sec. 2.1).

DIRA the cosine of the direction angle, *i.e.* the angle between the momentum of the particle and the displacement vector, DIRA $\equiv (\vec{p}\cdot\vec{d})/(|\vec{p}||\vec{d}|)$. For a fully reconstructed particle its total momentum tends to be aligned to the displacement vector resulting into a DIRA close to the unit. This is useful in reducing the contribution of the partially reconstructed backgrounds of the D^0 meson.

DOCA the three-dimensional distance of closest approach between the trajectories of two particles. Particles coming from a decay of a common mother particle are likely close to each other translating into a small DOCA.

χ^2-distance the distance in χ^2 unit between two spatial points. Given two points, $\vec{v}_1$ and $\vec{v}_2$, with covariance matrices $\mathbf{cov}_1$ and $\mathbf{cov}_2$, respectively, the χ^2-distance is defined as $(\vec{v}_1-\vec{v}_2)^T(\mathbf{cov}_1-\mathbf{cov}_2)^{-1}(\vec{v}_1-\vec{v}_2)$.

χ^2_{IP} the χ^2_{IP} for a particle is defined as the difference in χ^2 of the primary vertex fit *with and without* considering the particle in the fit. For a particle not coming from the PV, χ^2_{IP} assumes grater values than a prompt particle (*i.e.* coming from the PV).

Δm the mass difference between the reconstructed invariant mass of the D^{*+} and the invariant mass of D^0. The Δm variable as a natural cut-off limit at the mass of the π^+. The small Q-value of the $D^{*+}\to D^0\pi^+$ decays translates to a very narrow peak in the Δm distribution allowing an efficient separation with respect to the random background.

4.2 Trigger system

The first selection of D^0 candidates decaying to two hadrons is performed by the trigger. Only candidates that have fired a specific trigger chain are used. The trigger chain (see sub-sec. 3.2.9) aiming at selecting $D^0\to h^+h^-$ decays is a specific combination of triggers requirements in the three levels: L0, HLT1 and HLT2.

The L0 hadron trigger (see sub-sec. 3.2.9) selects decays of B and D mesons basing its decision on the deposit energy in the calorimeter system. However, its discriminator power is not particularly remarkable, having an efficiency of about 50% in selecting $D^0\to h^+h^-$ decays. Requiring at the offline level D^0 candidates that fired the L0 hadron trigger would translate into a loss of a significant fraction of collected events. Therefore, no L0 trigger requirements are applied, asking for the logical `OR` of all the L0 triggers. In principle, this choice may be difficult to treat since different thresholds in momentum and different event topologies coexist in the same sample. However, this is mitigated by tighter requirements of further trigger stages and of the offline selection. Possible residual biases due to this choice are assessed to be completely negligible at the current sensitivity, as reported in sec. 8.4.

At HLT1 level, at least one of the D^0 daughters has to fire the `Hlt1TrackAllL0` line. This line aims at selecting a single detached high momentum good-quality track to identify B and D mesons decays, independently from which L0 trigger line fired. Requirements on the total

Table 4.1 – Summary of trigger requirements. The letter h is for K or π.

Trigger Line	Quantity	Requirement	Unit
`Hlt1TrackAllL0`	VELO hits	> 9	-
	VELO missing hits	< 3	-
	hits	> 16	-
	track χ^2/ndf	< 2	-
	$p(h)$	> 3	GeV/c
	$p_{\mathrm{T}}(h)$	> 1.6	GeV/c
	$\chi^2_{\mathrm{IP}}(h)$	> 16	-
	IP(h)	> 0.1	mm
`Hlt2CharmHadD02HH_D02xx`	track χ^2/ndf	< 3	
	$p(h)$	> 5	GeV/c
	$p_{\mathrm{T}}(h)$	> 800	MeV/c
	$\chi^2_{\mathrm{IP}}(h)$	> 9	-
	$p_{\mathrm{T}}(hh)$	> 2	GeV/c
	DOCA	< 0.1	mm
	largest h p_{T}	> 1.5	GeV/c
	$m(\sum p^\mu)$	$\in [1715, 2065]$	MeV/c^2
	fit vertex $\chi^2(D^0)$/ndf	< 10	-
	DIRA	> 0.99985	-
	DV χ^2-distance from PV	> 40	-
	$m(D^0)$	$\in [1790, 1930]$	MeV/c^2

number of hits, the number hits in the VELO and χ^2/ndf of the track assure its good-quality. Requirements on the momentum and on the p_{T} are also applied, as reported in tab. 4.1. In order to select tracks coming from long-lived particles (as the D^0 meson) requirements on the IP and the χ^2_{IP} of the track with respect to the primary vertex are also applied.

At the second level of the HLT, D^0 candidates have to fire one of the following two trigger lines `Hlt2CharmHadD02xx OR Hlt2CharmHadD02HH_D02xx`, where `xx` stands for: `RS` in $D^0 \to K^-\pi^+$ decays, `KK` in $D^0 \to K^+K^-$ decays and `PiPi` in $D^0 \to \pi^+\pi^-$ decays. `Hlt2CharmHadD02xx` triggers did run at the beginning of 2011 data taking being superseded later by the trigger `Hlt2CharmHadD02HH_D02xx`. These triggers aim at selecting two tracks which made a good vertex (detached from the primary vertex) and with an invariant mass compatible with the D^0 mass. The D^0 candidates reconstruction starts looking for two tracks. These should have a good quality (χ^2/ndf <3) and should not come from the primary vertex (χ^2_{IP} >9) since the D^0 mesons travels few millimetres before decaying. In addition, minimal requirements on the momentum ($p > 5\,\mathrm{GeV}/c$) and the transverse momentum ($p_{\mathrm{T}} > 800\,\mathrm{MeV}/c$) of the tracks are also applied. Then, tracks are combined to form a D^0 candidate, they have to be close to each other, and the requirement on the DOCA (< 0.1 mm) is applied with this purpose. Their invariant mass, calculated as the sum of the four-momenta vectors ($m(\sum p^\mu)$) has to

be compatible with the D^0 meson mass, lying in the range [1715, 2065] MeV/c^2. In addition, the transverse momentum of the pair is required to be greater than 2 GeV/c and at least one daughter should have a p_T greater than 1.5 GeV/c. If a pair of tracks survives all these requirements, it is considered a good candidate for a $D^0 \to h^+h^-$ decay. Thus, the two tracks are combined performing a vertex fit, in which the χ^2/ndf is required to be lower that 10. The detached nature of the decay is re-required on the D^0 candidate, asking for a χ^2-distance between the secondary vertex and the primary vertex larger than 40. Partially-reconstructed background is suppressed requiring the DIRA to be greater than 0.99985. At the end, a mass window around the D^0 nominal mass is applied. The list of cuts required on the data sample are summarised in tab. 4.1.

4.3 Preselection

The event reconstruction and a loose preselection of D^0 and D^{*+} candidates are centrally made by the collaboration. This process is called *stripping* as explained in sub-sec. 3.2.10, and the different set of cuts applied to select a particular decay are grouped in the so-called *stripping line*. The relevant stripping lines for the measurement reported in this thesis are the `D2hhPromptDst2DxxLine` lines, where `xx` stands for `RS` in the case of $D^0 \to K^-\pi^+$ decays, `KK` for $D^0 \to K^+K^-$ decays and `PiPi` for $D^0 \to \pi^+\pi^-$ decays, and requirements are summarised in tab. 4.2. The reconstruction of D^0 candidates proceeds as in the trigger. First of all a set of *good* tracks are selected. Then, all the possible pairs are formed, and those passing all the requirements are retained as D^0 candidates. An additional pion is searched to form the D^{*+} candidates.

The preselection re-confirms the good quality of tracks (χ^2/ndf < 3), the momentum thresholds ($p > 5$ GeV/c, $p_T > 800$ MeV/c) and their displaced nature ($\chi^2_{IP} > 9$) required at the trigger level. In addition, to further reduce the number of clones, a selection on the Kullback-Liebler distance (D_{KL}, see sub-sec. 3.2.11) is applied. To suppress mis-reconstructed backgrounds, particle identification (PID) requirements are applied to the daughters tracks, through the $\mathrm{DLL}_{K\pi}$ variable. As described in sub-sec. 3.2.11, positively larger values of the $\mathrm{DLL}_{K\pi}$ correspond to an higher probability to be a kaon, and viceversa, negatively lower values to a pion. Thus, $\mathrm{DLL}_{K\pi} > 0$ is required for kaons and $\mathrm{DLL}_{K\pi} < 0$ for pions in $D^0 \to K^+K^-$ and $D^0 \to \pi^+\pi^-$ decay modes. The kaons from $D^0 \to K^-\pi^+$ decays have to meet a $\mathrm{DLL}_{K\pi}$ requirement equal to $\mathrm{DLL}_{K\pi} > 5$.

D^0 candidates are then obtained from the selected tracks, and the same selection of the trigger (tab. 4.1) is required on D^0 candidates, except for tighter requirements on the DIRA, the DOCA and the mass window corresponding to [1765, 2065] MeV/c^2.

The D^0 candidates are then combined with pions to form D^{*+} candidates. No requirements are applied on soft pions but χ^2/ndf lower than 5. Only two requirements on the D^{*+} candidates are applied, on the χ^2/ndf and on the mass difference between the D^{*+} and the D^0 candidates,

Table 4.2 – Summary of stripping requirements. The letter h is for K or π.

Candidate	Quantity	Requirement	Unit
h	$D_{KL}(h)$	> 5000	-
	$p_{\mathrm{T}}(h)$	> 800	MeV/c
	$p(h)$	> 5	GeV/c
	track χ^2/ndf(h)	< 3	-
	$\chi^2_{\mathrm{IP}}(h)$	> 9	-
	$(D^0 \to K^-\pi^+)$ $\mathrm{DLL}_{K\pi}(\pi)$, $\mathrm{DLL}_{K\pi}(K)$	$< 0, > 5$	-
	$(D^0 \to K^+K^-)$ $\mathrm{DLL}_{K\pi}(K)$	> 0	-
	$(D^0 \to \pi^+\pi^-)$ $\mathrm{DLL}_{K\pi}(\pi)$	< 0	-
D^0	$p_{\mathrm{T}}(D^0)$	> 2	GeV/c
	$p(D^0)$	> 5	GeV/c
	DV χ^2-distance from PV	> 40	-
	DIRA	> 0.9999	-
	DOCA	< 0.07	mm
	p_{T} of at least one daughter	> 1.5	GeV/c
	fit vertex $\chi^2(D^0)$/ndf	< 10	-
	$m(D^0)$	$\in [1765, 2065]$	MeV/c^2
D^{*+}	π_s track χ^2/ndf	< 5	-
	fit vertex $\chi^2(D^*)$/ndf	< 100	-
	$\Delta m = m(D^0\pi^+) - m(D^0)$	< 160	MeV/c^2

as reported in tab. 4.2.

4.4 Offline Selection

Additional requirements are added on top of the stripping selection, as reported in tab. 4.3. In particular, to further suppress the contamination from misidentified events, pions and kaons from D^0 decays are required to meet tighter PID criteria with respect to the preselection, namely $\mathrm{DLL}_{K\pi}(\pi) < -5$ and $\mathrm{DLL}_{K\pi}(K) > 5$, respectively. Contamination from D decays not produced in the primary pp interaction vertex (secondary D decays), is also reduced by requiring the χ^2_{IP} of the D^0 candidates not to exceed 9 (see fig. 4.2).[2] As described in subsec. 3.2.3, the VELO detector is shielded by the radio-frequency by a thin aluminium foil (RF-foil). Particles can interact with the matter of the RF-foil producing D mesons. In order to remove these candidates, the signed distance R_{xy} between the D^0 decay vertex (DV) and the primary vertex (PV) in the transverse plane defined as

$$R_{xy} = \mathrm{sgn}(\mathrm{DV}_x)\sqrt{(\mathrm{DV}_x - \mathrm{PV}_x)^2 + (\mathrm{DV}_y - \mathrm{PV}_y)^2},$$

[2] A systematic uncertainty will be assigned to the residual contamination of secondary decays in chap. 7.

Table 4.3 – Offline requirements added on the top of the stripping selection of tab. 4.2.

Quantity	Requirement	Unit
$\mathrm{DLL}_{K\pi}(K)$	> 5	-
$\mathrm{DLL}_{K\pi}(\pi)$	< -5	-
$\chi^2_{\mathrm{IP}}(D^0)$	< 9	-
$\lvert R_{xy}\rvert$	< 4	mm
$m(D^0)$	$\in [1840.84, 1888.84]$	MeV/c^2

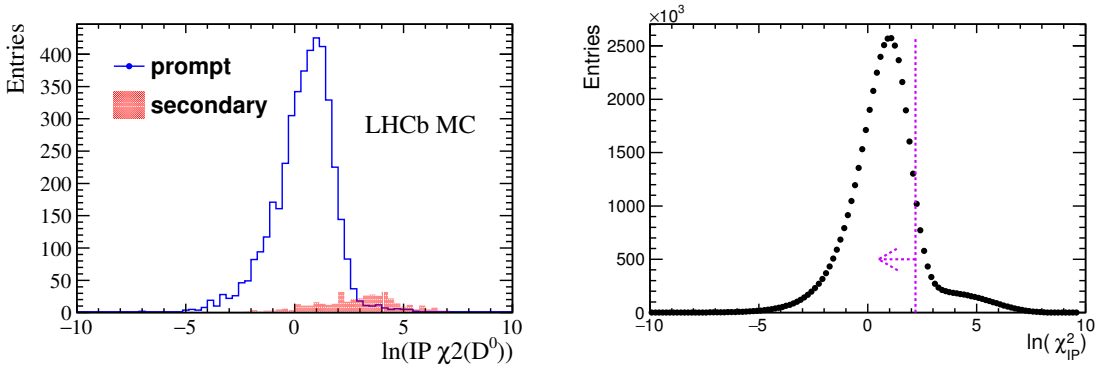

(a) LHCb MC **(b)** LHCb data

Figure 4.2 – Distribution of the logarithmic of the $\chi^2_{\mathrm{IP}}(D^0)$ variable: (a) in LHCb Monte Carlo sample and (b) in the data, where the dashed line and arrow indicate the cut applied.

where the subscripted index indicates the x or y coordinates of the vertices, has to be less than 4 mm in modulus (the inner radius of the RF-foil is about 4.5 mm [56]), as shown in fig. 4.3. A signal region in the D^0 mass is defined by further restricting to D^0 candidates with an invariant mass within $\pm 24\,\mathrm{MeV}/c^2$ ($\approx \pm 3\sigma$ of mass resolution) (see fig. 4.4) of the known D^0 mass [20].

The mass difference $\Delta m \equiv m(hh\pi_s) - m(hh)$, where h stands for K or π and π_s is the soft pion of the $D^{*+} \to D^0\pi^+$ decays, provides a powerful discrimination between signal and background. The signal $D^{*+} \to D^0\pi^+$ decays features a narrow peak centred at the nominal value $m_{D^{*+}} - m_{D^0} = (145.43 \pm 0.07)\,\mathrm{MeV}/c^2$ [20], consistent with the experimental resolution. The background from properly-reconstructed D^0 decays associated with a random pion features as smoothly-growing, square-root-like shape in the Δm distribution. Mis- and partially-reconstructed decays show a peaking enhancement in the Δm distribution although somewhat broader than the experimental resolution (see sec. 8.3), not visible in fig. 4.5 having a small fraction compared to the signal.

The resolution of the Δm distribution is essential to separate the signal from the background components. To improve the signal resolution of the Δm distribution, the D^{*+} mesons are constrained to originate in the primary vertex, refitting the entire decay chain $D^{*+} \to D^0(\to$

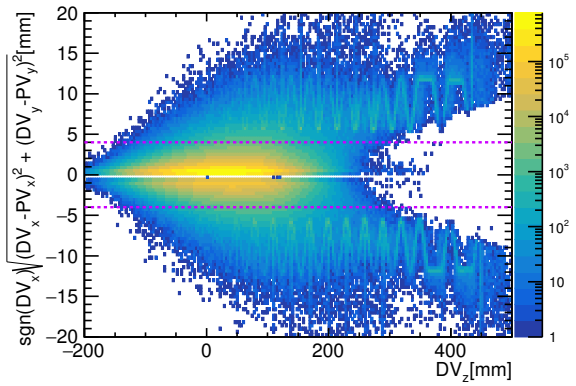

Figure 4.3 – Distribution of signed radial distance, R_{xy}, for D^0 decay vertices. The visible structures are due to the RF-foil and to the VELO layers. The dashed line represents the cut applied, $|R_{xy}| < 4\,\text{mm}$ (see text for details).

$hh)\pi^+$ as a whole [57]. The resolution of the Δm distribution is shrunk of about a factor 3, as shown in fig. 4.5. However, this constraint may sculpt the Δm distribution of backgrounds in a non trivial way, making more complicated the extraction of signal decays. For instance, D^{*+} mesons coming from a B meson decay do not point to primary vertex. The application of such a constrain re-adjusts the values of the momenta and of the opening angles of the particles resulting into a biased invariant mass for D^{*+} and D^0 mesons, sculpting the Δm distribution in a non trivial way. However, the selection on the $\chi^2_{\text{IP}}(D^0)$ to be lower than 9 reduces drastically the fraction of secondary decays in the sample to a few percents. Therefore, the Δm distribution is not significantly affected.

The resulting Δm distributions after requiring the final offline selection are shown in fig. 4.6 for all the subsamples. Prominent signals are observed over moderate backgrounds, dominated by random associations of real D^0 decays with uncorrelated pions.

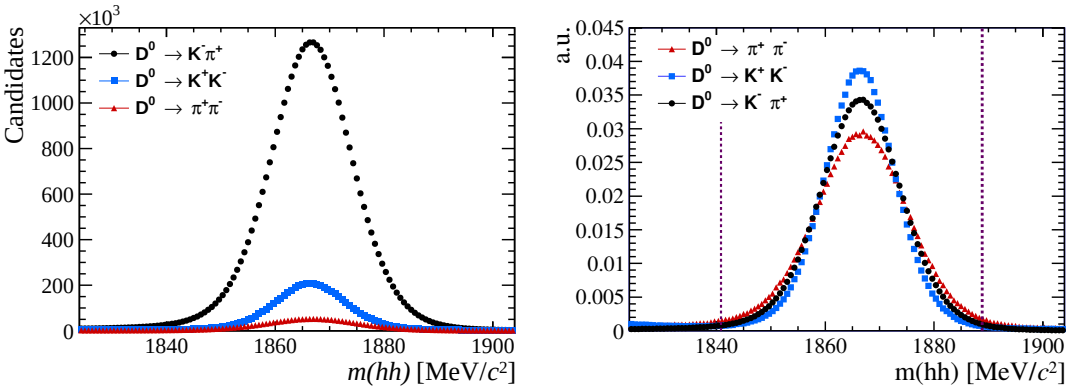

(a) 2012 *MagDown* sample. **(b)** Normalised distribution.

Figure 4.4 – Invariant mass distribution $m(h^+h^-)$ for $D^0 \to K^-\pi^+$, $D^0 \to K^+K^-$ and $D^0 \to \pi^+\pi^-$ for (a) 2012 *MagDown* data sample. The same distribution but normalised to one is shown on (b). The dotted vertical lines represent the considered signal window, see tab. 4.3.

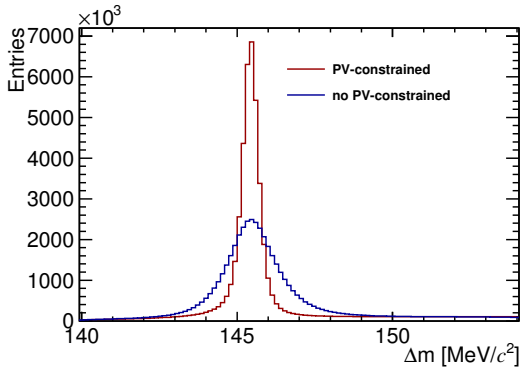

Figure 4.5 – Comparison of the Δm distribution with (in red) and without (in blue) the application of the primary vertex constrain in the full decay chain vertex fit.

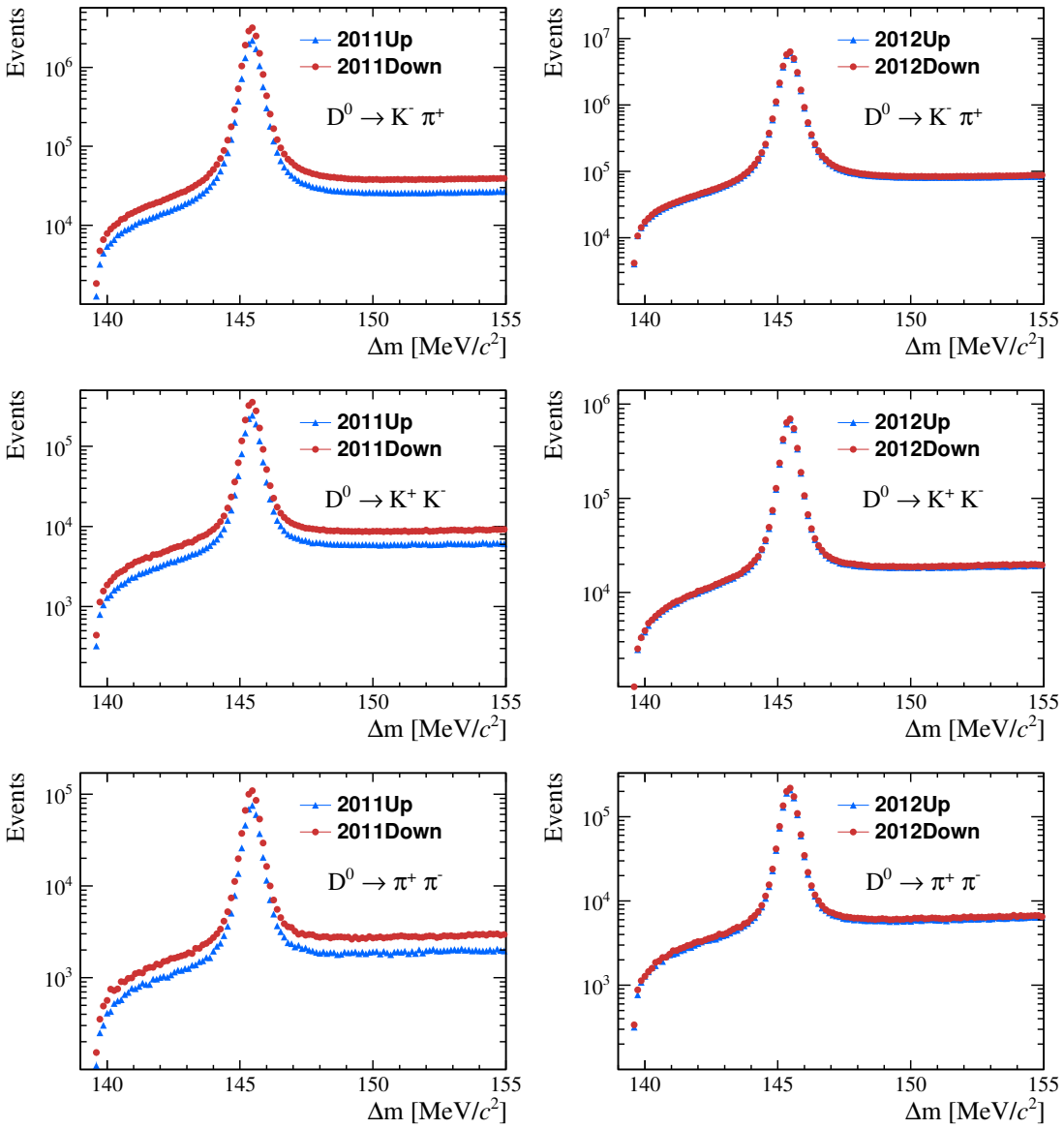

Figure 4.6 – Δm distributions for $D^0 \to K^- \pi^+$, $D^0 \to K^+ K^-$ and $D^0 \to \pi^+ \pi^-$ decay mode. The offline selection, described in sec. 4.4, is required. Logarithmic scale.

4.5 Multiple candidates

A fraction of events contains the so-called multiple candidates where the same D^0 candidate is associated with different soft pions to create a "good" different D^* candidates, able to pass all the requirements entering the final data sample. The fraction of multiple candidates found is about 8% (12%) for the $D^0 \to K^-\pi^+$ decays in 2011 (2012) sample. A slightly higher fraction of multiple candidate is found for $D^0 \to K^+K^-$ and $D^0 \to \pi^+\pi^-$, equal to 15% (17%) for 2011 (2012) sample for both the decays. In order to avoid possible biases, one D^* candidate is chosen randomly discarding the others of the same events. This choice is reproducible since a fixed seed is used in the procedure. The impact of such a choice is evaluated in sec. 8.5, where the differences with alternative approaches are quantified to be much lesser than the final statistical and systematic uncertainties.

4.6 Sideband subtraction and Δm fit

The small residual random pion background under the signal peak, clearly visible in fig. 4.6, is removed by performing a sideband subtraction using the Δm mass difference, by choosing a range within $[144.45, 146.45]\,\mathrm{MeV}/c^2$ for the signal region, corresponding to about $\pm 5\sigma$ region around the measured mean value of the peak, and a range within $[149, 154]\,\mathrm{MeV}/c^2$ for the background, as shown in fig. 4.7. All the distributions of interested observables, except those of Δm, are filled with the candidates within the signal and background mass region, as defined above. Candidates falling in the signal mass region enter the distribution with a weight of one, while candidates falling in the background mass region enter with an appropriate negative weight, proportional to the ratio of number of background candidates in the signal region to those in the background region. This ratio is extracted by fitting the Δm distribution with a binned maximum likelihood fit. A Johnson distribution [58], $\mathscr{J}$, plus the sum of three Gaussians, $\mathscr{G}$, is used, as probability density function (PDF), to empirically model the distribution of the signal peak:

$$\begin{aligned}\mathscr{P}_{\mathrm{sgn}}(\Delta m|\boldsymbol{\theta}_{\mathrm{sgn}}) = f_J\mathscr{J}(\Delta m|\mu_J,\sigma_J,\delta_J,\gamma_J) + f_1\mathscr{G}(\Delta m|\mu_1,\sigma_1) + \\ + f_2\mathscr{G}(\Delta m|\mu_2,\sigma_2) + (1-f_J-f_1-f_2)\mathscr{G}(\Delta m|\mu_3,\sigma_3),\end{aligned}$$

where

$$\begin{aligned}\mathscr{J}(x|\mu,\sigma,\delta,\gamma) &= \frac{1}{I_J}\frac{\exp\left[-\frac{1}{2}\left(\gamma+\delta\sinh^{-1}\left(\frac{x-\mu}{\sigma}\right)\right)^2\right]}{\sqrt{1+\left(\frac{x-\mu}{\sigma}\right)^2}},\\ \mathscr{G}(x|\mu,\sigma) &= \frac{1}{I_G}\exp\left[-\frac{1}{2}\left(\frac{x-\mu}{\sigma}\right)^2\right],\end{aligned}$$

and where I_J and I_G are the normalisation factor in the mass fit range $[139.6, 154.5]\,\mathrm{MeV}/c^2$. $\boldsymbol{\theta}_{\mathrm{sgn}} = (f_J,\mu_J,\sigma_J,\delta_J,\gamma_J,f_1,\mu_1,\sigma_1,f_2,\mu_2,\sigma_2,\mu_3,\sigma_3)$ is the vector of signal parameters to be determined from the fit. The random pion background is modeled with an empirical threshold

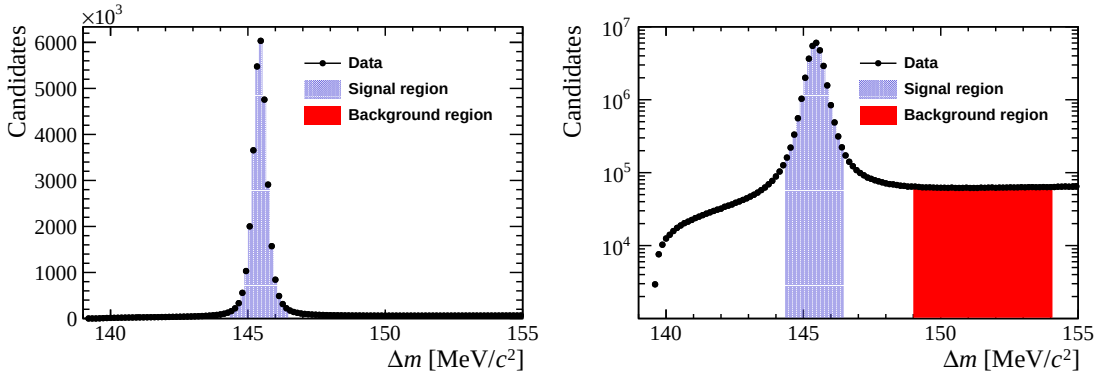

Figure 4.7 – Sideband subtraction regions: in blue the signal region, in red the background region. (Left) linear scale, (right) logarithmic scale.

function, defined as

$$\mathscr{P}_{\text{bkg}}(\Delta m|\boldsymbol{\theta}_{\text{bkg}}) = \frac{1}{I_B}\left(1 - \exp\left[-\frac{\Delta m - m_0}{c}\right] + b\left(\frac{\Delta m}{m_0} - 1\right)\right),$$

where the $\boldsymbol{\theta}_{\text{bkg}} = (m_0, c, b)$ is the vector of background parameters to be determined from the fit and I_B is the normalisation factor in the mass fit range $[139.6, 154.5]\,\text{MeV}/c^2$. The total extended PDF can be then written as

$$\mathscr{P}(\Delta m|\boldsymbol{\theta}) = \frac{N_{\text{sgn}}}{N_{\text{sgn}} + N_{\text{bkg}}}\mathscr{P}_{\text{sgn}}(\Delta m|\boldsymbol{\theta}_{\text{sgn}}) + \frac{N_{\text{bkg}}}{N_{\text{sgn}} + N_{\text{bkg}}}\mathscr{P}_{\text{bkg}}(\Delta m|\boldsymbol{\theta}_{\text{bkg}}),$$

where N_{sgn}, N_{bkg} and $\boldsymbol{\theta} = (\boldsymbol{\theta}_{\text{sgn}}, \boldsymbol{\theta}_{\text{bkg}})$ are free parameters to be determined from the fit. The fits projection for $D^0 \to K^+K^-$, $D^0 \to \pi^+\pi^-$ and $D^0 \to K^-\pi^+$ candidates, passing the final offline selection and the multiple candidates rejection, are reported in fig. 4.8, fig. 4.9 and fig. 4.10, respectively. All the subsamples separated by magnet polarity and energy are fitted independently. In addition, the fits are performed integrating over all the proper decay time values and not in each decay time bin. This choice reduces drastically the complexity of the measurement since only one fit per subsample (4) per decay mode (3) is performed for a total of twelve fits, these are much less than the total number of fits that should have been done in the other case (360). A systematic uncertainty is assessed on the final measurement regarding this procedure (see sec. 8.2).

The purity of the samples is above 96%, and S/B in the signal region is of about 29, for all the sub-samples. Signal yields are reported in tab. 4.4. In the following chapters all plots and numbers are sideband subtracted.

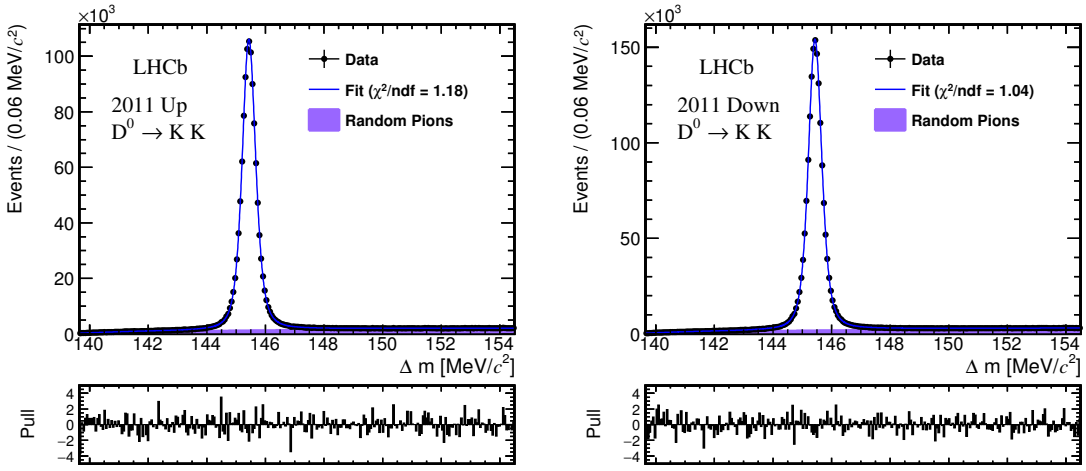

(a) 2011 *MagUp*.

(b) 2011 *MagDown*.

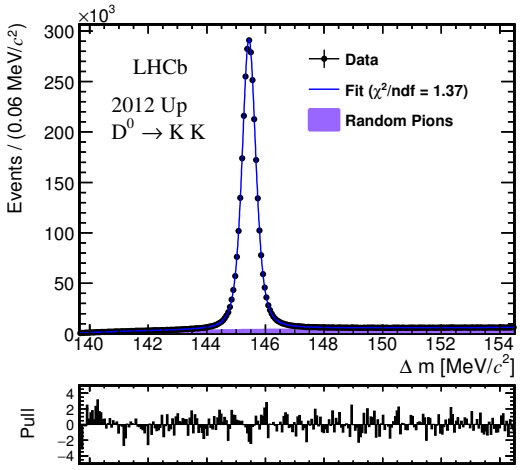

(c) 2012 *MagUp*.

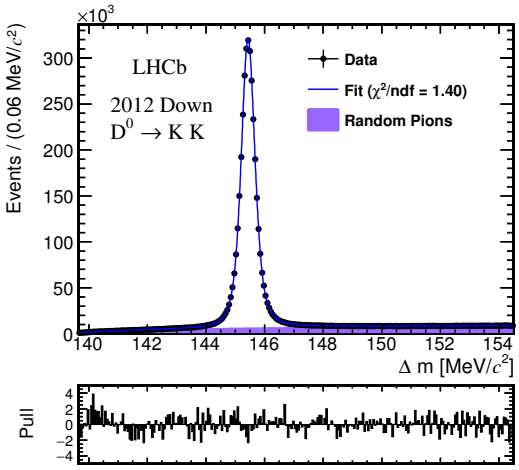

(d) 2012 *MagDown*.

Figure 4.8 – Distribution of the mass difference Δm for the $D^0 \to K^+K^-$ decays. The fit result is overlaid.

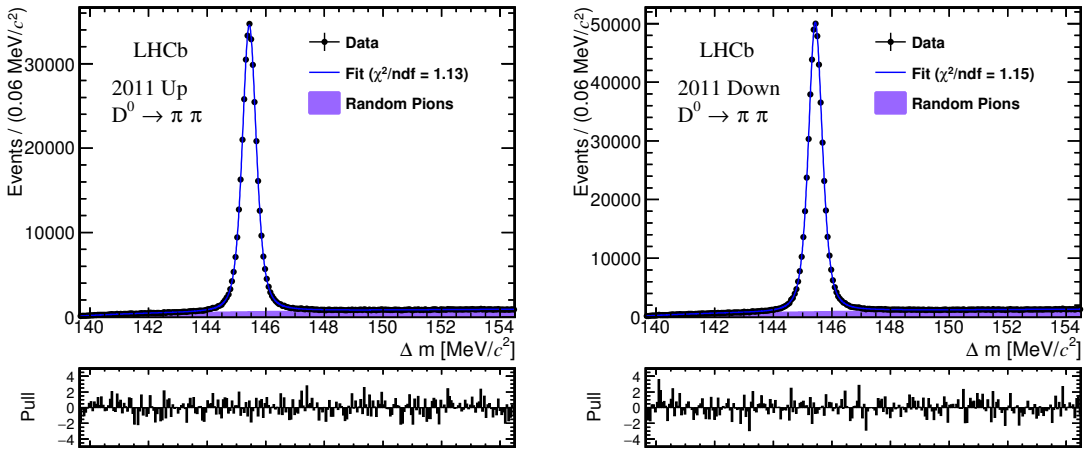

(a) 2011 *MagUp*.

(b) 2011 *MagDown*.

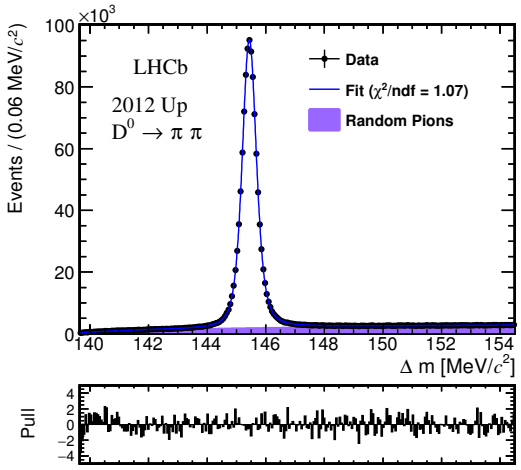

(c) 2012 *MagUp*.

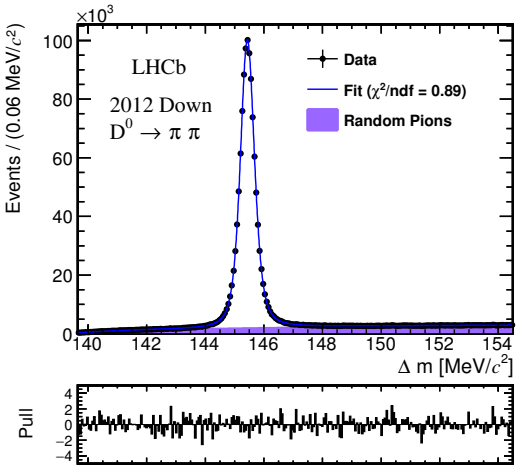

(d) 2012 *MagDown*.

Figure 4.9 – Distribution of the mass difference Δm for the $D^0 \to \pi^+\pi^-$ decays. The fit result is overlaid.

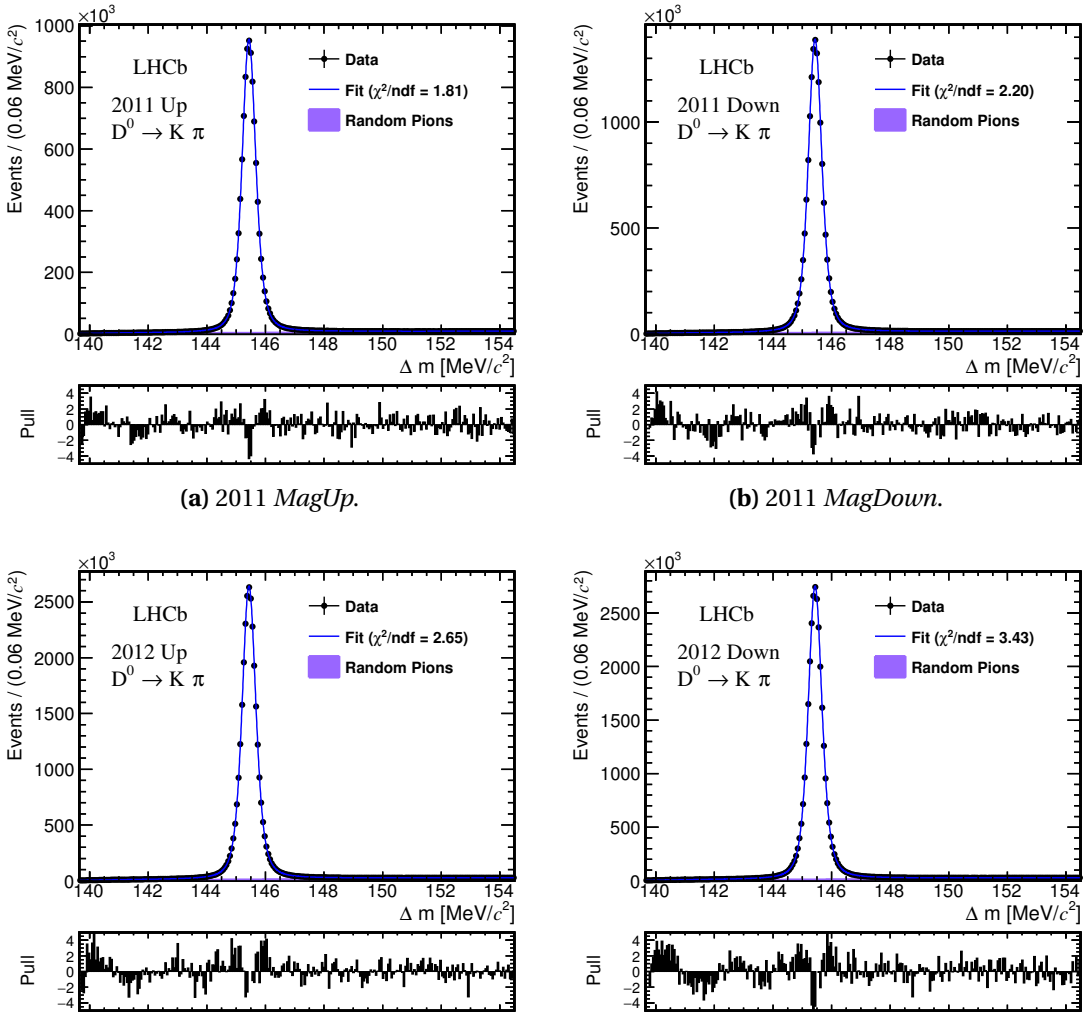

(a) 2011 *MagUp*.

(b) 2011 *MagDown*.

(c) 2012 *MagUp*.

(d) 2012 *MagDown*.

Figure 4.10 – Distribution of the mass difference Δm for the $D^0 \to K^-\pi^+$ decays. The fit result is overlaid.

Table 4.4 – Signal yields in millions of candidates, extracted from fits of Δm-distributions (as described in sec. 4.6), after requiring the offline selection described in sec. 4.4.

sample/$[10^6]$	$D^0 \to K^-\pi^+$	$D^0 \to K^+K^-$	$D^0 \to \pi^+\pi^-$
2011 Up	10.7	1.2	0.36
2011 Down	15.5	1.7	0.53
2012 Up	30.0	3.3	1.02
2012 Down	31.3	3.4	1.07
Total	87.5	9.6	2.98

4.7 Charge-randomised sample

In general any experimental technique may posses some unknown subtle biases, that must be studied and quantified to perform a robust and reliable measurement. This is particularly true when the target, as in the A_Γ measurement, is a very precise measurement of *CP* asymmetry. Generally, these biases are studied through detailed Monte Carlo samples generated accordingly to the features of the signal sample. However, in the measurement reported in this thesis the generation of a large sample of simulated decays is impracticable due to the required huge statistics. Thus, a data-driven method is developed to search for hidden biases using the so-called *charge-randomised* samples. The flavour of the D^0 meson is inferred from the charge of the soft pion in the $D^{*+} \to D^0\pi^+$ decay chain, as explained in chap. 2. Therefore, if one randomly re-assigns the charge of the soft pions, the correspondence between the D^0 flavour and the sign of the charge of the soft pion is lost. Thus, the charge-randomised sample is made by the same events used in the final measurement where the charge of the soft pions has been randomly chosen. In this sample all the asymmetries (physical or induced by the detection) are zero by definition. That is why any possible bias introduced by the used experimental technique, can easily be detected. A benefit of the charge-randomised samples is the extreme facility and rapidity to generate them. Indeed, only an addition call to a random generator function with respect to the time to run over all the events is needed.

5 Detector-induced time-dependent charge asymmetries

This chapter is devised to the evaluation of the non-negligible residual detector induced charge asymmetries affecting the measurement of A_Γ. A fully data driven correction to account for these asymmetries has been developed using the high statistics Cabibbo-favoured $D^0 \to K^-\pi^+$ decay mode and tested at very high precision.

5.1 Introduction

The measurement of *CP* asymmetries is an experimental challenge, and this is particularly true at hadron colliders, where events are much more complex than those produced and collected at e^+e^- machine. The need to implement very selective requirements at the trigger stage can introduce biases in the collected events, sculpting the kinematic distributions of the decays. Particles with different charges result into different reconstruction efficiencies and acceptances (especially if they have a low momenta). The situation is further complicated by production asymmetries, since the production of a meson and its anti-meson differs in the case of pp collisions. As a result two nuisance parameters are present: the detection charge asymmetry, $A_{\rm D}$, and the production asymmetry, $A_{\rm P}$, which accounts for the different probability of producing a meson or an anti-meson. Therefore, the measured raw asymmetry can be written as the sum of different terms

$$A_{\rm raw}(t) = A_{CP}(t) + A_{\rm D} + A_{\rm P} + \mathcal{O}(A^3),$$

as reported in eq. (2.3), where the observable of interest $A_{CP}(t)$ must be disentangled from $A_{\rm D}$ and $A_{\rm P}$. Measuring the integrated *CP* asymmetry, $\int A_{CP}(t)\mathrm{d}t$, requires to know the values of the production and the detection asymmetries with a precision of the same order or better than that one of the final measurement. It is easy to understand that this is a tough job. However, time-dependent asymmetries, as the measurement of A_Γ described in this thesis, bypass some of these hurdles since all the global charge asymmetries, as the detection and the production asymmetries do not depend on the D^0 meson decay time. Thus, in the A_Γ measurement the production asymmetry $A_{\rm P}$, which is the asymmetry in production D^{*+}

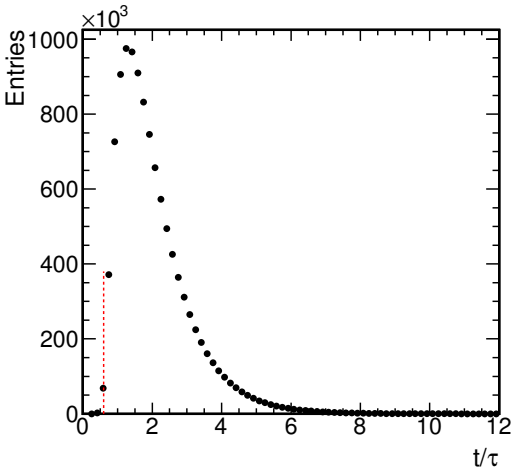

Figure 5.1 – Proper decay time distribution of $D^0 \to K^-\pi^+$ candidates. Events with proper decay time lower than $0.6\tau_{D^0}$ (dashed red line) are excluded as described in the text.

mesons, and the detection asymmetry $A_{\rm D}$, which is the asymmetry in reconstructing the $D^{*+} \to D^0\pi^+$ decays are not, at least in principle, nuisance parameters. However, studying in detail the $D^0 \to K^-\pi^+$ control channel decay, it was found that the detection asymmetry is not completely independent of the D^0 proper decay time. This is unexpected and it can be explained through an artificial detection-induced correlation between momentum and proper decay time of the D^0 meson, likely due to the complex and highly selective requirements (both at online and offline level) used to reconstruct $D^{*+} \to D^0\pi^+$ candidates. Thus, it results that the detection asymmetry needs to be accurately assessed in order to measure A_Γ, since it has a very dangerous time-dependent nature. Following sections are therefore entirely devoted to this item.

5.2 Control channel pseudo-A_Γ

Time-dependent instrumental effects are studied through the measurement of pseudo-A_Γ on $D^0 \to K^-\pi^+$ decays, as described in sec. 2.3. Candidates are required to satisfy the offline selection described in sec. 4.4. The secondary decays contribution, estimated to be below 3% with respect to the prompt component, can be safely neglected in these studies. This is a good approximation for studying detector-induced charge asymmetries, since secondary contribution is assessed to be a small contribution to A_Γ ($\lesssim \mathcal{O}(10^{-3})$) and a systematic uncertainty will be assigned (see chap. 7). Sample is split into 29 bins of proper decay time (see app. D for the definition of bins range) in the range $[0.6, 20]\tau_{D^0}$ (where $\tau_{D^0} \simeq 0.41\,$ps is the current measured value of the D^0 lifetime [20]), with about the same number of events and different sizes. Candidates with $t \in [0, 0.6]\tau_{D^0}$ are excluded (see fig. 5.1) to remove regions in which the LHCb efficiency is particularly low. These events are prone to large uncertainties due to very low acceptance values and might not cancel out properly in the ratio. In each proper decay

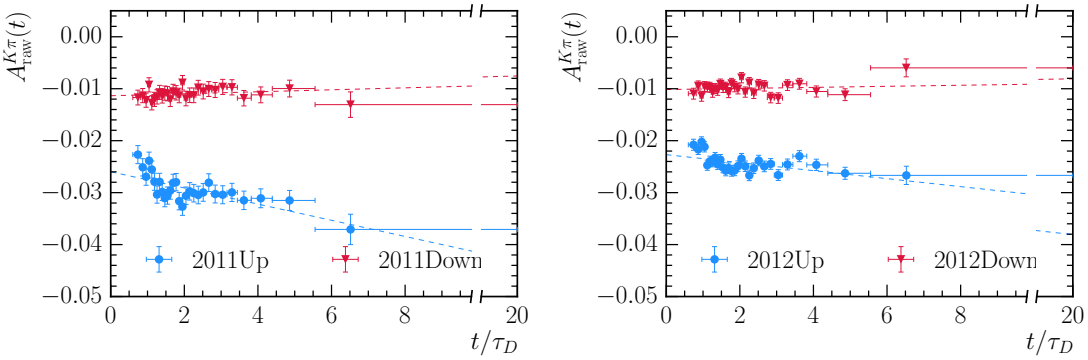

Figure 5.2 – Raw asymmetry $A_{\rm raw}^{K\pi}$ as function of D^0 proper decay time for *MagUp* and *MagDown* samples, in 2011 (left) and 2012 (right), with offline selection described in sec. 4.4.

time bin $i^{\rm th}$ the raw asymmetry is measured as

$$A_{\rm raw}^{K\pi}(t_i) = \frac{N^+(t_i) - N^-(t_i)}{N^+(t_i) + N^-(t_i)},$$

where $i = 1,\ldots,29$, $N^\pm(t_i)$ is the number of reconstructed $D^\pm$ candidates in the time bin $i^{\rm th}$, and t_i is the average measured proper decay time of the reconstructed D^0 meson in the time bin $i^{\rm th}$. $N^\pm$ are extracted by counting the number of events in the Δm mass range within $[144.45, 146.45]\,{\rm MeV}/c^2$ corresponding to about $\pm 5\sigma$ region around the measured mean value of the signal peak. The random pion background is sideband subtracted, as described in sec. 4.6.

The value of pseudo-A_Γ ($A_\Gamma^{K\pi}$) is extracted through a linear fit of $A_{\rm raw}^{K\pi}(t_i)$ measurements as a function of the proper decay time using the following linear function

$$A_{\rm raw}^{K\pi}(t) = A_0 - A_\Gamma^{K\pi}\frac{t}{\tau_{D^0}}.$$

where A_0 is a constant including all non time-dependent asymmetries. If all instrumental asymmetries are time-independent $A_\Gamma^{K\pi}$ would be compatible with zero within the statistical uncertainty reached with the present data. Results of the linear fit of the $D^0 \to K^-\pi^+$ data samples are reported in fig. 5.2 and tab. 5.1, for 2011, 2012, *MagUp* and *MagDown* data samples, respectively. A significant slope is observed with *MagUp* polarity, at 5.5σ and 4.3σ from zero for 2011 and 2012 data, respectively. The weighted average is far from zero at 4.1σ level, with a statistical uncertainty of 0.10×10^{-3}. Since no *CP* violation occurs in the Cabibbo-favoured $D^0 \to K^-\pi^+$ mode (see app. A), the observed significant slopes can only be ascribed to detector-induced effects and no measurement of A_Γ can be attempted until they are understood and corrected.

Table 5.1 – Pseudo-A_Γ results. The offline selection described in sec. 4.4 is applied to the $D^0 \to K^-\pi^+$ control sample. The significance with respect to zero is also reported.

sample	$A_\Gamma^{K\pi}$ [10^{-3}]	significance [σ]
2011 *MagUp*	1.65 ± 0.30	5.5
2011 *MagDown*	-0.11 ± 0.25	0.4
2012 *MagUp*	0.77 ± 0.18	4.3
2012 *MagDown*	-0.06 ± 0.17	0.3
weighted average	0.41 ± 0.10	4.1

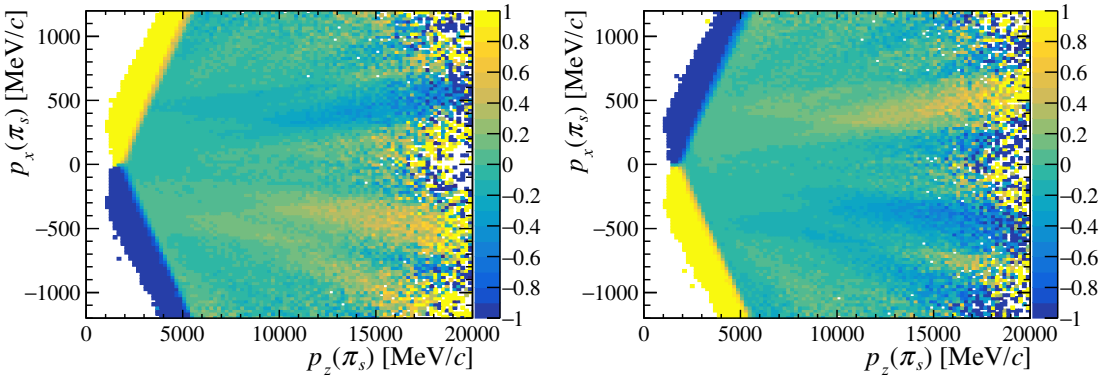

Figure 5.3 – Raw asymmetry as function of p_x and p_z of soft-pions, for the $D^0 \to K^-\pi^+$ 2012 sample with *MagUp* (left) and *MagDown* (right) polarity.

5.3 Time-dependent instrumental effects

As mentioned in sec. 2.3, eq. (2.5)

$$A_{\text{raw}}^{K\pi} = A_{\text{D}} + A_{\text{P}} + \mathcal{O}(A^3)$$

assumes that A_{D} and A_{P} are time-independent, and that the physics asymmetry $A_{CP}(t)$ can be neglected. However, a time dependence may be hidden in the detection asymmetry A_{D}. If the detection asymmetry depends on the decay kinematics (which is not an uncommon occurrence), and at the same time the kinematics and proper decay time are not statistically independent, the detection asymmetry may indirectly acquire a time dependence.

The charge asymmetries in the reconstruction and selection of soft pions like the ones used in the present measurement to identify the D^0 flavour are sizeable and strongly momentum-dependent. A pion with a $p_z \simeq 5\,\text{GeV}/c$ and $p_x \sim 100 \div 200\,\text{MeV}/c$ changes its direction, due to the magnetic field, of a quantity of $\approx 250\,\text{mrad}$, which is comparable to the entire LHCb acceptance of 300 mrad; this generates large differences in acceptance for positively and negatively charged pions, as can be seen in fig. 5.3. In addition, it must be noted that even

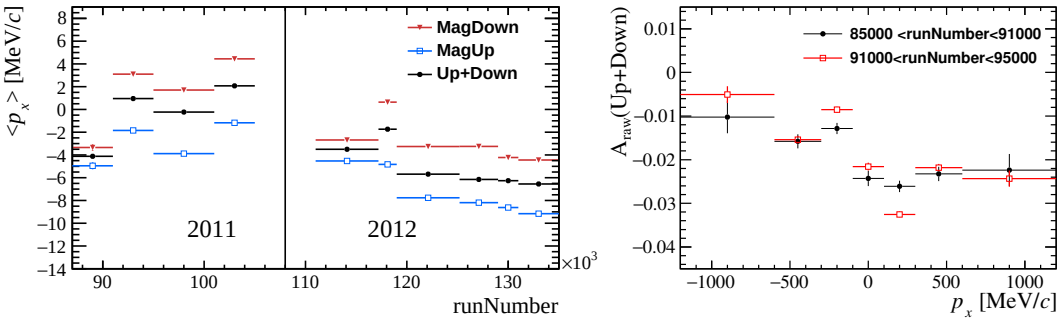

Figure 5.4 – Left, mean x-coordinate of the soft pion momentum in different blocks of run number with about the same population. Right, average raw asymmetry, between *MagUp* and *MagDown* samples, as function of x-coordinate of the soft pion momentum in two different run periods.

particles hitting the same location on a given detector layer, will intersect different sub-detectors with different trajectories according to their charge and momentum. Averaging the results from the two magnet polarities does not necessarily eliminate the problem with the degree of precision needed in analyses like the present one, because of variation of run and detector conditions over time. This is manifest in fig. 5.4 where the average asymmetry between *MagUp* and *MagDown* samples changes significantly with the run number.

On the other hand, the existence of a statistical dependence between decay time and kinematics can be clearly seen, for instance, from the momentum distributions of D^0 candidates in different proper decay time bins, as shown in fig. 5.5. To check whether the observed correlations are actually capable of generating significant time-dependent asymmetries, the value of $A_\Gamma^{K\pi}$ is measured in different bins of D^0 momentum, by splitting the sample in three independent subsamples with roughly equal populations:

- $0 < p(D^0)/(\text{GeV}/c) \leq 50$,
- $50 < p(D^0)/(\text{GeV}/c) \leq 75$,
- $p(D^0)/(\text{GeV}/c) > 75$.

The results are reported in fig. 5.6, where to quantify the compatibility of the different $A_\Gamma^{K\pi}$ values they are fit to a common constant. The value of pseudo-A_Γ returned from the fit is $A_\Gamma^{K\pi} = (0.48 \pm 0.10) \times 10^{-3}$, in close agreement with the weighted average reported in tab. 5.1, while the $\chi^2/\text{ndf} = 46/11$ indicates that they are strongly statistically incompatible ($\text{Prob}(\chi^2|\text{ndf}) \approx 3 \times 10^{-6}$).

5.4 Symmetrisation procedure

Generally speaking, the observed distribution of a set of observables in data can be thought of as the product of the actual distribution (as produced by the physics process), multiplied

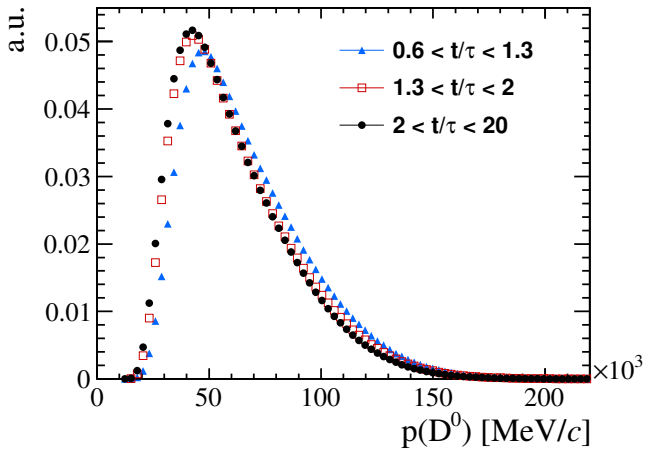

Figure 5.5 – Momentum distribution of D^0 candidates in different bin of proper decay time. The sample showed is 2012 *MagUp*.

by the acceptance/efficiency function of the detector. If such data is then used to perform a *CP* asymmetry measurement, the results will in general be different from the true value of the observable in the original data, due to dis-uniformities in detector efficiency. However, in order to avoid biasing the *CP* asymmetry of data, it is not really necessary for the detector effciency to be uniform over the whole space; all is really necessary is for the efficiency of the detector to be *CP-symmetric*.

By design, the nominal geometry of the LHCb detector is indeed approximately *CP*-symmetric.[1] If one considers a transformation formed by a reflection around a vertical plane passing through the z-axis, and charge inversion, this will transform a curved track trajectory into a mirror trajectory on the other side of the detector - which is expected to have the same acceptance, at least under nominal geometry assumptions and neglecting material effects. In practice, this nominal symmetry is broken by the various real-life effects. What is most important for the present measurement is not a global deviation of the efficiency from *CP*-symmetry (that would only produce a constant shift), but the fact that such asymmetry may be dependent on event observables - in particular, on the D^0 decay time.

As discussed in the previous section, such asymmetry actually exists and is not negligible, so the detector efficiency needs to be corrected to eliminate or reduce its *CP* asymmetry, or at least its dependence on particle momentum, that is the relevant factor causing a decay-time dependence. A further evidence of the lack of *CP*-symmetry of the acceptance can be obtained by comparing the observed charge asymmetries for different magnet polarities as shown in fig. 5.7: they would be expected to be equal, but in fact their difference are strongly statistically significant. Indeed, these differences have been driving the largest systematic uncertainty in

[1] Here, material effects are neglected, otherwise for a complete *CP*-symmetry the detector should be swapped with its antimatter counterpart.

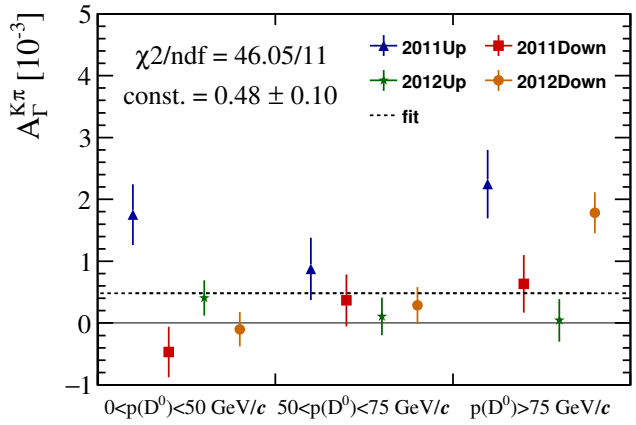

Figure 5.6 – $A_\Gamma^{K\pi}$ as function of D^0 momentum for both years and polarities.

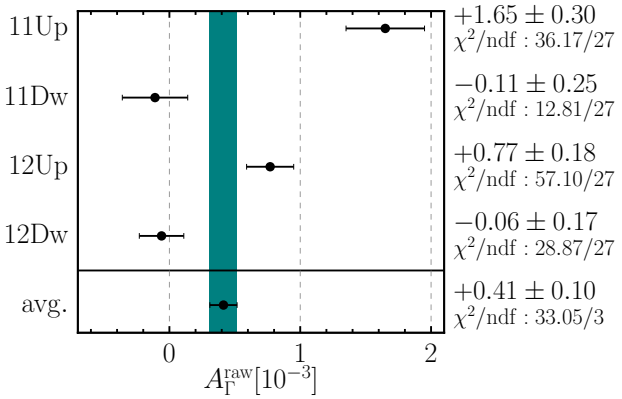

Figure 5.7 – Pseudo-A_Γ results with offline selection for different years and polarities. Label 2011 (2012) is abbreviated 11 (12) and *MagUp* (*MagDown*) is abbreviated Up (Dw).

the previous LHCb A_Γ measurement described in ref. [36], as also explained in sub-sec. 2.5.2. In order to measure this effect, the distribution of observed charge asymmetry of the soft pion is plotted as a function of its emission angle theta θ_x and k, a variable proportional to the track curvature, defined as

$$k = \frac{1}{\sqrt{p_x^2 + p_z^2}}, \qquad \theta_x = \arctan\left(\frac{p_x}{p_z}\right),$$

where p_x and p_z are the x and z components of the soft pion momentum, and the y direction is perpendicular to the bending plane. Distributions of (k, θ_x) space for positively- and negatively-charged soft pions are shown in fig. 5.8, while fig. 5.9 shows the ratio in this space, once the sign of θ_x is flipped in the denominator. If there was no *CP* asymmetry in the sample or in the detector, this distribution would be symmetric under the *CP* transformation

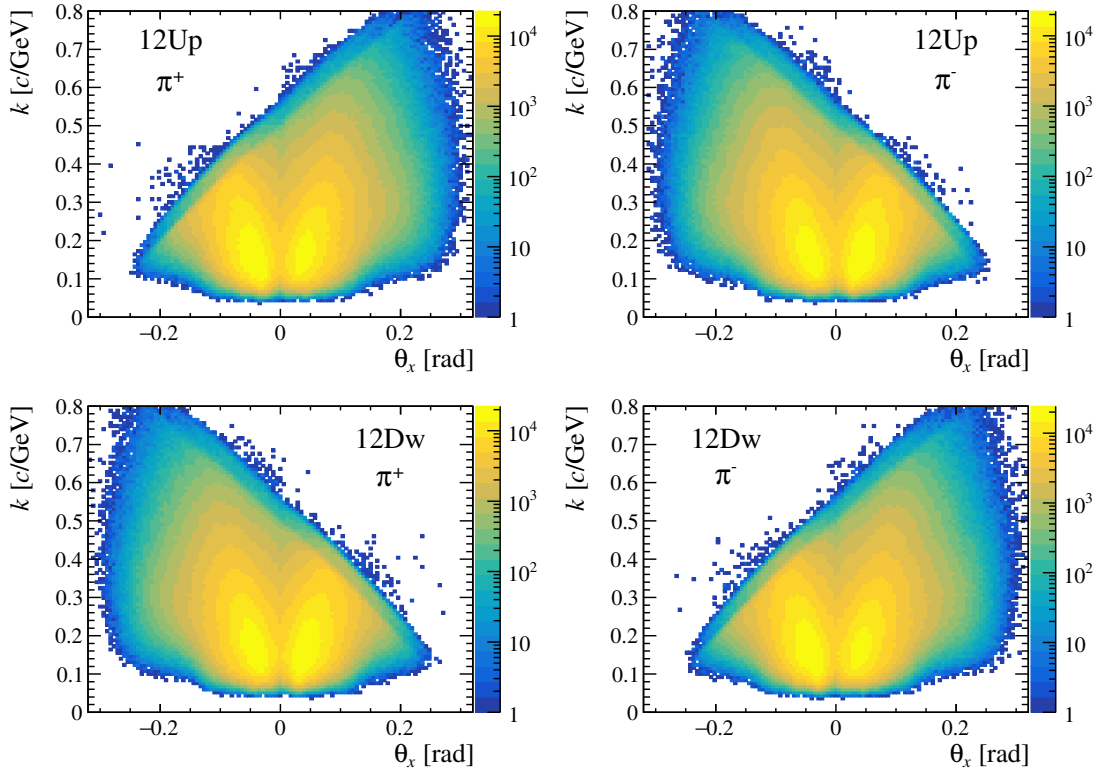

Figure 5.8 – Distributions of (k, θ_x) for positively-charged soft pions (left) and negatively-charge soft pions. The $D^0 \to K^-\pi^+$ decays sample it is represented.

$N^+(k,\theta_x) \to N^-(k,-\theta_x)$.

The data clearly show that this distribution is not symmetric, and in fact the variations are much larger in size than those expected from the physics *CP* asymmetry of the sample, which are expected below the percent level. There are strong point-to-point variations that must clearly be attributed to detector effects, not to the physics. In order to remedy this situation the distribution is used as a measurement of detector deviations from the *CP*-symmetry. Applying an acceptance correction to the data based on this distribution, reweighing the number of events $N^+(k,\theta_x)$ to be the same to the number of events $N^-(k,-\theta_x)$ the most of the *CP*-asymmetries of the detector are corrected. Small dis-uniformities in $\theta_y = \arctan(p_y/p_z)$ are also present (see fig. 5.10) and they cannot be neglected, therefore the acceptance correction is applied in bins of the three-dimensional (k,θ_x,θ_y) space reweighing the number of the D^{*+} events $N^+(k,\theta_x,\theta_y)$ to be equal to the θ_x flipped number of D^{*-} events $N^-(k,-\theta_x,\theta_y)$. This appears as the most natural choice being the kinematics of the soft pion entirely described by the (k,θ_x,θ_y) space and since any observed instrumental effects must be ascribed to the soft pion. Details on how the reweigh is done are reported in app. E.

A residual global asymmetry may still survive due to the physical *CP* asymmetry present in the

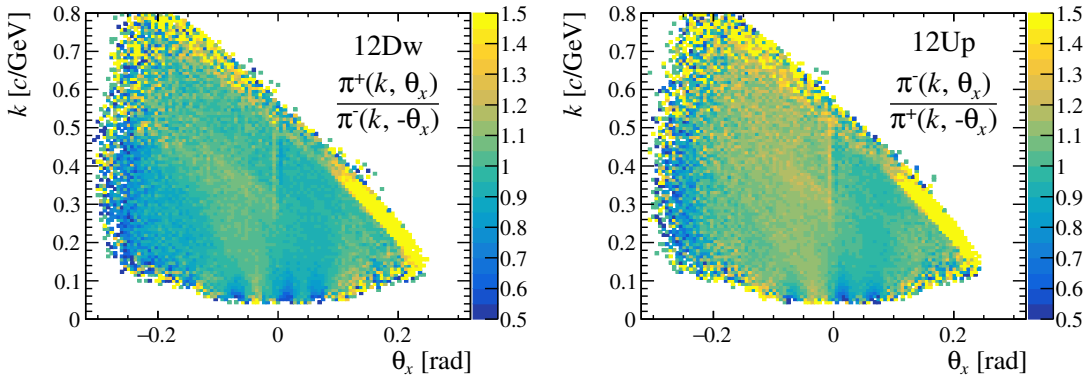

Figure 5.9 – Ratio in the (k,θ_x) space, where the sign of θ_x is flipped in $-\theta_x$ for negatively-charged soft pions in *MagDown* sample (left) and for positively-charged soft pions in *MagUp* sample (right), in order to compare the two polarities directly.

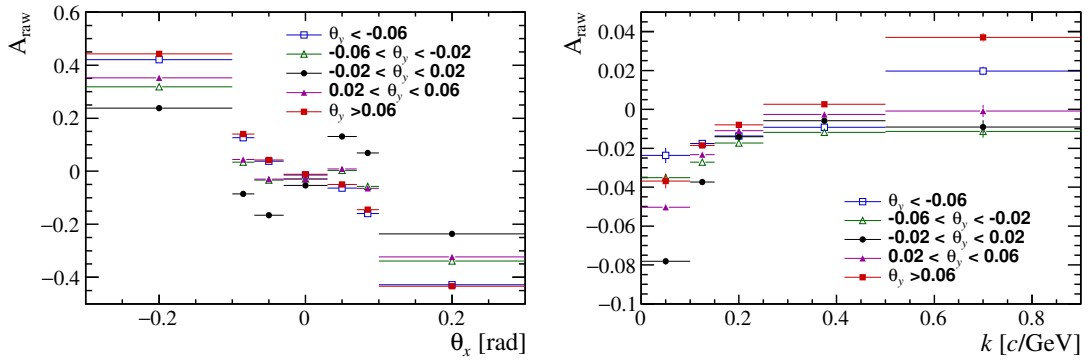

Figure 5.10 – Asymmetry as a function of the (left) soft pion θ_x and (right) curvature k in different range of θ_y (expressed in radiants). $D^0 \to K^-\pi^+$ decays data of subsample 2012 *MagDown* are shown.

original data, but what is most important is that any dependence of such detector asymmetry on momenta is removed, because the correction is performed separately for every bin of track curvature. A confirmation of the effectiveness of this procedure is given by the fact that, when applying the procedure separately and independently to each subsample, the results spontaneously converge to agree with each other as reported in fig. 5.12. The symmetrisation is applied separately to each period, as there is no guarantee that the detector asymmetries stayed constant in time (see fig. 5.4), although an overall correction for the whole sample should give a similar result. Of course, this correction has the side effect of also canceling any net average physics *CP* asymmetry of the sample - this is however irrelevant for the purpose of A_Γ measurement, that is only relying on the *slope* of that asymmetry as a function of decay time. As a cross-check, sec. 5.4.2 shows the effect of injecting an artificial slope into the sample, and then correcting with the procedure described: the average *CP* asymmetry is zeroed, but

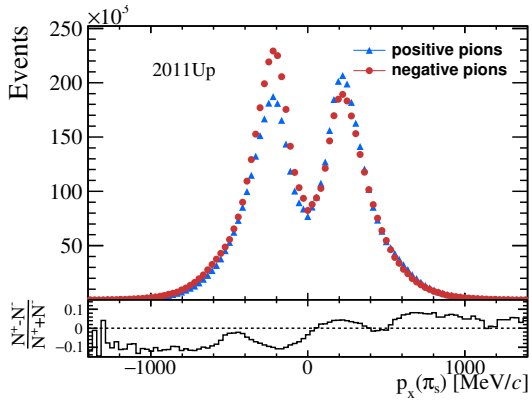

(a) p_x distribution.

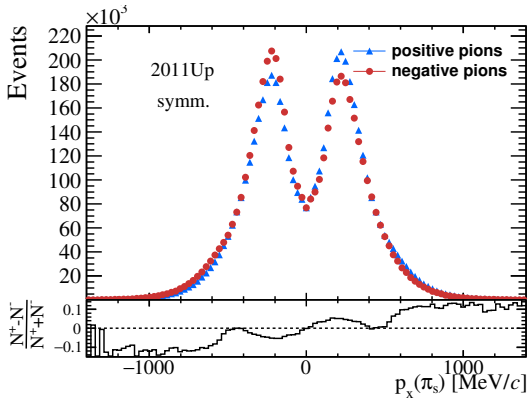

(b) p_x distribution after the correction.

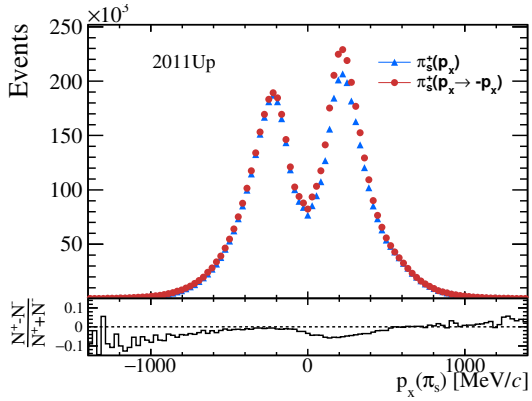

(c) p_x distribution (with negative distribution flipped).

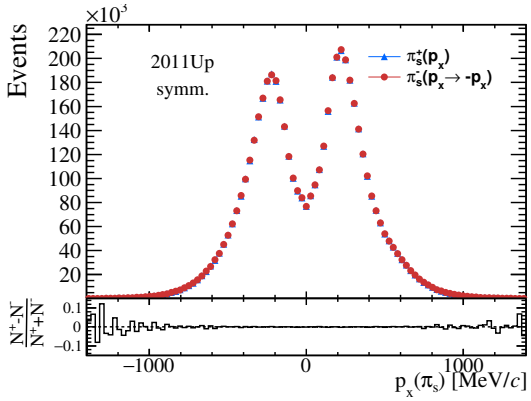

(d) p_x distribution after the correction (with negative distribution flipped).

Figure 5.11 – Soft pions p_x distribution. Left, the distribution before the (k,θ_x) symmetrisation and right, after the (k,θ_x) symmetrisation. At the bottom the same distributions where the sign of p_x has been flipped for the distributions of negative pions ($p_x \to -p_x$).

the slope is unaffected.

5.4.1 Effects of the correction

An alternative visualisation of the (k,θ_x) space can be obtained in the more familiar (p_x,p_z) space, which is in one-to-one correspondence with it. Figure 5.11 shows the distributions of p_x of the soft pion before (5.11a) and after (5.11b) the symmetrisation procedure in the (k,θ_x,θ_y) space for 2011 *MagUp* sub-sample. The momentum-dependent asymmetry is clearly visible as is the lack of symmetry in the comparison of the two distributions after flipping the sign of θ_x, fig. 5.11c. In tab. 5.2, fig. 5.12 and fig. 5.13 are shown the results for different periods and as a function of D^0 momentum when the symmetrisation procedure is applied to the data samples selected using the offline selection. Comparison with results without symmetrisation of

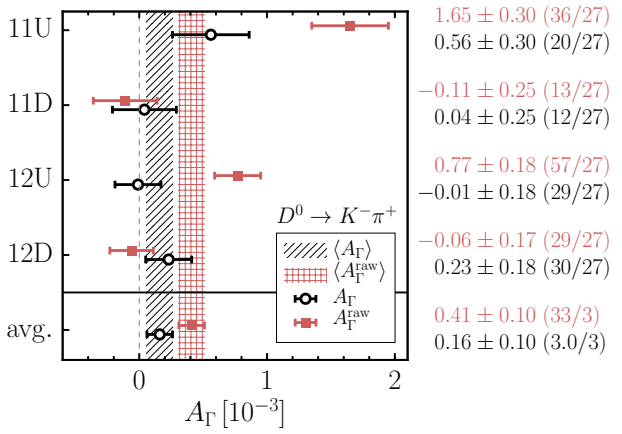

Figure 5.12 – Results for $A_\Gamma^{K\pi}$ in different years and polarities (left) before and (right) after *CP* symmetrisation. Label 2011 (2012) is abbreviated 11 (12) and *MagUp* (*MagDown*) is abbreviated Up (Dw).

tab. 5.1 is also reported. It can be seen from these results that after the correction the weighted

Table 5.2 – Results for $A_\Gamma^{K\pi}$ before and after the symmetrisation procedure.

sample	$A_\Gamma^{K\pi}$(raw)$[10^{-3}]$	$A_\Gamma^{K\pi}[10^{-3}]$
2011 *MagUp*	1.65 ± 0.30	0.56 ± 0.30
2011 *MagDown*	-0.11 ± 0.25	0.04 ± 0.25
2012 *MagUp*	0.77 ± 0.18	-0.01 ± 0.18
2012 *MagDown*	-0.06 ± 0.17	0.23 ± 0.18
weighted average	0.41 ± 0.10	0.16 ± 0.10

average of $A_\Gamma^{K\pi}$ gets closer to zero, going from $(0.41 \pm 0.10) \times 10^{-3}$ to $(0.16 \pm 0.10) \times 10^{-3}$ (1.6σ). The χ^2/ndf between the four sub-samples moves to 3.01/3 from 33.05/3, corresponding to a change of 30 units. The level of compatibility of $A_\Gamma^{K\pi}$ between the different sub-samples as a function of D^0 momentum improves as well, going from $\chi^2/\text{ndf} = 46.05/11$ to 12.59/11. In summary, the correction devised causes a dramatic improvement of the quality of the results, being fully compatible with no slope hypothesis.

5.4.2 Could the symmetrisation procedure bias the value of A_Γ?

A possible concern is whether the correction procedure might suppress or reduce a possible physical *CP* asymmetry actually present in the data, thus harming the measurement. To check for this possibility, a test is made by artificially injecting an asymmetry in the data. To disentangle the effect of the correction on the true A_Γ from the fake A_Γ induced by detector-effects, a data sample where the charge of the soft pions has been chosen randomly is used (see

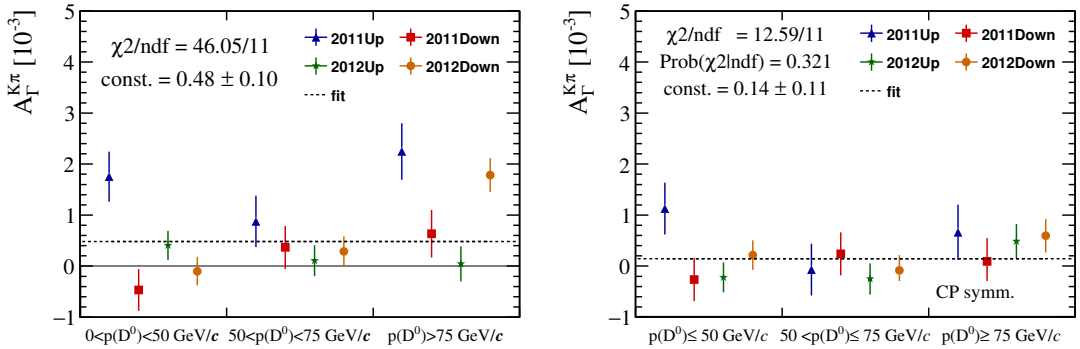

Figure 5.13 – $A_\Gamma^{K\pi}$ results with offline selection for different years and polarities as a function of D^0 momentum with no (left) and with (right) *CP* symmetrisation.

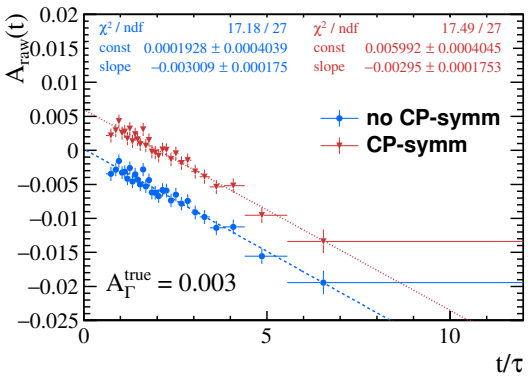

Figure 5.14 – $A_\Gamma^{K\pi}$ in 2012 *MagUp* charge-randomised sample with and without the symmetrisation procedure applied, when an artificial time-dependent asymmetry, independent of kinematics, is injected in data.

sec. 4.7). In this way, any detector-induced effect cancel, the net effect of the correction can be spotted. An artificial sample is created by applying a random filtering of D^{*+} candidates according to an efficiency proportional to proper decay time, with a value of $A_\Gamma^{K\pi}$(artificial) = 3.00×10^{-3}, (about a factor 10 larger than the statistical uncertainty of this subsample), and then applied our usual fitting and symmetrisation procedures (fig. 5.14). There results for A_Γ are

$$A_\Gamma^{K\pi}\text{(before symmetrisation)} = (3.00 \pm 0.17) \times 10^{-3},$$
$$A_\Gamma^{K\pi}\text{(after symmetrisation)} = (2.95 \pm 0.17) \times 10^{-3}.$$

that are both in agreement with the true value of $A_\Gamma^{K\pi} = 3.00 \times 10^{-3}$.

5.4.3 Indirect generation of time-dependent asymmetries

To verify the hypothesised mechanism of generation of a time-dependent asymmetry from a purely momentum-dependent asymmetry in the (k, θ_x) distribution, an artificial test sample is produced by reweighing the p_x distributions in the data, as reported in fig. 5.15. Distributions of positively and negatively charge pions in $p_x > 0$ region are scaled by a constant factor, to generate a much larger *CP* asymmetry. As a results, a large time-dependent asymmetry becomes clearly visible (fig. 5.15), with a dependence that is not even compatible with a straight line. This clearly demonstrates the actual effectiveness of the hypothesised mechanism in generating significant time-dependent effects through the presence of a correlation between momentum and proper decay time. As a further cross-check of the hypothesis, the correction procedure is applied to this artificially created $A_\Gamma^{K\pi}$ and it is checked that artificial slope disappears, as reported in fig. 5.15 (bottom right). This is a further confirmation of the robustness and of the validity of the correction procedure.

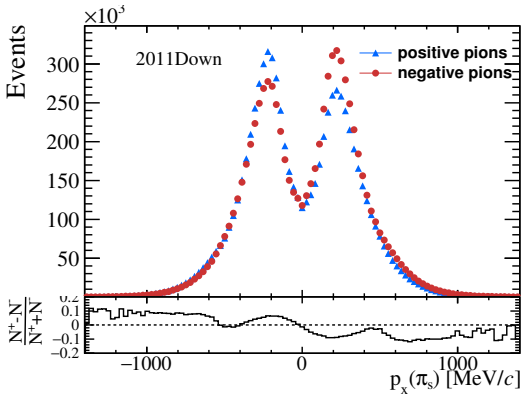

(a) Soft pions p_x distribution.

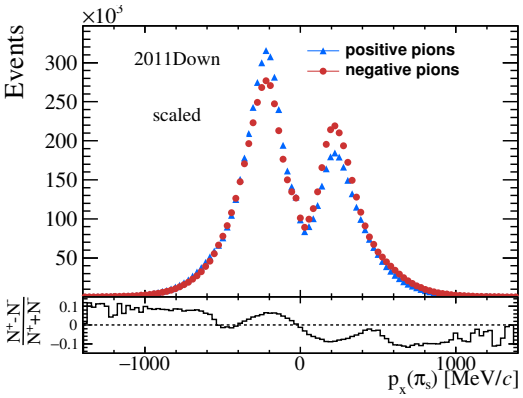

(b) Soft pions p_x distribution artificially reweigh.

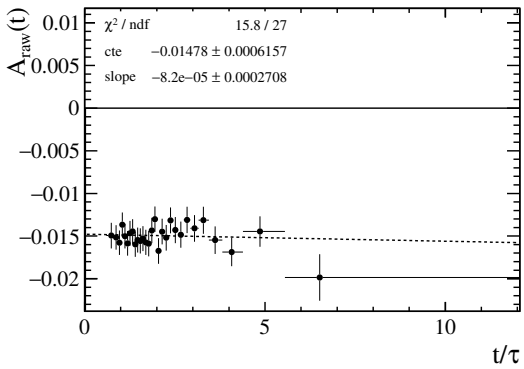

(c) Time-dependent asymmetry for 2011 *MagDown* sample corresponding to the p_x distribution reported in (a).

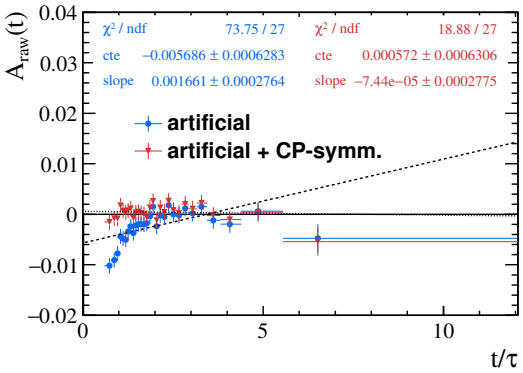

(d) Time-dependent asymmetry for 2011 *MagDown* sample corresponding to the p_x distribution reported in (b), before and after the symmetrisation.

Figure 5.15 – Soft pions p_x distribution for 2011 *MagDown* sample and relative measured $A_\Gamma^{K\pi}$, before and after the artificially reweighing of p_x distribution.

5.5 Robustness cross-checks

To test the robustness of the procedure used, the value of $A_\Gamma^{K\pi}$ is cross-checked versus several variables. First of all, the value of $A_\Gamma^{K\pi}$ as function of the D^0 momentum has been checked as already shown (see fig. 5.14), and also as function of the p_T and the p_x of the D^0 meson, is evaluated. In addition, the value of $A_\Gamma^{K\pi}$ is further evaluated as function of D^0 pseudo-rapidity, η, and the number of primary vertices in the event, nPV. The range of bins chosen is reported in tab. 5.3. Figures 5.16 and 5.17 reports the value of $A_\Gamma^{K\pi}$ as function of the variable discussed above, before and after the correction. Since the A_Γ value is expected to be independent of these variables the compatibility to be a constant is checked through a χ^2 fit, as reported in the figures. Before the reweigh, besides the aforementioned D^0 momentum, the value of $A_\Gamma^{K\pi}$ has a strong dependence on η of the D^0 meson ($\chi^2/\text{ndf} = 48.79/11$) and the number of primary vertices ($\chi^2/\text{ndf} = 47.11/11$). These are in agreement with the fact that the detection asymmetry depends on the momentum of the soft pion. In addition a mild dependence on $p_x(D^0)$ ($\chi^2/\text{ndf} = 20.30/11$) is present. All these dependencies are cured after applying the correction, confirming its reliability.

Table 5.3 – Bins definition for each variable reported.

variable	bin 1	bin 2	bin 3	unit
$p(D^0)$	$[0, 50]$	$]50, 75]$	$[75, \infty[$	GeV/c
$p_T(D^0)$	$[0, 5]$	$]5, 7]$	$[7, \infty[$	GeV/c
$\lvert p_x(D^0)\rvert$	$[0, 2]$	$]2, 4]$	$[4, \infty[$	GeV/c
$\eta(D^0)$	$[2, 3.1]$	$]3.1, 3.6]$	$[3.6, 5]$	-
nPV	1	2	$[3, \infty[$	-

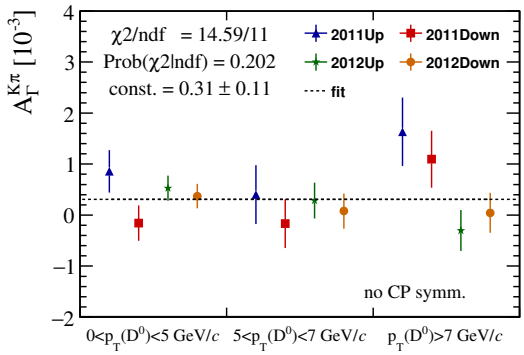

(a) $A_\Gamma^{K\pi}$ vs. p_{T} (D^0) before the correction.

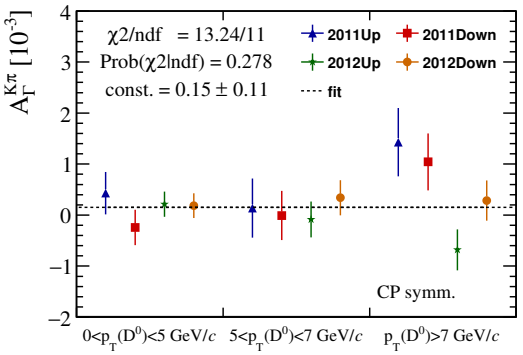

(b) $A_\Gamma^{K\pi}$ vs. p_{T} (D^0) after the correction.

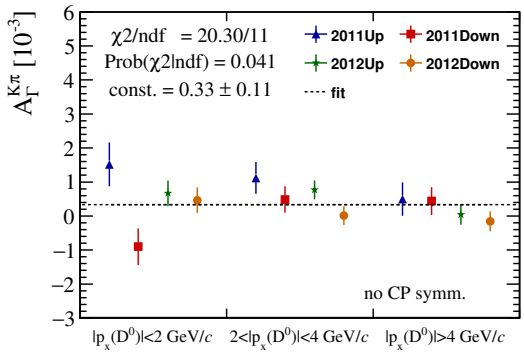

(c) $A_\Gamma^{K\pi}$ vs. $|p_x(D^0)|$ before the correction.

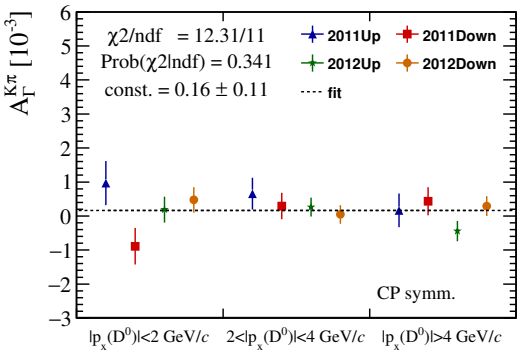

(d) $A_\Gamma^{K\pi}$ vs. $|p_x(D^0)|$ after the correction.

Figure 5.16 – Value of $A_\Gamma^{K\pi}$ as a function of p_{T} and p_x of the D^0 meson, (left) before and (right) after the correction.

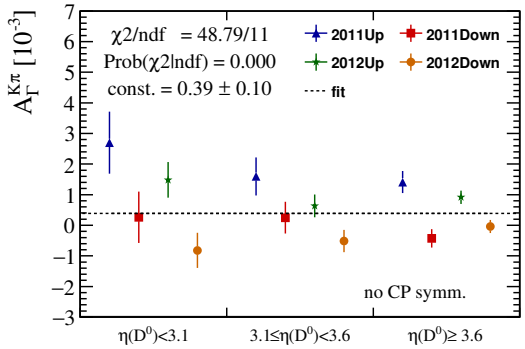

(a) $A_\Gamma^{K\pi}$ vs. $\eta(D^0)$ before the correction.

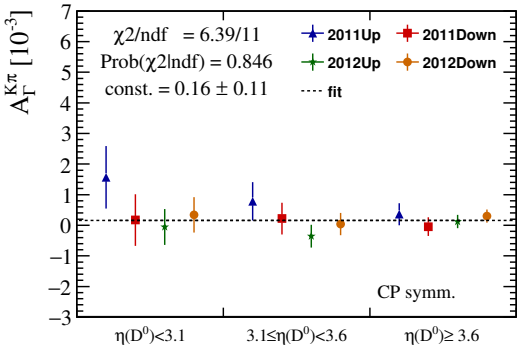

(b) $A_\Gamma^{K\pi}$ vs. $\eta(D^0)$ after the correction.

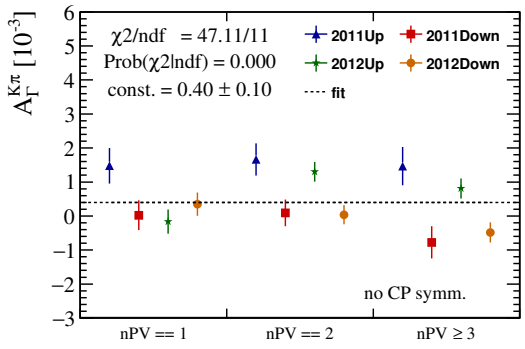

(c) $A_\Gamma^{K\pi}$ vs. nPV before the correction.

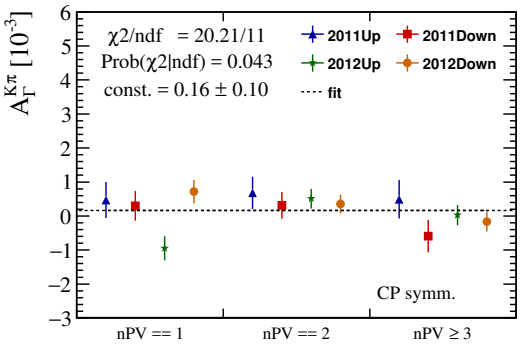

(d) $A_\Gamma^{K\pi}$ vs. nPV after the correction.

Figure 5.17 – Value of $A_\Gamma^{K\pi}$ as a function of pseudorapidity of the D^0 meson and the number of primary vertices, (left) before and (right) after the correction.

6 The extraction of A_Γ parameter

This chapter is devoted to the extraction of the A_Γ observable in $D^0 \to K^+K^-$ and $D^0 \to \pi^+\pi^-$ decays with its final statistical uncertainty.

6.1 Analysis strategy

The A_Γ observable in $D^0 \to K^+K^-$ and $D^0 \to \pi^+\pi^-$ decays is measured exactly as in the $D^0 \to K^-\pi^+$ decay control sample. The method devised to *calibrate* the detector response to the detection charge asymmetries described in chap. 5 is used in the final measurements. The residual contamination from secondary decays from b-hadrons is still present, at few percents level, and a systematic uncertainty is discussed and assessed in chap. 7.

To avoid any potential bias, the measurement was finalised, determining either the statistical and the systematic uncertainties, prior to examine the results (blind analysis). A random shift between $[-0.03, 0.03]$ was applied to the extracted A_Γ, the same for all the four subsamples and for $D^0 \to K^+K^-$ and $D^0 \to \pi^+\pi^-$ decays. The A_Γ values were unblinded only after the final approval by the LHCb collaboration.

An overview of the analysis for extracting A_Γ from $D^0 \to K^+K^-$ and $D^0 \to \pi^+\pi^-$ decays, follows.

1. Samples are selected using the criteria described in chap. 4. The same selection is applied to all the three decay modes. The only differences are due to the PID requirements for obvious reasons (see tab. 4.2).
2. The random pion background is subtracted using the Δm sideband, as described in sec. 4.6.
3. Detection charge asymmetries are corrected reweighing the data in the (k, θ_x, θ_y) space of the soft pion kinematics, as described in chap. 5. The weights for the correction are extracted independently for each decay mode from data itself (see Appendix E for weights details).
4. Samples are split in bins of D^0 proper decay time. The decay time bins boundaries are

the same for all the three decay modes, but the central value is calculated independently taking into account the decay time distribution inside the bin.

5. A_Γ is extracted through a linear fit to the asymmetries as function of the D^0 proper decay time.

6.2 Results

The final measurements on the full Run I data sample, corresponding to $3\,\text{fb}^{-1}$ of integrated luminosity, are

$$\begin{aligned} A_\Gamma(D^0 \to K^+K^-) &= (-0.30 \pm 0.32) \times 10^{-3}, \\ A_\Gamma(D^0 \to \pi^+\pi^-) &= (\ \ 0.46 \pm 0.58) \times 10^{-3}, \end{aligned} \tag{6.1}$$

where only statistical uncertainty is reported. Results for each subsample are plotted in fig. 6.1 and reported in tab. 6.1. Straight line fits of the time-dependent asymmetry are reported in fig. 6.2, while the residuals of individual fits, for all the four subsamples are reported in fig. 6.3. The weighted average asymmetries are reported in fig. 6.4.

Table 6.1 – Results of A_Γ in $D^0 \to K^+K^-$, A_Γ^{KK}, and $D^0 \to \pi^+\pi^-$, $A_\Gamma^{\pi\pi}$, decay before (raw) and after the correction procedure. All the results are reported in units of 10^{-3}.

sample	A_Γ^{KK}(raw)	A_Γ^{KK}	$A_\Gamma^{\pi\pi}$(raw)	$A_\Gamma^{\pi\pi}$
2011 *MagUp*	2.23 ± 0.89	0.46 ± 0.90	4.94 ± 1.62	3.80 ± 1.65
2011 *MagDown*	0.29 ± 0.74	-0.54 ± 0.75	-0.71 ± 1.35	-1.76 ± 1.37
2012 *MagUp*	1.13 ± 0.54	-0.86 ± 0.54	3.54 ± 0.98	1.42 ± 0.99
2012 *MagDown*	0.61 ± 0.53	0.10 ± 0.53	0.23 ± 0.95	-0.50 ± 0.96
weighted average	0.93 ± 0.31	-0.30 ± 0.32	1.77 ± 0.57	0.46 ± 0.58

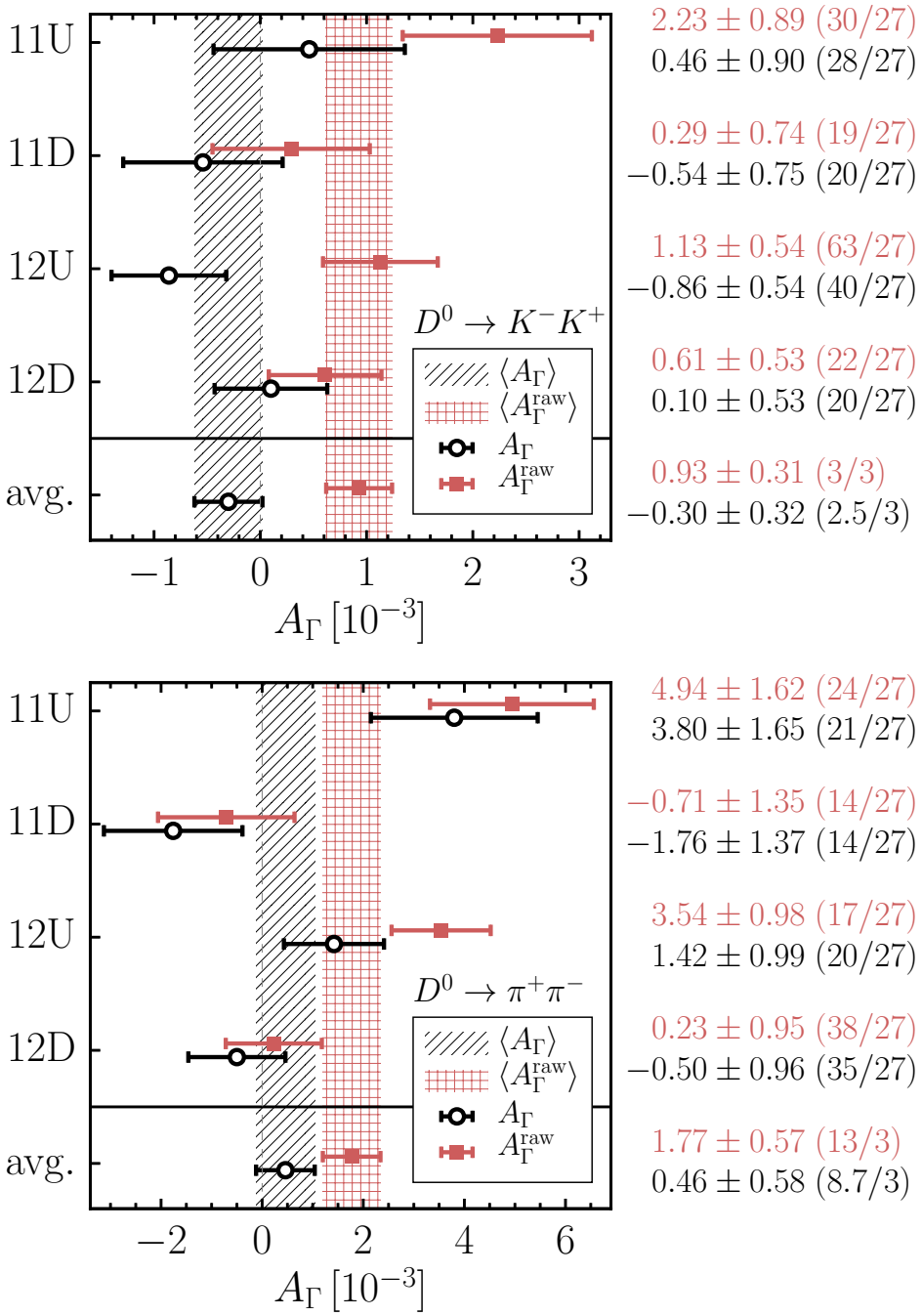

Figure 6.1 – Results for (top) A_Γ^{KK} and (bottom) $A_\Gamma^{\pi\pi}$. The black open markers represent the value of A_Γ after the *CP*-symmetrisation. The red squared markers are the raw A_Γ values, before correcting for detector-induced charge asymmetries. The hatched regions represent the weighted averages over the four subsamples of A_Γ. The label 2011 (2012) is abbreviated 11 (12) and *MagUp* (*MagDown*) is abbreviated U (D).

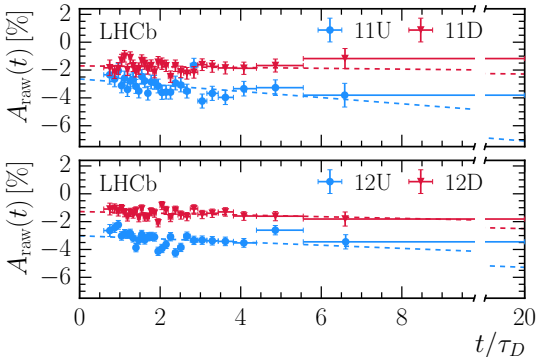

(a) $D^0 \to K^+K^-$, before the correction

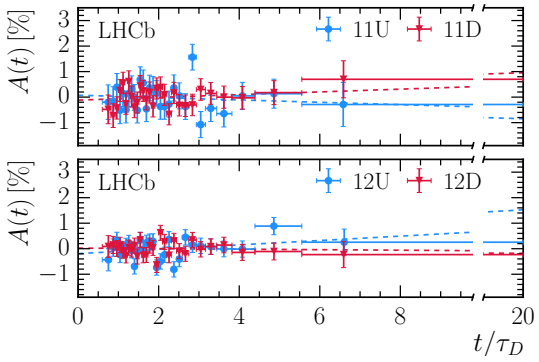

(b) $D^0 \to K^+K^-$

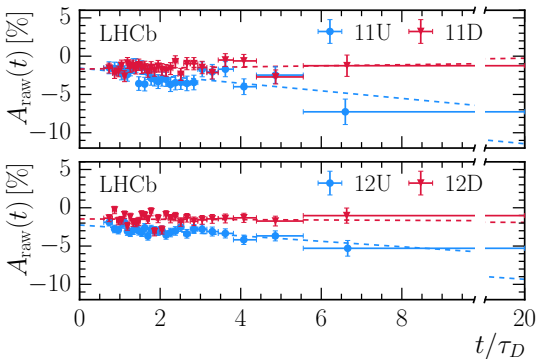

(c) $D^0 \to \pi^+\pi^-$, before the correction

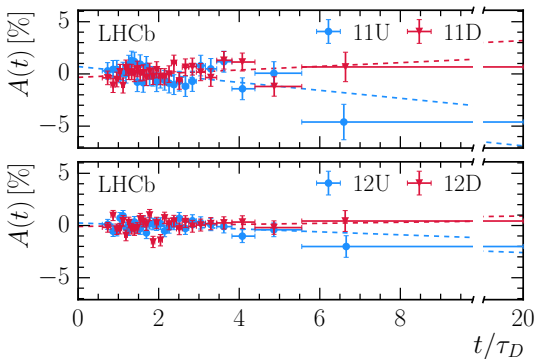

(d) $D^0 \to \pi^+\pi^-$

Figure 6.2 – Asymmetry as function of t/τ_D (left) before and (right) after the correction, for $D^0 \to K^+K^-$ and $D^0 \to \pi^+\pi^-$ decay modes, with the straight line fit overlaid.

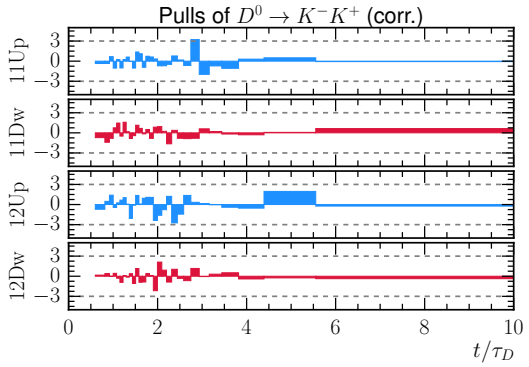

(a) $D^0 \to K^+K^-$.

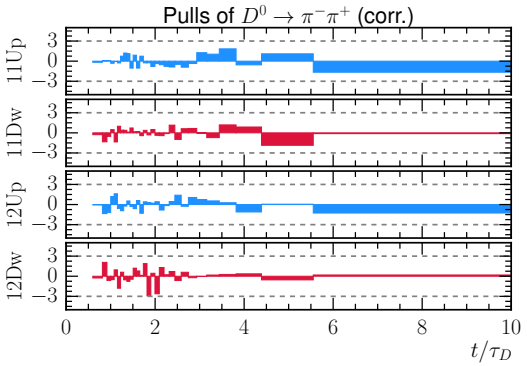

(b) $D^0 \to \pi^+\pi^-$.

Figure 6.3 – Normalised residual distribution for A_Γ fits in $D^0 \to K^+K^-$ and $D^0 \to \pi^+\pi^-$ decay modes, after the correction, for all the four subsamples.

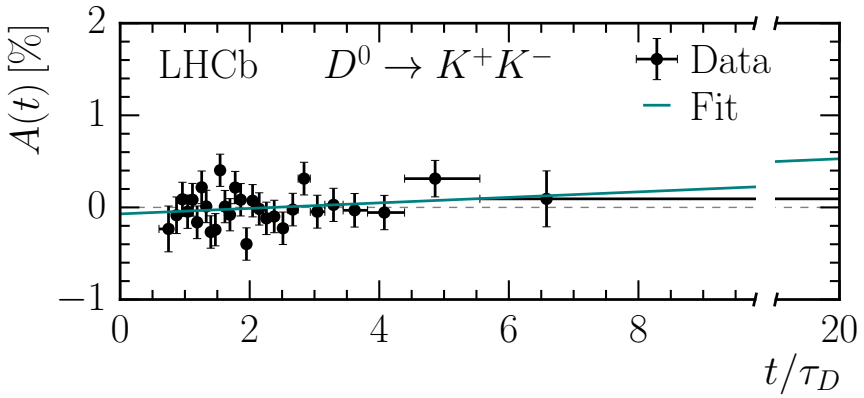

(a) A_Γ in $D^0 \to K^+K^-$ decays.

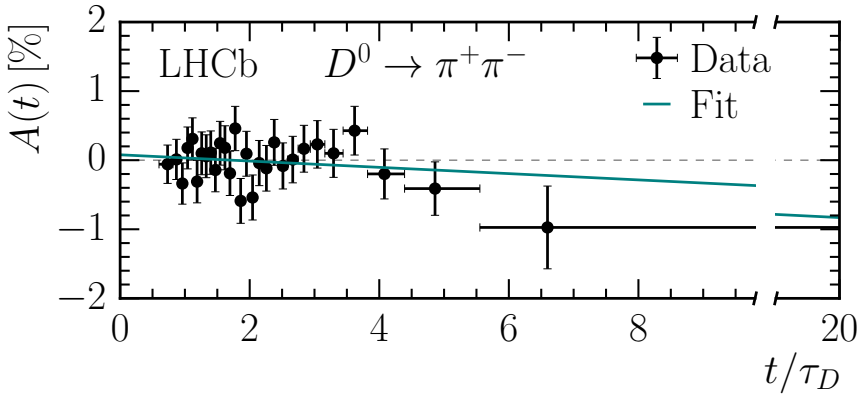

(b) A_Γ in $D^0 \to \pi^+\pi^-$ decays.

Figure 6.4 – Corrected weighted average asymmetry over the four subsamples as function of the D^0 decay time for (a) $D^0 \to K^+K^-$ and (b) $D^0 \to \pi^+\pi^-$ decay modes. The solid green line represent the best fit.

6.3 Robustness cross-checks

Several checks have been performed, as done for the $D^0 \to K^-\pi^+$ decay mode. The value of A_Γ in $D^0 \to K^+K^-$ and $D^0 \to \pi^+\pi^-$ decay modes is measured as a function of the following variables: $p(D^0)$, $p_T(D^0)$, $|p_x(D^0)|$, $\eta(D^0)$ and nPV, in order to verify the robustness and the reliability of the analysis procedure. The range of the chosen bins for each variable is the same used for the measurement of $A_\Gamma^{K\pi}$ (see tab. 5.3), and are reported in tab. 6.2 for convenience. Figures 6.5 and 6.6 show A_Γ^{KK} values returned from the fits in the different bins for each of the chosen observable, while figures 6.7 and 6.8 show the same values for $A_\Gamma^{\pi\pi}$. It can be seen from these results that after the symmetrisation correction, the values of A_Γ are in agreement with the hypothesis of no dependence among several observables. Although an incompatibility with a constant survives after the correction in transverse momentum of the D^0 meson for the $D^0 \to \pi^+\pi^-$ decay sample (see fig. 6.7), it cannot be excluded to be just a statistical fluctuation. Indeed, this A_Γ dependence over the transverse momentum of the D^0 meson is not observed in the $D^0 \to K^+K^-$ and $D^0 \to K^-\pi^+$ decay modes after the correction, which has a statistics about a factor 3 and 30 larger than the $D^0 \to \pi^+\pi^-$ decay (see tab. 4.4), respectively.

Table 6.2 – Bins definition for each variable reported.

variable	bin 1	bin 2	bin 3	unit
$p(D^0)$	$[0, 50]$	$]50, 75]$	$[75, \infty[$	GeV/c
$p_T(D^0)$	$[0, 5]$	$]5, 7]$	$[7, \infty[$	GeV/c
$\lvert p_x(D^0)\rvert$	$[0, 2]$	$]2, 4]$	$[4, \infty[$	GeV/c
$\eta(D^0)$	$[2, 3.1]$	$]3.1, 3.6]$	$[3.6, 5]$	-
nPV	1	2	$[3, \infty[$	-

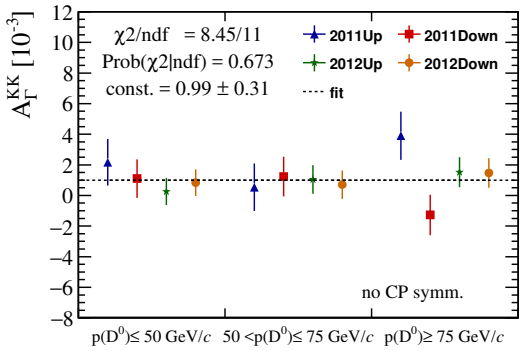

(a) A_Γ^{KK} vs. p (D^0) before the correction.

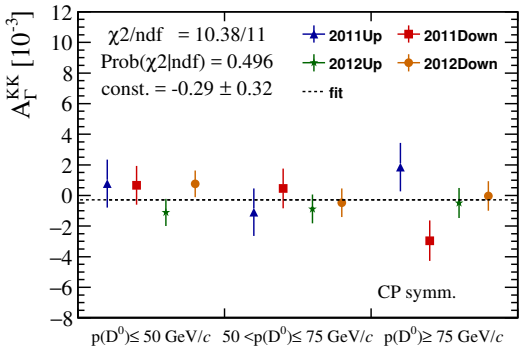

(b) A_Γ^{KK} vs. p (D^0) after the correction.

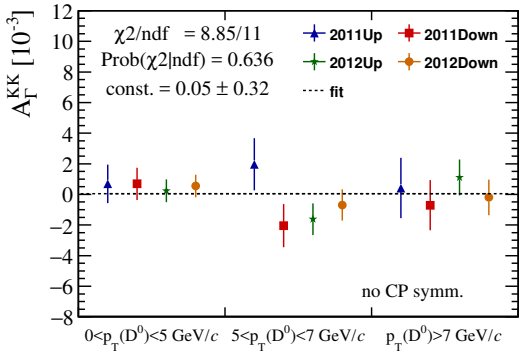

(c) A_Γ^{KK} vs. p_{T} (D^0) before the correction.

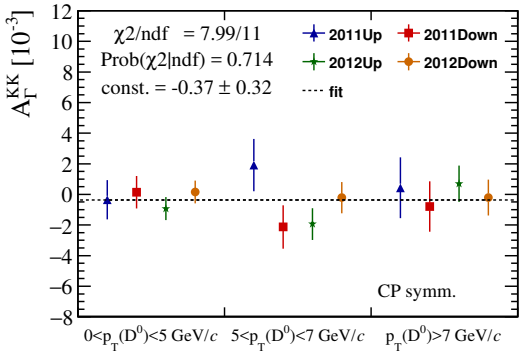

(d) A_Γ^{KK} vs. p_{T} (D^0) after the correction.

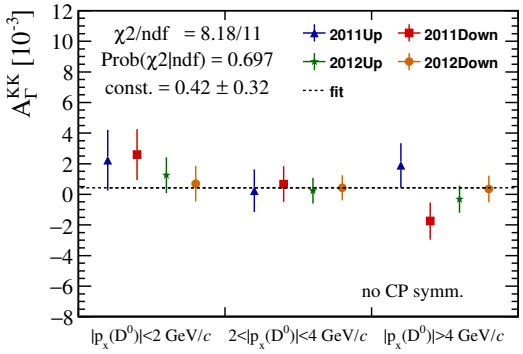

(e) A_Γ^{KK} vs. $p_x(D^0)$ before the correction.

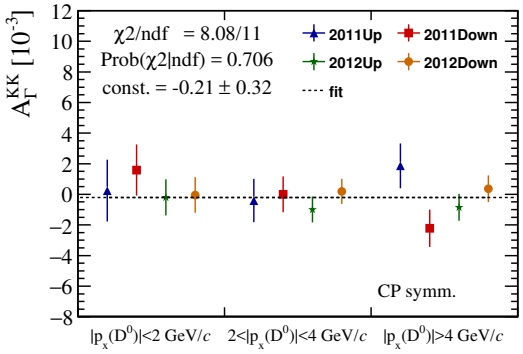

(f) A_Γ^{KK} vs. $p_x(D^0)$ after the correction.

Figure 6.5 – Measured A_Γ in $D^0 \to K^+K^-$ decays (A_Γ^{KK}) as a function of p, p_{T} and p_x of the D^0 meson, before (left) and after (right) the correction.

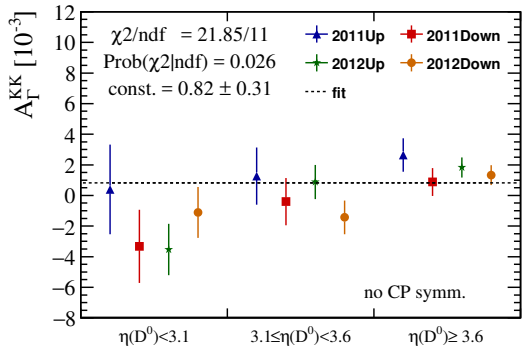

(a) A_Γ^{KK} vs. $\eta(D^0)$ before the correction.

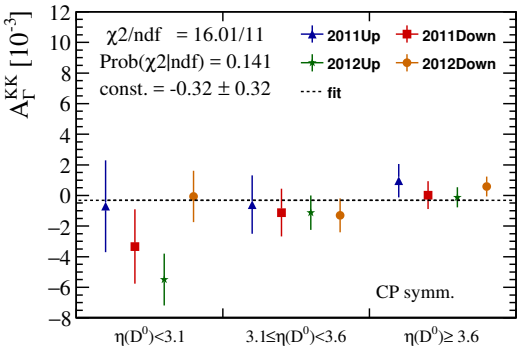

(b) A_Γ^{KK} vs. $\eta(D^0)$ after the correction.

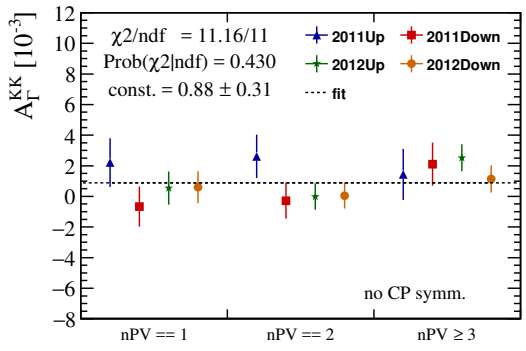

(c) A_Γ^{KK} vs. nPV before the correction.

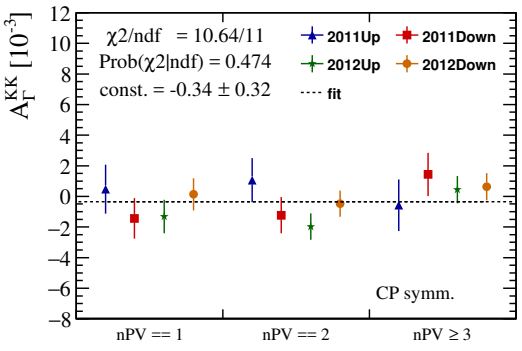

(d) A_Γ^{KK} vs. nPV after the correction.

Figure 6.6 – Measured A_Γ in $D^0 \to K^+K^-$ decays (A_Γ^{KK}) as a function of η of the D^0 meson and the number of primary vertex, nPV, before (left) and after (right) the correction.

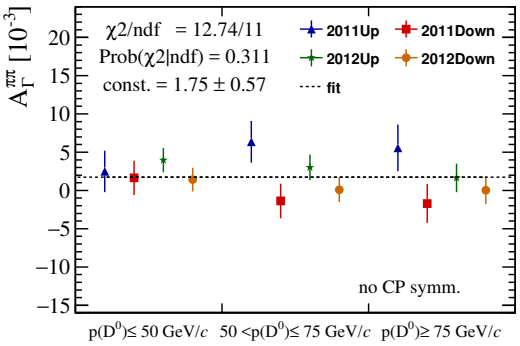

(a) $A_\Gamma^{\pi\pi}$ vs. p (D^0) before the correction.

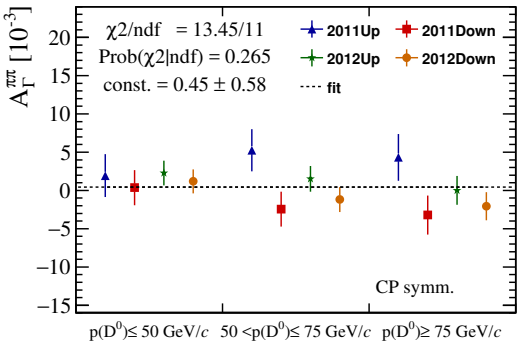

(b) $A_\Gamma^{\pi\pi}$ vs. p (D^0) after the correction.

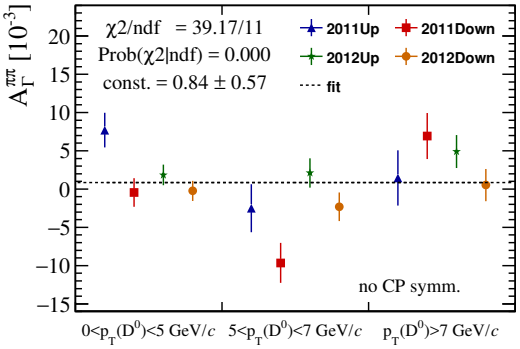

(c) $A_\Gamma^{\pi\pi}$ vs. p_{T} (D^0) before the correction.

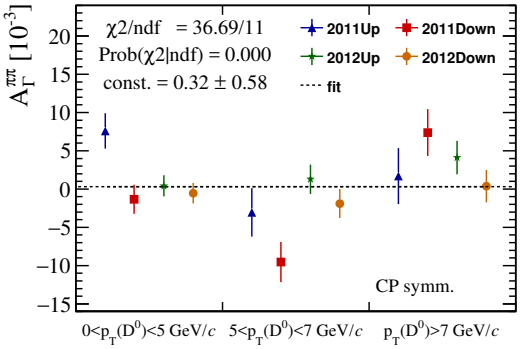

(d) $A_\Gamma^{\pi\pi}$ vs. p (D^0) after the correction.

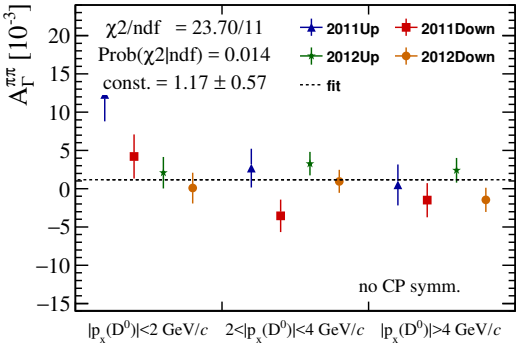

(e) $A_\Gamma^{\pi\pi}$ vs. $p_x(D^0)$ before the correction.

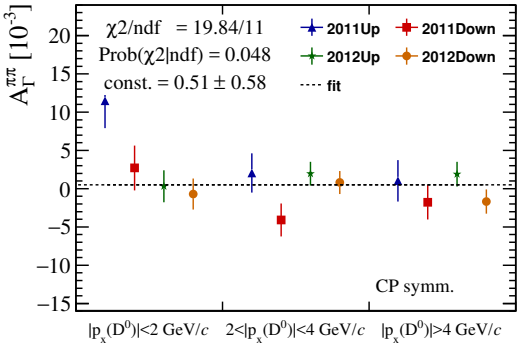

(f) $A_\Gamma^{\pi\pi}$ vs. $p_x(D^0)$ after the correction.

Figure 6.7 – Measured A_Γ in $D^0 \to \pi^+\pi^-$ decays ($A_\Gamma^{\pi\pi}$) as a function of p, p_{T} and p_x of the D^0 meson, before (left) and after (right) the correction.

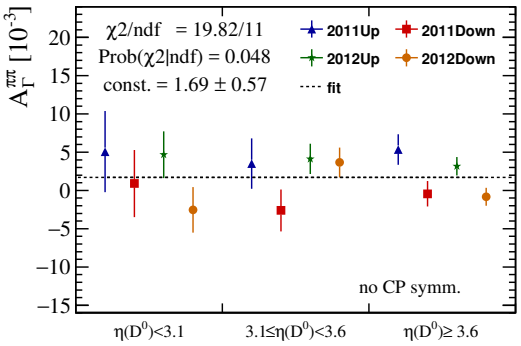

(a) $A_\Gamma^{\pi\pi}$ vs. $\eta(D^0)$ before the correction.

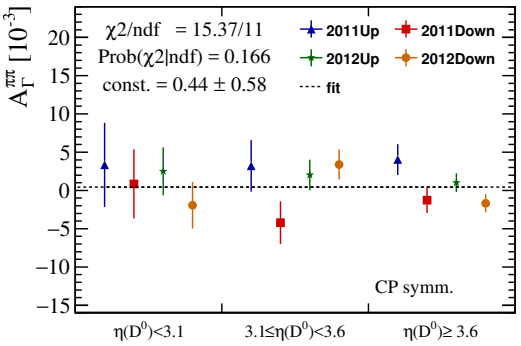

(b) $A_\Gamma^{\pi\pi}$ vs. $\eta(D^0)$ after the correction.

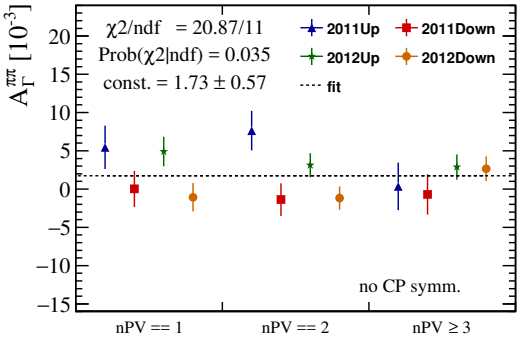

(c) $A_\Gamma^{\pi\pi}$ vs. nPV before the correction.

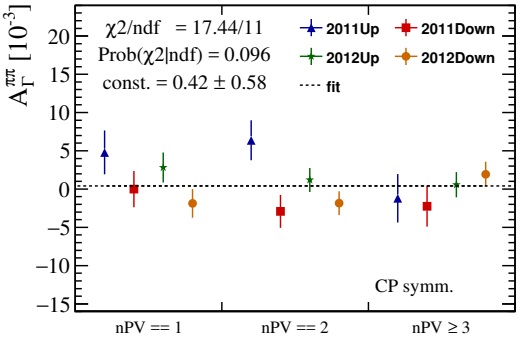

(d) $A_\Gamma^{\pi\pi}$ vs. nPV after the correction.

Figure 6.8 – Measured A_Γ in $D^0 \to \pi^+\pi^-$ decays ($A_\Gamma^{\pi\pi}$) as a function of η of the D^0 meson and the number of primary vertex, nPV, before (left) and after (right) the correction.

6.4 Analysis validation

To further validate the analysis procedure, 10^3 "pseudo-experiments" are generated from the data itself. These samples are generated resetting any possible existing *CP* asymmetry by artificially reassigning a random charge to the soft pion, as explained in sec. 4.7. Then, these samples are reprocessed using exactly the same code machinery used to perform the main measurement. This is done for all four subsamples $(2011, 2012) \times (MagUp, MagDown)$, and then the average is calculated, exactly as in the real measurements. Figure 6.9 shows the normalised residuals (defines as the difference between the true value of A_Γ and the reconstructed one divided for its statistical uncertainty) obtained for the $D^0 \to K^+K^-$ and $D^0 \to \pi^+\pi^-$ decay modes. The results exhibit means compatible with zero at a level of precision of 3.2% and standard deviations compatible with the unit at a level of precision of 2.3%, thus confirming the reliability of our analysis procedure and associated statistical uncertainties.

In addition, five different values of artificial A_Γ are generated in order to check the linearity of the analysis procedure. This test is done with charge-randomised sample (see sec. 4.7) from $D^0 \to K^+K^-$ decays. The results are reported in fig. 6.10, and as it can be seen the measurement accurately tracks the input value of A_Γ.

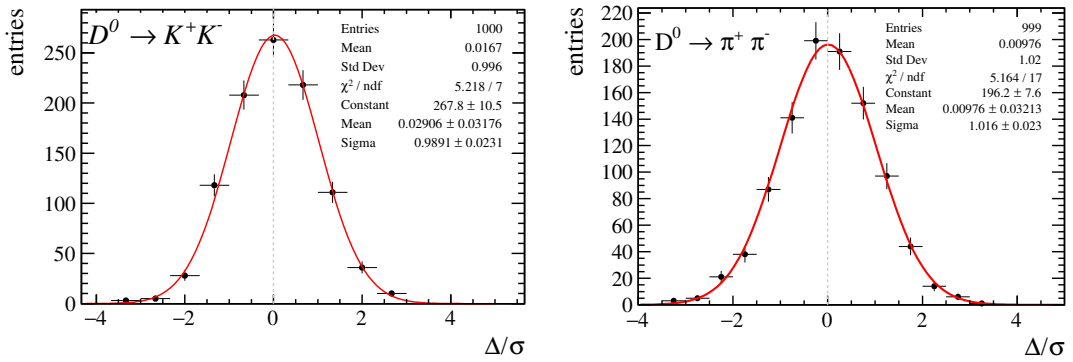

(a) $D^0 \to K^+K^-$. **(b)** $D^0 \to \pi^+\pi^-$.

Figure 6.9 – Normalised residuals for A_Γ in $D^0 \to K^+K^-$ and $D^0 \to \pi^+\pi^-$ decay modes obtained in toys based on random soft pion charge assignment after the correction procedure (see text for details).

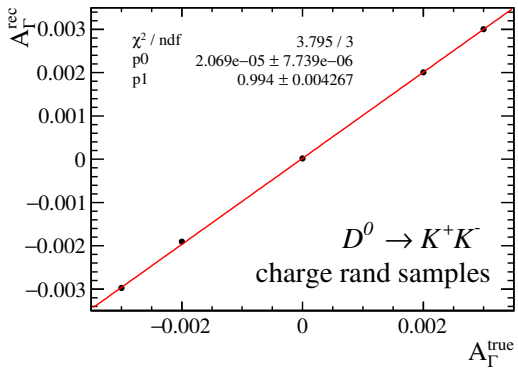

Figure 6.10 – Measured A_Γ as function of the true A_Γ, using charge-randomised samples of $D^0 \to K^+K^-$ decay mode.

7 Systematic uncertainty on secondary decays

Contribution of secondary decays to the measured A_Γ has been neglected so far, although a residual contamination persists in the final data sample. This chapter is devoted to an accurate study of such a contamination, and a systematic uncertainty is assessed to cover any possible bias on A_Γ.

7.1 Introduction

A contamination of charm mesons produced in b-hadron decays (secondary decays) in the final sample may introduce time-dependent dangerous biases that may affect the measurement of A_Γ. The reconstructed decay-time of the D^0 mesons candidates is systematically larger than their genuine decay time, being calculated with respect to the primary vertex, which does not coincide with the D^0 production vertex, as schematically shown in fig. 7.1. Even if the contamination from secondary decays in the final data sample is reduced to a few percent level, thanks to the the requirement on the impact parameter χ^2_{IP} of the D^0 candidate (see chap. 4), its impact on the A_Γ measurement must be accurately quantified.

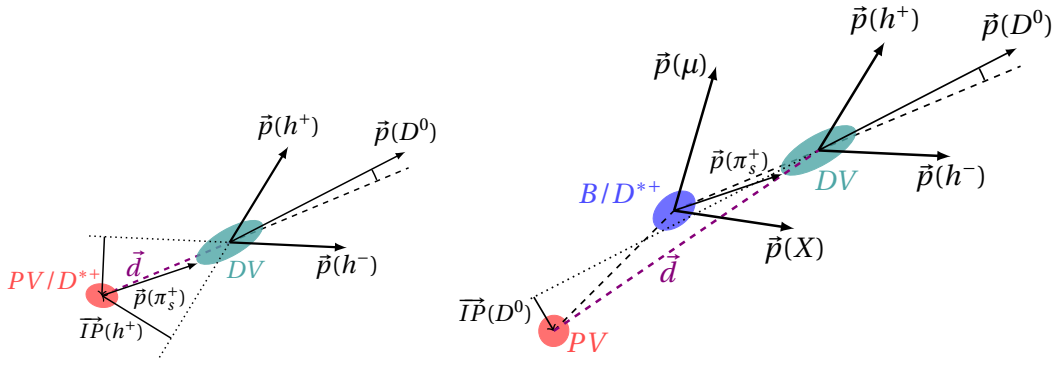

Figure 7.1 – Simple sketch of a prompt D^* decay (left) and a secondary D^* decay (right), not drawn to scale.

The reconstructed D^0 proper decay time is defined as

$$t(D^0) = \frac{|\vec{d}|}{\gamma\beta c} = |\vec{d}|\frac{m_{D^0}}{p_{D^0}},$$

where $|\vec{d}|$ is the reconstructed spatial distance between the D^0 decay vertex and the primary vertex of the collision, and $\gamma\beta = p_{D^0}/m_{D^0}c$ is the reconstructed Lorentz boost of the D^0 meson. m_{D^0} and p_{D^0} are the invariant mass and the momentum of the D^0 meson, respectively. In the case of a secondary decay the distance $|\vec{d}|$ does not correspond to the true distance travelled by the D^0 meson, since the D^* does not decay immediately in the PV, as can be seen in fig. 7.1. Hence, for secondary decays the D^0 proper decay time is biased to higher values, and the contribution of secondary decays to the measured raw asymmetry can be easily written as

$$A_{\text{raw}}(t) = (1 - f_{\text{sec}}(t))A_{\text{ppt}}(t) + f_{\text{sec}}(t)A_{\text{sec}}(t), \tag{7.1}$$

where A_{ppt} and A_{sec} are the raw asymmetry for the prompt and secondary component, respectively, equal to

$$A_{\text{ppt}}(t) = \frac{N^+_{\text{ppt}}(t) - N^-_{\text{ppt}}(t)}{N^+_{\text{ppt}}(t) + N^-_{\text{ppt}}(t)},$$
$$A_{\text{sec}}(t) = \frac{N^+_{\text{sec}}(t) - N^-_{\text{sec}}(t)}{N^+_{\text{sec}}(t) + N^-_{\text{sec}}(t)}.$$

The fraction of secondary decays in the sample is $f_{\text{sec}}(t) = N_{\text{sec}}(t)/(N_{\text{sec}}(t) + N_{\text{ppt}}(t))$, where $N_{\text{sec}}(t) = N^+_{\text{sec}}(t) + N^-_{\text{sec}}(t)$ and $N_{\text{ppt}}(t) = N^+_{\text{ppt}}(t) + N^-_{\text{ppt}}(t)$ are the total number of reconstructed prompt and secondary decays, respectively. In order to measure the asymmetry of prompt component, A_{ppt}, the contribution of secondary decays must be accurately accounted for.

A rough estimation of the fraction of secondary decays can be easily extracted using the available information from past LHCb measurements on the same data sample [8, 59]. $f_{\text{sec}}(t)$ can be considered, as a good approximation, to increase almost linearly with decay time from about 0.0% at $t/\tau_{D^0} = 0$, up to about 14% at decay time equal to $t/\tau_{D^0} = 10$. The production asymmetry of B mesons has been measured to be about $\mathcal{O}(1\%)$ [60], and can be safely assumed to be time-independent and the dominant contribution of A_{sec}. Thus, a rough estimate of the bias on A_Γ, due to the presence of such a contamination is about 10^{-4}. Since the statistical uncertainties on A_Γ^{KK} and $A_\Gamma^{\pi\pi}$ are larger than 10^{-4}, secondary contribution is thus not subtracted but a systematic uncertainty is associated to such a choice.

7.2 Model of secondary decays

The fraction of secondary decays can be calculated with a good level of approximation just using a simple analytical approach, with some reasonable assumptions

- the $B \to D^* X \to [D^0\pi]_{D^*} X$ decay occurs in one spatial dimension, the z-direction (b-

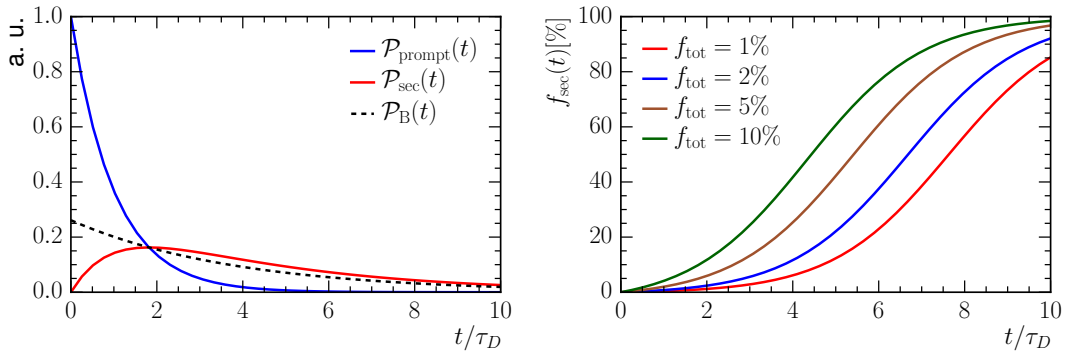

(a) PDF of prompt and secondary decays.

(b) $f_{\text{sec}}(t)$.

Figure 7.2 – Secondary PDF (a) and the relative fraction (b) as function of D^0 proper decay time assuming that secondary decays happens in one spatial dimension.

hadrons decays have a large boost in the z-direction);

- same acceptance function on proper decay time both for prompt and secondary decays.

The first assumption is motivated by the LHCb geometry. In fact, b-hadrons decays are reconstructed only at very high values of pseudo-rapidity, and consequently they have a large boost. The second assumption, instead, comes from the fact that secondary decays are similar to prompt decays at lower values of decay time. For a detailed discussion on the accuracy of these assumptions see app. F and sec. 7.5, where all possible systematic effects on the procedure are studied and quantified.

The PDF of prompt decays is a simple exponential function with a coefficient equal to the measured D^0 lifetime $\tau_{D^0} \approx 0.41\,\text{ps}$ [20]

$$\mathscr{P}_{\text{ppt}}(t) = \mathscr{P}_{D^0}(t) = \frac{1}{\tau_{D^0}} \exp\left[-\frac{t}{\tau_{D^0}}\right] \quad (t \geq 0).$$

For secondary decays, under the assumptions listed above, the total PDF of a D^0 decay coming from a b-hadron decay can be written as the convolution of the PDF of the B decay and the PDF of the D^0 decay

$$\begin{aligned}\mathscr{P}_{\text{sec}}(t) &= \left(\mathscr{P}_B * \mathscr{P}_{D^0}\right)(t) = \\ &= \int_0^t \frac{1}{\tau_B} \exp\left[-\frac{t-t'}{\tau_B}\right] \cdot \frac{1}{\tau_{D^0}} \exp\left[-\frac{t'}{\tau_{D^0}}\right] \mathrm{d}t' \\ &= \frac{\exp\left[-\frac{t}{\tau_B}\right] - \exp\left[-\frac{t}{\tau_{D^0}}\right]}{\tau_B - \tau_{D^0}} \quad (t \geq 0);\end{aligned}$$

where $\tau_B \approx 1.57\,\text{ps}$ [20] is the measured average lifetime of the mixture of b-hadrons produced in the pp collisions. The PDF for prompt and secondary decays are reported in fig. 7.2a. The

fraction of secondary decays as a function of the D^0 proper decay time can be written as

$$f_{\text{sec}}(t) = \frac{n_{\text{sec}} \cdot A(t)\mathscr{P}_{\text{sec}}(t)}{n_{\text{ppt}} \cdot A(t)\mathscr{P}_{\text{ppt}}(t) + n_{\text{sec}} \cdot A(t)\mathscr{P}_{\text{sec}}(t)} \tag{7.2}$$

where n_{sec} is the total number of secondary decays and n_{ppt} the total number of prompt decays. A is the total acceptance function in reconstructing a D^* decay, assumed to be the same for prompt and secondary decays. The fraction of secondary decays is plotted in in fig. 7.2b for different values of the total fraction of secondary decays $f_{\text{tot}} = n_{\text{sec}}/(n_{\text{sec}} + n_{\text{ppt}}) = 1\%, 2\%, 5\%, 10\%$.

7.3 Evaluation of secondary fraction f_{sec}

In order to estimate with a good level of approximation the behaviour of f_{sec} as a function of the decay time of the D^0 meson both data and the analytical model described above are used. The main challenge to extract f_{sec} is the level of knowledge of the sculpting caused by the selection requirements on the decay time distribution $\mathscr{P}_{\text{sec}}(t)$ of the secondary decays. This sculpting is mainly driven by the requirement on the χ^2_{IP} of the D^0 meson, necessary to suppress the contamination of secondary decays, see chap. 4. Its impact cannot be assessed relying on the full realistic LHCb simulation since the available statistics is not sufficient by large to achieve the desired level of precision. Furthermore, even without any statistical limitation, it is very hard to only rely on the MC for reproducing with the sufficient level of precision such effects.

However, it can be safely assumed that the effect of requiring $\chi^2_{\text{IP}}(D^0) < 9$ increases as a function of the the decay time, thus $f_{\text{sec}}(t)$ tends to be equal to the secondary fraction that one would obtain without applying any requirement on $\chi^2_{\text{IP}}(D^0)$ going towards lower time values. From the other side the distribution of the proper decay time at lower time values ($t < 2\tau_{D^0}$) is namely sculpted by the requirements on the χ^2_{IP} and on the momenta of the D^0 decay products, however the total acceptance function can be approximately extracted from data by looking at the ratio between the proper decay time distribution and a pure exponential function with the D^0 lifetime as a slope (see fig. 7.3). As said above, the acceptance is assumed to be the same for prompt and secondary components. Using the simple analytical model described in sec. 7.2 and the acceptance function of fig. 7.3 the PDF $\mathscr{P}_{\text{sec}}(t)$ for secondary decays can be analytically written.

The absolute normalisation of secondary PDF can be measured by data itself by fitting a distribution where prompt and secondary decays can be distinguished, as the $\chi^2_{\text{IP}}(D^0)$ distribution. In order to fit this, the model of prompt component is extracted from the first bin of the proper decay time distribution and it is fixed in the fit of other time bins. In particular, the fit is performed only for the last four bins (higher decay time), where the measurement of f_{sec} is much more reliable, being the relative fraction of secondary decays large and the two separate peaks are clearly visible. The fit projections are reported in fig. 7.4. While the quality of the fits

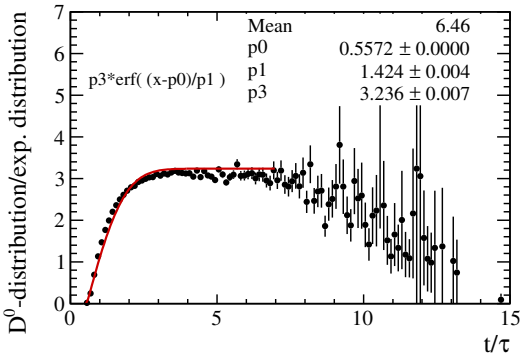

Figure 7.3 – Selection acceptance relative to a pure exponential distribution.

is not excellent, it is totally satisfactory for the purpose of assessing a systematic uncertainty.

Using the analytical function $\mathscr{P}_{sec}(t)$, along with the absolute normalisation extracted as described above, the absolute number of secondary decays $N_{sec}(t)$ as a function of the decay time can be extracted without any requirement on the $\chi^2_{IP}(D^0)$ variable, being the analytical model very reliable in absence of sculpting of the distribution at higher time values. At this point, by making the difference (bin by bin) with the observed total decay time distribution, the number of prompt decay $N_{ppt}(t)$ as a function of time can be easily extracted, for obtaining f_{sec}. This is shown by blue triangles in fig. 7.5 where the last four bins are extracted directly from data without any input from the analytical model.

For the final measurement, however, the fraction of secondary decays requiring $\chi^2_{IP}(D^0) < 9$ is needed. For the last four bins of the decay time distribution the fits to data (see fig. 7.4) directly provide the prompt and secondary contribution, interpolating over the range $\log(\chi^2_{IP}(D^0)) < \log(9) \simeq 2.2$, and the results are reported in fig. 7.5 with black dots. Since at lower time the effect of the sculpting of the requirement on the $\chi^2_{IP}(D^0)$ tends to disappear, $f_{sec}(t)$ is empirically approximated as the function (red dashed line) intersecting the black dots at higher proper decay time and the blue triangles at lower proper decay time. This represents with a good approximation the fraction of secondary decays when the requirement $\chi^2_{IP}(D^0) < 9$ is applied.

7.4 Evaluation of A_{sec}

In order to asses the systematic uncertainty on A_Γ using eq. (7.1) $A_{sec}(t)$ needs to be estimated. This is extracted by data itself, by inverting the cut on $\chi^2_{IP}(D^0)$, requiring $\log(\chi^2_{IP}(D^0)) > 4$, in order to have a pure sample of secondary decays, without any contamination of prompt decays. $A_{sec}(t)$ is fit to a constant, see fig. 7.6, and results are reported on tab. 7.1 for the different subsamples. The fact that $A_{sec}(t)$ may receive a small time dependent contribution from A_Γ^{KK} and $A_\Gamma^{\pi\pi}$ is discussed in the next section.

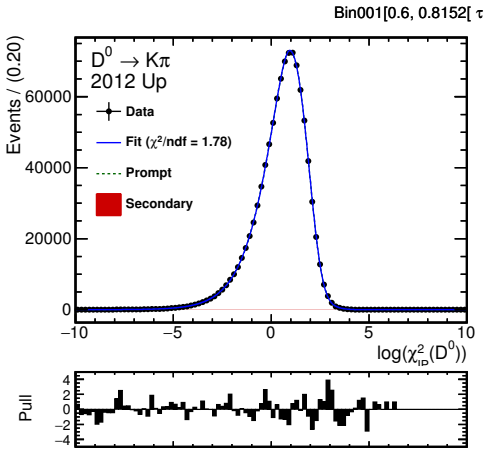

(a) Bin 1: $t/\tau_D \in [0.6, 0.81[$

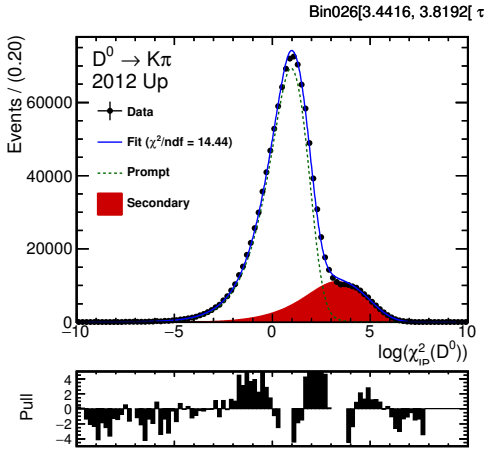

(b) Bin 26: $t/\tau_D \in [3.44, 3.82[$

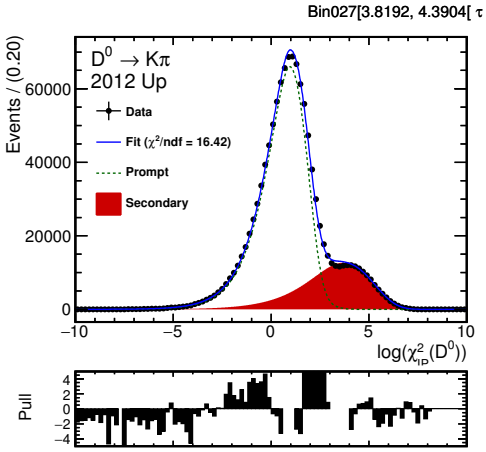

(c) Bin 27: $t/\tau_D \in [3.82, 4.39[$

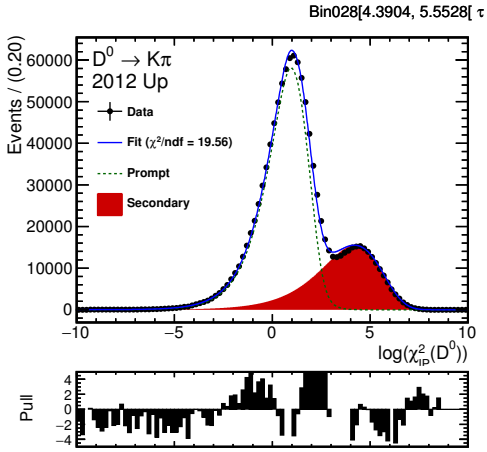

(d) Bin 28: $t/\tau_D \in [4.39, 5.55[$

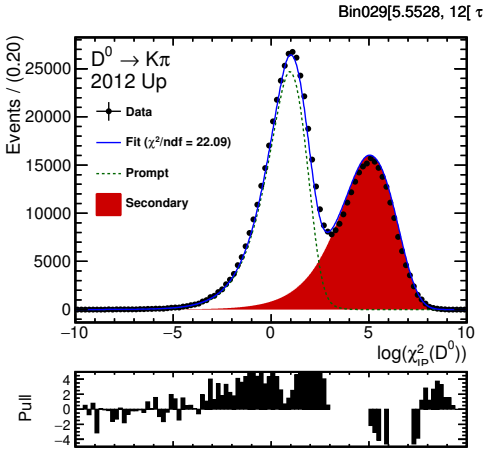

(e) Bin 29: $t/\tau_D \in [5.55, 20[$

Figure 7.4 – Projections of $\chi^2_{\rm IP}(D^0)$ distribution fits in different bins of the D^0 meson decay time to extract the normalisation factor. The model of prompt decays is extracted from the first bin of the decay time reported in (a).

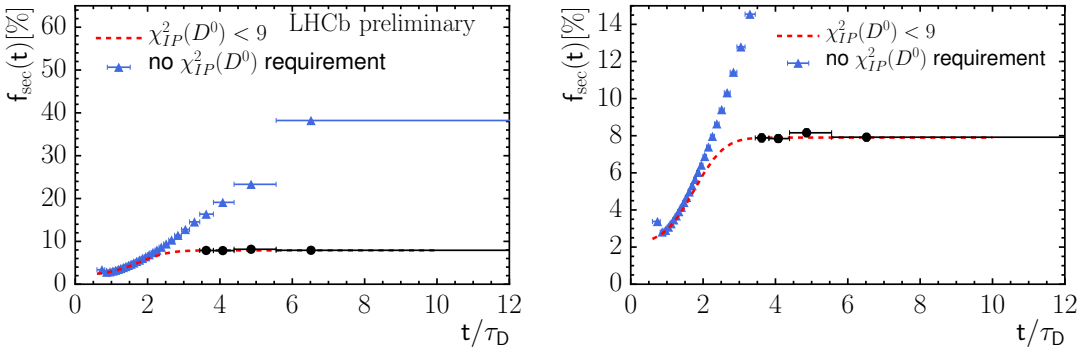

Figure 7.5 – Secondary fraction $f_{\rm sec}(t)$. Zoom on y-axis is shown on the right.

Table 7.1 – Fit results of $A_{\rm sec}(t)$ to a constant.

sample	const $[10^{-3}]$
2011 *MagUp*	5.60 ± 2.12
2011 *MagDown*	3.15 ± 1.77
2012 *MagUp*	5.87 ± 1.28
2012 *MagDown*	4.32 ± 1.26
weighted average	4.80 ± 0.75

7.5 Systematic uncertainty and robustness checks

In order to quantify the effect of secondary decays on the A_Γ measurement in each time bin t_i, $A_{\rm ppt}(t_i)$ is evaluated by inverting eq. (7.1), as follows

$$A_{\rm ppt}(t_i) = \frac{1}{1 - f_{\rm sec}(t_i)} (A_{\rm raw}(t_i) - f_{\rm sec}(t_i) A_{\rm sec}(t_i)).$$

The difference between the slopes resulting from the fit of $A_{\rm raw}(t_i)$ and $A_{\rm ppt}(t_i)$ values is named Δ, and it is separately measured for the $D^0 \to \pi^+\pi^-$, $D^0 \to K^+K^-$ and $D^0 \to K^-\pi^+$ decay modes. While $A_{\rm raw}(t_i)$ values are the measured asymmetries in each time bin, and are separately taken for each decay mode to estimate the correction Δ, $A_{\rm sec}(t_i)$ and $f_{\rm sec}(t_i)$ are evaluated using the analytical functions $A_{\rm sec}(t)$ and $f_{\rm sec}(t)$ extracted from the high statistics $D^0 \to K^-\pi^+$ mode, as described in sec. 7.3 and sec. 7.4. No appreciable differences are expected for $f_{\rm sec}(t)$ in the three different data samples, and therefore it can be safely assumed to be the same. As far as $A_{\rm sec}$, the only difference may come from a possible time dependent contribution from the measured A_Γ, however it has been verified that such an effect is negligible because of the dilution due to the larger time values of secondary decays with respect to prompt decays. Figure 7.7 shows the slopes of $A_{\rm ppt}(t)$ and $A_{\rm sec}(t)$ when an A_Γ equal to 1σ of the statistical uncertainty of A_Γ^{KK} and $A_\Gamma^{\pi\pi}$ is injected.

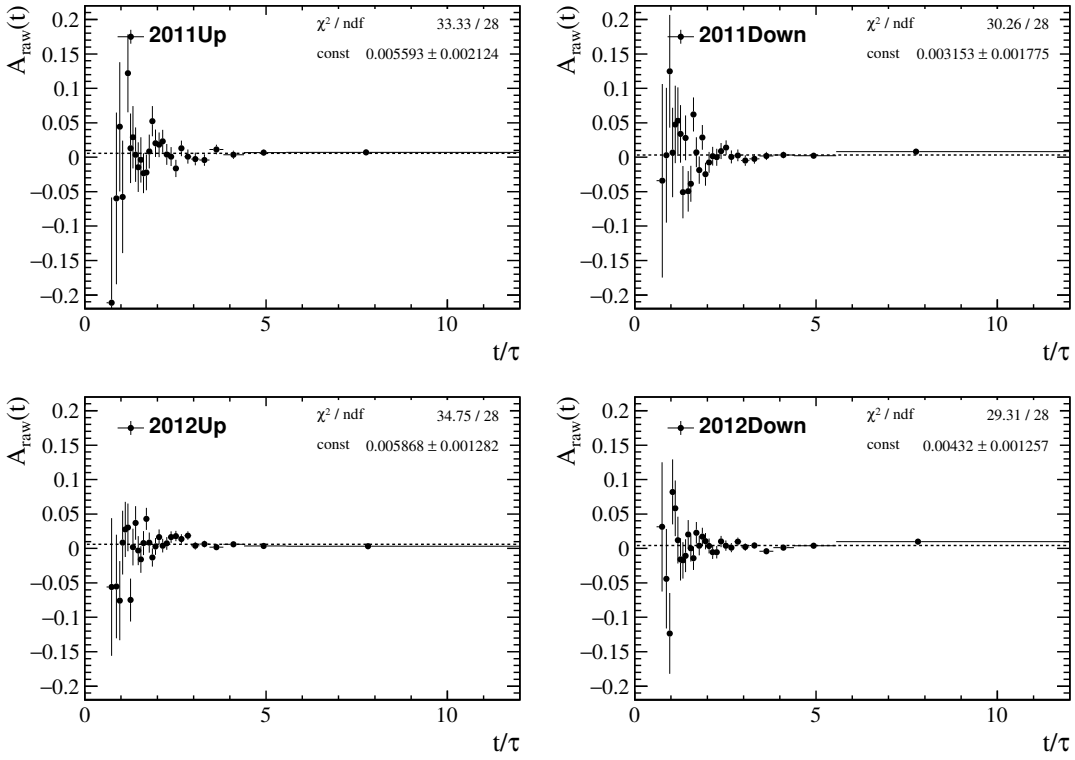

Figure 7.6 – $A_{\text{sec}}(t)$ for all the four subsamples, in the $D^0 \to K^-\pi^+$ mode.

To keep into account the effect due to a time dependent contribution of the measured A_Γ through the $A_{\text{raw}}(t_i)$ values, the extraction of Δ is repeated on 1000 pseudo-experiments, that are generated by randomly varying $A_{\text{raw}}(t_i)$ within their Gaussian statistical uncertainties. For each pseudo-experiment $A_{\text{raw}}(t_i)$ and $A_{\text{ppt}}(t_i)$ are fitted to a straight line and the distribution of the difference Δ between the two slopes is plotted. Results are reported in fig. 7.8 where the fit to a Gaussian is overlaid, while tab. 7.2 summarises the values returned from the fit, of each data sample, for the mean (Δ) and its uncertainty sigma (σ_{A_Γ}).

The impact on Δ of the uncertainty on A_{sec} and $f_{\text{sec}}(t)$ are also studied. If A_{sec} is varied within $\pm 1\sigma$ of its statistical uncertainty a variation on Δ of $\sigma_{A_{\text{sec}}} = 0.012 \times 10^{-3}$ is found, the same for all data samples. Different empirical models for $f_{\text{sec}}(t)$ are studied, as shown in fig. 7.9.

Table 7.2 – Δ results from pseudo-experiments in unit of 10^{-3}.

sample	Δ	σ_{A_Γ}	$\sigma_{A_{\text{sec}}}$	$\sigma_{f_{\text{sec}}}$	$\sqrt{\Delta^2 + \sigma^2_{A_\Gamma} + \sigma^2_{A_{\text{sec}}} + \sigma^2_{f_{\text{sec}}}}$
$D^0 \to K^-\pi^+$	0.094	0.008	0.012	0.035	0.101
$D^0 \to K^+K^-$	0.065	0.022	0.012	0.041	0.081
$D^0 \to \pi^+\pi^-$	0.113	0.041	0.012	0.026	0.123

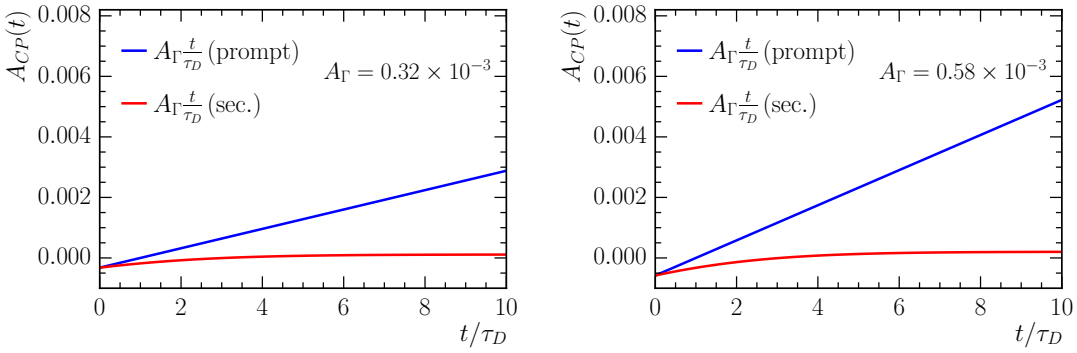

(a) $D^0 \to K^+K^-$.

(b) $D^0 \to \pi^+\pi^-$.

Figure 7.7 – $A_{\text{ppt}}(t)$ and $A_{\text{sec}}(t)$ when an A_Γ equal to 1σ of the statistical uncertainty of (left) A_Γ^{KK} and (right) $A_\Gamma^{\pi\pi}$ is injected.

The maximum variation of Δ is equal to $\sigma_{f_{\text{sec}}} = (0.035, 0.041, 0.026) \times 10^{-3}$ for the ($D^0 \to K^-\pi^+$, $D^0 \to K^+K^-$, $D^0 \to \pi^+\pi^-$), respectively. They correspond to the same black-dashed curve reported in fig. 7.9, that has to be compared with the red-dashed curve corresponding to our nominal and best estimate of $f_{\text{sec}}(t)$. The obtained values for $\sigma_{f_{\text{sec}}}$, reported in tab. 7.2, are smaller than the values obtained for the correction Δ, despite the wild variations covered by the used empirical models for f_{sec}. Possible differences in the acceptance function between prompt and secondary decays (assumed to be the same for extracting $f_{\text{sec}}(t)$) result, therefore, well covered by the range spanned by this test, being much smaller (see app. F).

In conclusions a conservative systematic uncertainty on the presence of a residual contamination of secondary decays is assessed, for $D^0 \to K^+K^-$ and $D^0 \to \pi^+\pi^-$, equal to the sum in quadrature

$$\Delta A_\Gamma = \sqrt{\Delta^2 + \sigma^2_{A_\Gamma} + \sigma^2_{A_{\text{sec}}} + \sigma^2_{f_{\text{sec}}}}$$

obtaining a total uncertainty for $D^0 \to K^+K^-$ and the $D^0 \to \pi^+\pi^-$

$$\Delta A_\Gamma^{KK} = 0.08 \times 10^{-3},$$
$$\Delta A_\Gamma^{\pi\pi} = 0.12 \times 10^{-3}.$$

These correspond to the total effect of not subtracting at all such a background from the final data sample and, as expected, they come out to be much smaller than the current statistical uncertainty both for the $D^0 \to K^+K^-$ and $D^0 \to \pi^+\pi^-$.

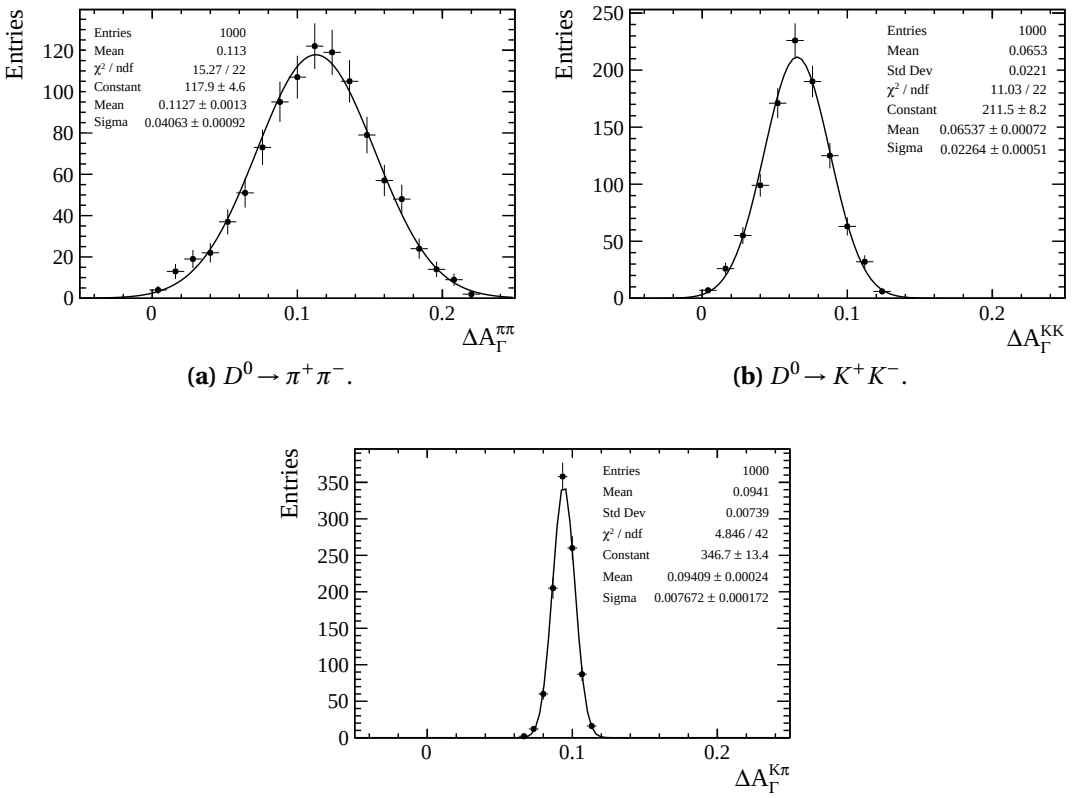

(a) $D^0 \to \pi^+\pi^-$. **(b)** $D^0 \to K^+K^-$.

(c) $D^0 \to K^-\pi^+$.

Figure 7.8 – Δ results from pseudo-experiments. Δ is expressed in 10^{-3} units.

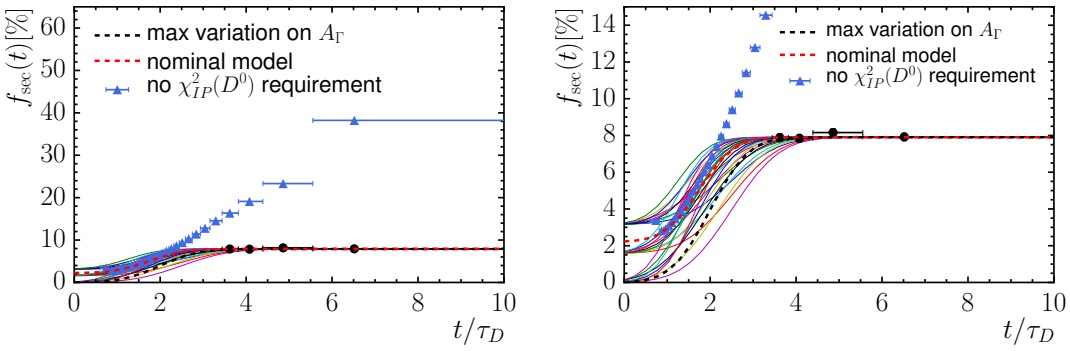

Figure 7.9 – Different empirical models for secondary fraction f_{sec} (t). Zoom on y-axis is shown on the right panel.

8 Robusteness checks and systematic uncertanties

This chapter is focussed on describing in detail the cross-checks performed to confirm the stability of the analysis and the residual systematic effects that may impact the A_Γ measurement. It turned out that all studied systematic effects are significantly smaller than the statistical uncertainties.

8.1 Discretisation of the correction procedure

The choice of the binning size of the reweigh procedure to correct time dependent detection asymmetries is driven by the statistics of the less abundant $D^0 \to \pi^+\pi^-$ data sample. The size of the bins cannot be too large in order to avoid the degradation of the effect of the correction[1], while on the other hand it cannot be too fine to avoid to make statistical fluctuations too large. While the effect of statistical fluctuations due to the finite bin size is measured with randomised samples (see sec. 6.4), and is included in the quoted statistical uncertainty, the fact of approximating a continuous function, in the three-dimensional (k, θ_x, θ_y) space, with an histogram (in each bin the reweighing function is assumed to be constant) may affect the A_Γ measurement.

In order to investigate such an effect the measurement of $A_\Gamma^{K\pi}$ on the high statistics $D^0 \to K^-\pi^+$ mode is repeated varying the size of the binning scheme[2] by a factor $s = 1/8, 1/4, 1/2, 2, 4, 8$, where each space dimension is rescaled with the same factor $s^{1/3}$. Results are reported in tab. 8.1 and in fig. 8.1, where $s = 1$ obviously corresponds to the binning size of the central analysis. The behaviour of $A_\Gamma^{K\pi}$ as a function of the binning size is as expected and confirms that the binning size of the central analysis is optimal, by minimising the statistical fluctuations without degrading the correction.

Conservatively, a systematic uncertainty equal to $\Delta A_\Gamma = 0.02 \times 10^{-3}$ is assessed, which is the

[1] The limiting case of a reweighing with just one single bin would correspond to do not apply any correction, but only an equalisation of the total number of D^0 and $\overline{D}^0$ candidates.

[2] In the central analysis (50, 55, 11) bins for the (k, θ_x, θ_y) space are used, respectively. See app. E for details.

Table 8.1 – $A_\Gamma^{K\pi}$ results with different bin size of the correction reweighing.

s	1/8	1/4	1/2	1	2	4	8
$A_\Gamma^{K\pi}$ $[10^{-3}]$	0.25	0.19	0.18	0.16	0.15	0.16	0.15

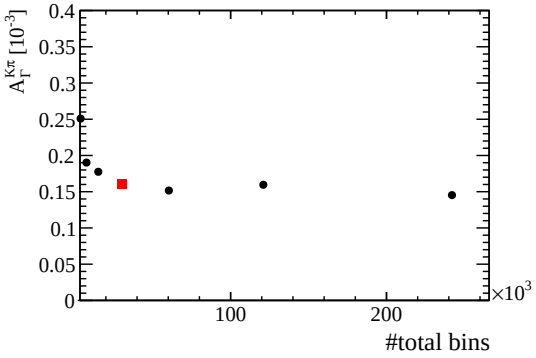

Figure 8.1 – $A_\Gamma^{K\pi}$ as a function of binning size of the correction reweighing. The red square represents the nominal binning scheme.

larger value of the difference between $A_\Gamma^{K\pi}$ obtained with factors $s = 1/2$ and $s = 2$ and the central analysis $s = 1$.

8.2 Subtraction of random pion background

The small random pion background is removed by performing a sideband subtraction based on the mass difference Δm, as described sec. 4.6. The signal region is $[144.45, 146.45]$ MeV/c^2, corresponding to about $\pm 5\sigma$ around the mean value of the peak, and the sideband is taken in the interval $[149, 154]$ MeV/c^2. The contribution of events in the sideband is subtracted by giving them a negative weight, determined by a normalisation factor given by the ratio of the total number of background events in the peak region to the number of such events in the sideband region.

As a check of the overall impact of the background subtraction on the final measurement the analysis is repeated without performing any background subtraction. The changes relative to the nominal fit are $\Delta A_\Gamma^{KK} = 0.12 \times 10^{-3}$ and $\Delta A_\Gamma^{\pi\pi} = 0.08 \times 10^{-3}$. These variations may also contain a statistical component; what is clear it that it is a small effect, and the systematic uncertainty associated to this subtraction is expected to be quite small.

The subtraction procedure relies on two things: (i) the correct determination of the normalisation factor and (ii) the assumption that the impact on A_Γ of the background events located under the peak is the same as for those found in the sideband. The effect of uncertainties on the result of the subtraction is therefore given by two contributions: one is of the order of

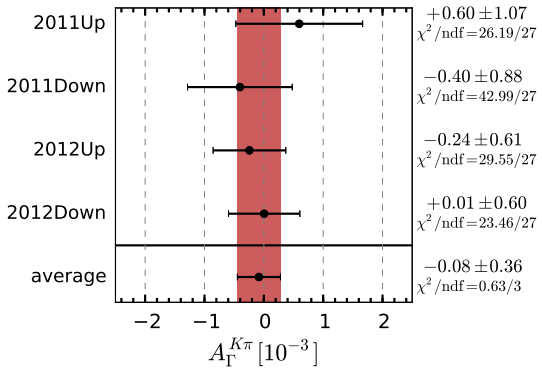

Figure 8.2 – Measurement of $A_\Gamma^{K\pi}$ in the Δm sideband.

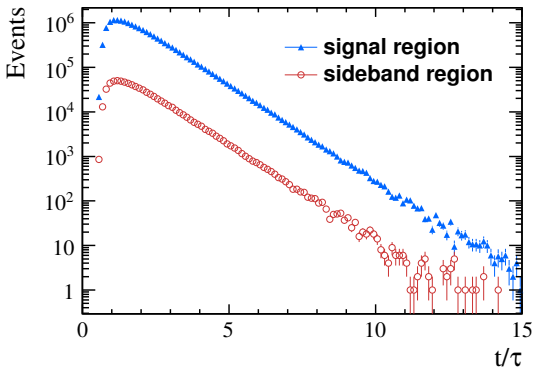

Figure 8.3 – Distribution of decay time in the Δm peak and sideband regions.

$\sigma_f \times |A_\Gamma(\text{bkg})|$, the other is about $f \times \sigma(A_\Gamma(\text{bkg}))$, where f is the background to signal ratio under the peak, and $A_\Gamma(\text{bkg})$ is the value of A_Γ for the background events. As it can be seen in fig. 8.2, the value of $A_\Gamma(\text{bkg})$ is quite small $\mathcal{O}(10^{-4})$; this, combined with the smallness of the background fraction $f \simeq 0.03$, implies that the first contribution to the uncertainty will necessarily be $\ll 10^{-6}$, and therefore completely negligible.

The second point essentially translates into requiring that the slope of the asymmetry of the events in the sideband is the same as the background events under the peak - and secondarily that the sample distribution over decay time is not too different. The latter assumption is checked in fig. 8.3 where it can be clearly seen that the distributions of decay times in the peak and sideband regions are remarkably similar to each other. This implies that in any linearly weighted combination of the two samples, the slopes of their asymmetries will linearly combine. Finally, in order to test the reliability of the chosen sideband in reproducing the distribution of background events under the peak, additional studies are performed taking 3 different sidebands, one to the left and two to the right of the signal peak (covering a region similar to the one chosen for the measurement). By measuring the asymmetry slope in these

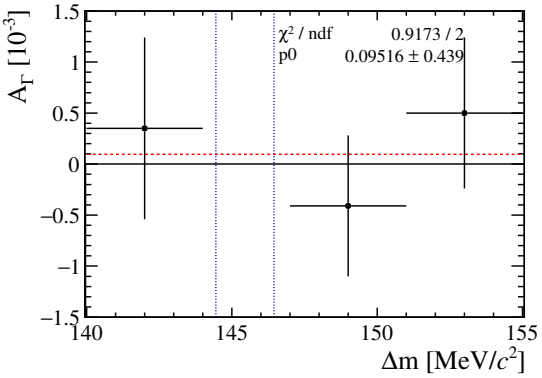

Figure 8.4 – Measurement of $A_\Gamma^{K\pi}$ in the different Δm sidebands. The blue vertical lines represent the signal region. The red horizontal line is the average value of the data points.

3 regions, it can be checked whether there are any significant variations in different regions of Δm. In principle no significant effects are expected, being this a random combinatorial background. The results are shown in fig. 8.4. It can be seen that the values are all quite small and there is no statistically significant dependence. The uncertainty of the extrapolation under the peak is even lower that the statistical fluctuation associated with the events in the sideband that are used for the actual subtraction. While there is a statistical component to that number, conservatively its full value is taken as systematic uncertainty on the extrapolation from the sideband region to the peak region. Therefore, the uncertainty contribution $f \times \sigma(A_\Gamma(\text{bkg}))$ is determined as 0.011×10^{-3}, for both KK and $\pi\pi$ modes.

8.3 Peaking backgrounds

While the combinatorial background is accurately subtracted with the Δm sideband procedure, partially- or mis-identified D^0 decays may peak in the Δm distribution, thus mimicking the signal distribution of a real $D^* \to D^0\pi \to [h^+h^-]\pi$ decays, and represent a background component ("peaking background") that is not removed by the sideband-subtraction procedure. In particular, the D^0 mass distribution of $D^0 \to K^+K^-$ decays is most likely affected by "peaking background" since the kaon mass hypothesis can compensate for a loss in invariant mass when decays as $D^0 \to K^-\pi^+\pi^0$, $D^+ \to K^+\pi^+\pi^-$ and $D_s^+ \to K^+K^-\pi^+$ are partially-reconstructed. These decays, however, do not peak in the D^0 mass, but they appear as having a broad distribution, in some cases contaminating the D^0 signal mass window (see refs. [8, 36, 59]).

In order to assess the systematic uncertainty due to the presence of these residual backgrounds under the signal region of Δm distribution, the D^0 mass sidebands, defined as the region within $[m_{D^0} - 6\sigma, m_{D^0} - 3\sigma] \cup [m_{D^0} + 3\sigma, m_{D^0} + 6\sigma]$ MeV/c^2 where $\sigma = 8$ MeV/c^2, are studied[3].

[3] As reminder, the signal region is defined as candidates falling in the D^0 mass window within $[m_{D^0} - 3\sigma, m_{D^0} + 3\sigma]$ MeV/c^2 see chap. 4

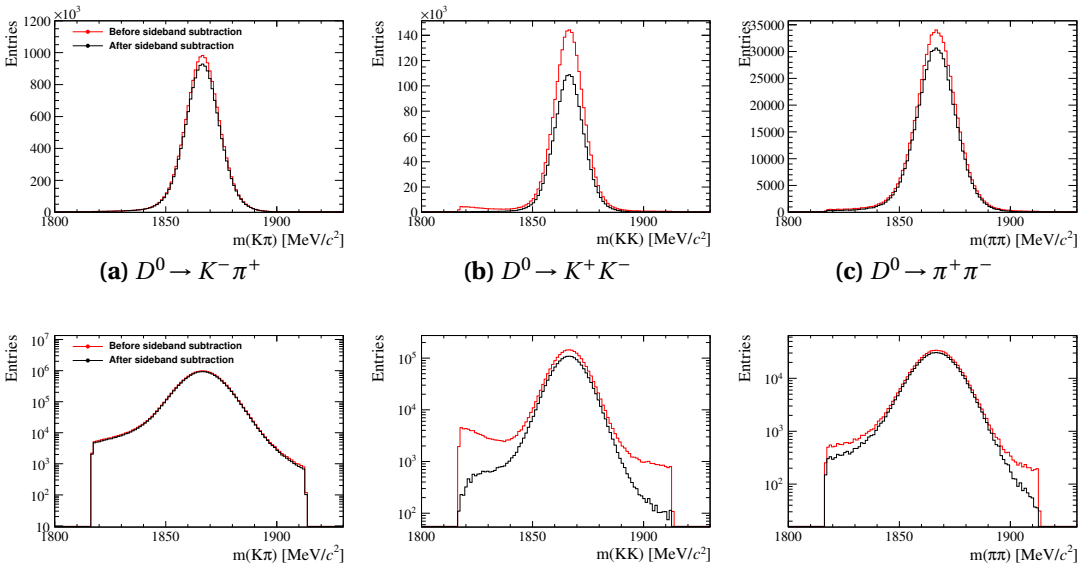

(a) $D^0 \to K^-\pi^+$ **(b)** $D^0 \to K^+K^-$ **(c)** $D^0 \to \pi^+\pi^-$

(d) $D^0 \to K^-\pi^+$, log scale **(e)** $D^0 \to K^+K^-$, log scale **(f)** $D^0 \to \pi^+\pi^-$, log scale

Figure 8.5 – The distributions of the D^0 mass, before (in red) and after (in black) the Δm sideband subtraction.

The distributions of the D^0 mass, before and after the Δm sideband subtraction, are shown in fig. 8.5, where the requirement of belonging to the signal mass region $[m_{D^0} - 3\sigma, m_{D^0} + 3\sigma]$ MeV/c^2 is relaxed with respect to the final measurement, in order to visualise what happens in the D^0 mass sidebands. The presence of a small residual background cannot be excluded, also after the Δm sideband subtraction, in particular for the $D^0 \to K^+K^-$ decay mode. In order to quantify the size of this "peaking background" in the sample, the Δm distribution in the D^0 mass sidebands is fit, using the same PDF for signal and random pion background, as described in sec. 4.6. All the parameters for the signal and the random pion background are fixed to those extracted from the fit to the full data sample, except for the addition of a scale factor ($\sigma_i \to s \cdot \sigma_i$) to the signal shape, in order to take into account that D^0 candidates are selected in the D^0 mass sidebands (including also candidates with soft photon emission) and a wider signal peak in Δm distribution is expected. A Gaussian component is also added to model contribution of mis-reconstructed decays. The fit results are reported in fig. 8.6 for the $D^0 \to K^+K^-$ and $D^0 \to \pi^+\pi^-$ decay modes. For the $D^0 \to K^+K^-$ decay mode a contribution (grey region) of mis-reconstructed decays is clearly visible, while for $D^0 \to \pi^+\pi^-$ the returned fraction is compatible with zero. The number of mis-reconstructed decays within the Δm signal region of fig. 8.6a is about 17×10^3 for the $D^0 \to K^+K^-$ decay mode, and assuming a linear behaviour for the background in the D^0 mass (motivated by previous studies [8, 36, 59, 61]) it is possible to extrapolate a contamination of mis-reconstructed decays of about 0.51%, under the nominal signal region.

In order to assess a systematic uncertainty associated to this small contamination on the

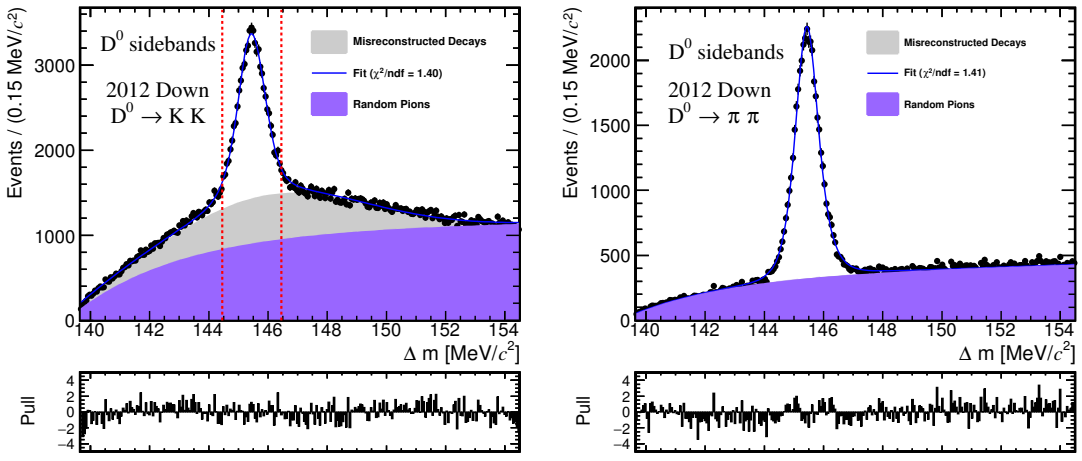

(a) $D^0 \to K^+K^-$ **(b)** $D^0 \to \pi^+\pi^-$

Figure 8.6 – Δm distribution of the (a) $D^0 \to K^+K^-$ and (b) $D^0 \to \pi^+\pi^-$ candidates in the D^0 mass sidebands. The vertical red dotted line represents our signal region.

final measurement, the measurement of A_Γ^{KK} has been repeated in the D^0 mass sidebands and outside the signal region of fig. 8.6a, obtaining a value of $(1.70 \pm 0.90) \times 10^{-3}$. This measurement receives contributions both from random pions background (76%) and from misreconstructed background (24%), that must be disentangled. However, A_Γ of random pions background can be measured using the Δm sidebands (within the D^0 signal region $[m_{D^0} - 3\sigma, m_{D^0} + 3\sigma]$ MeV/c^2) and it comes out to be compatible with zero at a level of precision of 0.36×10^{-3} as reported in fig. 8.2.[4] Thus, the value of A_Γ due to peaking background, A_Γ^{mis}, is extracted by $(1.70 \pm 0.90) \times 10^{-3} = 0.24 \cdot A_\Gamma^{\text{mis}} + 0.76 \cdot A_\Gamma^{\text{rnd}}$, where substituting $A_\Gamma^{\text{rnd}} = 0.36 \times 10^{-3}$, it comes out $A_\Gamma^{\text{mis}} = (5.94 \pm 2.61) \times 10^{-3}$. Thus, the assigned systematic uncertainty is 0.05×10^{-3} ($\approx \max(0.51\% \cdot (5.94 \pm 2.61) \times 10^{-3})$) because of the presence of misreconstructed decays in the $D^0 \to K^+K^-$ decay mode. As far as the $D^0 \to \pi^+\pi^-$ decay mode is concerned any systematic uncertainty is assigned, because the same effect is $\lesssim \mathcal{O}(10^{-6})$.

8.4 L0 trigger effects

No requirement is applied at the first level of the LHCb trigger, as described in sec. 4.2, and this translates into the logical `OR` of all the L0 triggers. In order to check the stability of the measurement because of this choice, all samples are split into two statistically independent subsamples, according to two different trigger categories, and the measurement is repeated independently on each of them. The two trigger categories are

[4] Since no difference is expected between the $D^0 \to K^-\pi^+$, $D^0 \to K^+K^-$ and $D^0 \to \pi^+\pi^-$ in the random pion background, the high statistics $D^0 \to K^-\pi^+$ data sample is used to extract A_Γ (see fig. 8.2 and fig. 8.4). However, the same measurement in the $D^0 \to K^+K^-$ mode return A_Γ compatible with zero with a precision of about 1.5×10^{-3}.

- L0TOS - if the D^0 candidate fired the L0Hadron (see sec. 4.2);
- $\overline{\text{L0TOS}}$ - otherwise (including also events where the L0Hadron did not fire at all);

where TOS stands for *Trigger On Signal* and means that the signal decay is sufficient to generate a positive trigger response. Repeating the measurements on the high statistics $D^0 \to K^-\pi^+$ decay mode, the value obtained are $A_\Gamma^{K\pi}(\text{L0TOS}) = (0.17 \pm 0.17) \times 10^{-3}$ and $A_\Gamma^{K\pi}(\overline{\text{L0TOS}}) = (0.12 \pm 0.13) \times 10^{-3}$ in perfect agreement with each other. Thus, no systematic uncertainty is assigned on this trigger choice.

8.5 Multiple candidates

Multiple candidates are randomly chosen (see sec. 4.5) in order to avoid possible biases. In order to check the impact of such a choice on the final measurement, $A_\Gamma^{K\pi}$ is measured retaining all multiple candidates. In this way, a possible effect due to the presence of multiple candidates would be amplified in the final measurement. The returned value is $(0.14 \pm 0.10) \times 10^{-3}$. The very small shift of 0.02×10^{-3} with respect to the central value cannot be only ascribed to a possible bias generated by multiple candidates. A statistical component is entangled and it should be considered in the comparison between the two values. However, the obtained shift is small with respect to the current statistical uncertainty and a rigorous evaluation of statistical correlations of the two samples would further reduce the size of the observed shift. Thus, no systematic uncertainty is assigned.

8.6 Decay time resolution

The decay time resolution $\sigma_t \approx 50\,\text{fs}$ is expected to have a negligible impact on the measurement, since it is much smaller than the D^0 lifetime and since it is the same for D^0 and $\overline{D}^0$. However, it does affect the observed time scale and therefore the measured A_Γ. The size of this effect is quantified by measuring A_Γ on 900 pseudo-experiments by generating 10^6 D candidates for each of them. An exponential function sculpted by the acceptance function is smeared with a Gaussian resolution function having a standard deviation equal to σ_t, and is used to generate the proper decay time distribution for D^0 and $\overline{D}^0$ candidates, for different values of A_Γ. The difference between the measured value (A_Γ^{meas}) and the true value (A_Γ^{true}) is distributed as a Gaussian with a mean compatible with zero at the level of 0.01×10^{-3}. This is repeated for three different values of $A_\Gamma^{\text{true}} = -0.6 \times 10^{-3}, 0, +0.6 \times 10^{-3}$, and results are reported in fig. 8.7. The values $A_\Gamma^{\text{true}} = \pm 0.6 \times 10^{-3}$ are chosen because of the statistical uncertainty of the $D^0 \to \pi^+\pi^-$ measurement, being the larger one. The value $A_\Gamma^{\text{true}} = 0$ is just a crosscheck between the two values of interest, since for $A_\Gamma^{\text{true}} = 0$ any bias is expected by construction at any value of the time resolution.

In conclusion, the bias on the A_Γ measurement, due to the decay time resolution, is certainly below 0.01×10^{-3} since no significant deviation from zero is observed at this level of precision. This is smaller than our dominant systematic uncertainty by about a factor of 10; therefore, no

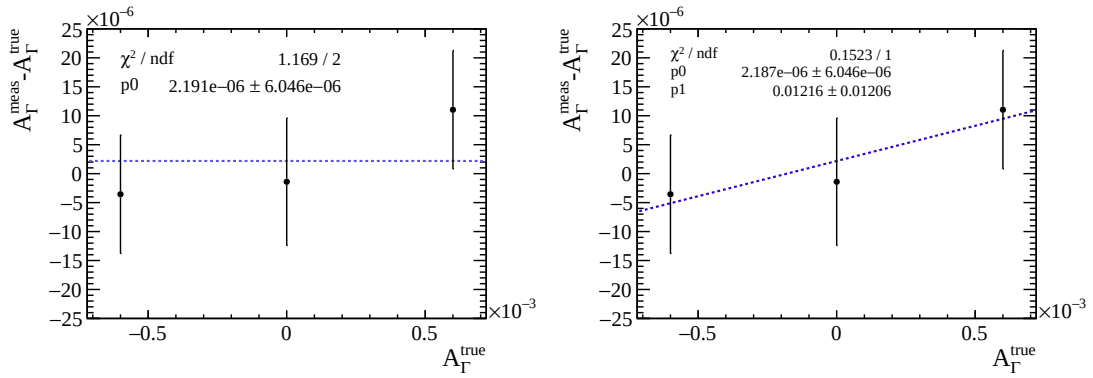

(a) Fit to a constant.

(b) Fit to a straight line.

Figure 8.7 – A_Γ^{meas} - A_Γ^{true} as a function of different values of A_Γ^{true}. The fit to a (left) constant and to (right) a straight line are overlaid.

systematic uncertainty is assigned.

8.7 Summary

Summary of systematic uncertainties is reported in tab. 8.2. The dominant systematic uncertainty comes from the residual secondary contribution (see chap. 7). The systematic uncertainty associated to the secondary contribution corresponds to the whole size of the effect, as explained in chap. 7, resulting into a conservative estimation, where large room of improvement is possible. In the $D^0 \to K^+K^-$ decay mode also the contribution of the peaking background translates into a significant systematic uncertainty. Nevertheless, the total systematic uncertainty is less than one third of the statistical uncertainty (see chap. 6) confirming the robustness and reliability of the measurement.

Table 8.2 – Summary of systematic uncertainties reported in units of 10^{-3}.

Syst. sources	$\Delta A_\Gamma(D^0 \to K^+K^-)$	$\Delta A_\Gamma(D^0 \to \pi^+\pi^-)$
Secondary decays	0.08	0.12
Correction discretisation	0.02	0.02
Background subtraction	0.01	0.01
Peaking background	0.05	–
Total	0.10	0.12

9 Results and conclusion

This chapter presents the final result of this thesis and a discussion of its impact in the current experimental landscape.

9.1 Final results

The full LHCb Run I data sample, corresponding to $3\,\text{fb}^{-1}$ of integrated luminosity, is used to measure the *CP* violation A_Γ parameter in the singly-Cabibbo suppressed $D^0 \to K^+K^-$ and $D^0 \to \pi^+\pi^-$ decay modes, obtaining

$$A_\Gamma(D^0 \to K^+K^-) = (-0.30 \pm 0.32 \pm 0.10) \times 10^{-3},$$
$$A_\Gamma(D^0 \to \pi^+\pi^-) = (\ \ 0.46 \pm 0.58 \pm 0.12) \times 10^{-3},$$

where the first uncertainties are statistical and the second are systematic. The results for the two decay modes are consistent and show no evidence of *CP* violation. These results are the most precise measurements to date of these quantities and are consistent with previous measurements [33, 34, 38] and with the previous LHCb results [36] obtained from a subsample of the data analysed in this thesis, that they supersede with an improvement in precision of nearly a factor 2. They are also consistent with the A_Γ measurements [39] performed by LHCb in the separate muon-tagged sample over the same data taking period.

9.1.1 Combination

Assuming that the value of A_Γ is universal, *i.e.* independent from the final state as described in sub-sec. 1.8.1, the results for the $D^0 \to K^+K^-$ and the $D^0 \to \pi^+\pi^-$ decay modes can be combined together being the measurement of the same quantity. The statistical uncertainties between the two measurements are independent, while the systematic uncertainties are not and they have to be appropriately treated. Systematic uncertainties and their correlations between the two measurements are reported in tab. 9.1. Systematic uncertainties on secondary decays are conservatively assumed to be fully correlated between the two measurements. The

Table 9.1 – Systematic uncertainties on A_Γ^{KK} and $A_\Gamma^{\pi\pi}$ along with their correlations.

syst. uncertainty source	A_Γ^{KK}	$A_\Gamma^{\pi\pi}$	correlation
Secondary decays	0.08	0.12	100%
CP-sym. reweighing	0.02	0.02	100%
Background subtraction	0.01	0.01	100%
Peaking background	0.05	–	0%

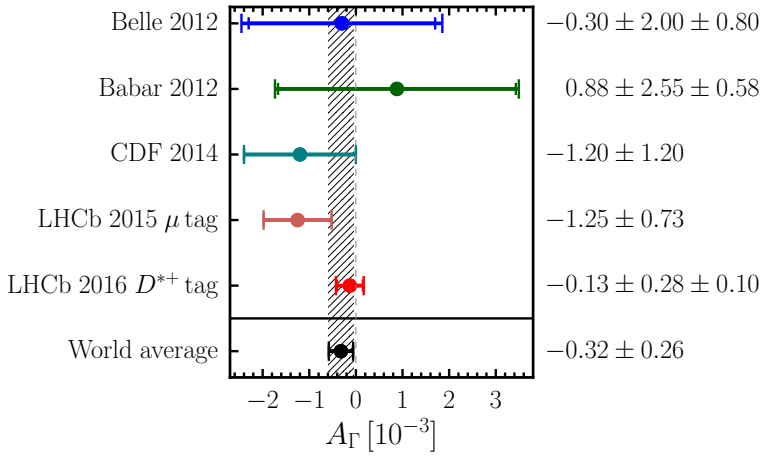

Figure 9.1 – World weighted average of A_Γ including the measurement reported in this thesis (LHCb 2016 D^{*+} tag, reported in red). The hatched region represents the 1σ band for the world average. The other measurements are Belle 2012 [33], BaBar 2012 [34], CDF 2014 [38] and LHCb 2015 μ-tag [39].

two measurements are then combined using the best linear unbiased estimator (BLUE) [62] obtaining the following value

$$A_\Gamma(KK+\pi\pi) = (-0.13 \pm 0.28 \pm 0.10) \times 10^{-3}.$$

where the first uncertainty is statistical and the second one is systematic. This is the most precise measurement of *CP* violation in the charm sector, leading the world average, as shown in fig. 9.1.

The result is also compatible with the A_Γ measurement [39] performed by LHCb in the statistically independent muon-tagged sample over the same data-taking period. Therefore, they are combined to yield the overall LHCb Run I result

$$A_\Gamma(KK+\pi\pi, \text{LHCb Run I}) = (-0.29 \pm 0.28) \times 10^{-3}.$$

9.2 A_Γ implications on charm CP violating parameters

While the value of A_Γ is directly related to the indirect CP violation, $A_\Gamma = -A_{CP}^{\text{ind}}$, as described in chap. 1, the direct CP violation, A_{CP}^{dir}, can be inferred by measuring the time-integrated CP asymmetry $\langle A_{CP}(t)\rangle$. It comes from the integral of the time-dependent asymmetry, $A_{CP}(t)$ (see eq. (1.26)), over the observed decay time distribution, $\mathscr{D}(t)$,

$$\begin{aligned}\langle A_{CP}(t)\rangle &= \frac{\int \mathrm{d}t\, A_{CP}(t)\mathscr{D}(t)}{\int \mathrm{d}t\, \mathscr{D}(t)} = \int \mathrm{d}t \left(A_{CP}^{\text{dir}} + A_{CP}^{\text{ind}}\frac{t}{\tau_{D^0}}\right)\mathscr{D}(t)\Big/\left(\int \mathrm{d}t\,\mathscr{D}(t)\right)\\ &= A_{CP}^{\text{dir}} + \frac{\langle t\rangle}{\tau_{D^0}}A_{CP}^{\text{ind}},\end{aligned}$$

where $\langle t\rangle = \int \mathrm{d}t\, t\mathscr{D}(t)/\left(\int \mathrm{d}t\,\mathscr{D}(t)\right)$ is the average decay time in the reconstructed sample. As for A_Γ, $\langle A_{CP}(t)\rangle$ can be separately measured both for $D^0\to\pi^+\pi^-$ and $D^0\to K^+K^-$. However, absolute CP asymmetry measurements are experimentally challenging in LHCb, because of the presence of nuisance parameters, as the production and the detection asymmetries (see sub-sec. 2.2.1). Thus, the difference between the asymmetry of the $D^0\to K^+K^-$ and the $D^0\to\pi^+\pi^-$ decay modes, ΔA_{CP}, where the detection and the production asymmetries cancel out, is a better observable and its value is

$$\begin{aligned}\Delta A_{CP} &\equiv A_{CP}(D^0\to K^+K^-) - A_{CP}(D^0\to\pi^+\pi^-)\\ &\approx \Delta A_{CP}^{\text{dir}} + \frac{\Delta\langle t\rangle}{\tau}A_{CP}^{\text{ind}},\end{aligned}$$

where $\Delta A_{CP}^{\text{dir}}$ is the difference between the direct CP violation in $D^0\to K^+K^-$ and $D^0\to\pi^+\pi^-$ decay modes and $\Delta\langle t\rangle$ is the difference between the average reconstructed decay times $\langle t(K^+K^-)\rangle$ and $\langle t(\pi^+\pi^-)\rangle$. The measurements of ΔA_{CP} and A_Γ observables by LHCb are combined to infer the individual values of $\Delta A_{CP}^{\text{dir}}$ and A_{CP}^{ind}, where the latter is assumed to be the same for $D^0\to K^+K^-$ and $D^0\to\pi^+\pi^-$ modes. All the measurements are assumed to be statistically independent and systematic uncertainties are assumed to be fully uncorrelated. A χ^2 is used to combine all the measurements and the final results are shown in the $(A_{CP}^{\text{ind}}, \Delta A_{CP}^{\text{dir}})$ plane of fig. 9.2. The values of the indirect and the direct CP asymmetries are found to be

$$\begin{aligned}A_{CP}^{\text{ind}} &= (\ \ 0.29\pm 0.28)\times 10^{-3},\\ \Delta A_{CP}^{\text{dir}} &= (-0.56\pm 0.76)\times 10^{-3},\end{aligned}$$

and are consistent with the hypothesis of CP symmetry with a p-value of 0.79. These are definitively the "final words" of the LHCb experiment on the CP violation of D^0 mesons decaying to two bodies.

LHCb has also recently provided individual time-integrated measurements of $A_{CP}(D^0\to K^+K^-)$ and $A_{CP}(D^0\to\pi^+\pi^-)$ [66]. The same procedure described above can be separately repeated for the $D^0\to K^+K^-$ and the $D^0\to\pi^+\pi^-$ to infer values of the indirect and the direct

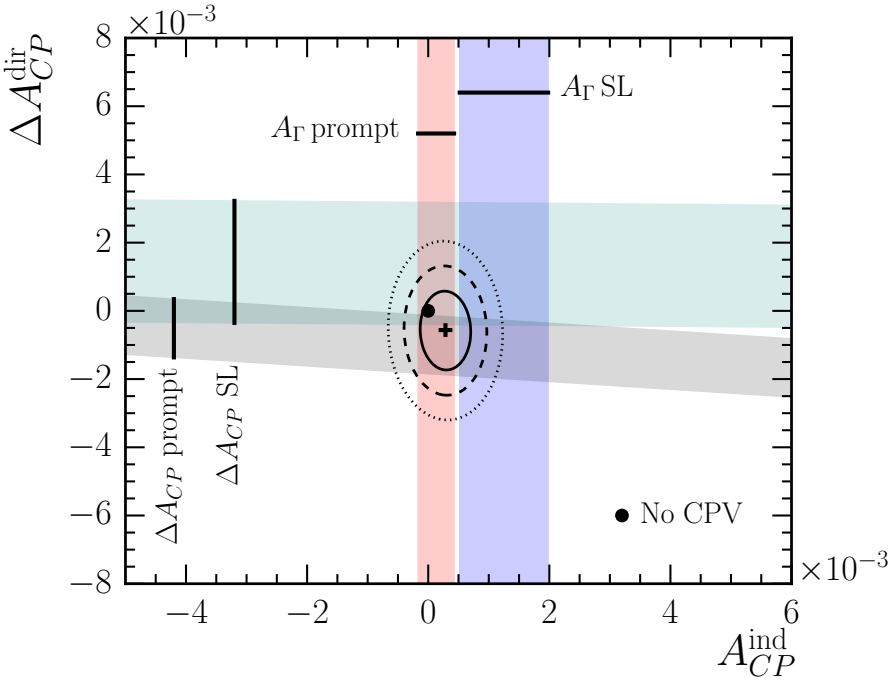

Figure 9.2 – Contour plot of $\Delta A_{CP}^{\rm dir}$ and $A_{CP}^{\rm ind}$. The point at (0,0) denotes the hypothesis of no *CP* violation. The solid bands represent the measurements in refs. [39, 63, 64] and those reported in this thesis (A_Γ prompt). The value of y_{CP} is taken from ref. [65]. The contour lines shows the 68% (solid), 95% (dashed) and 99% (dotted) confidence-level intervals from the combination.

CP violation in the two decay modes. The results are

$$A_{CP}^{\rm ind}(D^0 \to K^+K^-) = (\ \ 0.45 \pm 0.29) \times 10^{-3}, \qquad A_{CP}^{\rm ind}(D^0 \to \pi^+\pi^-) = (-0.27 \pm 0.49) \times 10^{-3},$$
$$A_{CP}^{\rm dir}(D^0 \to K^+K^-) = (-0.37 \pm 1.56) \times 10^{-3}. \qquad A_{CP}^{\rm dir}(D^0 \to \pi^+\pi^-) = (\ \ 1.13 \pm 1.78) \times 10^{-3}.$$

and are reported also in fig. 9.3. Both results are compatible with the *CP* symmetry hypothesis, and they are the most precise measurements of these observables. However, contrary to the combination of $\Delta A_{CP}^{\rm dir}$ and $A_{CP}^{\rm ind}$ reported in fig. 9.2, which is free from any external experimental and theoretical constraint, $A_{CP}(D^0 \to K^+K^-)$ and $A_{CP}(D^0 \to \pi^+\pi^-)$ [66] are measured assuming no *CP* violation in the charm-mixing and in the Cabibbo-favoured $D^0 \to K^-\pi^+$, $D^+ \to K^-\pi^+\pi^+$ and $D^+ \to \overline{K}^0\pi^+$ decay modes.

9.3 Future perspectives

This thesis describes the measurement of A_Γ with the full Run I data sample collected by the LHCb experiment, corresponding to 3 fb^{-1} of integrated luminosity. The large statistics accumulated during the Run I will be exceeded during the current Run II. The total recorded

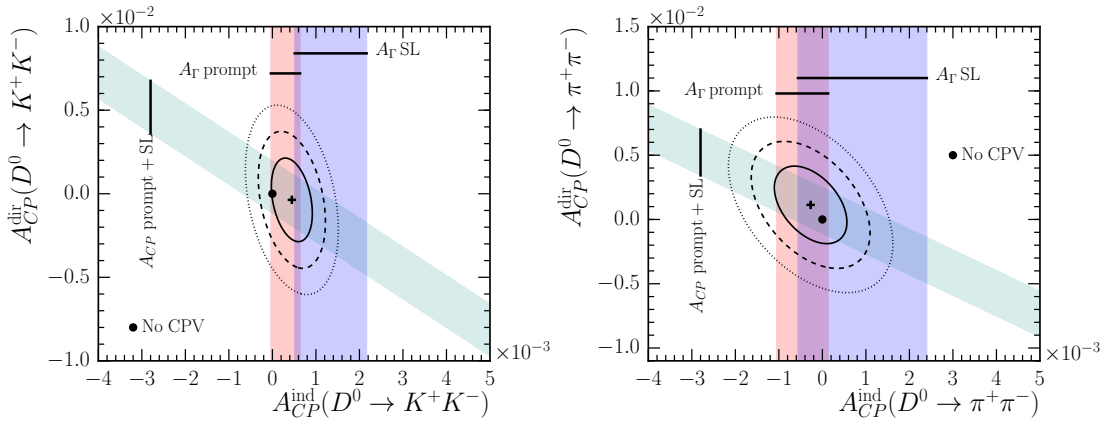

Figure 9.3 – Contour plot of $A_{CP}^{\rm dir}$ and $A_{CP}^{\rm ind}$ in the (left) $D^0 \to K^+K^-$ and the (right) $D^0 \to \pi^+\pi^-$ decay modes. The point at (0,0) denotes the hypothesis of no *CP* violation. The solid bands represent the measurements in ref. [66] (A_{CP} prompt + SL), ref. [39] (A_Γ SL) and those reported in this thesis (A_Γ prompt). The contour lines shows the 68% (solid), 95% (dashed) and 99% (dotted) confidence-level intervals from the combination.

luminosity during the 2015 and 2016 is about 0.3 fb^{-1} and 1.7 fb^{-1}, respectively, for a total integrated luminosity of 2 fb^{-1}. Due to the increasing of the centre-of-mass energy, from 8 TeV to 13 TeV, and several improvements in the trigger and data acquisition systems, the number of reconstructed $D^0 \to h^+h^-$ is about a factor 3 per fb^{-1} times larger than in Run I. Thus, it is very likely to expect a statistical sensitivity to A_Γ with the total Run I and Run II data sample of about[1]

$$\sigma_{A_\Gamma}(\text{Run I \& Run II}) = \sigma_{A_\Gamma}(\text{Run I})\sqrt{\frac{3}{3+2\times 3}} = 0.32\times 10^{-3}\sqrt{\frac{3}{9}} \approx 0.18\times 10^{-3},$$

still far away from the systematic uncertainty of the measurement reported in this thesis. The Run II will continue in 2017 and 2018, assuming the same performances of the 2016, the total integrated luminosity (Run I + Run II) recorded by LHCb will be about 8.4 fb^{-1}. The sensitivity to A_Γ will be about 0.11×10^{-3}, compatible with the systematic uncertainty assessed in the measurement reported in this thesis.

An upgrade of the LHCb detector is expected to be installed in the Long Shutdown II (2019-2020), in order to collect up to 50 fb^{-1} of integrated luminosity during the Run III (2021-2023). Assuming to have the same efficiency of the Run II, the collected statistics will be about 150 times the Run I statistics (about 1.5 billion of $D^0 \to K^+K^-$ events), leading to a sensitivity for A_Γ of

$$\sigma_{A_\Gamma}(\text{Run III}) = \sigma_{A_\Gamma}(\text{Run I})\sqrt{\frac{3}{150}} \approx 0.05\times 10^{-3},$$

[1] The statistical error on A_Γ is assumed to scale as the inverse of the square root of the number of events.

which is only a factor two smaller than the current systematic uncertainty. This point is extremely relevant because it demonstrates that the measurement of the A_Γ parameter, as described in this work, can be easily extended, as it is, to the future LHCb-Upgrade sample. It is not absurd to think that with some extra work LHCb will be able to extract the effect due to the contamination of secondary decays in the final data sample with a rough precision of about 10%, reducing the current systematic uncertainty (corresponding to the whole size of the effect) to the value of about 0.06×10^{-3}, compatible with the expected statistical uncertainty of the Run III.

9.4 Conclusions

This thesis reports the world best measurement of the time-dependent *CP* asymmetries in the decay rates (A_Γ) of the singly Cabibbo-suppressed decays $D^0 \to K^+K^-$ and $D^0 \to \pi^+\pi^-$ in pp collision data at centre-of-mass energies of 7 and 8 TeV collected by the LHCb detector during the LHC Run I, corresponding to an integrated luminosity of $3\,\text{fb}^{-1}$. The results are consistent with *CP* conservation and improve by nearly a factor two the previous world leading measurements, also obtained by LHCb using the 2011 subsample of the current data. In the end, they are the LHCb final words with the Run I data sample and are the most precise result of *CP* violation of the experiment to date.

The presented measurements are statistical limited and the current precision of the assessed systematic uncertainty will be reached in the next years only with the full data sample that will be collected by the future LHCb upgrade (2021-2023). Therefore, beyond the intrinsic value of performing the world best measurement of the A_Γ observable, in order to search first hints of *CP* violation in the charm sector, the work documented in this thesis proves that high precision *CP* violation measurements will be feasible in the future with an unprecedented level of precision, greatly increasing the possibility of observing the *CP* violation in the charm sector.

A $D^0 \to K^{\mp}\pi^{\pm}$ decay rates

The high statistics Cabibbo-favoured (CF) $D^0 \to K^-\pi^+$ decays data sample plays a central role in the analysis being an excellent control channel. In fact, the expected value of pseudo-A_Γ on this data sample is undetectable at the current experimental sensitivity. While the time-dependent decay rates for a D^0 meson decaying to CP eigenstate f are reported in chap. 1, here the calculation of the pseudo-A_Γ is reported in detail.

The amplitudes for CF $D^0 \to K^-\pi^+$ decays and doubly Cabibbo-suppressed (DCS) $D^0 \to K^+\pi^-$ decays are defined as

$$
\begin{aligned}
A_{K^-\pi^+} &= \langle K^-\pi^+|\mathscr{H}|D^0\rangle, \qquad \overline{A}_{K^+\pi^-} = \langle K^+\pi^-|\mathscr{H}|\overline{D}^0\rangle, \\
A_{K^+\pi^-} &= \langle K^+\pi^-|\mathscr{H}|D^0\rangle, \qquad \overline{A}_{K^-\pi^+} = \langle K^-\pi^+|\mathscr{H}|\overline{D}^0\rangle,
\end{aligned}
$$

where $\mathscr{H}$ is the decay Hamiltonian.

The time-dependent decay rates for the CF $D^0 \to K^-\pi^+$ and $\overline{D}^0 \to K^+\pi^-$ decays are

$$
\begin{aligned}
\Gamma(D^0(t) \to K^-\pi^+) = \frac{1}{2}\mathrm{e}^{-\Gamma t}|A_{K^-\pi^+}|^2\{&(1+|\lambda_{K^-\pi^+}|^2)\cosh(y\Gamma t) + (1-|\lambda_{K^-\pi^+}|^2)\cos(x\Gamma t) \\
&+2\Re(\lambda_{K^-\pi^+})\sinh(y\Gamma t) - 2\Im(\lambda_{K^-\pi^+})\sin(x\Gamma t)\}, \\
\Gamma(\overline{D}^0(t) \to K^+\pi^-) = \frac{1}{2}\mathrm{e}^{-\Gamma t}|\overline{A}_{K^+\pi^-}|^2\{&(1+|\lambda^{-1}_{K^+\pi^-}|^2)\cosh(y\Gamma t) + (1-|\lambda^{-1}_{K^+\pi^-}|^2)\cos(x\Gamma t) \\
&+2\Re(\lambda^{-1}_{K^+\pi^-})\sinh(y\Gamma t) - 2\Im(\lambda^{-1}_{K^+\pi^-})\sin(x\Gamma t)\}.
\end{aligned}
$$

Expanding at the first order in $x\Gamma t$ and $y\Gamma t$ the decay rates for the CF D^0 decays are

$$
\begin{aligned}
\Gamma(D^0(t) \to K^-\pi^+) &= \mathrm{e}^{-\Gamma t}|A_{K^-\pi^+}|^2\{1+\Re(\lambda_{K^-\pi^+})\,y\Gamma t - \Im(\lambda_{K^-\pi^+})\,x\Gamma t\}, \\
\Gamma(\overline{D}^0(t) \to K^+\pi^-) &= \mathrm{e}^{-\Gamma t}|\overline{A}_{K^+\pi^-}|^2\{1+\Re(\lambda^{-1}_{K^+\pi^-})\,y\Gamma t - \Im(\lambda^{-1}_{K^+\pi^-})\,x\Gamma t\}.
\end{aligned}
$$

where

$$
|\lambda_{K^-\pi^+}| = \left|\frac{q\overline{A}_{K^-\pi^+}}{pA_{K^-\pi^+}}\right| \approx \mathscr{O}(10^{-2}), \qquad |\lambda^{-1}_{K^+\pi^-}| = \left|\frac{pA_{K^+\pi^-}}{q\overline{A}_{K^+\pi^-}}\right| \approx \mathscr{O}(10^{-2}), \tag{A.1}
$$

because of the ratio DCS/CF $\approx \lambda^2 = \mathcal{O}(10^{-2})$.

For completeness, the decay rates of DCS $D^0 \to K^+\pi^-$ and $\overline{D}^0 \to K^-\pi^+$ decays are also reported, and they are

$$\begin{aligned}\Gamma(D^0(t) \to K^+\pi^-) = \frac{1}{2}e^{-\Gamma t}|A_{K^+\pi^-}|^2\{&(1+|\lambda_{K^+\pi^-}|^2)\cosh(y\Gamma t) + (1-|\lambda_{K^+\pi^-}|^2)\cos(x\Gamma t) \\ &+2\Re(\lambda_{K^+\pi^-})\sinh(y\Gamma t) - 2\Im(\lambda_{K^+\pi^-})\sin(x\Gamma t)\},\\ \Gamma(\overline{D}^0(t) \to K^-\pi^+) = \frac{1}{2}e^{-\Gamma t}|\overline{A}_{K^-\pi^+}|^2\{&(1+|\lambda^{-1}_{K^-\pi^+}|^2)\cosh(y\Gamma t) + (1-|\lambda^{-1}_{K^-\pi^+}|^2)\cos(x\Gamma t) \\ &+2\Re(\lambda^{-1}_{K^-\pi^+})\sinh(y\Gamma t) - 2\Im(\lambda^{-1}_{K^-\pi^+})\sin(x\Gamma t)\}.\end{aligned}$$

Since $|A_{K^+\pi^-}|^2 \approx |\overline{A}_{K^-\pi^+}|^2 \approx \mathcal{O}(\lambda^4)$ at least the second order in $x\Gamma t$ and $y\Gamma t$ has to be retained, thus

$$\begin{aligned}\Gamma(D^0(t) \to K^+\pi^-) = e^{-\Gamma t}|A_{K^+\pi^-}|^2\Big\{&1 + \Re(\lambda_{K^+\pi^-})y\Gamma t - \Im(\lambda_{K^+\pi^-})x\Gamma t \\ &+ \frac{(1+|\lambda_{K^+\pi^-}|^2)y^2 - (1-|\lambda_{K^+\pi^-}|^2)x^2}{4}\Gamma^2 t^2\Big\},\\ \Gamma(\overline{D}^0(t) \to K^-\pi^+) = e^{-\Gamma t}|\overline{A}_{K^-\pi^+}|^2\Big\{&1 + \Re(\lambda^{-1}_{K^-\pi^+})y\Gamma t - \Im(\lambda^{-1}_{K^-\pi^+})x\Gamma t \\ &+ \frac{(1+|\lambda_{K^-\pi^+}|^2)y^2 - (1-|\lambda_{K^-\pi^+}|^2)x^2}{4}\Big\}.\end{aligned}$$

Expanding calculations and neglecting terms as $|A_{K^+\pi^-}|^2x^2$, $|A_{K^+\pi^-}|^2y^2$, $|\overline{A}_{K^-\pi^+}|^2x^2$ and $|\overline{A}_{K^-\pi^+}|^2y^2$ that are of the order $\mathcal{O}(10^{-7})$, the time-dependent decay rates of DCS decays are

$$\begin{aligned}\Gamma(D^0(t) \to K^+\pi^-) &= e^{-\Gamma t}|\overline{A}_{K^+\pi^-}|^2\left|\frac{q^2}{p^2}\right|\left\{|\lambda^{-1}_{K^+\pi^-}|^2 + \Re(\lambda^{-1}_{K^+\pi^-})y\Gamma t + \Im(\lambda^{-1}_{K^+\pi^-})x\Gamma t + \frac{x^2+y^2}{4}\Gamma^2 t^2\right\},\\ \Gamma(\overline{D}^0(t) \to K^-\pi^+) &= e^{-\Gamma t}|A_{K^-\pi^+}|^2\left|\frac{p^2}{q^2}\right|\left\{|\lambda_{K^-\pi^+}|^2 + \Re(\lambda_{K^-\pi^+})y\Gamma t + \Im(\lambda_{K^-\pi^+})x\Gamma t + \frac{x^2+y^2}{4}\Gamma^2 t^2\right\}.\end{aligned}$$

A.1 Pseudo-A_Γ

The time-dependent asymmetry of the control sample used in the A_Γ measurement is defined as

$$A_{CP}(t) = \frac{\Gamma(D^0(t) \to K^-\pi^+) - \Gamma(\overline{D}^0(t) \to K^+\pi^-)}{\Gamma(D^0(t) \to K^-\pi^+) + \Gamma(\overline{D}^0(t) \to K^+\pi^-)}.$$

Expanding $A_{CP}(t)$ at the first order in $x\Gamma t$, $y\Gamma t$ one obtains

$$A_{CP}(t) = A_{CP}^{\text{dir}} + A_{CP}^{\text{ind}}\Gamma t,$$

where

$$A_{CP}^{\text{dir}} = \frac{|A_{K^-\pi^+}|^2 - |\overline{A}_{K^+\pi^-}|^2}{|A_{K^-\pi^+}|^2 + |\overline{A}_{K^+\pi^-}|^2},$$

and

$$A_{CP}^{\text{ind}} = \frac{2|\overline{A}_{K^+\pi^-}|^2|A_{K^-\pi^+}|^2}{\left(|A_{K^-\pi^+}|^2 + |\overline{A}_{K^+\pi^-}|^2\right)^2}\left[y\left(\Re(\lambda_{K^-\pi^+}) - \Re(\lambda^{-1}_{K^+\pi^-})\right) - x\left(\Im(\lambda_{K^-\pi^+}) - \Im(\lambda^{-1}_{K^+\pi^-})\right)\right].$$

In order to estimate an upper bound for the indirect *CP* violation in the $D^0 \to K^-\pi^+$ decays, the current experimental knowledge [10] is used to set $x \approx 0.3 \times 10^{-2}$, $y \approx 0.7 \times 10^{-2}$, and $R_D = |A_{K^+\pi^-}|^2/|A_{K^-\pi^+}|^2 = |\overline{A}_{K^-\pi^+}|^2/|\overline{A}_{K^+\pi^-}|^2$ equal to $\approx 0.35 \times 10^{-2}$. The maximum value of A_{CP}^{ind} is realised when $\lambda_{K^-\pi^+}$ and $\lambda^{-1}_{K^+\pi^-}$ are real and have opposite signs, obtaining $A_{CP}^{\text{ind}} \approx 5 \times 10^{-5}$ which is a factor of two below the current statistical uncertainty of 10×10^{-5} on pseudo-A_Γ (see chap. 5). Therefore, the indirect *CP* violation of the CF $D^0 \to K^-\pi^+$ decay can be safely assumed to be undetectable with the current sensitivity.

B Mathematical formalism

B.1 Tagged $D^0 \to h^+h^-$ events

The number of reconstructed $D^{*\pm}$, as a function of the D^0 proper decay time, t, can be written as

$$N^{\pm}(t) = \frac{N_*}{2}\mathscr{B}^*_{D\pi}\int \mathrm{d}p_*\mathrm{d}p_{h^+}\mathrm{d}p_{h^-}\mathrm{d}p_s\,\rho^{\pm}_*(p_*) \times \rho^{\pm}_0(t)\rho^*_{hh}(p_{h^-},p_{h^+},p_s|p_*)\epsilon_{hh}(p_{h^-},p_{h^+},t)\epsilon^{\pm}_s(p_s) \quad \text{(B.1)}$$

where N^* is the total number of D^{*+} and D^{*-} mesons, p_*, p_{h^-}, p_{h^+}, p_s are the three-momenta of the D^*, h^-, h^+ and the soft pion, respectively. ρ^+_* and ρ^-_* are the densities in phase space of D^{*+} and D^{*-} (they are function of the production cross sections and experimental acceptances); $\mathscr{B}^*_{D\pi}$ is the branching fraction of $D^{*+}\to D^0\pi^+$ and $D^{*-}\to\overline{D}^0\pi^-$, assumed to be charge symmetric; ρ^*_{hh} is the density in phase space of the soft pion and h^+h^- pair from D^0 decay; ρ^+_0 and ρ^-_0 are the densities in decay time of the D^0 and $\overline{D}^0$ mesons; ϵ_{hh} is the detection efficiency of the h^+h^- pair from D^0 decay; and ϵ^+_s and ϵ^-_s are the detection efficiencies of the positive and negative soft pions, respectively[1]. Conservation of four-momenta is implicitly assumed in all the densities. Densities are normalised as $\int \mathrm{d}p_*\rho(p^{\pm}_*) = 1$ and $\int \mathrm{d}p_{h^+}\mathrm{d}p_{h^-}\mathrm{d}p_s\rho^*_{hh}(p_{h^-},p_{h^+},p_s|p_*) = 1$ for each p_*.

The difference between the yields is therefore

$$N^+(t) - N^-(t) = \frac{N_*}{2}\mathscr{B}^*_{D\pi}\int \mathrm{d}p_*\mathrm{d}p_{h^+}\mathrm{d}p_{h^-}\mathrm{d}p_s\,\rho^*_{hh}(p_{h^-},p_{h^+},p_s|p_*)\epsilon_{hh}(p_{h^-},p_{h^+},t) \times \left[\rho^+_*(p_*)\rho^+_0(t)\epsilon^+_s(p_s) - \rho^-_*(p_*)\rho^-_0(t)\epsilon^-_s(p_s)\right];$$

defining $\rho_* = (\rho^+_* + \rho^-_*)/2$, $\delta\rho_* = (\rho^+_* - \rho^-_*)/(\rho^+_* + \rho^-_*)$, $\rho_0 = (\rho^+_0 + \rho^-_0)/2$, $A_{CP}(t) = (\rho^+_0 - \rho^-_0)/(\rho^+_0 +$

[1] The efficiency for detecting a D^{*+} is assumed to be factorable in the detection efficiency of the D^0 daughters and the detection efficiency of the soft pion, namely $\epsilon^{s\pm}_{hh}(p_{h^-},p_{h^+},p_s,t) = \epsilon_{hh}(p_{h^-},p_{h^+},t)\epsilon^{\pm}_s(p_s)$.

$\rho_0^-)$, $\epsilon_s = (\epsilon_s^+ + \epsilon_s^-)/2$, $\delta\epsilon_s = (\epsilon_s^+ - \epsilon_s^-)/(\epsilon_s^+ + \epsilon_s^-)$, the difference can be written as[2]

$$N^+(t) - N^-(t) = \frac{N_*}{2}\mathscr{B}^*_{D\pi}\int \mathrm{d}p_*\mathrm{d}p_{h^+}\mathrm{d}p_{h^-}\mathrm{d}p_s\,\rho^*_{hh}(p_{h^-},p_{h^+},p_s|p_*)\rho_*(p_*)\rho_0(t)$$
$$\times\,\epsilon_{hh}(p_{h^-},p_{h^+},t)\epsilon_s(p_s)\big[(1+\delta\rho_*)(1+A_{CP})(1+\delta\epsilon_s)-(1-\delta\rho_*)(1-A_{CP})(1-\delta\epsilon_s)\big].$$

Since all these asymmetries are of the order $\mathscr{O}(10^{-2})$, expanding the products and neglecting third order $A_{CP}\delta^2$ and δ^3 terms, the difference is

$$N^+(t) - N^-(t) = N_*\mathscr{B}^*_{D\pi}\int \mathrm{d}p_*\mathrm{d}p_{h^+}\mathrm{d}p_{h^-}\mathrm{d}p_s\,\rho^*_{hh}(p_{h^-},p_{h^+},p_s|p_*)\rho_*(p_*)\rho_0(t)$$
$$\times\,\epsilon_{hh}(p_{h^-},p_{h^+},t)\epsilon_s(p_s)\big[\delta\rho_*(p_*)+A_{CP}(t)+\delta\epsilon_s(p_s)\big], \quad \text{(B.2)}$$

In similar way, neglecting second order terms $A_{CP}\delta$ and δ^2, it can be obtained for the sum

$$N^+(t) + N^-(t) = N_*\mathscr{B}^*_{D\pi}\int \mathrm{d}p_*\mathrm{d}p_{h^+}\mathrm{d}p_{h^-}\mathrm{d}p_s\,\rho^*_{hh}(p_{h^-},p_{h^+},p_s|p_*)\rho_*(p_*)\rho_0(t)$$
$$\times\,\epsilon_{hh}(p_{h^-},p_{h^+},t)\epsilon_s(p_s).$$

Therefore, the raw asymmetry can be written as

$$\begin{aligned} A_{\mathrm{raw}}(t) &= \frac{N^+(t)-N^-(t)}{N^+(t)+N^-(t)} \\ &= A_{CP}(t) + \int \mathrm{d}p_*\,F^{hh*}_*(p_*,t)\delta\rho_*(p_*) + \int \mathrm{d}p_s\,F^{hh*}_s(p_s,t)\delta\epsilon_s(p_s), \end{aligned} \quad \text{(B.3)}$$

where

$$\begin{aligned} F^{hh*}_*(p_*,t) &= \frac{\int \mathrm{d}p_{h^+}\mathrm{d}p_{h^-}\mathrm{d}p_s\,\rho^*_{hh}(p_{h^-},p_{h^+},p_s|p_*)\rho_*(p_*)\epsilon_{hh}(p_{h^-},p_{h^+},t)\epsilon_s(p_s)}{\int \mathrm{d}p_*\mathrm{d}p_{h^+}\mathrm{d}p_{h^-}\mathrm{d}p_s\,\rho^*_{hh}(p_{h^-},p_{h^+},p_s|p_*)\rho_*(p_*)\epsilon_{hh}(p_{h^-},p_{h^+},t)\epsilon_s(p_s)}, \\ F^{hh*}_s(p_s,t) &= \frac{\int \mathrm{d}p_*\mathrm{d}p_{h^+}\mathrm{d}p_{h^-}\,\rho^*_{hh}(p_{h^-},p_{h^+},p_s|p_*)\rho_*(p_*)\epsilon_{hh}(p_{h^-},p_{h^+},t)\epsilon_s(p_s)}{\int \mathrm{d}p_*\mathrm{d}p_{h^+}\mathrm{d}p_{h^-}\mathrm{d}p_s\,\rho^*_{hh}(p_{h^-},p_{h^+},p_s|p_*)\rho_*(p_*)\epsilon_{hh}(p_{h^-},p_{h^+},t)\epsilon_s(p_s)}. \end{aligned} \quad \text{(B.4)}$$

$F^{hh*}_*(p_*,t)$ is the normalised density phase space of the D^* meson, and $F_s(p_s,t)$ is the reconstructed density phase space of the soft pion. Two terms can be recognised in eq. (B.3) besides the physical time-dependent *CP* violation $A_{CP}(t)$ (see chap. 1): the first one $\int \mathrm{d}p_*\,F^{hh*}_*(p_*,t)\delta\rho_*(p_*)$ is the asymmetry between the observed phase spaces of D^{*+} and D^{*-} integrated over the phase space (with the constraint $p_* = p_{h^-} + p_{h^+} + p_s$), which is by definition the production asymmetry of the D^* meson in the sample, A_{P}; the second term is the asymmetry of the observed phase spaces of the soft pion efficiency integrated over the phase space, namely the detection asymmetry of soft pions, $A_{\mathrm{D}}^{\pi_s}$. The raw asymmetry can be written as

$$A_{\mathrm{raw}}(t) = A_{CP}(t) + A_{\mathrm{P}}(t) + A_{\mathrm{D}}^{\pi_s}(t),$$

[2] The following relation is exploited $\alpha^+ - \alpha^- = \alpha((1+\delta\alpha)-(1-\delta\alpha))$, with $\alpha = (\alpha^+ + \alpha^-)/2$ and $\delta\alpha = (\alpha^+ - \alpha^-)/(\alpha^+ + \alpha^-)$.

which is the same expression used in chap. 2 (see eq. (2.3)). The detection asymmetry of the $D^{*+} \to D^0\pi^+ \to [h^+h^-]\pi^+$ decay chain is due only to the reconstruction efficiency asymmetry of soft pions $\delta\epsilon_s(p_s)$ as expected. Both the production asymmetry and the detection asymmetry acquire a time-dependency if the detection efficiency of reconstructing a D^0 meson decaying to h^+h^- final state is time-dependent.

The time-dependency of the production and soft pion detection asymmetries vanish if the time-dependent term of the efficiency for detecting $D^0 \to h^+h^-$ decays can be factorised, namely $\epsilon_{hh}(p_{h^-}, p_{h^+}, t) = \epsilon_{hh}(p_{h^-}, p_{h^+}) \cdot \epsilon(t)$. It is easy to prove that F_*^{hh*} and F_s^{hh*} are time-independent in this case.

B.2 Tagged $D^0 \to K^-\pi^+$ events

The number of reconstructed $D^{*\pm}$, as a function of the D^0 decay time, t, for $D^0 \to K^-\pi^+$ decays can be written as

$$N^{\pm}(t) = \frac{N_*}{2}\mathscr{B}^*_{D\pi}\int \mathrm{d}p_*\mathrm{d}p_K\mathrm{d}p_\pi\mathrm{d}p_s\,\rho^{\pm}_*(p_*) \times \rho^{\pm}_{0K\pi}(t)\rho^*_{K\pi}(p_K, p_\pi, p_s|p_*)\epsilon_{K^\mp\pi^\pm}(p_K, p_\pi, t)\epsilon^{\pm}_s(p_s) \quad \text{(B.5)}$$

where N^* is the total number of D^{*+} and D^{*-} mesons, p_K and p_π are the three-momenta of the the kaon and the pion; $\epsilon_{K^-\pi^+}$ and $\epsilon_{K^+\pi^-}$ are the detection efficiencies of the $K^-\pi^+$ and $K^+\pi^-$ pairs from D^0 and $\overline{D}^0$ decays, respectively. The difference between D^{*+} and D^{*-} event yields is

$$\begin{aligned}
N^+(t) - N^-(t) &= \frac{N_*}{2}\mathscr{B}^*_{D\pi}\int \mathrm{d}p_*\mathrm{d}p_K\mathrm{d}p_\pi\mathrm{d}p_s\,\rho^*_{K\pi}(p_K, p_\pi, p_s|p_*) \\
&\quad \times\big[\rho^+_*(p_*)\rho^+_{0K\pi}(t)\epsilon_{K^-\pi^+}(p_K, p_\pi, t)\epsilon^+_s(p_s) \\
&\quad\quad - \rho^-_*(p_*)\rho^-_{0K\pi}(t)\epsilon_{K^+\pi^-}(p_K, p_\pi, t)\epsilon^-_s(p_s)\big] \\
&= \frac{N_*}{2}\mathscr{B}^*_{D\pi}\int \mathrm{d}p_*\mathrm{d}p_K\mathrm{d}p_\pi\mathrm{d}p_s\,\rho^*_{K\pi}(p_K, p_\pi, p_s|p_*)\rho_*(p_*)\rho_0(t) \\
&\quad \times\epsilon_{K\pi}(p_K, p_\pi, t)\epsilon_s(p_s)\big[(1+\delta\rho_*)(1+A^{K\pi}_{CP})(1+\delta\epsilon_s)(1+\delta\epsilon_{K\pi}) \\
&\quad\quad - (1-\delta\rho_*)(1-A^{K\pi}_{CP})(1-\delta\epsilon_s)(1-\delta\epsilon_{K\pi})\big],
\end{aligned}$$

where the following additional quantities are defined: $\epsilon_{K\pi} = (\epsilon_{K^-\pi^+} + \epsilon_{K^+\pi^-})/2$ and $\delta\epsilon_{K\pi} = (\epsilon_{K^-\pi^+} - \epsilon_{K^+\pi^-})/(\epsilon_{K^-\pi^+} + \epsilon_{K^+\pi^-})$. Expanding the products and neglecting terms of the order $A_{CP}\delta^2$ and δ^3

$$\begin{aligned}
N^+(t) - N^-(t) &= N_*\mathscr{B}^*_{D\pi}\int \mathrm{d}p_*\mathrm{d}p_K\mathrm{d}p_\pi\mathrm{d}p_s\,\rho^*_{K\pi}(p_K, p_\pi, p_s|p_*)\rho_*(p_*)\rho_0(t) \\
&\quad \times\epsilon_{K\pi}(p_K, p_\pi, t)\epsilon_s(p_s)\big[\delta\rho_*(p_*) + A^{K\pi}_{CP}(t) + \delta\epsilon_{K\pi}(p_K, p_\pi, t) + \delta\epsilon_s(p_s)\big],
\end{aligned}$$

Similarly, neglecting all terms of the order δ^2 and $A_{CP}\delta$, the sum of the reconstructed number of D^{*+} and D^{*-} is

$$N^+(t) + N^-(t) = N_* \mathscr{B}^*_{D\pi} \int \mathrm{d}p_* \mathrm{d}p_K \mathrm{d}p_\pi \mathrm{d}p_s \, \rho^*_{K\pi}(p_K, p_\pi, p_s | p_*) \rho_*(p_*) \rho_0(t) \mathscr{B}_{K\pi} \times \epsilon_{K\pi}(p_K, p_\pi, t) \epsilon_s(p_s),$$

The raw time-dependent asymmetry is therefore

$$\begin{aligned} A^{K\pi}_{\text{raw}}(t) &= \frac{N^+(t) - N^-(t)}{N^+(t) + N^-(t)} \\ &= A^{K\pi}_{CP}(t) + \int \mathrm{d}p_* \, F^{K\pi *}_*(p_*, t) \delta\rho_*(p_*) \\ &+ \int \mathrm{d}p_K \mathrm{d}p_\pi \, F^{K\pi *}_{K\pi}(p_K, p_\pi, t) \delta\epsilon_{K\pi}(p_K, p_\pi, t) + \int \mathrm{d}p_s \, F^{K\pi *}_s(p_s, t) \delta\epsilon_s(p_s), \end{aligned}$$

where

$$F^{K\pi *}_{K\pi}(p_K, p_\pi, t) = \frac{\int \mathrm{d}p_* \mathrm{d}p_s \, \rho^*_{K\pi}(p_K, p_\pi, p_s | p_*) \rho_*(p_*) \epsilon_{K\pi}(p_K, p_\pi, t) \epsilon_s(p_s)}{\int \mathrm{d}p_* \mathrm{d}p_K \mathrm{d}p_\pi \mathrm{d}p_s \, \rho^*_{K\pi}(p_K, p_\pi, p_s | p_*) \rho_*(p_*) \epsilon_{K\pi}(p_K, p_\pi, t) \epsilon_s(p_s)}$$

is normalised density phase space of $K\pi$ pair for the events in the data sample. While $F^{K\pi *}_*$ and $F^{K\pi *}_s$ are the analogous of F^{hh*}_* and F^{hh*}_s, respectively, for $D^0 \to h^+h^-$ decays as reported in eq. (B.4). The following terms can be recognised: the D^{*+} production asymmetry $A_{\text{P}}(t) = \int \mathrm{d}p_* \, F^{K\pi *}_*(p_*, t) \delta\rho_*(p_*)$; the soft pion detection asymmetry $A^{\pi_s}_{\text{D}}(t) = \int \mathrm{d}p_s \, F^{K\pi *}_s(p_s, t)$, and there is the detection asymmetry of the $K\pi$ pair $A^{K\pi}_{\text{D}}(t) = \int \mathrm{d}p_K \mathrm{d}p_\pi \, F^{K\pi *}_{K\pi}(p_K, p_\pi, t) \delta\epsilon_{K\pi}(p_K, p_\pi, t)$, an additional term with respect to the $D^0 \to h^+h^-$ case. Therefore, the time-dependent asymmetry of D^*-tagged $D^0 \to K^-\pi^+$ decays can be compactly written as

$$A^{K\pi}_{\text{raw}}(t) = A_{\text{P}}(t) + A^{K\pi}_{\text{D}}(t) + A^{\pi_s}_{\text{D}}(t),$$

where the time-dependent CP asymmetry, $A^{K\pi}_{CP}(t)$, is not reported since it is negligible with the current sensitivity (see app. A).

C A_Γ plots Legend

In order to simplify the visualisation of all the information coming from the individual A_Γ measurement on the four subsamples (2011 *MagUp*, 2011 *MagDown*, 2012 *MagUp*, 2012 *MagDown*) and their weighted average, a plot as the one reported in fig. C.1 is often shown across the thesis. Here a short explanation of the notation used is given. The measured values of A_Γ

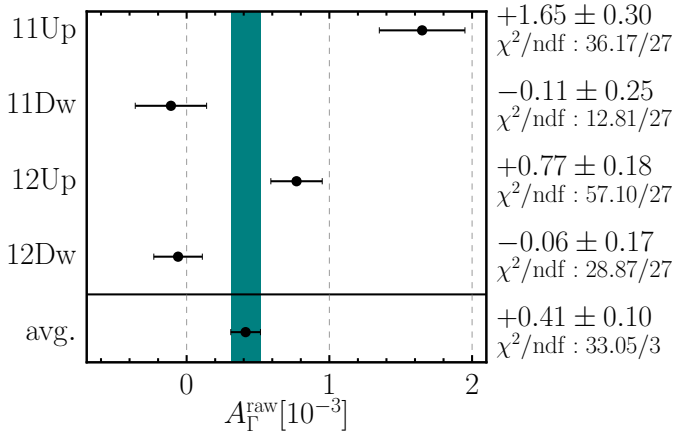

Figure C.1 – Sample plot of A_Γ measured values to explain the information that contains.

for each of the four subsamples are reported with black dots (the first four points from the top). The name of the relative subsample is on the left. The values of A_Γ returned from the linear fit to $A_{\rm raw}(t)$ are reported on the right along with the returned fit quality χ^2/ndf, below each A_Γ value. The value of the weighted average of the measurements performed on the four subsamples is shown at the bottom, and the χ^2/ndf of the compatibility among the subsamples is also reported on the right.

D Proper decay time bins

The intervals of the decay time bins, used in the analysis, are reported along with the number of reconstructed candidates in each bin. The decay time bins are the same for all three decays $D^0 \to K^-\pi^+$, $D^0 \to K^+K^-$ and $D^0 \to \pi^+\pi^-$ and are reported in tab. D.1, tab. D.2 and tab. D.3, respectively.

Table D.1 – Proper decay time bins definition. For each bin and for each subsample, the number of events after the sideband subtraction is reported. The events reported are for the $D^0 \to K^-\pi^+$ decays sample.

$D^0 \to K^-\pi^+$	11Up	11Dw	12Up	12Dw
$0.600 < t/\tau_{D^0} \leq 0.815$	3.39×10^5	5.04×10^5	9.04×10^5	9.42×10^5
$0.815 < t/\tau_{D^0} \leq 0.918$	3.69×10^5	5.51×10^5	1.05×10^6	1.10×10^6
$0.918 < t/\tau_{D^0} \leq 1.002$	3.76×10^5	5.57×10^5	1.08×10^6	1.12×10^6
$1.002 < t/\tau_{D^0} \leq 1.079$	3.75×10^5	5.53×10^5	1.07×10^6	1.11×10^6
$1.079 < t/\tau_{D^0} \leq 1.153$	3.79×10^5	5.58×10^5	1.08×10^6	1.13×10^6
$1.153 < t/\tau_{D^0} \leq 1.224$	3.79×10^5	5.55×10^5	1.07×10^6	1.12×10^6
$1.224 < t/\tau_{D^0} \leq 1.294$	3.77×10^5	5.48×10^5	1.06×10^6	1.10×10^6
$1.294 < t/\tau_{D^0} \leq 1.364$	3.80×10^5	5.55×10^5	1.07×10^6	1.11×10^6
$1.364 < t/\tau_{D^0} \leq 1.434$	3.77×10^5	5.47×10^5	1.06×10^6	1.10×10^6
$1.434 < t/\tau_{D^0} \leq 1.506$	3.78×10^5	5.49×10^5	1.06×10^6	1.10×10^6
$1.506 < t/\tau_{D^0} \leq 1.580$	3.76×10^5	5.45×10^5	1.05×10^6	1.09×10^6
$1.580 < t/\tau_{D^0} \leq 1.656$	3.73×10^5	5.41×10^5	1.04×10^6	1.09×10^6
$1.656 < t/\tau_{D^0} \leq 1.735$	3.74×10^5	5.40×10^5	1.04×10^6	1.08×10^6
$1.735 < t/\tau_{D^0} \leq 1.818$	3.71×10^5	5.37×10^5	1.03×10^6	1.07×10^6
$1.818 < t/\tau_{D^0} \leq 1.904$	3.68×10^5	5.29×10^5	1.02×10^6	1.06×10^6
$1.904 < t/\tau_{D^0} \leq 1.996$	3.68×10^5	5.30×10^5	1.02×10^6	1.07×10^6
$1.996 < t/\tau_{D^0} \leq 2.094$	3.67×10^5	5.25×10^5	1.02×10^6	1.06×10^6
$2.094 < t/\tau_{D^0} \leq 2.201$	3.65×10^5	5.25×10^5	1.02×10^6	1.06×10^6
$2.201 < t/\tau_{D^0} \leq 2.316$	3.61×10^5	5.16×10^5	1.01×10^6	1.05×10^6
$2.316 < t/\tau_{D^0} \leq 2.443$	3.58×10^5	5.14×10^5	1.00×10^6	1.04×10^6
$2.443 < t/\tau_{D^0} \leq 2.586$	3.56×10^5	5.10×10^5	9.96×10^5	1.04×10^6
$2.586 < t/\tau_{D^0} \leq 2.747$	3.52×10^5	5.05×10^5	9.85×10^5	1.02×10^6
$2.747 < t/\tau_{D^0} \leq 2.935$	3.49×10^5	4.98×10^5	9.74×10^5	1.01×10^6
$2.935 < t/\tau_{D^0} \leq 3.160$	3.43×10^5	4.91×10^5	9.57×10^5	9.95×10^5
$3.160 < t/\tau_{D^0} \leq 3.442$	3.37×10^5	4.81×10^5	9.41×10^5	9.78×10^5
$3.442 < t/\tau_{D^0} \leq 3.819$	3.28×10^5	4.68×10^5	9.17×10^5	9.54×10^5
$3.819 < t/\tau_{D^0} \leq 4.390$	3.13×10^5	4.45×10^5	8.74×10^5	9.08×10^5
$4.390 < t/\tau_{D^0} \leq 5.553$	2.79×10^5	3.98×10^5	7.75×10^5	8.07×10^5
$5.553 < t/\tau_{D^0} \leq 20.00$	1.21×10^5	1.73×10^5	3.37×10^5	3.51×10^5
$0.600 < t/\tau_{D^0} \leq 20.00$	1.02×10^7	1.47×10^7	2.85×10^7	2.97×10^7

Table D.2 – Proper decay time bins definition. For each bin and for each subsample, the number of events after the sideband subtraction is reported. The events reported are for the $D^0 \to K^+K^-$ decays sample.

$D^0 \to K^+K^-$	11Up	11Dw	12Up	12Dw
$0.600 < t/\tau_{D^0} \leq 0.815$	2.32×10^4	3.35×10^4	5.69×10^4	5.88×10^4
$0.815 < t/\tau_{D^0} \leq 0.918$	3.33×10^4	4.95×10^4	9.32×10^4	9.59×10^4
$0.918 < t/\tau_{D^0} \leq 1.002$	3.78×10^4	5.65×10^4	1.08×10^5	1.11×10^5
$1.002 < t/\tau_{D^0} \leq 1.079$	3.95×10^4	5.89×10^4	1.15×10^5	1.17×10^5
$1.079 < t/\tau_{D^0} \leq 1.153$	4.14×10^4	6.12×10^4	1.19×10^5	1.22×10^5
$1.153 < t/\tau_{D^0} \leq 1.224$	4.19×10^4	6.22×10^4	1.20×10^5	1.23×10^5
$1.224 < t/\tau_{D^0} \leq 1.294$	4.21×10^4	6.22×10^4	1.20×10^5	1.24×10^5
$1.294 < t/\tau_{D^0} \leq 1.364$	4.27×10^4	6.36×10^4	1.23×10^5	1.26×10^5
$1.364 < t/\tau_{D^0} \leq 1.434$	4.33×10^4	6.32×10^4	1.22×10^5	1.27×10^5
$1.434 < t/\tau_{D^0} \leq 1.506$	4.36×10^4	6.40×10^4	1.24×10^5	1.28×10^5
$1.506 < t/\tau_{D^0} \leq 1.580$	4.39×10^4	6.43×10^4	1.24×10^5	1.28×10^5
$1.580 < t/\tau_{D^0} \leq 1.656$	4.42×10^4	6.40×10^4	1.24×10^5	1.27×10^5
$1.656 < t/\tau_{D^0} \leq 1.735$	4.44×10^4	6.44×10^4	1.24×10^5	1.28×10^5
$1.735 < t/\tau_{D^0} \leq 1.818$	4.45×10^4	6.48×10^4	1.24×10^5	1.27×10^5
$1.818 < t/\tau_{D^0} \leq 1.904$	4.40×10^4	6.38×10^4	1.23×10^5	1.27×10^5
$1.904 < t/\tau_{D^0} \leq 1.996$	4.44×10^4	6.44×10^4	1.24×10^5	1.27×10^5
$1.996 < t/\tau_{D^0} \leq 2.094$	4.44×10^4	6.40×10^4	1.23×10^5	1.28×10^5
$2.094 < t/\tau_{D^0} \leq 2.201$	4.46×10^4	6.47×10^4	1.24×10^5	1.28×10^5
$2.201 < t/\tau_{D^0} \leq 2.316$	4.41×10^4	6.42×10^4	1.23×10^5	1.27×10^5
$2.316 < t/\tau_{D^0} \leq 2.443$	4.43×10^4	6.36×10^4	1.24×10^5	1.27×10^5
$2.443 < t/\tau_{D^0} \leq 2.586$	4.42×10^4	6.34×10^4	1.24×10^5	1.27×10^5
$2.586 < t/\tau_{D^0} \leq 2.747$	4.40×10^4	6.26×10^4	1.23×10^5	1.26×10^5
$2.747 < t/\tau_{D^0} \leq 2.935$	4.36×10^4	6.23×10^4	1.21×10^5	1.25×10^5
$2.935 < t/\tau_{D^0} \leq 3.160$	4.30×10^4	6.18×10^4	1.21×10^5	1.24×10^5
$3.160 < t/\tau_{D^0} \leq 3.442$	4.22×10^4	6.10×10^4	1.19×10^5	1.22×10^5
$3.442 < t/\tau_{D^0} \leq 3.819$	4.13×10^4	5.87×10^4	1.16×10^5	1.19×10^5
$3.819 < t/\tau_{D^0} \leq 4.390$	3.96×10^4	5.65×10^4	1.11×10^5	1.14×10^5
$4.390 < t/\tau_{D^0} \leq 5.553$	3.50×10^4	5.03×10^4	9.82×10^4	1.02×10^5
$5.553 < t/\tau_{D^0} \leq 20.00$	1.54×10^4	2.15×10^4	4.29×10^4	4.39×10^4
$0.600 < t/\tau_{D^0} \leq 20.00$	1.18×10^6	1.71×10^6	3.32×10^6	3.41×10^6

Table D.3 – Proper decay time bins definition. For each bin and for each subsample, the number of events after the sideband subtraction is reported. The events reported are for the $D^0 \to \pi^+\pi^-$ decays sample.

$D^0 \to \pi^+\pi^-$	11Up	11Dw	12Up	12Dw
$0.600 < t/\tau_{D^0} \leq 0.815$	1.73×10^4	2.55×10^4	4.74×10^4	5.01×10^4
$0.815 < t/\tau_{D^0} \leq 0.918$	1.54×10^4	2.32×10^4	4.42×10^4	4.64×10^4
$0.918 < t/\tau_{D^0} \leq 1.002$	1.47×10^4	2.19×10^4	4.24×10^4	4.41×10^4
$1.002 < t/\tau_{D^0} \leq 1.079$	1.44×10^4	2.15×10^4	4.08×10^4	4.32×10^4
$1.079 < t/\tau_{D^0} \leq 1.153$	1.43×10^4	2.12×10^4	4.11×10^4	4.31×10^4
$1.153 < t/\tau_{D^0} \leq 1.224$	1.41×10^4	2.08×10^4	4.01×10^4	4.20×10^4
$1.224 < t/\tau_{D^0} \leq 1.294$	1.40×10^4	2.06×10^4	3.93×10^4	4.13×10^4
$1.294 < t/\tau_{D^0} \leq 1.364$	1.40×10^4	2.06×10^4	3.93×10^4	4.14×10^4
$1.364 < t/\tau_{D^0} \leq 1.434$	1.38×10^4	1.99×10^4	3.88×10^4	4.02×10^4
$1.434 < t/\tau_{D^0} \leq 1.506$	1.37×10^4	1.99×10^4	3.83×10^4	3.99×10^4
$1.506 < t/\tau_{D^0} \leq 1.580$	1.38×10^4	1.96×10^4	3.79×10^4	3.94×10^4
$1.580 < t/\tau_{D^0} \leq 1.656$	1.36×10^4	1.92×10^4	3.74×10^4	3.92×10^4
$1.656 < t/\tau_{D^0} \leq 1.735$	1.35×10^4	1.91×10^4	3.72×10^4	3.89×10^4
$1.735 < t/\tau_{D^0} \leq 1.818$	1.33×10^4	1.92×10^4	3.68×10^4	3.90×10^4
$1.818 < t/\tau_{D^0} \leq 1.904$	1.29×10^4	1.86×10^4	3.62×10^4	3.81×10^4
$1.904 < t/\tau_{D^0} \leq 1.996$	1.32×10^4	1.86×10^4	3.59×10^4	3.77×10^4
$1.996 < t/\tau_{D^0} \leq 2.094$	1.28×10^4	1.86×10^4	3.56×10^4	3.77×10^4
$2.094 < t/\tau_{D^0} \leq 2.201$	1.27×10^4	1.84×10^4	3.59×10^4	3.71×10^4
$2.201 < t/\tau_{D^0} \leq 2.316$	1.26×10^4	1.78×10^4	3.49×10^4	3.67×10^4
$2.316 < t/\tau_{D^0} \leq 2.443$	1.24×10^4	1.77×10^4	3.48×10^4	3.62×10^4
$2.443 < t/\tau_{D^0} \leq 2.586$	1.24×10^4	1.75×10^4	3.44×10^4	3.58×10^4
$2.586 < t/\tau_{D^0} \leq 2.747$	1.20×10^4	1.73×10^4	3.40×10^4	3.50×10^4
$2.747 < t/\tau_{D^0} \leq 2.935$	1.19×10^4	1.70×10^4	3.32×10^4	3.48×10^4
$2.935 < t/\tau_{D^0} \leq 3.160$	1.15×10^4	1.66×10^4	3.26×10^4	3.39×10^4
$3.160 < t/\tau_{D^0} \leq 3.442$	1.15×10^4	1.59×10^4	3.19×10^4	3.31×10^4
$3.442 < t/\tau_{D^0} \leq 3.819$	1.12×10^4	1.57×10^4	3.07×10^4	3.22×10^4
$3.819 < t/\tau_{D^0} \leq 4.390$	1.03×10^4	1.51×10^4	2.92×10^4	3.06×10^4
$4.390 < t/\tau_{D^0} \leq 5.553$	9.27×10^3	1.30×10^4	2.57×10^4	2.71×10^4
$5.553 < t/\tau_{D^0} \leq 20.00$	4.03×10^3	5.78×10^3	1.08×10^4	1.16×10^4
$0.600 < t/\tau_{D^0} \leq 20.00$	3.71×10^5	5.36×10^5	1.04×10^6	1.09×10^6

E Reweighing details

The procedure of reweighing is a common technique used in the high energy physics, in order to equalise the distributions of one or several variables. It is performed in several different ways, here the standard approach is discussed along with its drawbacks, particularly dangerous in an high precision measurement of *CP* asymmetry, as A_Γ. In order to overcome these difficulties, a new procedure to reweigh the data has been specifically developed for the measurement of A_Γ described in this thesis.

E.1 Symmetric reweigh

Let us suppose to have two classes of events, positive and negative events. Given a certain observable x, each class has its own distribution for x, as shown in fig. E.1a. Let us also suppose to known that these distributions are generated from the same parent distribution but they have been differently modified by the fact that events are reconstructed by a real detector. The idea is two use a reweigh procedure to restore their equality. A common choice is to reweigh one category, the negative events, to the other one, using as weights the ratio of the positive distribution to the negative distribution

$$\omega(x) = \frac{n^+(x)}{n^-(x)},$$

where $n^+(x)$ and $n^-(x)$ are the distributions of x for positive and negative events, respectively. Then, negative events are multiplied by the relative weight $\omega(x)$, obtaining the reweighed distribution $n^-_\omega(x)$, which is equal to the positive distribution $n^+(x)$ by construction, as shown in fig. E.1b. However, the choice of reweighing the negative events to the positive ones is arbitrary, since one can do the same thing reversing the procedure, namely reweighing the positive distribution to match the negative one, using the inverse weights

$$\nu(x) = \frac{n^-(x)}{n^+(x)},$$

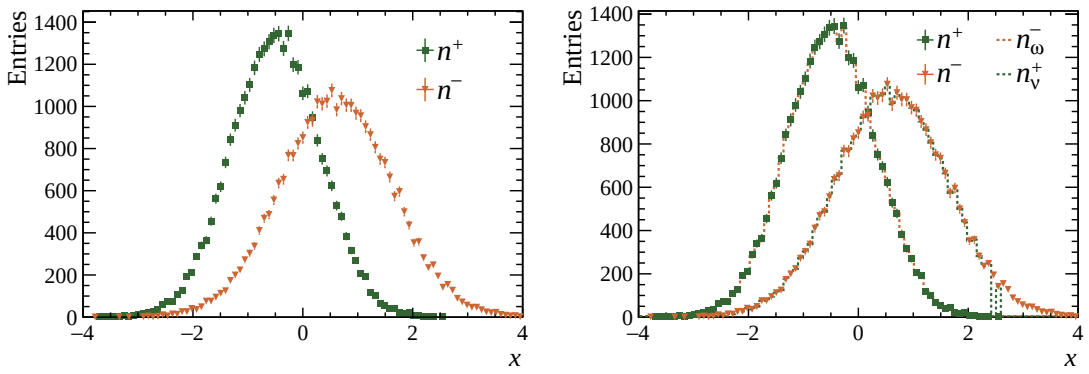

(a) Distribution of x.

(b) Distribution of x after the reweigh.

Figure E.1 – Distribution of x for positive and negative events and relative reweighed distributions.

as shown fig. E.1b. Applying these two procedures leads to an asymmetric situation since the final reweighed distributions are different, even achieving the purpose of making equal the two initial distributions. This is particularly dangerous when a measurement of asymmetry between two classes of events is performed because it is intrinsically asymmetric and it may introduce undesired artificial biases in the final measurement. Thus, a new method to reweigh the two categories is devised, where the final reweighed distribution is the same and it does not depend on the direction of the reweighing. This consists in reweighing the positive or the negative distribution using the following weights

$$v(x) = \sqrt{\frac{n^-(x)}{n^+(x)}} \text{ and } w(x) = \sqrt{\frac{n^+(x)}{n^-(x)}},$$

respectively. Thus, the reweighed distributions n^+_v and n^-_w are identical. They are placed somewhere between the two original distributions, and they do not depend on the choice to reweigh the negative to the positive events or the other way around, as shown in fig. E.2.

E.2 Reweigh procedure of the asymmetry

In each proper decay time bin, labelled by the index $\alpha = 1, \ldots, 29$, the time-dependent asymmetry, a^α_{raw}, is given by the expression

$$a^\alpha_{\text{raw}} = \frac{n^{\alpha+} - n^{\alpha-}}{n^{\alpha+} + n^{\alpha-}},$$

where $n^{\alpha\pm}$ are the number of reconstructed $D^{*\pm}$ decays in the decay time bin α. In order to correct for the detector-induced charge asymmetries, as explained in chap. 5, the distributions of positive and the negative charged soft pions must be opportunely equalised. Before de-

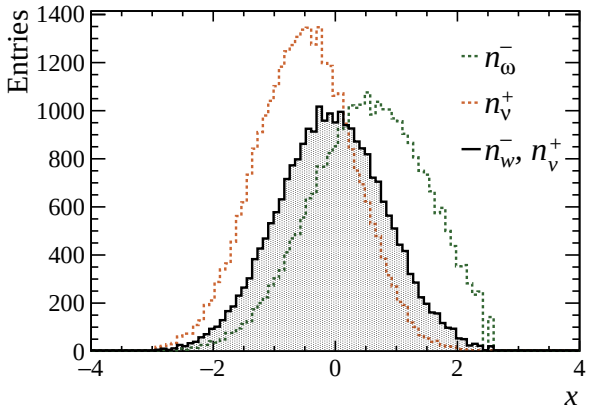

Figure E.2 – Distribution of x for positive and negative events along with the symmetric reweighed distribution, see text for details.

scribing the new devised reweigh procedure it is, however, very instructive to use the standard technique and show how it fails in the measurement of A_Γ described in this thesis.

With the standard procedure the reweigh can be done associating to each negative event a weight equal to

$$\omega_{l,i,j} = \frac{\sum_\alpha n^{\alpha+}_{l,-i,j}}{\sum_\alpha n^{\alpha-}_{l,i,j}}, \tag{E.1}$$

where the (k,θ_x,θ_y) bin is identified by the indexes (l,i,j). Thus, in each proper decay time bin the, the corrected asymmetry, $a^{\alpha}_{\mathrm{corr},w}$ is

$$a^{\alpha}_{\mathrm{corr},\omega} = \frac{\sum_{l,i,j} n^{\alpha+}_{l,i,j} - \sum_{l,i,j} \omega_{l,i,j}\, n^{\alpha-}_{l,i,j}}{\sum_{l,i,j} n^{\alpha+}_{l,i,j} + \sum_{l,i,j} \omega_{l,i,j}\, n^{\alpha-}_{l,i,j}}. \tag{E.2}$$

Alternatively, the positive events can be reweighed using as weights

$$\nu_{l,i,j} = \frac{\sum_\alpha n^{\alpha-}_{l,-i,j}}{\sum_\alpha n^{\alpha+}_{l,i,j}}, \tag{E.3}$$

and the relative corrected asymmetry is

$$a^{\alpha}_{\mathrm{corr},\nu} = \frac{\sum_{l,i,j} \nu_{l,i,j}\, n^{\alpha+}_{l,i,j} - \sum_{l,i,j} n^{\alpha-}_{l,i,j}}{\sum_{l,i,j} \nu_{l,i,j}\, n^{\alpha+}_{l,i,j} + \sum_{l,i,j} n^{\alpha-}_{l,i,j}}. \tag{E.4}$$

The two choices seem equivalent but they are not. Although these procedures correct the asymmetry and are widely used, they introduce a charge-bias in the corrected asymmetry, A_{corr}, since as explained in the previous section they are intrinsically asymmetric. The

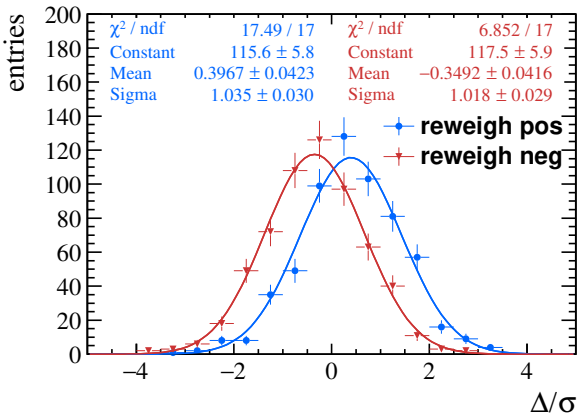

Figure E.3 – Results of A_Γ measured on charge-randomised $D^0 \to \pi^+\pi^-$ toys, reweighing positive events (blue dots) with weights reported in eq. (E.1) or negative events (red triangles) with weights reported in eq. (E.3).

amount of the bias introduced is generally very small and can be safely neglected, however the measurement described in this thesis does not allows such an approximation. A set of 600 pseudo-experiments based on charge randomised samples is generated and the two ways of reweighing, as reported in eq. (E.2) and eq. (E.4), are both applied to the same charge randomised sample (see sec. 4.7). The residuals of the A_Γ measurement on the charge randomised samples are reported in fig. E.3. Both the reweighing procedures introduce a bias in the measurement of A_Γ– the biases have almost the same magnitude but opposite sign. In the case of a *CP* measurement, as the one reported in this thesis, biases can be tracked down testing the procedure under the *CP* operator. Indeed, if the procedure does not introduce any bias the symmetry of the observable under *CP* remains unchanged. Thus, the correct asymmetry has to change sign under *CP*. To verify this, the *CP* operator is applied to the corrected asymmetry reported in eq. (E.2) obtaining

$$\begin{aligned} CP(a^{\alpha}_{\text{corr},\omega}) &= \frac{\sum_{l,i,j} n^{\alpha-}_{l,-i,j} - \sum_{l,i,j} CP(\omega_{l,i,j}) n^{\alpha+}_{l,-i,j}}{\sum_{l,i,j} n^{\alpha-}_{l,-i,j} + \sum_{l,i,j} CP(\omega_{l,i,j}) n^{\alpha+}_{l,-i,j}} \\ &= \frac{\sum_{l,i,j} n^{\alpha-}_{l,-i,j} - \sum_{l,i,j} \nu_{l,-i,j} n^{\alpha+}_{l,-i,j}}{\sum_{l,i,j} n^{\alpha-}_{l,-i,j} + \sum_{l,i,j} \nu_{l,-i,j} n^{\alpha+}_{l,-i,j}} = -a^{\alpha}_{\text{corr},\nu}. \end{aligned}$$

Reweighing the negative events with weights ω or the positive events with weights ν leads to a different result, thus the corrected asymmetry is not antisymmetric under *CP*, and this explains the observed biases.

Therefore, a new method to reweigh the (k, θ_x, θ_y) distribution of positive and negative charged pions is devised. The method consists into the reweigh of the positive and negative events

with the following weights

$$w_{l,i,j} = \sqrt{\omega_{l,i,j}} = \sqrt{\frac{\sum_\alpha n^{\alpha+}_{l,-i,j}}{\sum_\alpha n^{\alpha-}_{l,i,j}}} \quad \text{and} \quad v_{l,i,j} = \sqrt{\nu_{l,i,j}} = \sqrt{\frac{\sum_\alpha n^{\alpha-}_{l,-i,j}}{\sum_\alpha n^{\alpha+}_{l,i,j}}},$$

respectively. The corrected asymmetry is then

$$a^\alpha_{\text{corr}} = \frac{\sum_{l,i,j} v_{l,i,j} n^{\alpha+}_{l,i,j} - \sum_{l,i,j} w_{l,i,j} n^{\alpha-}_{l,i,j}}{\sum_{l,i,j} v_{l,i,j} n^{\alpha+}_{l,i,j} + \sum_{l,i,j} w_{l,i,j} n^{\alpha-}_{l,i,j}}, \tag{E.5}$$

and it can be easily proven that it does change sign under CP, $CP(a^\alpha_{\text{corr}}) = -a^\alpha_{\text{corr}}$, as the raw asymmetry. Thus, this new devised method overcomes the issues of the standard procedure, since the reweighing procedure cannot introduce any bias by definition. This is confirmed repeating the measurement on pseudo-experiments as explained in sec. 6.4.

E.3 Reweighing weights

The corrected asymmetry, reported in eq. (E.5), is calculated determining the weights for the reweighing from each decay mode. The number of the bins is driven by the $\pi^+\pi^-$ data sample, having the lower statistics, leading to a binning scheme of $(50 \times 55 \times 11)$ for the (k, θ_x, θ_y) distribution. Two-dimensional projections of the weights are reported in fig. E.4 for all the three decay modes: $D^0 \to K^-\pi^+$, $D^0 \to K^+K^-$ and $D^0 \to \pi^+\pi^-$. The weights are also compared between different modes, and in order to quantify the level of compatibility in each (k, θ_x, θ_y)-bin a pull variable is calculated as

$$\Delta_{\alpha,\beta}(k, \theta_x, \theta_y) = \frac{w_\alpha(k, \theta_x, \theta_y) - w_\beta(k, \theta_x, \theta_y)}{\sqrt{\sigma^2_\alpha + \sigma^2_\beta}},$$

where α, β represent the two decays modes in the comparison. w represents the weights and σ is its statistical uncertainty. The weights comparisons $\Delta_{K\pi,KK}$, $\Delta_{K\pi,\pi\pi}$ and $\Delta_{KK,\pi\pi}$ are reported in E.5.

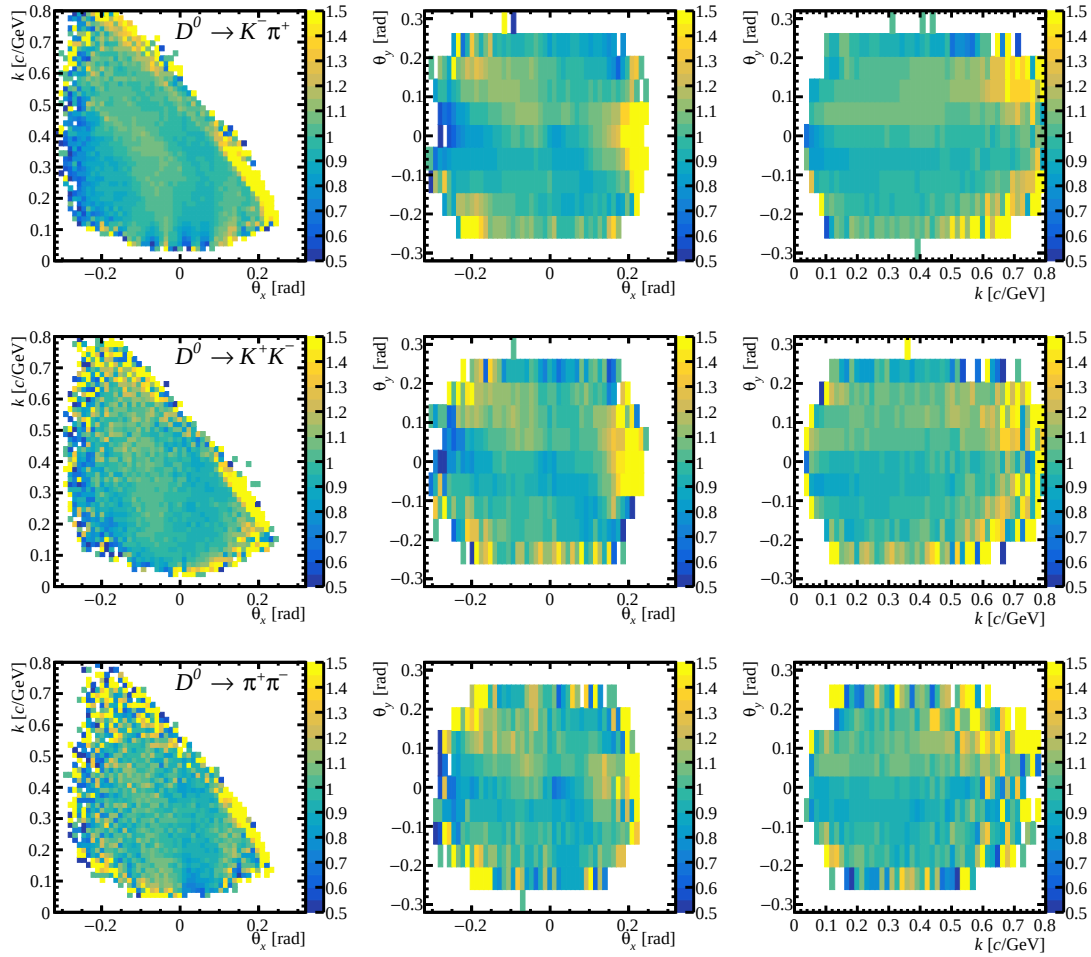

Figure E.4 – Symmetrisation procedure weights for (top) $D^0 \to K^-\pi^+$, (middle) $D^0 \to K^+K^-$ and (bottom) $D^0 \to \pi^+\pi^-$ decay modes, in 2012 *MagDown* sample.

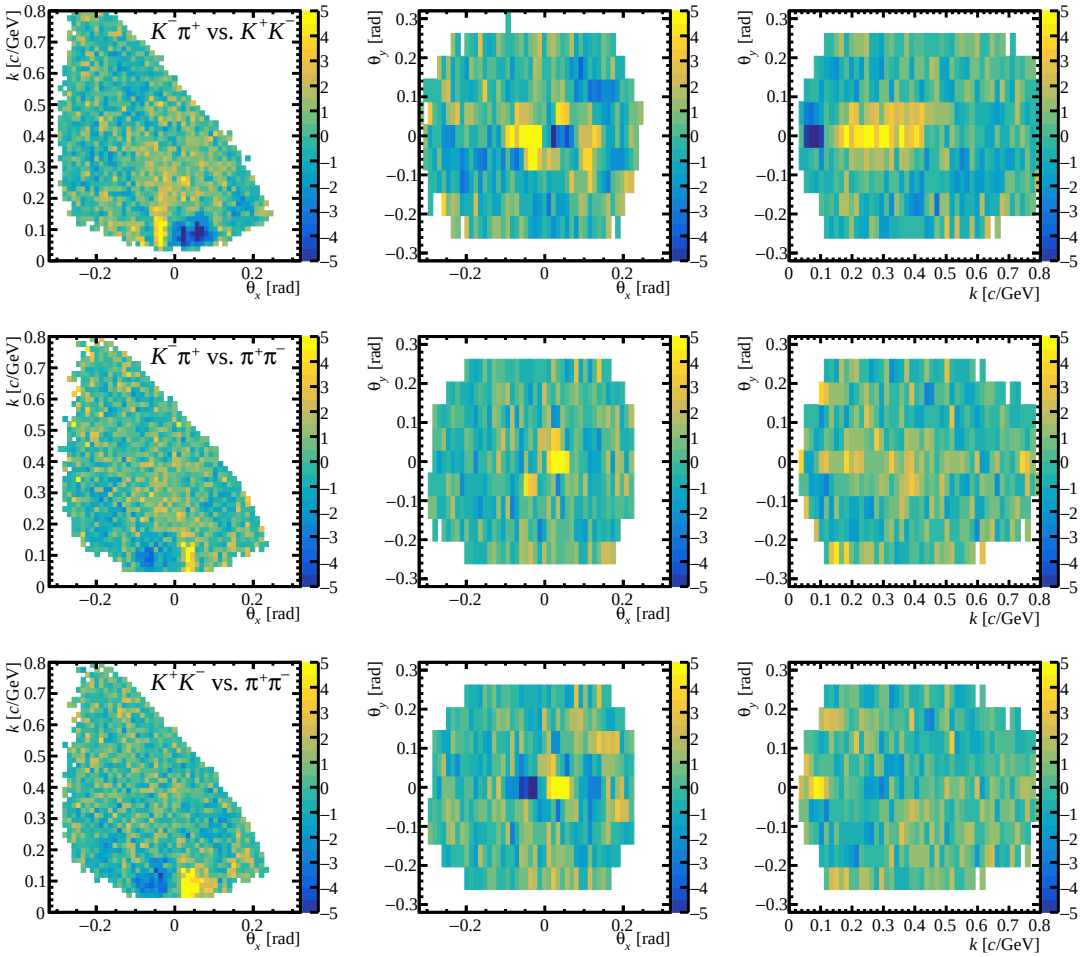

Figure E.5 – Comparison of weights of $D^0 \to K^-\pi^+$, $D^0 \to K^+K^-$ and $D^0 \to \pi^+\pi^-$ for 2012*MagDown* sample. The $\Delta_{\alpha,\beta}(k,\theta_x,\theta_y)$ distribution is plotted, see text for details.

E.4 Statistical degradation

The reweighing of the sample reduces the total number of events, N_{tot}, to an effective number of events, N_{eff}. The statistical degradation due the reweighing procedure can be calculated as

$$\frac{N_{\text{eff}}}{N_{\text{tot}}} = \frac{1}{N_{\text{tot}}} \frac{(\sum_\beta h_\beta)^2}{\sum_\beta h_\beta^2},$$

where h_β represents a generic weight $w_{l,i,j}$ or $v_{l,i,j}$ and β runs over the total number of events. Results are reported in tab. E.1, for $D^0 \to K^-\pi^+$, $D^0 \to K^+K^-$ and $D^0 \to \pi^+\pi^-$, while fig. E.6 reports the one-dimensional histogram of the weights. The net effect of degradation of the statistical uncertainties is very small, negligible with the quoted number of significant figures (see fig. 5.12). Some large weights may impact the measurement, thus a sanity check rejecting those events with weights outside the range $[2/3, 3/2]$ is performed. The value of $A_\Gamma^{K\pi}$ is unchanged.

Table E.1 – Statistical degradation due to correction procedure.

data sample	$D^0 \to K^-\pi^+$	$D^0 \to K^+K^-$	$D^0 \to \pi^+\pi^-$
2011 *MagUp*	0.996	0.963	0.965
2011 *MagDown*	0.997	0.988	0.975
2012 *MagUp*	0.997	0.988	0.982
2012 *MagDown*	0.997	0.989	0.985

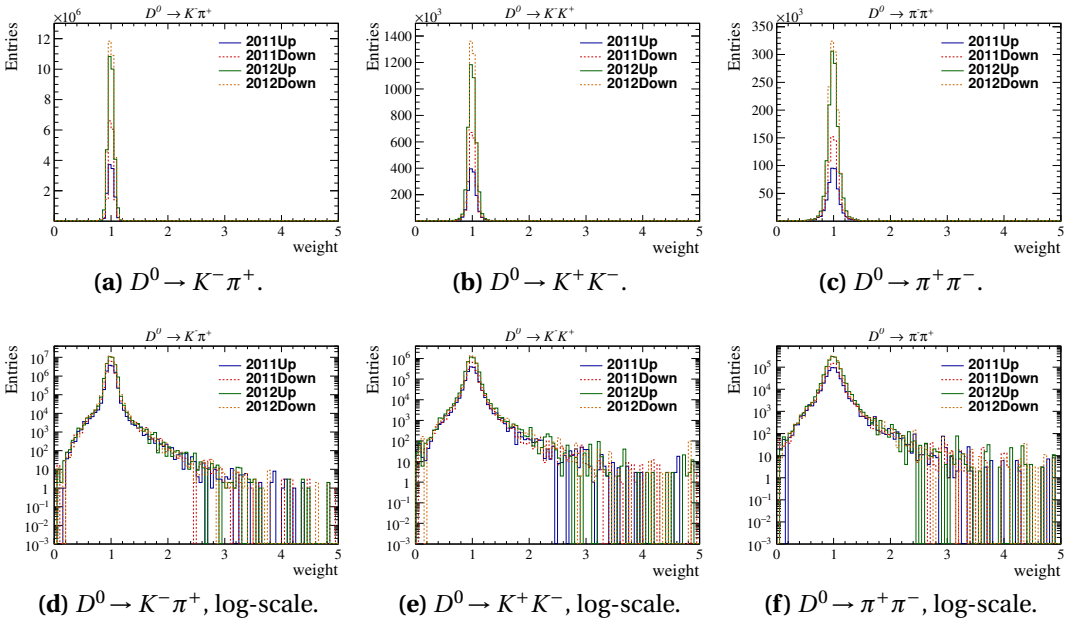

(a) $D^0 \to K^-\pi^+$. **(b)** $D^0 \to K^+K^-$. **(c)** $D^0 \to \pi^+\pi^-$.

(d) $D^0 \to K^-\pi^+$, log-scale. **(e)** $D^0 \to K^+K^-$, log-scale. **(f)** $D^0 \to \pi^+\pi^-$, log-scale.

Figure E.6 – Distribution of weights for the $D^0 \to K^-\pi^+$, $D^0 \to K^+K^-$ and $D^0 \to \pi^+\pi^-$ decay modes. Top in linear scale, bottom logarithmic scale.

F Studies of assumptions about secondary decays model

In order to determine the relative fraction of secondary decays $f_{\text{sec}}(t)$ the same acceptance function for prompt and secondary components is assumed, since the topology of a prompt D^* decay is close to the topology of a secondary decay at lower decay time values (see chap. 7). Here it is verified that the assessed systematic uncertainty on the presence of the secondary decays in our final data sample conservatively covers for any effect due to possible differences in the acceptance function between prompt and secondary component.

A kinematic phase space simulation (toy-MC) of prompt $D^{*+} \to D^0\pi^+$ decays and secondary D^{*+} decays coming from $B^0 \to D^{*+}\mu^-\overline{\nu}_\mu$ decays, as a representative of the mixture of secondary decays, where the standard LHCb distributions for the input momenta spectra, extracted from PYTHIA, of B^0 and D^{*+} mother particles are used and the returned decay time is smeared with a Gaussian resolution of $\sigma_t = 50\,\text{fs}$. In order to approximately reproduce the main features of momenta and lifetimes related quantities in the LHCb geometrical acceptance a set of minimal kinematic requirements are applied, that are reported on tab. F.1. Since

Table F.1 – Summary of kinematic requirements applied in the toy-MC. The letter h stands for either K or π.

Quantity	Requirements	Units
$\theta(h)$	$\in [150, 300]$	mrad
$p_{\text{T}}(h)$	> 800	MeV/c
$p(h)$	> 5	GeV/c
Impact parameter IP(h)	> 0.08	mm
$p_{\text{T}}(D^0)$	> 2	GeV/c
$p(D^0)$	> 5	GeV/c
Cosine of D^0 pointing angle (a.k.a. DIRA)	> 0.9999	-

the PV is not simulated in this simple toy-MC (this is well beyond the aim of these studies), the effect of cutting on the $\chi^2_{\text{IP}}(h)$ is reproduced by requiring the impact parameter of the D^0 daughters to be larger than 0.08 mm. This value has been chosen to reproduce the falling of

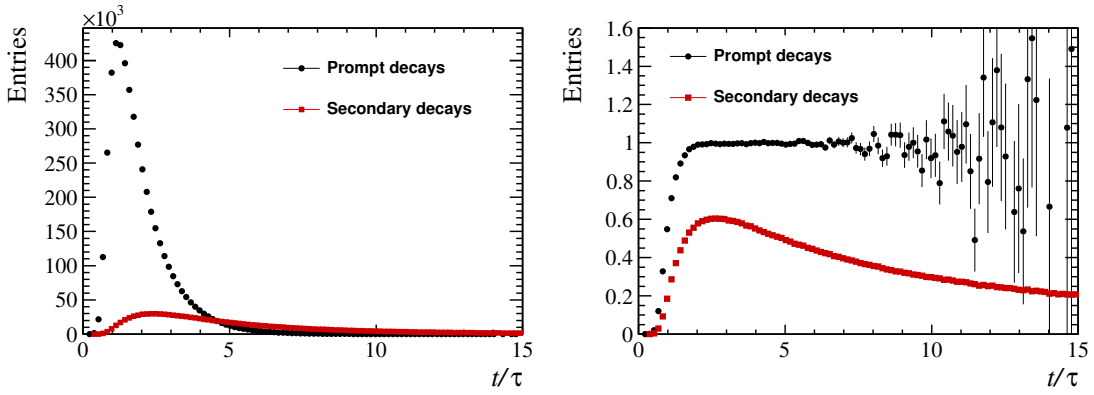

(a) Reconstructed decay time.

(b) Acceptance functions.

Figure F.1 – Reconstructed decay time distribution and acceptances of simulated prompt and secondary components.

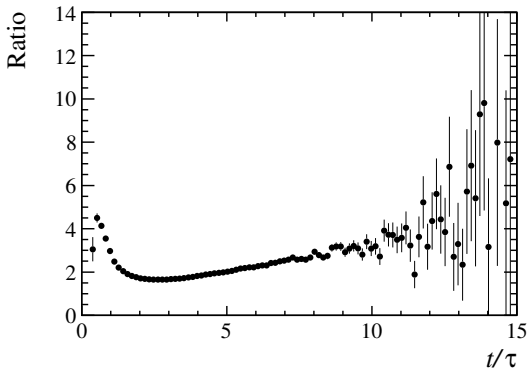

Figure F.2 – Ratio between acceptance functions of prompt component to secondary component.

the IP(h) distribution observed in data.

10^9 prompt decays and 10^9 secondary decays are generated, and the proper decay time distributions for both the components, passing the selection of tab. F.1, is reported in fig. F.1, along with the total reconstruction acceptances. The resulting decay time distribution of prompt component is similar to that one extracted from data of fig. 5.1, reassuring that this simple toy-MC simulation is able to reproduce at least the main kinematic features of data.

The ratio between the two acceptance functions, of prompt and secondary components, is shown in fig. F.2 and, as expected, is not flat. The extraction of $f_{\text{sec}}(t)$ is repeated using the same procedure described in chap. 7 by scaling the proper decay time distribution of secondary decays of the central analysis (analytical model sculpted with the acceptance from data) with the acceptance ratio of fig. F.2 extracted from the toy-MC. Figure F.3 shows the

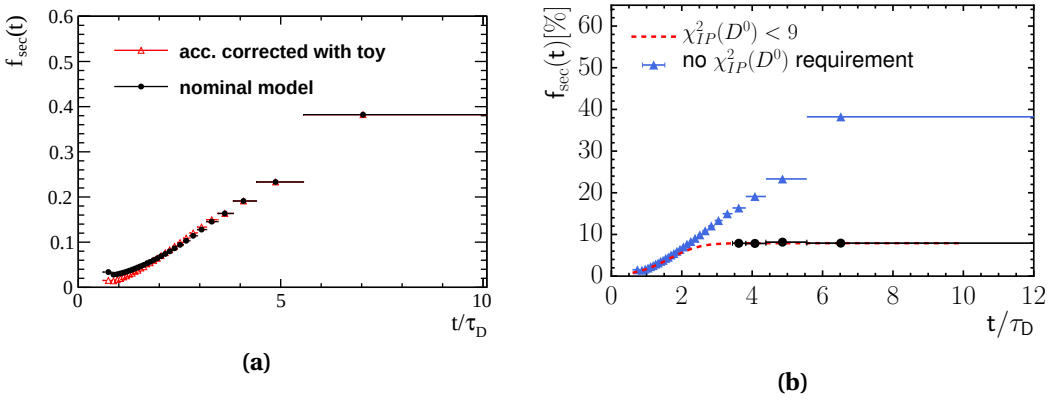

Figure F.3 – (a) Comparison between f_{sec} extracted by using the model of the central analysis and f_{sec} extracted by accounting for the acceptance ratio between prompt and secondary component. (b) Extraction of f_{sec} when the acceptance ratio is accounted for.

comparison between $f_{\text{sec}}(t)$ extracted by using the model of the central analysis and $f_{\text{sec}}(t)$ extracted by accounting for the acceptance ratio between prompt and secondary component (fig. F.3a), and the extraction of $f_{\text{sec}}(t)$ when the acceptance ratio is accounted for (fig. F.3b). The two curves are very close and the difference in assessing the systematic uncertainty by using and not using the acceptance ratio is equal to 0.02×10^{-3}. This is smaller than the quoted uncertainties for the secondary contamination due to the variations of $f_{\text{sec}}(t)$ of 0.041×10^{-3} and 0.026×10^{-3} for the $D^0 \to K^+K^-$ and $D^0 \to \pi^+\pi^-$, respectively, as reported in tab. 7.2, and it is much smaller than the total systematic uncertainties assessed for the presence of secondary decays contamination, 0.08×10^{-3} and 0.12×10^{-3} for the $D^0 \to K^+K^-$ and $D^0 \to \pi^+\pi^-$, respectively

Bibliography

[1] N. Cabibbo, "Unitary Symmetry and Leptonic Decays", Phys. Rev. Lett. **10**, 531–533 (1963) (cit. on pp. 1, 9).

[2] M. Kobayashi and T. Maskawa, "*CP* Violation in the Renormalizable Theory of Weak Interaction", Prog. Theor. Phys. **49**, 652–657 (1973) (cit. on pp. 1, 9).

[3] S. Bianco et al., "A Cicerone for the physics of charm", Riv. Nuovo Cim. **26N7**, 1–200 (2003), arXiv:hep-ex/0309021 [hep-ex] (cit. on p. 2).

[4] G. Burdman and I. Shipsey, "D^0 - $\overline{D}^0$ mixing and rare charm decays", Ann. Rev. Nucl. Part. Sci. **53**, 431–499 (2003), arXiv:hep-ph/0310076 [hep-ph] (cit. on p. 2).

[5] I. Shipsey, "Status of charm flavor physics", Int. J. Mod. Phys. **A21**, 5381–5403 (2006), arXiv:hep-ex/0607070 [hep-ex] (cit. on p. 2).

[6] M. Artuso et al., "Charm Meson Decays", Ann. Rev. Nucl. Part. Sci. **58**, 249–291 (2008), arXiv:0802.2934 [hep-ph] (cit. on p. 2).

[7] I. I. Y. Bigi et al., "Production and Decay Properties of Ultraheavy Quarks", Phys. Lett. **B181**, 157–163 (1986) (cit. on p. 2).

[8] R. Aaij et al. (LHCb collaboration), "Observation of D^0–$\overline{D}^0$ oscillations", Phys. Rev. Lett. **110**, 101802 (2013), arXiv:1211.1230 [hep-ex] (cit. on pp. 2, 106, 118, 119).

[9] M. Bobrowski et al., "How Large Can the SM Contribution to *CP* Violation in D^0–$\overline{D}^0$ Mixing Be?", JHEP **03**, 009 (2010), arXiv:1002.4794 [hep-ph] (cit. on pp. 2, 17).

[10] Y. Amhis et al., "Averages of b-hadron, c-hadron, and τ-lepton properties as of summer 2016", updated results and plots available at `http://www.slac.stanford.edu/xorg/hfag/` (2016), arXiv:1612.07233 [hep-ex] (cit. on pp. 3, 21, 22, 25, 27, 131).

[11] P. Marino, "Mixing and indirect *CP* violation using two-body decays at LHCb", in VIII International Workshop On Charm Physics (2016) (cit. on p. 3).

[12] P. Marino et al. (LHCb collaboration), *CP-violating asymmetries from the decay-time distribution of prompt $D^0 \to K^+K^-$ and $D^0 \to \pi^+\pi^-$ decays in the full LHCb Run 1 data sample. Measurement using yield asymmetries in bins of decay time.* Tech. rep. (LHCb-CONF-2016-009, 2016) (cit. on p. 3).

[13] R. Aaij et al. (LHCb collaboration), "Measurement of the *CP* violation parameter A_Γ in $D^0 \to K^+K^-$ and $D^0 \to \pi^+\pi^-$ decays", Accepted for publication to Physical Review Letters (2017), arXiv:1702.06490 [hep-ex] (cit. on p. 3).

[14] Y. Nir, "*CP* violation in and beyond the standard model", in Proceedings, 27th SLAC Summer Institute on Particle Physics (SSI 99) (1999), pp. 165–243, arXiv:hep-ph/9911321 [hep-ph] (cit. on p. 5).

[15] M. E. Peskin and D. V. Schroeder, *An Introduction to quantum field theory* (Addison–Wesley, 1995) (cit. on p. 5).

[16] S. L. Glashow, "Partial Symmetries of Weak Interactions", Nucl. Phys. **22**, 579–588 (1961) (cit. on p. 5).

[17] S. Weinberg, "A Model of Leptons", Phys. Rev. Lett. **19**, 1264–1266 (1967) (cit. on p. 5).

[18] A. Salam, *Elementary Particle Theory*, edited by N. Svartholm (Almquist and Wiksells, Stockholm, 1969) (cit. on p. 5).

[19] I. I. Y. Bigi, "*CP* violation: An Essential mystery in nature's grand design", Surveys High Energ. Phys. **12**, 269–336 (1998), arXiv:hep-ph/9712475 [hep-ph] (cit. on p. 8).

[20] C. Patrignani et al., "Review of Particle Physics", Chin. Phys. **C40**, 100001 (2016) (cit. on pp. 10, 14, 21, 29, 30, 41, 59, 65, 76, 107).

[21] Y. H. Ahn et al., "Wolfenstein Parametrization at Higher Order: Seeming Discrepancies and Their Resolution", Phys. Lett. **B703**, 571–575 (2011), arXiv:1106.0935 [hep-ph] (cit. on p. 10).

[22] J. Charles et al. (CKMfitter Group collaboration), "*CP* violation and the CKM matrix: Assessing the impact of the asymmetric *B* factories", Eur. Phys. J. **C41**, 1–131 (2005), arXiv:hep-ph/0406184 [hep-ph] (cit. on pp. 11, 12).

[23] V. Weisskopf and E. Wigner, "Berechnung der natürlichen linienbreite auf grund der diracschen lichttheorie", Zeitschrift für Physik **63**, 54–73 (1930) (cit. on p. 14).

[24] A. F. Falk et al., "$SU(3)$ breaking and D^0–$\overline{D}^0$ mixing", Phys. Rev. **D65**, 054034 (2002), arXiv:hep-ph/0110317 [hep-ph] (cit. on p. 17).

[25] E. Golowich and A. A. Petrov, "Short distance analysis of D^0–$\overline{D}^0$ mixing", Phys. Lett. **B625**, 53–62 (2005), arXiv:hep-ph/0506185 [hep-ph] (cit. on p. 17).

[26] A. A. Petrov, "Charm mixing in the Standard Model and beyond", Int. J. Mod. Phys. **A21**, 5686–5693 (2006), arXiv:hep-ph/0611361 [hep-ph] (cit. on p. 18).

[27] I. I. Y. Bigi and N. G. Uraltsev, "D^0–$\overline{D}^0$ oscillations as a probe of quark hadron duality", Nucl. Phys. **B592**, 92–106 (2001), arXiv:hep-ph/0005089 [hep-ph] (cit. on p. 18).

[28] T. Ohl et al., "D^0–$\overline{D}^0$ mixing in heavy quark effective field theory: The Sequel", Nucl. Phys. **B403**, 605–632 (1993), arXiv:hep-ph/9301212 [hep-ph] (cit. on p. 18).

[29] H.-Y. Cheng and C.-W. Chiang, "Long-Distance Contributions to D^0–$\overline{D}^0$ Mixing Parameters", Phys. Rev. **D81**, 114020 (2010), arXiv:1005.1106 [hep-ph] (cit. on p. 18).

[30] T. Gershon et al., "Contributions to the width difference in the neutral D system from hadronic decays", Phys. Lett. **B750**, 338–343 (2015), arXiv:1506.08594 [hep-ph] (cit. on p. 18).

[31] A. L. Kagan and M. D. Sokoloff, "On Indirect CP Violation and Implications for D^0-$\overline{D}^0$ and B_s^0-$\overline{B}_s^0$ mixing", Phys. Rev. **D80**, 076008 (2009), arXiv:0907.3917 [hep-ph] (cit. on p. 22).

[32] D.-s. Du, "Searching for Possible Large CP Violation Effects in Neutral Charm Meson Decays", Phys. Rev. **D34**, 3428 (1986) (cit. on p. 26).

[33] M. Staric (Belle collaboration), "New Belle results on D^0-$\overline{D}^0$ mixing", in Proceedings, 5th International Workshop on Charm Physics (Charm 2012) (2012), arXiv:1212.3478 (cit. on pp. 31, 34, 35, 123, 124).

[34] J. P. Lees et al. (BaBar collaboration), "Measurement of $D^0 - \overline{D}^0$ Mixing and CP Violation in Two-Body D^0 Decays", Phys. Rev. **D87**, 012004 (2013), arXiv:1209.3896 [hep-ex] (cit. on pp. 31, 34, 35, 123, 124).

[35] M. Gersabeck et al., "A Monte Carlo simulation free method of measuring lifetimes using event-by-event acceptance functions at LHCb", CERN-LHCb-PUB-2009-022 (2009) (cit. on p. 31).

[36] R. Aaij et al. (LHCb collaboration), "Measurements of indirect CP asymmetries in $D^0 \to K^-K^+$ and $D^0 \to \pi^-\pi^+$ decays", Phys. Rev. Lett. **112**, 041801 (2014), arXiv:1310.7201 [hep-ex] (cit. on pp. 31, 34, 36–38, 81, 118, 119, 123).

[37] V. V. Gligorov et al., "Swimming: A data driven acceptance correction algorithm", J. Phys. Conf. Ser. **396**, 022016 (2012) (cit. on p. 31).

[38] T. A. Aaltonen et al. (CDF collaboration), "Measurement of indirect CP-violating asymmetries in $D^0 \to K^+K^-$ and $D^0 \to \pi^+\pi^-$ decays at CDF", Phys. Rev. **D90**, 111103 (2014), arXiv:1410.5435 [hep-ex] (cit. on pp. 31, 34, 35, 123, 124).

[39] R. Aaij et al. (LHCb collaboration), "Measurement of indirect CP asymmetries in $D^0 \to K^-K^+$ and $D^0 \to \pi^-\pi^+$ decays using semileptonic B decays", JHEP **04**, 043 (2015), arXiv:1501.06777 [hep-ex] (cit. on pp. 31, 34, 36, 123, 124, 126, 127).

[40] S. Bergmann et al., "Lessons from CLEO and FOCUS measurements of D^0-$\overline{D}^0$ mixing parameters", Phys. Lett. **B486**, 418–425 (2000), arXiv:hep-ph/0005181 [hep-ph] (cit. on p. 33).

[41] L. Evans and P. Bryant, "LHC Machine", JINST **3**, S08001 (2008) (cit. on pp. 39, 40).

[42] T. Sjostrand et al., "PYTHIA 6.4 Physics and Manual", JHEP **05**, 026 (2006), arXiv:hep-ph/0603175 [hep-ph] (cit. on p. 42).

[43] R. Aaij et al. (LHCb collaboration), "LHCb Detector Performance", Int. J. Mod. Phys. **A30**, 1530022 (2015), arXiv:1412.6352 [hep-ex] (cit. on pp. 44, 55).

[44] P. R. Barbosa-Marinho et al., *LHCb VELO (VErtex LOcator): Technical Design Report*, tech. rep. (CERN-LHCC-2001-011, Geneva, 2001) (cit. on p. 45).

[45] A. A. Alves Jr. et al. (LHCb collaboration), "The LHCb Detector at the LHC", JINST **3**, S08005 (2008) (cit. on pp. 46, 50, 51).

[46] P. R. Barbosa-Marinho et al. (LHCb collaboration), *LHCb inner tracker: Technical Design Report*, tech. rep. (CERN-LHCC-2002-029, Geneva, 2002) (cit. on pp. 47, 48).

[47] Silicon Tracker UZH Group, *Material for publications*, accessed 5 November 2016, http://lhcb.physik.uzh.ch/ST/public/material/index.php (cit. on p. 47).

[48] R. Arink et al. (LHCb Outer Tracker collaboration), "Performance of the LHCb Outer Tracker", JINST **9**, P01002 (2014), arXiv:1311.3893 [physics.ins-det] (cit. on pp. 48, 49).

[49] S. Amato et al. (LHCb collaboration), *LHCb calorimeters: Technical Design Report*, tech. rep. (CERN-LHCC-2000-036, Geneva, 2000) (cit. on p. 50).

[50] E. Picatoste Olloqui (LHCb collaboration), "LHCb preshower(PS) and scintillating pad detector (SPD): Commissioning, calibration, and monitoring", J. Phys. Conf. Ser. **160**, 012046 (2009) (cit. on p. 51).

[51] I. Machikhiliyan (LHCb collaboration), "Current status and performance of the LHCb electromagnetic and hadron calorimeters", J. Phys. Conf. Ser. **293**, 012052 (2011) (cit. on p. 51).

[52] A. A. Alves Jr. et al., "Performance of the LHCb muon system", JINST **8**, P02022 (2013), arXiv:1211.1346 [physics.ins-det] (cit. on pp. 51, 52).

[53] R. Fruhwirth, "Application of Kalman filtering to track and vertex fitting", Nucl. Instrum. Meth. **A262**, 444–450 (1987) (cit. on p. 55).

[54] M. Needham, *Clone Track Identification using the Kullback-Liebler Distance*, tech. rep. LHCb-2008-002. CERN-LHCb-2008-002. LPHE-2008-002 (CERN, Geneva, 2008) (cit. on p. 55).

[55] M. Adinolfi et al. (LHCb RICH Group collaboration), "Performance of the LHCb RICH detector at the LHC", Eur. Phys. J. **C73**, 2431 (2013), arXiv:1211.6759 [physics.ins-det] (cit. on p. 57).

[56] M. Ferro-Luzzi et al., *Determination of the aperture of the LHCb VELO RF foil*, tech. rep. (LHCb-PUB-2014-012, Geneva, 2014) (cit. on p. 65).

[57] W. D. Hulsbergen, "Decay chain fitting with a Kalman filter", Nucl. Instrum. Meth. **A552**, 566–575 (2005), arXiv:physics/0503191 [physics] (cit. on p. 66).

[58] N. L. Johnson, "Systems of frequency curves generated by methods of translation", Biometrika **36**, 149–176 (1949) (cit. on p. 69).

[59] R. Aaij et al. (LHCb collaboration), "Measurement of D^0–$\overline{D}^0$ Mixing Parameters and Search for *CP* Violation Using $D^0 \to K^+\pi^-$ Decays", Phys. Rev. Lett. **111**, 251801 (2013), arXiv:1309.6534 [hep-ex] (cit. on pp. 106, 118, 119).

[60] R. Aaij et al. (LHCb collaboration), "Measurement of the $\overline{B}^0$–B^0 and $\overline{B}^0_s$–B^0_s production asymmetries in pp collisions at $\sqrt{s} = 7\,\text{TeV}$", Phys. Lett. **B739**, 218–228 (2014), arXiv:1408.0275 [hep-ex] (cit. on p. 106).

[61] R. Aaij et al. (LHCb collaboration), "Evidence for *CP* violation in time-integrated $D^0 \to h^- h^+$ decay rates", Phys. Rev. Lett. **108**, 111602 (2012), arXiv:1112.0938 [hep-ex] (cit. on p. 119).

[62] R. Nisius, "On the combination of correlated estimates of a physics observable", Eur. Phys. J. **C74**, 3004 (2014), arXiv:1402.4016 [physics.data-an] (cit. on p. 124).

[63] R. Aaij et al. (LHCb collaboration), "Measurement of the difference of time-integrated *CP* asymmetries in $D^0 \to K^- K^+$ and $D^0 \to \pi^- \pi^+$ decays", Phys. Rev. Lett. **116**, 191601 (2016), arXiv:1602.03160 [hep-ex] (cit. on p. 126).

[64] R. Aaij et al. (LHCb collaboration), "Measurement of *CP* asymmetry in $D^0 \to K^- K^+$ and $D^0 \to \pi^- \pi^+$ decays", JHEP **07**, 041 (2014), arXiv:1405.2797 [hep-ex] (cit. on p. 126).

[65] R. Aaij et al. (LHCb collaboration), "Measurement of mixing and *CP* violation parameters in two-body charm decays", JHEP **04**, 129 (2012), arXiv:1112.4698 [hep-ex] (cit. on p. 126).

[66] R. Aaij et al. (LHCb collaboration), "Measurement of *CP* asymmetry in $D^0 \to K^- K^+$ decays", (2016), arXiv:1610.09476 [hep-ex] (cit. on pp. 125–127).